TESIS DE LA UNIVERSIDAD DE ZARAGOZA

2021 241

María Pilar Jiménez Cavero

Thermal spin transport in maghemite-based thin film structures

Director/es
Morellón Alquézar, Luis Alberto
Lucas del Pozo, Irene

ISSN 2254-7606

Prensas de la Universidad
Universidad Zaragoza

ISSN 2254-7606

Universidad Zaragoza
1542

Tesis Doctoral

THERMAL SPIN TRANSPORT IN MAGHEMITE-BASED THIN FILM STRUCTURES

Autor

María Pilar Jiménez Cavero

Director/es

Morellón Alquézar, Luis Alberto
Lucas del Pozo, Irene

UNIVERSIDAD DE ZARAGOZA
Escuela de Doctorado

2021

PhD Thesis

Thermal spin transport in maghemite-based thin film structures

María del Pilar Jiménez Cavero

February 2021

Departamento de Física de la Materia Condenasada
Facultad de Ciencias
Universidad de Zaragoza

Supervisors:
Dr. Irene Lucas del Pozo
Prof. Luis A. Morellón Alquézar

Thesis supervisors:

Prof. Luis Morellón Alquézar, full professor at the University of Zaragoza in the Condensed Matter Physics department and Dean of the Faculty of Science; and **Dr. Irene Lucas del Pozo**, assistant professor at the University of Zaragoza in the Condensed Matter Physics department.

Financial acknowledgment:

- Ayudas para la formación de profesorado universitario (programa FPU) del Ministerio de Educación, Cultura y Deporte. Referencia: FPU014/02546 (Predoctoral research grant of the Spanish Government).
- Ayudas de movilidad para estancias breves en centros en el extranjero para beneficiarios del programa FPU. Referencia: EST17/00382 (Grant for research stays abroad of the Spanish Government).
- Ayuda del Programa Ibercaja-CAI de Estancias de investigación. Referencia: CB 11/18 (Grant for research stays of the Ibercaja-CAI Foundation).

"It is better to be lucky. But I would rather be exact. Then when luck comes you are ready."

The Old Man and the Sea. E. Hemingway.

Contents

Agradecimientos (Acknowledgements)

El trabajo desarrollado en esta Tesis Doctoral ha involucrado el esfuerzo y apoyo de un gran número de personas y deben por tanto ser reconocidos aquí.

Comenzaré con mis directores de tesis: Luis Morellón e Irene Lucas. Luis me dio la oportunidad de acercarme por primera vez al trabajo científico en aquel verano después del tercer año de carrera: gracias por depositar tu confianza en mí en ese momento, que fue el detonador de todo lo que vino después. Quiero agradecerte también que siempre hayas sido capaz de sacar un hueco para mí, para guiarme, discutir resultados, ayudarme con la burocracia o simplemente hablar de cualquier cosa. Irene: gracias, porque desde el primer momento me acogiste en el laboratorio, y ejerciste no solo como mentora sino también como amiga. Hemos recorrido un largo camino juntas.

Quiero agradecer también el papel del profesor Pedro Algarabel, por sus comentarios siempre constructivos y por su enorme ayuda para sacar el trabajo adelante. Asimismo querría agradecer al profesor Ricardo Ibarra el haberme acogido en su grupo, las palabras de ánimo y el interés en mi tesis. También agradecer al profesor Jose María de Teresa su disposición constante a la colaboración.

Todos los usuarios del laboratorio de crecimiento de películas delgadas me han brindado su ayuda y sus enseñanzas en un momento u otro: José Ángel (muchas gracias por todas tus palabras de ánimo, y especialmente, por ayudarme a poner en marcha el láser nuevo el último día antes de las vacaciones de Semana Santa), Eric, Pavel, Lorena y Laura, gracias a todos. Pavel: muchas gracias por estar siempre disponible para ayudar a que las cosas funcionen, en el PLD y en el magnetocacharro. Igualmente, quiero agradecer al equipo de técnicos del INMA su disposición infinita

a ofrecer asistencia, soluciones y formación, así como a estimular la vida social del grupo: especialmente, a Carlos y Guillermo, que tanto me han ayudado con los problemas del laboratorio; pero también a Rubén, Laura, Isabel, Gala, Rodrigo, Alfonso, Teo y José Luis. Con todos ellos he pasado buenos ratos y aprendido muchas cosas valiosas.

Al profesor Francisco Rivadulla, de la Universidad de Santiago de Compostela: muchas gracias por la fructífera colaboración, decisiva en esta tesis. Gracias, David y Carlos, por las medidas de conductividad térmica. Gracias a todos los integrantes pasados y presentes de este grupo, por acogerme en las diversas visitas y mostrarme las maravillas de la ciudad de Santiago.

I would like to show my gratitude to Prof. Tobias Kampfrath at the Freie Universität in Berlin and his team for hosting me in their lab and give me the opportunity to join them for some months. I felt very welcome by the whole group and learnt a lot about terahertz physics. I would like to say thank you especially to the oscillator users: Reza, Olli and Lukáš; I am fortunate to have found such good friends in such a short period of time, and share not only work but also same great trips with you.

Quiero asimismo agradecer toda la asistencia recibida del personal de Administración, de todos ellos, pero muy especialmente de Raúl (que no es del valle del Cidacos pero casi) y María Jesús.

Quiero dar las gracias de corazón a la Dra. Soraya Sangiao, por estar disponible para ayudarme y resolver dudas de toda índole siempre que lo he necesitado, y por todas tus palabras de aliento.

Mcuhas gracias también al Dr. César Magén por los cafés, las conversaciones, las recomendaciones cinéfilas y literarias, y el tinticola; en suma, por tu amistad. Y, por supuesto, también por las imágenes y análisis varios de TEM.

Mi agradecimiento más profundo al ya Dr. Alberto Anadón, que me enseñó todos los secretos de las medidas termoeléctricas y siempre me ha echado un cable cuando lo he necesitado. Gracias también por ser uno de los amigos que he encontrado estos años; el trabajo se hace infinitamente más agradable cuando lo llevas a cabo rodeado

de amigos. Después de todo este tiempo, la lista es, por suerte para mí, larguísima. A todos os agradezco el haber estado ahí: Isma, gracias por tu conversación siempre interesante, por las aficiones compartidas y por enseñarme el camino al Monte Perdido; Jose, gracias por regalarnos tu maravilloso humor y por entendernos tan bien; Laura, mejor no decimos nada; Inés, gracias por ofrecer siempre tu visión sincera de las cosas; Mari, gracias por los buenos ratos compartidos; María, por tu alegría y tu estilazo, eres mi *it girl* de referencia; a la pequeña gran familia formada por Luis, Bea y el Cobra, daros las gracias se quedaría corto; gracias a Javi y Mario, que llegaron un poco tarde, y con los que he compartido el discurrir de la tesis; Pablo (que me ha adelantado por la derecha), para mí representas el nexo entre dos generaciones: la que acabo de mencionar y la de las últimas incorporaciones: Rubén, Amelia, Leyre, Rafa y Alba. Barri, me niego incluirte entre los nuevos; lo nuestro viene de lejos. Gracias a todos por los buenísimos ratos que hemos pasado juntos, dentro y fuera del IN(M)A.

Poder tratar de ayudar a otros como antes me ayudaron a mí ha sido una experiencia muy enriquecedora. Por eso, quiero mencionar a todos los estudiantes de TFG y TFM que han pasado: Raquel, Marta, Jorge, Javier, Eduardo y Abel. De todos vosotros aprendí algo. Ademas, he tenido la oportunidad de disfrutar enormemente de la experiencia de la docencia: quiero agradecer muy especialmente a Antonio Badía que me haya guiado en este proceso.

A los integrantes del Servicio de Medidas Físicas de la Universidad de Zaragoza, Ana Arauzo y Enrique Guerrero, les agradezco todo el tiempo que me han dedicado para ayudarme con el PPMS y el SQUID. A los profesores Juajo Mazo y Nieves Andrés, su prontitud y disposición a la hora de ayudarme con las dudas y problemas en los trámites relacionados con la tesis.

Me gustaría remontarme un poco más atrás en el tiempo para recordar al sanedrín el IES Tomás Mingot en Logroño: Marisa, Marisol, Isabel y Alicia, puesto que son ellas las que pusieron las primeras piedras del camino que he recorrido desde entonces. Gracias por siempre animarme y confiar en mí.

Por último, quiero agradecer a mi familia que siempre me hayan apoyado aunque

no siempre me hayan comprendido: a mí madre, por ayudarme todo y más para conseguir sacar esto adelante; a mi padre, que fue el primero en hablarme de los electrones, los protones y los neutrones; a mi hermano, que siempre me apoyó en mis decisiones más difíciles; a Julia y Celia, por iluminar el camino.

Gracias a Rubén y a Millán por enseñarme qué es lo verdaderamente importante en la vida. Sin vuestras risas (y llantos) de fondo esto no habría merecido la pena.

Abstract

Since its birth marked by the discovery of the Giant Magnetoresistance (GMR) in 1988, the field of spintronics has evolved rapidly, maturing and giving rise to new subfields. The ultimate goal of spintronics is the development of a new paradigm with potential to overcome the limits imposed by the Moore's law in conventional electronics. This paradigm is based on the use of the spin degree of freedom, together with the electrical charge.

A functional spintronic technology requires the capability to control three fundamental operations: generation, transport and detection of spin angular momentum. Therefore, spin dynamics are focus of an intense research aiming at the enhancement of the performance of these three operations. In particular, spin currents are a fundamental object in the field of spintronics. Furthermore, pure spin currents, which are not accompanied by a charge flow, allow to propagate spin without Joule power dissipation losses. In this regard, pure spin currents carried by collective magnetic excitations (magnons) bring the possibility of insulator-based spintronics using electrically insulating materials with long-range magnetic order (MOIs).

This thesis is devoted to the study of thermal spin transport, i.e., the coupling between spin and heat currents, which constitutes the area of research of the spintronics subfield of spin caloritronics or thermal spintronics. This field is envisaged to significantly contribute to the development of a new generation of highly efficient thermoelectric devices; to this end, a deeper understanding on the fundamental mechanisms governing thermal spin transport is still required.

Through the work developed in this thesis, the spin Seebeck effect (SSE) in maghemite (γ-Fe_2O_3) -based low-dimensional nanostructures has been exhaustively investigated. The SSE is one of the most prominent transport phenomenon integrating the field of spin caloritronics, as it enables the direct generation of a magnon spin current upon the application of a thermal gradient in magnetic materials. SSE is observed in FM/NM bilayers, where FM is a magnetically ordered material and NM is a paramagnetic or diamagnetic metal (most often, Pt).

In general, strategies aimed at improving the SSE efficiency can be targeted at three levels: (1) the heat-to-spin current conversion in the FM layer; (2) the interface level, comprising both interfacial heat-to-spin current generation and spin transfer from FM to NM; and (3) spin current detection at NM. This last step is usually performed by means of spin-to-charge conversion via the inverse spin Hall effect (ISHE) enabled by spin-orbit coupling (SOC).

The first part of this thesis is focused on the development as thin films of materials of interest within this topic. In particular, the preparation of high quality maghemite and iridium(IV) oxide (IrO_2) thin films is investigated. Additionally, the fabrication of $Y_3Fe_5O_{12}$ (YIG) by an affordable chemical method is also addressed. Maghemite and YIG constitute examples of MOIs holding an already successful history of applications in other fields. Meanwhile, IrO_2 is a NM metal with strong SOC and high electrical resistivity making it an appealing candidate for spin current detection via the ISHE.

Then, the SSE is extensively investigated in γ-Fe_2O_3/Pt bilayers of nanometric thickness. A thorough depiction of the SSE is reached, accounting for both contributions to the thermal spin current: the one originated at the FM/NM interface, and the one originated at the thickness of γ-Fe_2O_3 due to the thermally induced magnon accumulation. To this end, the influence of different transport parameters is discussed. Furthermore, a second method for measuring the SSE in steady heating conditions is implemented. This alternative method is based on the current-induced heating approach, in which the NM material holds a triple role: heater, thermometer, and spin-to-charge converter. The experimental

equivalence between both methods is analyzed. Additionally, this current-induced method enables the simultaneous detection of the recently discovered spin Hall magnetoresistance (SMR), which is hence characterized in the γ-Fe_2O_3/Pt bilayers.

Secondly, the ultrafast dynamics of the interfacial SSE is investigated by means of the Terahertz Emission Spectroscopy all-optical technique (TES). In this case. three different FM/NM structures using FM materials with different degree of electrical conductivity are used: insulating maghemite, half-metallic magnetite and metallic iron. The comparison of the photoinduced thermal spin currents in each sample enables the characterization of the time scale at which these spin currents rise and decay. Based on their different dynamics, the SSE and the spin-dependent version of the thermoelectric Seebeck effect (spin-dependent Seebeck effect, SDSD) are differentiated. The SDSE-associated thermal spin current is carried by electrons, in contrast to the magnonic nature of spin currents excited by the SSE, and thus SDSE is operative only in conductive materials.

Finally, the third level of the SSE —the spin current detection in the NM layer— is addressed using IrO_2 as NM in γ-Fe_2O_3/IrO_2 bilayers of nanometric thickness. To date, a few experimental works studying spin-to-charge conversion in polycrystalline or amorphous IrO_2 have been reported. In contrast, IrO_2 thin films investigated in this thesis are strongly textured in a preferential direction, and the role of the different SOC mechanisms contributing to ISHE in this kind of samples is analyzed. Besides, the striking differences found between ISHE spin-to-charge conversion in textured samples with respect to previous studies in polycrystalline or amorphous IrO_2 are discussed. The results open the door to the interesting possibility of tuning the desired functionality of high-resistance spin-Hall-based devices.

Resumen

Desde su nacimiento marcado por el descubrimiento de la magnetorresistencia gigante (GMR) en 1988, el campo de la espintrónica ha evolucionado rápidamente, madurando y dando lugar a nuevas subdisciplinas. El objetivo final de la espintrónica es el desarrollo de un nuevo paradigma con potencial para superar las limitaciones impuestas en la electrónica convencional por la ley de Moore. Este paradigma se basa en el uso del grado de libertad de espín, junto con la carga eléctrica.

Una tecnología espintrónica requiere, para ser funcional, de la capacidad para controlar tres operaciones fundamentales: generación, transporte y detección del momento angular de espín. De esta manera, la dinámica de espín es el foco de una intensa investigación con el objeto de aumentar la eficiencia en estas operaciones. En concreto, las corrientes de espín son un objeto fundamental en el campo de la espintrónica. Mas aún, las corrientes puras de espín, que no van acompañadas por una corriente de carga, permiten la propagación de espín sin pérdidas por disipación Joule. En este sentido, las corrientes puras de espín portadas por excitaciones magnéticas colectivas (magnones) brindan la posibilidad de una espintrónica basada en aislantes usando materiales eléctricamente aislantes con orden magnético de largo alcance (MOIs).

Esta tesis se ha dedicado al estudio del transporte térmico de espín, es decir, a la interacción entre corrientes de espín y de calor, que constituye el área de investigación de la subdisciplina (dentro de la espintrónica) de la caloritrónica de espín o termoespintrónica. Se prevé que este campo contribuya significativamente al desarrollo de una nueva generación de dispositivos termoeléctricos altamente

eficientes. Para ello, todavía es necesario profundizar más en la comprensión de los mecanismos fundamentales que gobiernan el transporte térmico de espín.

A través del trabajo desarrollado en esta tesis, se ha estudiado de manera exhaustiva el efecto Seebeck de espín (SSE) en nanoestructuras de baja dimensionalidad basadas en maghemita (γ-Fe_2O_3). El SSE es uno de los fenómenos de transporte más destacados en el campo de la caloritrónica de espín, puesto que permite la generación directa de una corriente de espín magnónica al aplicar un gradiente térmico en materiales magnéticos. El SSE se observa en bicapas FM/NM, donde FM es un material con orden magnético de largo alcance y NM es un metal paramagnético o diamagnético (habitualmente, Pt).

En general, las estrategias que pretendan mejorar la eficiencia del SSE pueden dirigirse a tres niveles: (1) conversión de corriente de calor en corriente de espín en la capa FM; (2) al nivel interfacial, que comprende tanto la conversión de corriente de calor en corriente de espín a este nivel como la transferencia de espín desde la capa FM hacia la capa NM; y (3) la detección de la corriente de espín en la capa NM. Este último paso se realiza habitualmente mediante la conversión de corriente de espín en corriente de carga a través del efecto Hall de espín inverso facilitado por el acoplamiento espín-órbita (SOC).

La primera parte de esta tesis se centra en el desarrollo de materiales de interés dentro de este tópico en forma de películas delgadas. En particular, se investiga la preparación de películas delgadas de alta calidad de maghemita de y óxido de iridio (IV) (IrO_2). Además, se aborda también la fabricación de $Y_3Fe_5O_{12}$ (YIG) mediante un método químico rápido y económico. La maghemita y el YIG constituyen ejemplos de MOIs que ya han sido aplicados exitosamente en otros campos. Por su parte, el IrO_2 es un material NM con elevado SOC y elevada resistividad eléctrica, propiedades que lo convierten en un candidato prometedor para la detección de corriente de espín mediante ISHE.

A continuación, se investiga extensamente el SSE en bicapas γ-Fe_2O_3/Pt de espesor nanométrico. Como resultado, se consigue elaborar una descripción precisa del SSE, que tiene en cuenta las dos contribuciones a la corriente espín térmica: la

originada en la intercara FM/NM, y la originada en el espesor de γ-Fe_2O_3 debido a la acumulación de magnones inducida térmicamente. Para ello, se analiza la influencia de diferentes parámetros de transporte. Además, se implementa un segundo método de medida del SSE en condiciones de calentamiento estable. Este método alternativo se basa en el enfoque del calentamiento inducido por corriente, en el que el material NM cumple una función triple: calentamiento, termometría y consversión de corriente de espín en corriente de carga. Por último, se analiza la equivalencia experimental entre los dos métodos. Además, el método de inducción por corriente permite la detección simultánea de la recientemente descubierta magnetorresistencia Hall (SMR), que es asimismo caracterizada en las bicapas γ-Fe_2O_3/Pt.

En segundo lugar, se investiga la dinámica ultrarrápida del SSE de intercara por medio de la técnica óptica de Espectroscopía de Emisión de Terahercios (TES). En este caso, se emplean tres estructuras FM/NM usando para la capa FM materiales con diferente grado de conductividad eléctrica: maghemita (aislante), magnetita (mediometal) y hierro (metal). La comparación entre las corrientes de espín térmicas fotoinducidas en cada muestra permite la caracterización de la escala temporal en las que estas corrientes se originan y decaen. Basándose en sus diferentes dinámicas, el SSE y la versión dependiente de espín del efecto Seebeck termoeléctrico (efecto Seebeck dependiente de espín, SDSE) se pueden distinguir y separar, dentro de un mismo experimento. La corriente térmica de espín asociada al SDSE es portada por electrones, a diferencia de las corrientes de espín excitadas mediante SSE, que son portadas por magnones. Por lo tanto, el SDSE solo se da en materiales conductores.

Por último, la tesis aborda el tercer nivel del SSE —la detección de la corriente de espín en la capa NM— usando IrO_2 para la capa NM en bicapas γ-Fe_2O_3/IrO_2. Hasta la fecha, sólo se han reportado unos pocos trabajos experimentales que estudian la conversión de espín a carga en IrO_2 policristalino o amorfo. Las muestras de IrO_2 estudiadas en esta tesis, por el contrario, presentan una estructura cristalina fuertemente texturada en una dirección preferencial; en la presente tesis se investiga por tanto el papel de los diferentes mecanismos originados por el SOC y que contribuyen al ISHE en este tipo de muestras. Además, se analizan las

llamativas diferencias encontradas en los procesos de conversión de corriente de espín en corriente de carga encontradas en las muestras texturadas con respecto a resultados previos en IrO_2 policristalino o amorfo publicados en la literatura. Estas diferencias abren la puerta a la interesante posibilidad de controlar la funcionalidad de dispositivos basados en el efecto Hall de espín en materiales altamente resistivos.

Acronyms

ADMR	angle-dependent magnetoresistance
AHE	anomalous Hall effect
ANE	anomalous Nernst effect
*b*LSSE	bulk magnon accumulation longitudinal spin Seebeck effect
CIQUS	Centro Singular de Investigación en Química Biolóxica e Materiais Moleculares (Center for Research in Biological Chemistry and Molecular Materials)
FHI	Fritz-Haber-Institut der Max-Planck-Gesellschaft (Fritz Haber Institute of the Max Planck Society)
FM	Material with long-range ferro-/ferrimagnetic order
FMR	ferromagnetic resonance
FU	Freie Universität Berlin (Free University of Berlin)
GMR	Giant Magnetoresistance
HRTEM	high resolution TEM
HRXRD	high resolution XRD
*i*LSSE	interfacial longitudinal spin Seebeck effect
INA	Instituto de Nanociencia de Aragón (Institute of Nanoscience of Aragón)
INMA	Instituto de Nanociencia y Materiales de Aragón (Institute of Nanoscience and Materials of Aragón)
ISHE	inverse spin Hall effect
IT	Information Technologies

JSSE	current-induced or Joule-induced spin Seebeck effect
LLG	Landau-Lifshitz-Gilbert equation
LSSE	longitudinal spin Seebeck effect
MOI	insulating material with long-range magnetic order
MPE	magnetic proximity effect
MR	magnetoresistance
NM	paramagnetic or diamagnetic metal
PAD	Polymer-Assisted Deposition
PLD	Pulsed Laser Deposition
RSM	Reciprocal Space Map
SDSE	spin-dependent Seebeck effect
SHE	spin Hall effect
SMR	spin Hall magnetoresistance
SOC	spin-orbit coupling
SOI	spin-orbit interaction
SPE	spin Peltier effect
SQUID	Superconducting Quantum Interference Device
SSE	spin Seebeck effect
STEM	scanning TEM
STT	spin-transfer torque
TEM	Transmission Electron Microscopy
TES	Terahertz Emission Spectroscopy
TMR	Tunnel Magnetoresistance
USC	Universidad de Santiago de Compostela (University of Santiago de Compostela)
VSM	Vibrating Sample Magnetometry
XPS	X-ray photoelectron spectroscopy
XRD	X-ray diffraction
XRR	X-ray reflectivity
YIG	yttrium iron garnet ($Y_3Fe_5O_{12}$)

Chapter 1

Introduction

1.1 Spintronics

Conventional electronics makes use of the charge degree of freedom of electrons in semiconductor devices for transmission and manipulation of information. However, the rapid development of information technologies (IT) relentlessly demands larger capacity data storage and faster data processing, together with increasingly higher levels of miniaturization. This continued increment in the levels of integration, known as Moore's law, leads to an increase of density power dissipation and chip temperature which has been announced to be currently approaching the limit for the reliable operation of integrated circuits [1]. This trend was predicted by Gordon Moore in 1975 [2, 3], and, even earlier, foreseen by Richard Feynman in his 1959 celebrated lecture *There's Plenty of Room at the Bottom* at the Annual Meeting of the American Physical Society in the California Institute of Technology [4].

Therefore, in order to maintain the IT development, new device concepts and new materials apart from silicon are needed (the "more than Moore" approach); thus, scientific efforts are currently focused in the search of a whole new paradigm of electronics [5]. In the light of this scenario, the use of the spin degree of freedom of electrons has emerged as an alternative candidate for information encoding, as it offers the potential advantages of nonvolatility, increased data processing speed,

decreased electric power consumption, and increased integration densities compared with conventional semiconductor devices [5, 6].

Spin electronics or spintronics is the name given to the field that exploits the spin degree of freedom of electrons, in addition to their electrical charge. It covers a wide scope, from the fundamental theoretical and experimental research to the development of technology ready to be placed into the market.

The discovery of the giant magnetoresistance (GMR), for which the Nobel Prize in Physics was awarded in 2007 to Albert Fert and Peter Grünberg [7, 8], is usually cited as the breakthrough of the field of spintronics. Remarkably, GMR also constitutes an outstanding example of extremely successful knowledge transfer between basic research and industry, since barely a decade after its first observation, GMR had already become an integral part of read heads in magnetic data storage, leading to strikingly increases in storage density of hard disk drives [9]. Such success stimulated an intense activity in the newly created field. In this sense, current applications of spintronics are devoted to storage and sensing of information; nonetheless, it shows potential also in logic operation in IT and energy harvesting [10–12].

In order to unlock this potential, several challenges need to be overcome. A spin-based operative technology requires the capabilities to create, transport and detect spin polarization on reasonable length and time scales. Therefore, the control of spin currents –the fundamental object of spintronics— is essential. Two different carriers are particularly relevant for the flow of spin angular momentum: mobile spin-and-charge carriers and collective excitations (magnons). Magnon spin currents present the important advantage of not requiring the actual motion of charged particles (e.g., electrons) in real space, thus avoiding Joule heating due to energy dissipation [13].

As research goes in depth, the field of spintronics is rapidly maturing and giving rise to new subfields which study the coupling of spin system to other systems within a material [14]. Outstanding examples are spin-orbit coupling (giving rise to *spin orbitronics*) spin-heat coupling (*spin caloritronics*), spin-spin coupling via spin

excitations (*magnonics*) and spin-photon coupling (*ultrafast spin photonics*).

1.2 The spin angular momentum

1.2.1 Development of the spin concept

The spin is a fundamental property of elementary particles (and composite particles or hadrons). It is an intrinsic angular momentum associated to an internal degree of freedom. Therefore, it represents a second kind of angular momentum carried by particles, the other one being the orbital (external) angular momentum associated to the three external degrees of freedom, i.e., the spatial coordinates x, y and z. Magnetism is originated by spin.

Spin is a quantum mechanical property with no classical analogous [15], but it is often visualized as an actual spin movement of spherical particles. This is in fact the idea first proposed in 1925 by Uhlenbeck and Goudsmit to interpret a number of experimental observations with could not be explained without the notion of an intrinsic angular momentum of particles [16]. Thus, historically, the experimental evidences of the spin preceded its theoretical derivation. These experimental evidences include the fine structure of spectral lines, the "anomalous" Zeeman effect and the result of the Stern-Gerlach experiment (the split in two of a beam of silver atoms sent through an inhomogeneous magnetic field) [15].

Theoretically, the notion of a spin angular momentum emerges naturally from the Dirac equation, which results from the linearization of the relativistic generalization of the Schrödinger equation [17]. The Schrödinger equation is a linear partial differential equation that describes the wave function of a quantum-mechanical system, but it is not relativistic-invariant. A first step to make it consistent with special relativity involves the introduction of the quantum-operator formalism into the relativistic-invariant four-momentum, leading to the Klein-Gordon equation. However, this equation is second-order in time derivative, a fact which is problematic for the probability density interpretation of the wave function. To solve this issue, Dirac and Fowler proposed in 1928 to linearize the wave equation. The Dirac

equation for a free particle in its original form reads [18]

$$\left(i\hbar\frac{\partial}{\partial t} - c\alpha\cdot\hat{\mathbf{p}} - \beta mc^2\right)\psi = 0 \tag{1.1}$$

where the coefficient α has three spatial components (α_x, α_y, α_z), each one of them as well as the coefficient β being 4×4 matrices (known as Dirac matrices) which satisfy certain relations; $\hat{\mathbf{p}} = -i\hbar\nabla$ is the quantum momentum operator; c is the speed of light; m is the rest mass of the free particle; $\hbar$ is the reduced Planck constant; and ψ is the wave function which here becomes a four component object (specifically, a *bispinor*, which describes together one particle's and its antiparticle's state).

The system described by the Dirac equation has rotational symmetry; hence the total angular momentum must be conserved. However, the orbital (external) angular momentum does not commute with the Dirac Hamiltonian meaning that it is not a constant of the motion. Therefore, the requirement of the conservation of the total angular momentum implies that an internal angular momentum must exist in addition to the orbital one [19]. A complete derivation of the Dirac equation can be found in Refs. [17–19].

As an angular momentum, spin operator $\hat{\mathbf{S}}$ satisfies the commutation relations [15, 17]

$$\left[\hat{S}_i, \hat{S}_j\right] = i\hbar\epsilon_{ijk}\hat{S}_k \tag{1.2}$$

where $\hat{S}_{i,j,k}$ represents the components of the spin operator in the three spatial directions. Conventionally, the spin state space is spanned using as basis the common eigenstates of $\hat{S}_z$ and $\hat{\mathbf{S}}^2$. The corresponding eigenvalues of these operators with respect such states are $m_\mathrm{s}\hbar$ and $s(s+1)\hbar^2$, respectively. For electrons, $s = 1/2$ and accordingly, $m_\mathrm{s} = \pm 1/2$ [15, 17]. Therefore, the component of the spin in a particular direction possess two possible states with eigenvalues $+\hbar/2$ and $-\hbar/2$, usually referred to as "spin-up" and "spin-down" states.

Importantly, both orbital and spin angular momenta ($\hat{\mathbf{L}}$ and $\hat{\mathbf{S}}$) of electrons are

associated with a magnetic moment:

$$\hat{\mathbf{m}}_{\mathrm{L}} = -\frac{\mu_{\mathrm{B}}}{\hbar}\hat{\mathbf{L}} \tag{1.3}$$

for the orbital angular momentum and

$$\hat{\mathbf{m}}_{\mathrm{S}} = -\frac{g\mu_{\mathrm{B}}}{\hbar}\hat{\mathbf{S}}, \tag{1.4}$$

for the spin angular momentum. $\mu_{\mathrm{B}} = e\hbar/2m_{\mathrm{e}}$ is the Bohr magneton with m_{e} the mass of the electron and e the elementary (positive) charge [20], and $g \approx 2$ is the electron g-factor. In the case of the spin, this relation between spin and magnetic moment is brought by the extension of Eq. 1.1 to include the electromagnetic potentials.

1.2.2 Spin interactions

Typical Fermi velocity of free electrons in a solid is in the order of $\sim 10^8$ cm/s [21], which amounts to $\sim 1\%$ of c. This is why relativistic corrections remain important and must be addressed in a description intended to account for the observed phenomena.

The nonrelativistic limit of the Dirac model can be taken in order to obtain the low-velocity relativistic corrections. The expansion of the Dirac Hamiltonian up to second order of the power series in $1/c^2$, including the interaction with a electromagnetic field represented by the scalar potential ϕ and the vector potential $\mathbf{A}$, leads to the following expression [15, 17, 20]:

$$\begin{aligned}\hat{H} = \overbrace{m_{\mathrm{e}}c^2}^{\mathrm{ME}} + \overbrace{\frac{1}{2m_{\mathrm{e}}}\left(\hat{\mathbf{p}} + e\mathbf{A}\right)^2 - e\phi(r)}^{\hat{H}_0} + \overbrace{\frac{\hat{\mathbf{p}}^4}{8m_{\mathrm{e}}^3c^2}}^{\hat{H}_{\mathrm{MV}}} + \\ + \underbrace{\frac{e}{m_{\mathrm{e}}}\left(\nabla \times \mathbf{A}\right)\cdot\hat{\mathbf{s}}}_{\hat{H}_{\mathrm{Z}}} - \underbrace{\frac{e}{2m_{\mathrm{e}}^2c^2}\frac{1}{r}\frac{\mathrm{d}\phi(r)}{\mathrm{d}r}\hat{\mathbf{L}}\cdot\hat{\mathbf{S}}}_{\hat{H}_{\mathrm{SO}}} + \underbrace{\frac{i\hbar}{4m_{\mathrm{e}}^2c^2}\left(\nabla\phi\cdot\mathbf{p}\right)}_{\hat{H}_{\mathrm{D}}} + \cdots\end{aligned} \tag{1.5}$$

Let us examine the different terms:

- The first term is the rest-mass energy of the electron.
- The second term, $\hat{H}_0$, is the nonrelativistic Hamiltonian.
- The third term, $\hat{H}_{\mathrm{MV}}$, is known as the mass-velocity term and represents the first-order correction to the kinetic energy, due to the relativistic variation of the mass with the velocity. It arises from the expansion in powers of $\hat{\mathbf{p}}/m_{\mathrm{e}}c$ of the relativistic energy of a particle of mass m_{e} and momentum $\mathbf{p}$: $E = c\sqrt{\mathbf{p}^2 + m_{\mathrm{e}}^2 c^2}$.
- The fourth term, $\hat{H}_{\mathrm{Z}}$, represents the contribution of the spin to the Zeeman energy, and will be more extensively discussed below.
- The fifth term, $\hat{H}_{\mathrm{SO}}$, is the spin-orbit interaction (SOI, or SOC for spin-orbit coupling) for a central potential. It is of capital interest in this thesis and will be described in more detail below.
- The last term, $\hat{H}_{\mathrm{D}}$, known as the Darwin term, constitutes a relativistic correction to the potential energy.

Zeeman interaction

The Zeeman term in Eq. 1.5 describes the interaction of the electron spin with a classic magnetic field $\mathbf{B} = \nabla \times \mathbf{A}$. This Hamiltonian has eigenvalues $g\mu_{\mathrm{B}} m_{\mathrm{s}} B \approx \pm\mu_{\mathrm{B}} B$, as $m_{\mathrm{s}} = \pm 1/2$ and $g \approx 2$ for electrons. The exact value of the electron g-factor, calculated from quantum electrodynamics, is $2(1 + \alpha/2\pi - \cdots) \approx 2.0023$, where α is the fine-structure constant [20]. Thus, these eigenvalues describe the energy levels of electron in a magnetic field, separated by a splitting $\Delta_{\mathrm{Z}} = 2\mu_{\mathrm{B}} B$.

Including the orbital angular momentum contribution, the complete expression for the Zeeman interaction is [20]:

$$\hat{H}_{\mathrm{Z}} = \frac{\mu_{\mathrm{B}}}{\hbar}\left(\hat{\mathbf{L}} + 2\hat{\mathbf{S}}\right) \tag{1.6}$$

Again, note that the 2 factor before $\hat{\mathbf{S}}$ is an approximation of the g-factor of the electron. This orbital contribution is contained in the nonrelativistic term, $\hat{H}_0$, in Eq. 1.5 (more precisely, it arises from the cross-term $\mathbf{A} \cdot \hat{\mathbf{p}}$ in the expansion of the

square $(\hat{\mathbf{p}} + e\mathbf{A})^2$). When $\mathbf{B}$ is in the z direction, we have

$$\hat{H}_{\mathrm{Z}} = \frac{\mu_{\mathrm{B}}}{\hbar}\left(\hat{L}_z + 2\hat{S}_z\right) \tag{1.7}$$

Spin-orbit coupling

The spin-orbit interaction is a foremost process in the field of spintronics. In fact, a whole new subfield focused on SOI-related phenomena in nonmagnetic materials has emerged in the last decade. It receives the name of *spin-orbitronics*.

SOI is a relativistic effect whose rigorous derivation requires the Dirac's theory. However, the idea behind can be pictured in semi-classical terms, as done in the following.

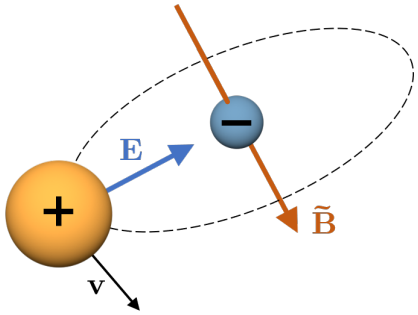

Figure 1.1 Semi-classical interpretation of the SOC. In the rest frame of the electron, the electrostatic field $\mathbf{E}$ generated by the nucleus moves with the electron's velocity $\mathbf{v}$, giving rise to a magnetic field $\tilde{\mathbf{B}}$ according to special relativity.

The electron moves in the surroundings of the positively-charge atom nucleus. The nucleus creates an electrostatic field which, in the rest frame of the nucleus, has the form

$$\mathbf{E} = -\nabla\phi \tag{1.8}$$

where ϕ is the electrostatic scalar potential. However, because the electron moves with velocity $\mathbf{v}$ with respect to the nucleus and to this electrostatic field, (see Fig. 1.1) special relativity indicates that, in this conditions, a magnetic field $\tilde{\mathbf{B}}$ appears

in the rest frame of the electron. Applying the Lorentz transformation:

$$\tilde{\mathbf{B}} = \gamma\left(\mathbf{B} - \frac{1}{c^2}\mathbf{v}\times\mathbf{E}\right) - \frac{\gamma^2}{1+\gamma}\frac{\mathbf{v}^2}{c^2}\mathbf{B}, \tag{1.9}$$

where γ is the Lorentz factor $\gamma = \left(1 - \mathbf{v}^2/c^2\right)^{-1/2}$, $\mathbf{E}$ and $\mathbf{B}$ are the electrostatic and magnetic field in the rest frame of the nucleus, and $\tilde{\mathbf{B}}$ is the magnetic field in the rest frame of the electron. Taking $\gamma \approx 0$ and in the absence of external magnetic field (i.e., $\mathbf{B} = \mathbf{0}$), we are left with

$$\tilde{\mathbf{B}} \approx -\frac{1}{c^2}\mathbf{v}\times\mathbf{E}. \tag{1.10}$$

This magnetic field *felt* by the electron is introduced in the Hamiltonian by addition of the following term:

$$H_{\mathrm{SO}} = \frac{2\mu_{\mathrm{B}}}{\hbar}\tilde{\mathbf{B}}\cdot\mathbf{S} = \frac{e}{m_{\mathrm{e}}c^2}\left(\mathbf{E}\times\mathbf{v}\right) \tag{1.11}$$

where the quantum-operator notation has been obviated. This is the SOI contribution to the Hamiltonian. In the case of a nucleus potential ϕ with spherical symmetry,

$$\mathbf{E} = -\frac{\mathbf{r}}{r}\frac{\mathrm{d}\phi}{\mathrm{d}r}. \tag{1.12}$$

In this conditions and using the definition of orbital angular momentum $\mathbf{L} = m_{\mathrm{e}}\mathbf{r}\times\mathbf{v}$, Eq. 1.11 results in

$$H_{\mathrm{SO}} = \frac{e}{m_{\mathrm{e}}^2c^2}\frac{1}{r}\frac{\mathrm{d}\phi}{\mathrm{d}r}\mathbf{L}\cdot\mathbf{S} = \frac{Ze^2}{m_{\mathrm{e}}^2c^2}\frac{1}{r^3}\mathbf{L}\cdot\mathbf{S} = \lambda_{\mathrm{SO}}\mathbf{L}\cdot\mathbf{S}, \tag{1.13}$$

where Z is the atomic number of the nucleus and λ_{SO} is the usual notation for the spin-orbit constant.

Finally, it must be noted that the radius $r \propto Z^{-1}$ [20] and therefore the SOC scales with the atomic number as

$$\lambda_{\mathrm{SO}} \propto Z^4. \tag{1.14}$$

1.3 Spin dynamics

In this section, topics related to spin dynamics which are especially relevant for the work presented in this thesis are discussed.

1.3.1 Magnons

The magnetic ground state in a exchange-coupled lattice corresponds to the total alignment of all the spins. This is described by the Heisenberg Hamiltonian, which accounts for the nearest-neighbors exchange coupling energy of localized spins:

$$H = -2J \sum_i \mathbf{S}_i \cdot \mathbf{S_{i+1}} \qquad (J > 0), \tag{1.15}$$

where J is the nearest-neighbors exchange constant. In presence of a magnetic field, a Zeeman term should be added.

Spin waves are the elementary excitations of the magnetically ordered fundamental state in an exchange-coupled lattice [17, 20]. They are collective excitations, whose energy-cost for lowering the total spin in one unit (i.e., in $\pm\hbar$) is lower than that of reversing an individual spin of the lattice [21]. In this case, the one-spin reversal is *shared* by all the spins in a wavelike form with periodic oscillation of their transverse spin orientation. In a quasiclassical picture, a spin wave is represented by the precession of every localized spin about the z-axis (see Fig. 1.2).

In other words, they represent the low-energy fluctuations that destroy the collective magnetic order. Their unit of quantization is called *magnon*. One-magnon states (such as that sketched in Fig. 1.2) are exact eigenstates of the Heisenberg Hamiltonian [17, 22].

A magnon constitutes a quasiparticle —the magnetic analogous to phonons— which behaves like a boson, since the lowest spin angular momentum carried by a magnon is the equivalent of flipping a single spin: $\pm\hbar$. Hence the average number of quantized spin waves in a mode q with frequency ω_q is given in thermal equilibrium

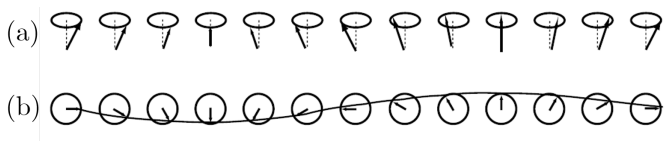

Figure 1.2 Illustration of a spin wave state in a chain of ferromagnetically aligned spins: side view (a) and top view (b).

by the Bose-Einstein distribution:

$$\langle n_q \rangle = \frac{1}{e^{\hbar\omega_q/k_\mathrm{B}T} - 1} \tag{1.16}$$

The subsequent increment in magnon population with increasing temperature is the reason why magnetization (which is destroyed by magnons) decreases. The energy in a frequency mode is:

$$\epsilon_q = \left(n_q + \frac{1}{2}\right)\hbar\omega_q. \tag{1.17}$$

However, magnon statistics are not described only by the local temperature: an important concept which has been developed in recent decades [23] is the *magnon chemical potential*, μ_m. This concept parametrizes long-living nonequilibrium magnon states that can be triggered by three mechanisms: (1) photon irradiation, (2) spin-transfer mechanism at an interface with a conducting material through which an electrical current flows and (3) application of thermal gradients [24]. These mechanisms are said to be magnon pumping. In the absence of pumping, i.e. at the thermodynamic equilibrium, $\mu_m = 0$. This chemical potential should be added to the Bose-Einstein distribution.

A magnon spin accumulation is then defined as the difference between chemical potentials, $\delta\mu_\mathrm{m}$. It acts as spin potential for the generation of spin currents (see next section). The magnon accumulation is governed by diffusion mechanisms with characteristic decay times and lengths. Thus, it satisfies the diffusion equation in the steady state [25]

$$\nabla^2\delta\mu_\mathrm{m} = \frac{1}{\Lambda_\mathrm{m}^2}\delta\mu_\mathrm{m} \tag{1.18}$$

where Λ_m is the characteristic length of the magnon accumulation, which is often

called magnon diffusion length or magnon propagation length.

1.3.2 Spin currents

A spin current is a flow of spin angular momentum. Attending to whether the spin current is accompanied or not by a charge current, we can distinguish between two types of spin currents: spin-polarized currents and pure spin currents.

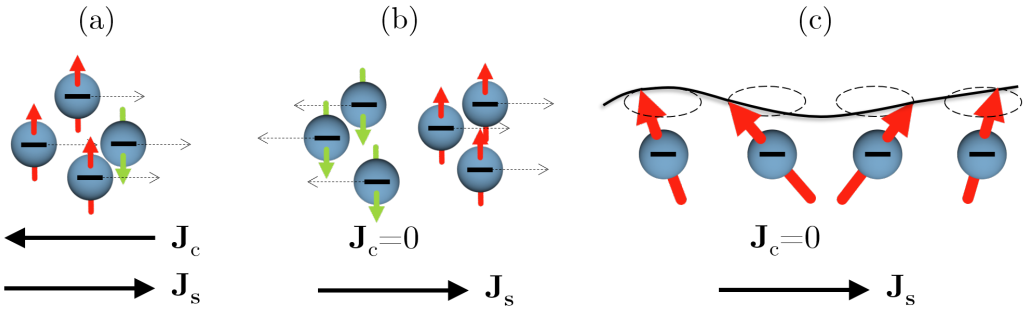

Figure 1.3 (a) Spin-polarized current. (b) Pure spin current carried by conduction electrons. (c) Pure spin current carried by magnons.

1. Spin-polarized currents A flow of electrons with a nonzero spin polarization is associated with a spin flow. In this situation, all the electrons move in the same direction, but there is an imbalance between spin-up and spin-down populations (spin polarization), as illustrated in Fig. 1.3(a). In other words, spin transport and charge transport are parallel to each other [26]. In this case, the spin current density can be simply defined as [27]:

$$\mathbf{J}_s = \frac{\hbar}{2e}\left(\mathbf{J}_\uparrow - \mathbf{J}_\downarrow\right) \tag{1.19}$$

where $\mathbf{J}_\uparrow$ and $\mathbf{J}_\downarrow$ are the charge current density of electrons with spin-up and spin-down, respectively. Note that electrical conductivity is indeed different for each spin channel, i.e., spin-dependent. This is the picture set by the Julliere's model in order to explain the tunneling magnetoresistance (TMR) in 1975 [28]. This model

treats both spin channels as separate contributions to the total charge current, with different transport properties.

2. Pure spin currents The flow spin current is not associated to a net charge current. In this case, a general definition for the spin current density is [19]

$$\mathbf{J}_{\mathrm{s}} = \sum_{\mathbf{k}} s^z_{\mathbf{k}} \mathbf{v}_{\mathbf{k}}, \tag{1.20}$$

where $s^z_{\mathbf{k}}$ is the z-component of the spin density $\mathbf{s}_{\mathbf{k}}$ and $\mathbf{v}_{\mathbf{k}}$ is the velocity of the excitations that transport the spin angular momentum. Note that, in this case, the velocity is not spin-dependent.

Remarkably, as mentioned in Section 1.1, there are two possible carriers for pure spin currents which are particular relevant: electrons and magnons.

In the first case, we have the following picture: same number of spin-up and spin-down electrons move in opposite directions; i.e., $\mathbf{J}_{\uparrow}+\mathbf{J}_{\downarrow} = 0$ whereas $\mathbf{J}_{\uparrow}-\mathbf{J}_{\downarrow} \neq 0$, as illustrated in Fig. 1.3(b). This is known as conduction-electron pure spin current. In this case, Eq. 1.20 particularizes to [29]:

$$\mathbf{J}_s^{\text{c-el}} = \sum_{\mathbf{k}} v_{\mathbf{k}} \left(\langle c^{\dagger}_{\mathbf{k},\uparrow} c_{\mathbf{k},\uparrow} \rangle - \langle c^{\dagger}_{\mathbf{k},\downarrow} c_{\mathbf{k},\downarrow} \rangle \right), \tag{1.21}$$

where $c^{\dagger}_{\mathbf{k},s}$ is the creation operator for conduction electrons with spin polarization $s =\uparrow, \downarrow$ and momentum $\mathbf{k}$ and $c_{\mathbf{k},s}$ is the corresponding annihilation operator.

Spin waves propagation carries spin angular momentum. In presence of these collective excitations, the z component of the spin density is given by $s^z_{\mathbf{k}} = S_0 - \langle b^{\dagger}_{\mathbf{k}} b_{\mathbf{k}} \rangle$, where $b^{\dagger}_{\mathbf{k}}$ is the creation operator for magnons with wave number $\mathbf{k}$, $b_{\mathbf{k}}$ is the corresponding annihilation operator, and S_0 the saturated spin density in absence of magnons. The magnon spin current density can be then formulated as [29]:

$$\mathbf{J}_s^{\text{mag}} = -\frac{1}{2} \sum_{\mathbf{k}} v_{\mathbf{k}} \left(\langle b^{\dagger}_{\mathbf{k}} b_{\mathbf{k}} \rangle - \langle b^{\dagger}_{-\mathbf{k}} b_{-\mathbf{k}} \rangle \right). \tag{1.22}$$

Remarkably, magnon spin currents can flow both in metallic and insulating

materials, because they do not involve the actual movement of charged particles (e.g. electrons). This constitutes an obvious advantage for the reduction of power dissipation due to Joule heating, and brings the possibility of insulator-based spintronics using magnetically ordered electrical insulators (MOIs).

For the sake of completeness, it must be mentioned that the motion of magnetic domains induced by a spin current through its walls can also transport spin [19].

It is important to note that, while charge current describes the flow of a scalar quantity, spin current refers to the flow of an axial vector, and therefore not only the direction of flow but also the orientation of the spin angular momentum must be specified (here, z). Hence, it is a tensor of second-rank rather than a vector.

In addition, there is another important difference between both type of currents: spin currents are not conservative, in contrast to charge currents. The two types of carriers —electrons and magnons— eventually relax their spin through interaction with other particles (e.g., magnon-magnon, magnon-electron, electron-phonon or magnon-phonon interactions), bringing the unbalanced population of spin states to equilibrium. These processes can be well described by diffusion mechanisms characterized by their respective length and time scales.

Notably, in MOIs the magnon spin current decay is significantly suppressed, due to the absence of the typically dominant magnon-electron interaction [30–32], giving rise for instance to decay lengths as large as several tens of micrometers at room temperature in the ferrimagnetic insulator yttrium iron garnet, $Y_3Fe_5O_{12}$ (YIG) [32–34]. These values however depend on the driving mechanism [35], the magnon energy and wave number, and the particular MOI material [36].

The non-conservative nature of spin currents can be reflected in a modified continuity equation [37]:

$$\frac{\mathrm{d}\mathbf{M}}{\mathrm{d}t} = -\nabla \cdot \mathbf{J}_\mathrm{s} + \mathbf{J}_\omega \tag{1.23}$$

This equation describes both the translational and rotational motion (precession) of spin, i.e., the linear spin current and the torques. Hence the spin torques can act as sinks or sources of spin current.

1.3.3 The Landau-Lifshitz-Gilbert equation and the spin pumping

The strong coupling between individual spins in a system with long-range order allows us to describe the individual localized spins in terms of the average local magnetic moment (magnetization). Very briefly, the dynamics of the magnetization $\mathbf{M}$ of a ferromagnetic system in the presence of a magnetic field $\mathbf{H}$ are often phenomenologically described by the Landau-Lifshitz-Gilbert (LLG) equation [20, 38]:

$$\frac{\mathrm{d}\mathbf{M}}{\mathrm{d}t} = -\gamma \mathbf{M} \times \mathbf{H}_{\mathrm{eff}} + \frac{\alpha}{M_{\mathrm{s}}} \mathbf{M} \times \frac{\mathrm{d}\mathbf{M}}{\mathrm{d}t}, \tag{1.24}$$

where $\mathbf{H}_{\mathrm{eff}}$ contains the external and anisotropy magnetic fields [20, 27]; γ is the gyromagnetic ratio and α is the damping or Gilbert damping parameter, which is characteristic of the material and determines the magnetization dissipation rate. The first term describes a precession motion —i.e., with a constant angle between both vectors— of $\mathbf{M}$ around $\mathbf{H}_{\mathrm{eff}}$ due to the torque exerted by $\mathbf{H}_{\mathrm{eff}}$ on $\mathbf{M}$. The second term is the damping term, which describes the motion of $\mathbf{M}$ to get aligned with $\mathbf{H}_{\mathrm{eff}}$, reducing the angle between both (see Fig. 1.4(a)) It is easy to show that both terms conserve the modulus of the magnetization vector, $||\mathbf{M}|| = M_{\mathrm{s}}$.

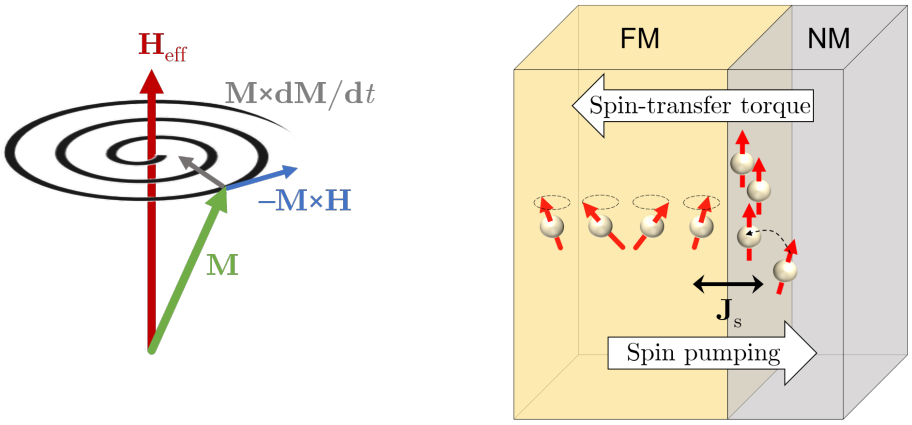

Figure 1.4 (a) Precession of magnetization $\mathbf{M}$ in a magnetic field $\mathbf{H}_{\mathrm{eff}}$. (b) Schematic depiction of the spin pumping and spin-transfer torque processes.

Note that the LLG equation can also describe spin waves or magnons, in which only the magnetization direction with respect to the equilibrium magnetization configuration is modulated for each individual (localized) spin —and not the modulus. This is done by replacing the full time derivatives in Eq. 1.24 with partial derivatives, to allow for spatial modulation [39].

A highly relevant application of magnetization precession dynamics is the *spin pumping* process. Spin pumping is a method to generate a spin accumulation and subsequent spin current from a material material with long-range ordered magnetic ground state (FM) into an adjacent nonmagnetic metal NM[1] in hybrid structures FM/NM using magnetization dynamics [38]. The angular momentum of localized spins in FM is transferred to conduction electrons of the adjacent metal to create spin accumulation and spin current via the precession of the localized spins. Magnetization $\mathbf{M}$ in FM exerts a torque on the magnetic moment $\mathbf{m}$ of the conduction electrons in NM; this raises a spin accumulation which finally generates a spin current of the form [39]:

$$\mathbf{J}_{\mathrm{s}}^{\mathrm{sp}} = \frac{\hbar}{4\pi M_{\mathrm{s}}^2}\left(g_{\uparrow\downarrow}^{r}\mathbf{M}\times\frac{\mathrm{d}\mathbf{M}}{\mathrm{d}t} - g_{\uparrow\downarrow}^{i}\frac{\mathrm{d}\mathbf{M}}{\mathrm{d}t}\right), \tag{1.25}$$

where $g_{\uparrow\downarrow}^{r}$ and $g_{\uparrow\downarrow}^{i}$ are the real and imaginary parts of the dimensionless interfacial spin mixing conductance (per unit area), a parameter that characterizes the transport across the FM/NM interface of spin angular momentum [40]. Spin pumping can be described by an effective LLG equation, introducing effective $\tilde{\gamma}$ and $\tilde{\alpha}$ coefficients [38, 39] to describe the $g_{\uparrow\downarrow}^{r}$-term in Eq. 1.25 and directly adding the $g_{\uparrow\downarrow}^{i}$-term [27].

As illustrated in Fig. 1.4(b), spin pumping is the reciprocal process of the *spin-transfer torque*, in which spin angular momentum is transferred from the conduction electrons flowing in a spin-polarized current in NM to the localized magnetic moments in FM, due to spin accumulation at NM [39]. Interestingly,

[1] By an abuse of terminology, in this thesis the term "nonmagnetic" is used for simplicity in reference to materials with a magnetic ground state that does not show long-range order; in particular, this use of "nonmagnetic" encompasses both paramagnetic and diamagnetic systems.

spin-transfer torque can be employed to control electrically the orientation of a FM layer by applying a spin-polarized current instead of an external magnetic field [41]. Spin-transfer torque is modelized by adding a torque term (the Slonczewski torque) to the LLG equation (Eq. 1.24).

There are different ways to stimulate spin pumping; a prominent example is the coherent spin pumping excited by ferromagnetic resonance (FMR). Another way to trigger spin pumping is via temperature bias across the FM/NM interface. This mechanism, labeled as thermal spin pumping, is the most relevant within this thesis.

1.4 Spin transport effects

The interactions and processes explained above give rise to various transport phenomena which are object of study in this thesis. In this section, the theoretical frame for these transport processes is provided.

1.4.1 The direct and inverse spin Hall effects

The spin Hall effect (SHE) refers to the creation of a spin current transverse to a charge current in a metallic material [19, 42–45]. It is originated by spin-dependent scattering due to SOC, which endows electrons with a spin-dependent component of velocity perpendicular to the charge current. Therefore, it emerges in materials with strong SOC. Due do small decay lengths of spin currents, nanometric materials are required for its observation [46].

Depending on whether the metal shows or not magnetic order, two different situations arise:

- If the metallic material shows long range magnetic order, there is an imbalance on the spin-up and spin-down populations (spin polarization); consequently, more electrons are scattered to one direction than to the other and hence the spin current is associated to a charge current: this is the anomalous Hall effect (AHE), depicted in Fig. 1.5(a).
- In the case of a nonmagnetic metal (NM), the spin-up population is equal

to spin-down population and hence the generated spin current is a pure spin current, as identical number of electrons are scattered in opposite directions. This situation is illustrated in Fig. 1.5(b).

Therefore, SHE and AHE refer to the same phenomena; SHE is the general manifestation and AHE a particular case [27][47].

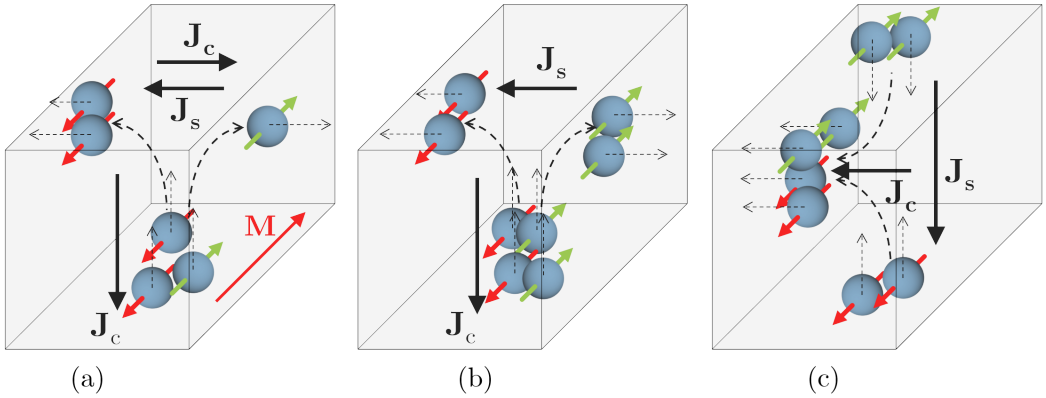

Figure 1.5 (a) AHE (SHE in a magnetically ordered material with net magnetization **M**). (b) SHE in a nonmagnetic metal. (c) ISHE in a nonmagnetic metal.

The reciprocal of the SHE is known as the inverse spin Hall effect (ISHE). It appears as a conventional charge current induced by a transverse spin current in metallic nanostructured materials with high SOC [19, 48, 49]. This charge current leads to charge accumulation at the edges of the device that can be easily detected as an electrical voltage. Importantly for spintronics, this phenomenology enables the use of ISHE as tool for spin current detection; currently, the spin-to-charge conversion by the ISHE is indeed the preferred method for spin current detection. In contrast, SHE constitutes a mechanism for spin-current generation.

It must be noted that the mechanism behind SHE and ISHE is the same: the spin-dependent scattering, which endows electrons with a transverse component of velocity of opposite sign for opposite spin orientations. In the case of ISHE, spin-up and spin-down electrons originally flow in opposite directions, forming a pure spin current, and, as a consequence, the spin-dependent scattering deflects both of them

towards the same transverse direction (but opposite with respect of their respective original flow direction). ISHE process is sketched in Fig. 1.5(c). In contrast, in the case of SHE spin-up and spin-down electrons move originally in the same direction, hence they are deflected towards opposite directions as a result of spin-dependent scattering.

The SHE was first predicted in 1971 by D'yakanov and Perel [42, 43], and named by Hirsch in 1999 [44]. Hirsch's publication, together with the development of nanotechnology tools, renewed the interest in this phenomenon and triggered the experimental work aiming —and succeeding— at its detection [45, 50]. For the ISHE, experimental evidence came only a couple of years later [48, 49, 51]. SHE and ISHE are the most prominent effects integrating the field of spin orbitronics.

The efficiency of the interconversion between charge and spin currents by SHE and ISHE is characterized by a parameter known as spin Hall angle, usually denoted by θ_{SH}. Therefore, the SHE and ISHE are expressed as:

$$\begin{aligned} \text{SHE:} \quad & \mathbf{J}_{\mathrm{s}} = \theta_{\mathrm{SH}} \frac{\hbar}{2e} \mathbf{J}_{\mathrm{c}} \times \mathbf{s} \\ \text{ISHE:} \quad & \mathbf{J}_{\mathrm{c}} = \theta_{\mathrm{SH}} \frac{2e}{\hbar} \mathbf{J}_{\mathrm{s}} \times \mathbf{s} \end{aligned} \tag{1.26}$$

where $\mathbf{J}_{\mathrm{s}}$ and $\mathbf{J}_{\mathrm{c}}$ denote spin and charge current, respectively; and $\mathbf{s}$, spin orientation. Note that this efficiency parameter θ_{SH} is the same for both processes, due to Onsager reciprocity [51]. Moreover, this is something to be expected provided that, as already discussed, SHE and ISHE refer to the same physical process (spin-dependent scattering) for two different initial situations: same or opposite flow direction of spin-up and spin-down electrons.

The spin Hall angle relates to the spin Hall conductivity, which in this thesis is defined as $\sigma_{\mathrm{SH}} = \sigma_{xy}^{\uparrow} - \sigma_{xy}^{\downarrow}$ [2], where σ_{xy} is the xy component of the conductivity tensor for up-spin polarized and down-spin polarized carriers. This transverse

[2] Other authors make use of the alternative definition $\sigma_{\mathrm{SH}} = (\sigma_{xy}^{\uparrow} - \sigma_{xy}^{\downarrow})/2$, such that θ_{SH} reduces to half value and the factor 2 in Eq. 1.26 disappears.

conductivity is related to its resistivity counterpart by:

$$\sigma_{xy} = -\frac{\rho_{xy}}{\rho_{xx}^2 + \rho_{xy}^2} \approx -\frac{\rho_{xy}}{\rho_{xx}^2} \tag{1.27}$$

where we have taken the limit $\rho_{xy} \ll \rho_{xx}$ [47, 52]. Renaming the longitudinal electrical conductivity and resistivity as $\sigma_{\mathrm{xx}} \equiv \sigma_c$ and $\rho_{\mathrm{xx}} \equiv \rho_c$, the spin Hall angle can be expressed as:

$$\theta_{\mathrm{SH}} = \frac{\sigma_{\mathrm{SH}}}{\sigma_{\mathrm{c}}} \approx -\frac{\rho_{\mathrm{SH}}}{\rho_{\mathrm{c}}} \tag{1.28}$$

where ρ_{SH} is the spin Hall resistivity.

Spin-dependent scattering is not a single mechanism; rather, SOC manifests its influence through different microscopic mechanisms leading to spin-dependent scattering. In other words, SHE and ISHE arise from different microscopic contributions, of extrinsic and intrinsic nature [11, 52]. The extrinsic SHE/ISHE results from spin-asymmetric scattering at impurities, boundaries or defects (non-periodic or disorder potential) [42–44, 53]. There are two mechanisms recognized as sources of this extrinsic spin-dependent displacement of electrons during scattering events: skew scattering [54, 55] and side jump [56]. The intrinsic contribution to the SHE/ISHE occurs between scattering events and arises from the band structure of the perfect crystal (periodic or lattice potential) [57, 58]. Let us briefly comment on each one:

1. (Extrisic) **skew scattering** contribution: it refers to the dependence of the sign of scattering angle on the electron spin. The contribution of skew scattering to σ_{SH} scales as $\sigma_{\mathrm{SH}}^{\mathrm{ss}} \propto \sigma_{\mathrm{xx}}$. Equivalently, $-\rho_{\mathrm{SH}}^{\mathrm{ss}} \propto \rho_{\mathrm{xx}}$ Therefore, θ_{SH} from skew scattering is independent of ρ_{c} (recall Eq. 1.28).
2. (Extrisic) **side jump** contribution: it refers to a sideways shift of the electron trajectory, transverse to the current, that is dependent on the spin. The side jump mechanism results in $\sigma_{\mathrm{SH}}^{\mathrm{sd}}$ independent of σ_{xx}, or $-\rho_{\mathrm{SH}}^{\mathrm{sd}} \propto \rho_{\mathrm{xx}}^2$. This yields $\theta_{\mathrm{SH}} \propto \rho_{xx}$.
3. **Intrinsic** contribution: it depends only on the band structure and was first proposed in 1954 [59]. More recently, it has been reformulated in terms of

the Berry curvature [60, 61]. For this contribution, $\sigma_{\mathrm{SH}}^{\mathrm{i}}$ is also independent of σ_{xx}, or, equivalently, $-\rho_{\mathrm{SH}}^{\mathrm{i}} \propto \rho_{\mathrm{xx}}^{2}$. Consequently, the spin Hall angle scales as $\theta_{\mathrm{SH}} \propto \rho_{xx}$.

The description of the AHE considers three regimes of the transverse conductivity [11, 47, 62] that can be directly generalized to the SHE, as recently demonstrated by Sagasta *et al.* [63]. The skew scattering is expected to dominate SHE/ISHE in highly conductive metals which are nearly perfect crystal, i.e. in the known as *clean regime* of conductivity [11, 47, 63]. Hence, in this region $\sigma_{\mathrm{SH}} \propto \sigma_{xx}$. Upon increasing impurity concentration and disorder, skew scattering gets suppressed due to its dependence on electrical conductivity; thus, in the moderately dirty or intermediate regime, SHE/ISHE is mainly attributed to the intrinsic contribution and σ_{SH} is roughly constant. Finally, in the dirty limit σ_{SH} reduces at a rate faster than linear in σ_{xx} [11, 64, 65].

Interestingly, this picture opens the possibility to observe the crossover between different SHE regions by tuning the metal conductivity σ_{xx}. For example, the crossover between the clean skew scattering- and moderately dirty intrinsic-governed regimes of the SHE has been observed in Pt using the spin absorption method in lateral spin valve devices [63].

I conclude this section with a simple but relevant observation concerning the design of SHE and ISHE devices: since spin Hall effects benefit from strong SOC, the materials of interest generally include heavy elements [11], as expressed by Eq. 1.14, either as constituent or as impurity.

1.4.2 Thermal spin transport: the spin Seebeck effect

Spin caloritronics

The interaction between heat and spin currents originates a wealth of phenomena; the fundamental and applied research of these phenomena integrates the field of thermal spin transport. This field is usually given the name of *spin caloritronics* or *thermal spintronics*.

The breakthrough of spin caloritronics is considered to be the first experimental

observation of the spin Seebeck effect (SSE) [66]. This work prompted a quick development of the field comprising the first realizations of the SSE in a MOI [67, 68] and in a ferromagnetic semiconductor [69]; the formulation of the first theories [29, 70–73]; the experimental observation of the SSE counterpart, i.e., the spin Peltier effect (SPE) [74]; the experimental demonstration of the SSE in paramagnetic [75] and antiferromagnetic materials [76, 77]; the observation of the spin-dependent Seebeck and Peltier effects [78–80]; and the dynamic study of SSE by optical methods [81–83].

Remarkably, theory development of the SSE has always followed in time the experimental results, and still today the univocal definition and explanation of the observed phenomena is incomplete. In this sense, spin-dependent effects carried by conduction electrons and effects related to collective phenomena were usually confused in the early days of spin caloritronics, until the establishment of a standard nomenclature [84]. A complete and clarifying classification of the thermal effects (spin- and charge-related) can be found in [85].

Fundamentals of the spin Seebeck effect

The SSE is **defined as** the generation of a spin current in a FM/NM structure in response of an applied thermal gradient. The the spin current detection is usually performed in NM by spin-to-charge current conversion via the ISHE. It is important to note that, according to current nomenclature, the SSE refers exclusively to the thermal spin current which is, in the FM layer, carried by magnons. In metallic FM, an additional contribution to the thermal spin current may be carried by spin-polarized conduction electrons: this is the spin-dependent version of the thermoelectric Seebeck effect, labelled as spin-dependent Seebeck effect [84, 86]. The effects arising from the interactions between spin, charge and heat currents are summarized in Fig. 1.6(a).

Two **experimental geometries** of the SSE have been used: the transverse (TSSE) and the longitudinal (LSSE) configurations [85, 87]. These configurations can be considered as thermal analogous of the non-local and local spin injection

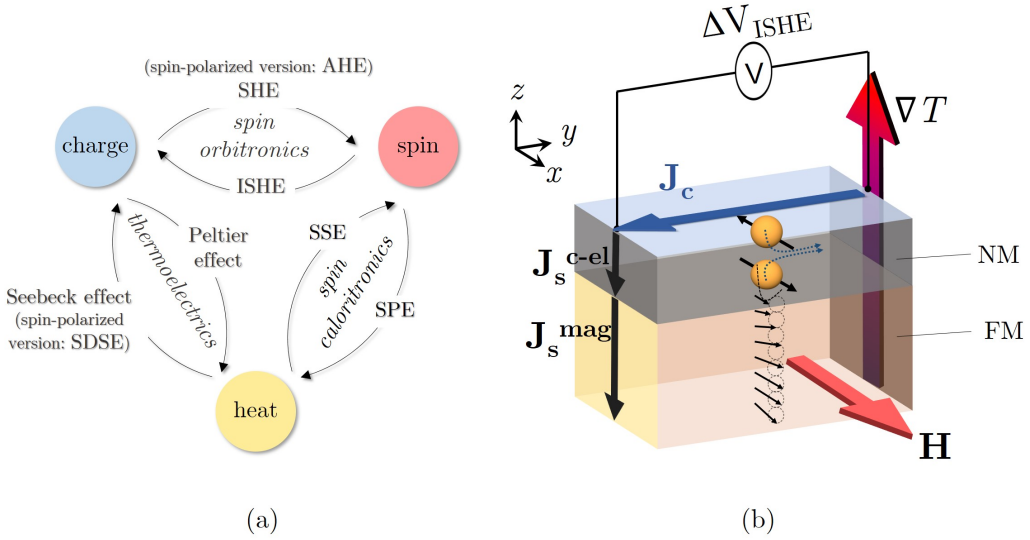

Figure 1.6 (a) Phenomena arising from the interconversion between charge, spin and heat current. (b) Experimental configuration of the LSSE.

[85]. The pioneering experiment in 2008 [66] used the TSSE configuration: in this geometry, the thermal gradient is applied in-plane of the FM layer; a spin current is excited in FM parallel to the thermal gradient. However, it diffuses laterally from the FM into an adjacent NM, resulting in a net pure spin current perpendicular to the interface and to the driving thermal gradient.

In the LSSE, the thermal gradient ∇T is applied perpendicularly to the FM/NM interface, i.e., out-of-plane. The spin current is excited and injected into the NM parallel to ∇T. This configuration is schematically depicted in Fig. 1.6(b), and is the geometry employed throughout this thesis. Despite being experimentally and theoretically simpler, the LSSE configuration presents nevertheless an important drawback: it is the same geometry in which other thermal spintronic effects arise in metallic NM, namely, the SDSE and the anomalous Nernst effect (ANE), which will be concisely describe below. Therefore, these effects may contribute to the measured signal. This is the reason why, in studies devoted to the SSE alone, an insulating material must be chosen as FM. Otherwise, additional measurements

using a perpendicular magnetization of FM and in-plane application of the thermal gradient are required to separate the ANE contribution [87]. The conduction electron contribution, however, cannot be disentangled by this method.

In brief, the LSSE process comprises the three following **steps**:

(1) A thermal gradient is applied perpendicular to the FM/NM interface (z direction in Fig. 1.6) as a consequence of which a nonequilibrium magnon population is launched leading to magnon accumulation. A magnetic field set in the x direction assists the observation of the phenomena by saturation of the magnetization. The magnon accumulation acts as a spin potential, generating a magnon spin current $J_{\mathrm{s}}^{\mathrm{mag}}$ in FM.

(2) At the interface, the exchange interaction between the precessing magnons associated to the magnon accumulation in the FM side and the conduction electrons of the NM side leads to spin pumping, creating a spin current in NM which is carried by conduction electrons $J_{\mathrm{s}}^{\text{c-el}}$. The spin current pumped into NM is given by [11, 73]

$$\mathbf{J}_{\mathrm{s}}(0) = \frac{\hbar g_{\uparrow\downarrow}^{r}}{4\pi M_{\mathrm{s}}^{2}} \mathbf{M} \times \frac{\mathrm{d}\mathbf{M}}{\mathrm{d}t}, \tag{1.29}$$

where $\mathbf{M}$ is the FM magnetization at the interface and $g_{\uparrow\downarrow}^{r}$ is the real part of the spin mixing conductance.

(3) In the NM layer, $J_{\mathrm{s}}^{\text{c-el}}$ is converted into a transverse charge current via the ISHE. This charge current can be detected as an electrical voltage ΔV_{ISHE}, given by [73]:

$$\Delta V_{\mathrm{ISHE}} = R_{\mathrm{NM}} \mathrm{w} \lambda_{\mathrm{NM}} \frac{2e}{\hbar} \theta_{\mathrm{SH}} \tanh\left(\frac{t_{\mathrm{NM}}}{2\lambda_{\mathrm{NM}}}\right) J_{\mathrm{s}}^{z}(0), \tag{1.30}$$

where R_{NM}, w, t_{NM} and λ_{NM} are the resistance, the width, the thickness and the spin diffusion length of the NM layer; and $J_{\mathrm{s}}^{z}(0)$ is the z-component of the spin current at the interface.

As evidenced by the presence of λ_{NM}, the existence of a spin current diffusion mechanism in the NM layer has been taken into accounted in order to calculate

this expression for ΔV_{ISHE}: as a consequence of this mechanism, the spin polarization is maximum at the FM/NM interface and diffuses away inside NM layer, with a characteristic length scale λ_{NM} which is defined through the spin-diffusion equation in the steady state [46, 88]:

$$\nabla^2 \left(\mu_\uparrow - \mu_\uparrow\right) = \frac{1}{\lambda_{\mathrm{NM}}^2} \left(\mu_\uparrow - \mu_\uparrow\right), \tag{1.31}$$

where $\mu_\uparrow$ and $\mu_\uparrow$ are the spin-dependent chemical potentials for spin-up and spin-down electrons, respectively.

As we see, the LSSE is a complex phenomenon that involves elements from not only spin caloritronics but also from spin orbitronics and magnonics. This complexity affects both theoretical and experimental aspects and is evidenced, e.g., by the difficulties found in the definition of a standard SSE coefficient [89, 90]. Often, a **spin Seebeck coefficient** defined as

$$S_{zy} = \frac{\Delta V_{\mathrm{ISHE}}}{\Delta T} \frac{t_z}{d_y} = -\frac{E_{\mathrm{ISHE}}}{\nabla T} \tag{1.32}$$

is used, where d_y is the distance between the transverse contacts to measure the transverse ISHE voltage (ΔV_{ISHE}) and t_z is the whole sample thickness (substrate included). Such definition allows for a quick comparison between thermal-to-electrical energy conversion performance of different devices, but does not reflect the fact that only a fraction of thermal energy is actually converted into electrical energy, and consequently does not offer hints about how to improve this performance.

Moreover, there are different physical mechanisms contributing to the SSE [81]. Two main theories have been developed so far which describe two different sources for a magnon spin current in a FM/NM system subjected to a thermal gradient.

(i) **The purely interfacial contribution**: the first theory points to the temperature difference between the metal electrons and the magnetic magnons

at the interface, such that the excited spin current is given by [29, 70]:

$$J_{\mathrm{s}}^{\mathrm{i}} \propto \Delta T_{\mathrm{i}}^{\mathrm{NM/FM}}, \tag{1.33}$$

where $\Delta T_{\mathrm{i}}^{\mathrm{NM/FM}}$ denotes the interfacial thermal drop.

(ii) **The magnon bulk accumulation contribution**: the second origin of the thermal spin current lies on the thermal gradient present in the bulk of the FM layer itself, rather than the temperature difference at the interface [11, 73, 91, 92]. This gradient creates a magnon accumulation which acts as a spin potential for the spin current. In this case, the spin current is determined by a finite magnon propagation length scale (Λ_{m}, defined in Eq. 1.18) and follows the expression [73, 92]:

$$J_{\mathrm{s}}^{\mathrm{b}} \propto \frac{\cosh\left(t_{\mathrm{FM}}/\Lambda_{\mathrm{m}}\right) - 1}{\sinh\left(t_{\mathrm{FM}}/\Lambda_{\mathrm{m}}\right)} \nabla T_{\mathrm{FM}}, \tag{1.34}$$

where ∇T_{FM} is the temperature gradient across the FM layer and t_{FM} denotes its thickness.

We will refer to each source as bulk and interfacial LSSE, respectively (*b*LSSE and *i*LSSE). It must be highlighted that in either case only a small fraction of the thermal energy is actually converted into electrical energy, i.e., because the main part of ΔT is expected to fall along the substrate instead of along the FM active layer, only a small fraction of ΔT participates in generating the output ISHE voltage.

FM layer	$\kappa_{\mathrm{FM}},\ \Lambda_{\mathrm{m}},\ \mathbf{M},\ t_{\mathrm{FM}}$
Interface	$g_{\uparrow\downarrow}$, (J_{sd}, interface quality), R_{i}
NM layer	$\kappa_{\mathrm{NM}},\ \sigma_{xx},\ \sigma_{\mathrm{SH}},\ t_{\mathrm{NM}}$

Table 1.1 Parameters which influence the measured ΔV_{ISHE} in a LSSE experiment. κ_{FM} and κ_{NM} denote the thermal conductivity of the FM and NM layers, R_{i} is the interfacial thermal resistivity, J_{sd} is the sd-exchange coupling, and t_{FM} and t_{NM} are the FM and NM layer thicknesses.

All in all, there are several parameters which characterize thermal transport,

magnetic properties, spin transport and charge transport, thus playing a crucial role in the overall effect. The most relevant in the case of electrical detection by ISHE in the steady state are summarized in Table 1.1.

Technological significance of the spin caloritronics

Beyond the fundamental research aiming at understanding the physics of the spin transport at the nanoscale, the interest aroused by the SSE is based on its potentiality to overcome the current limitations of conventional thermoelectric devices. These limitations stem from the necessity of simultaneous optimization in the same material of three competing properties in order to improve the thermoelectric efficiency [93]: these quantities are the electrical conductivity σ_c, the thermal conductivity κ and the thermopower S (which is the Seebeck coefficient in the case of thermoelectric generation). The three of them are related by the thermoelectric figure of merit ZT [24, 93, 94]:

$$ZT = \frac{S^2 \sigma_c T}{\kappa} \tag{1.35}$$

As evidenced by Eq. 1.35, in order to enhance ZT, S and σ_c need to be maximized, and κ needs to be minimized. However, those three optimizations are incompatible: on the one hand, decreasing κ entails a decrease in σ_c when the electronic contribution to the thermal conductivity is dominant, due to the Wiedemann–Franz law [24, 93, 94]. Attempting to overcome these correlations, semiconductors where the thermal transport is usually dominated by phonons and then the Wiedemann–Franz law does not apply have been used [94]. However, in this case the second correlation comes into play: the increment of σ_c by increasing the carrier concentration results in a reduction of S, due to the Pisarenko relation [24, 93, 94].

During last decades, the research in the field of thermoelectrics has focused on coping with these correlations. In this regard, the development of nanoscience and nanotechnology has enabled the engineering of nanomaterials with an improved

thermoelectric efficiency [93].

Here, SSE has two technological advantages to offer [85, 87]: first, because thermal and electrical currents flow in different materials, optimization of thermal and electrical conductivity are to be independently performed: thermal optimization of the FM layer and electrical optimization of the NM layer. Therefore, these quantities are not correlated anymore. Second, the ISHE electric field is perpendicular to the direction of the thermal gradient, which allows the enhancement of the measured ΔV_{ISHE} by simply increasing the physical size of the device.

Admittedly, the efficiency of spin caloritronic devices is still very much lower than that reached by conventional thermoelectrics; however, this young field represents a promise for a new paradigm with potential to transform the energy-conversion technologies.

1.4.3 Other spin caloritronic effects

As mentioned above, there are other effects coupling magnetic and thermal transport which may contribute to the measured ISHE voltage in the LSSE geometry, if FM is metallic. Here we briefly present the SDSE and the ANE.

The spin-dependent Seebeck effect

In the frame of the Stoner model, the transport properties in ferromagnets are spin-dependent, due to the spin-splitting of the electronic band structure. As a consequence, charge currents are spin-polarized, and they can be treated as the result of two independent contributions (see Section 1.3.2): the spin-up contribution ($\mathbf{J}_\uparrow$) and the spin-down contribution ($\mathbf{J}_\downarrow$), such that $\mathbf{J}_\uparrow \neq \mathbf{J}_\downarrow$. In other words, in ferromagnetic materials charge currents are spin-polarized and they are consequently linked to a spin current.

This is reflected into the thermoelectric language by defining the spin-dependent thermopowers or Seebeck coefficients $S_\uparrow$ and $S_\downarrow$, which contribute to total thermopower S:

$$S = \frac{S_\uparrow \sigma_\uparrow + S_\downarrow \sigma_\downarrow}{\sigma_\uparrow + \sigma_\downarrow} \tag{1.36}$$

where $\sigma_\uparrow$ and $\sigma_\downarrow$ are the electrical conductivities of the spin-up and spin-down channels.

Hence, the charge current induced by the classical Seebeck effect in a FM metal is accompanied by a net spin current. In the LSSE geometry, this charge and spin current is directed towards the FM surface, leading to a spin accumulation which decays over the length scale of the spin diffusion length [88]: this is the SDSE [29, 85]. Due to the presence of spin accumulation in the FM side, attaching a NM material results in the flow of a pure spin current across the FM/NM interface, which can be detected via the ISHE [78, 86].

In brief, when a thermal gradient is applied perpendicularly to a FM/NM interface with metallic FM, a charge current is generated in FM because of the classical Seebeck effect; as FM shows long-range magnetic order, this charge current is spin-polarized, thus leading to spin accumulation at the FM/NM interface and to the injection of a pure spin current into NM.

The anomalous Nernst Effect

The ANE consists of the generation, in a FM metal, of a transverse voltage induced by a thermal gradient ∇T perpendicular to the magnetization $\mathbf{M}$. The ANE electric

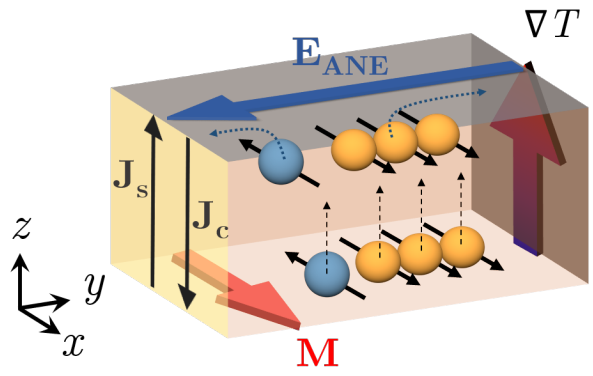

Figure 1.7 Phenomenology of the ANE process in a FM metallic material. Note that the spin-polarized current parallel to ∇T is generated by the SDSE. Note that the ANE geometry is equivalent to the LSSE geometry.

field is given by [95]

$$\mathbf{E}_{\mathrm{ANE}} = \mu_0 Q(\mathbf{M}) \times \nabla T, \tag{1.37}$$

where Q is the ANE coefficient and μ_0 is the vacuum magnetic permeability.

The ANE is the thermal analogous to the AHE [96]. In fact, it has been shown that the phenomenology of ANE follows the next picture [97, 98]: a spin-polarized current is excited by thermal gradients in FM materials due to the SDSE; this current is subsequently transformed into a spin current due to SHE, in materials with sufficiently high SOC. Because of the imbalance between spin-up and spin-down electrons, this spin current is accompanied by a charge current, leading to the generation of a mensurable electrical voltage, in a situation similar to that of the AHE. This process is schematically depicted in Fig. 1.7.

1.4.4 The spin Hall magnetoresistance

The spin Hall magnetoresistance (SMR) is the dependence of the measured resistance of a NM material on the angle between the charge current $\mathbf{J}_{\mathrm{c}}$ flowing through NM and the magnetization $\mathbf{M}$ of an adjacent MOI. Therefore, it is measured in MOI/NM structures (note that this is a particular version of the more general FM/NM structures). In contrast to other types of magnetoresistances, in SMR electrons do not flow through the FM layer; instead, SMR is a nonequilibrium proximity effect in which the resistance of a metallic film depends on the properties of an adjacent MOI.

SMR was reported for the first time in 2013 in Pt(12 nm)/YIG(single-crystal) structures [99]. In their initial work, Nakayama *et al.* already described the origin of the effect. The complete, rigorous theory was developed shortly after this first observation by Chen and *et al.* [100].

The SMR results from the simultaneous action of both the SHE and the ISHE. First, let us consider a freestanding NM film with strong SOC. When an in-plane charge current $\mathbf{J}_{\mathrm{c}}$ is applied in the y direction (z being the out-of-plane direction), the SOC gives rise to SHE which generates a spin current $\mathbf{J}_{\mathrm{s}}$ transverse to $\mathbf{J}_{\mathrm{c}}$. The spin polarization $\mathbf{s}$ of electrons that carry $\mathbf{J}_{\mathrm{s}}$ is oriented in the x direction, according

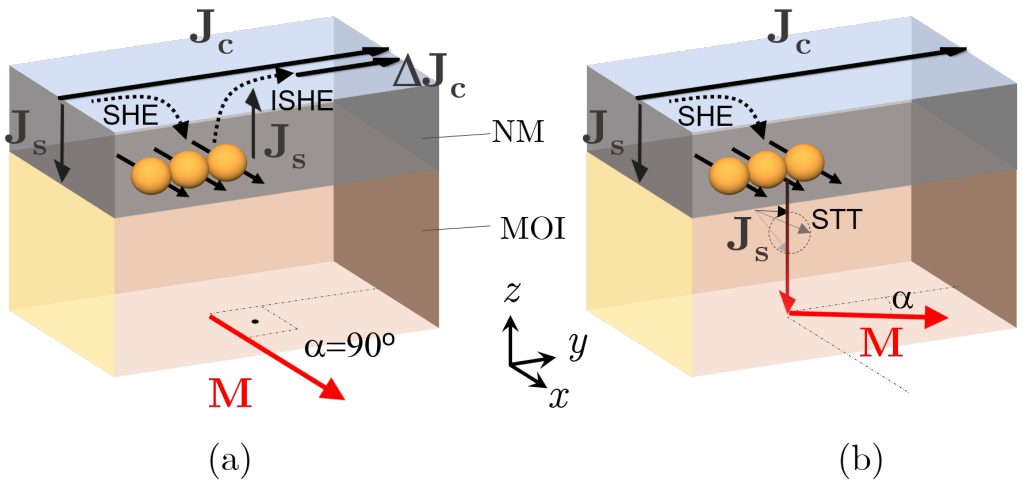

Figure 1.8 Schematic depiction of the SMR process. (a) Situation in which **M** has a component perpendicular to **s**. (b) Situation in which **M** is parallel to **s**.

to Eq. 1.26. This spin current flows perpendicularly to the NM surfaces, where generates a nonequilibium spin accumulation and is consequently reflected. Finally, ISHE operates over this reflected spin current generating a charge current $\Delta\mathbf{J}_c$ which is added to the original $\mathbf{J}_c$. Therefore, this SHE+ISHE source of charge current is always present in strongly spin-orbit coupled NM films.

However, this process can be tuned by the attachment of a MOI layer to one of the NM surfaces and the control of the angle between the MOI magnetization **M** direction and the spin polarization of conduction electrons, s, because part of the spin current $\mathbf{J}_s$ may be absorbed into the MOI due to **M** dynamics via spin-transfer torque (STT). Importantly, this happens only if **M** has a component perpendicular to **s**, as required by STT. Let us examine the different situations depending on the angle between **M** and **s**. The process comprises the next steps:

(1) A charge current $\mathbf{J}_c$ is driven along the y direction in NM.

(2) As explained, $\mathbf{J}_c$ is converted by SHE into a transverse spin current $\mathbf{J}_s$, which travels perpendicularly to the MOI/NM interface (along z direction).

(3) The spin current $\mathbf{J}_s$ reaches the NM/MOI interface leading to spin

accumulation.

(4) Depending on the relative orientation between **M** and **s**, different processes take place:

- If **M** has no component perpendicular to **s**, i.e., it fully lies in the x direction, as illustrated in Fig. 1.8(a), the spin-transfer torque is totally hindered and no spin absorption takes place. Thus, the spin current is fully reflected and converted by ISHE in an additional charge current $\Delta\mathbf{J}_c$. This situation is equivalent to that described for the freestanding NM. Because in this situation $\Delta\mathbf{J}_c$ is maximum, the measured resistance is minimum.
- If **M** has a component perpendicular to the **s** orientation (x direction), as illustrated in Fig. 1.8(b), spin current absorption from NM conduction electrons to MOI localized spins occurs via spin-transfer torque. Consequently, the reflection of spin current back to NM is partially suppressed, reducing the additional ISHE contribution $\Delta\mathbf{J}_c$ to the charge current in y direction, and generating an apparent increase of the NM resistance with respect to the situation in which **M** and **s** are parallel. This suppression is maximum for the maximum spin current absorption at the MOI/NM interface, i.e., when **M** is totally perpendicular to **s**, giving the maximum value of the measured resistance.

Note that, according to this phenomenology, SMR is expected to arise on sweeping **M** angle on the xy or on the xz planes (these angles are usually denoted by α and β). On the contrary, if **M** lies on the yz plane, it is always perpendicular to the spin polarization **s**, which is oriented in the x direction; consequently, there is always spin absorption and no SMR is observed. This behavior enables the angular-dependence magnetoresistance measurements (ADMR), which allows to unambiguously determine and quantify SMR even in the presence of other parasitic magnetoresistances when not totally insulating magnetic materials are used [101].

In this thesis, the xy situation was explored, i.e, in-plane magnetization. In this case, the resistance of the NM layer is maximum when **M** is in the y direction,

collinear to $\mathbf{J}_c$ and totally perpendicular to $\mathbf{s}$.

1.5 Structure of this thesis

This thesis is devoted to the experimental study of the thermal spin transport and to the deposition as thin films of materials which are of interest in this field. The aim of this work is to advance the current understanding of the studied phenomena and to contribute to develop their potential for technological exploitation.

The results may be grouped in three parts: the optimization of the thin film growth of the different materials (Chapter 3); the study of the SSE effect using mainly but not only maghemite/platinum bilayers, covering static and dynamic properties (Chapter 4 and 5); and the investigation of the ISHE in iridium(IV) oxide (Chapter 6). The manuscript is divided into seven chapters.

Chapter 1 presents the general framework of the work. A very brief introduction to the field of spintronics and the concept of the spin angular momentum, central to this thesis, is provided. Furthermore, concepts of spin dynamics and phenomena related to spin transport which are essential to this work are described. The objective of Chapter 1 is to provide the minimum theoretical background required for the comprehension of the thesis.

Chapter 2 summarizes the fundamentals of the main experimental techniques employed for the development of the work presented in this thesis, comprising fabrication and characterization techniques, and the experimental setups used for the different transport properties measurements.

Chapter 3 describes the optimization of the growth as thin films of different materials of interest in the field of thermal spin transport, which belong to one of these two groups: materials which combine insulating behavior with long-range magnetic order (MOI), and metals displaying a strong SOC. Concerning the first group, the optimal parameters for the fabrication of γ-Fe_2O_3 epitaxial thin films by pulsed laser deposition (PLD) are found; besides, preparation of epitaxial YIG thin films with nanometric thickness by means of a scalable chemical method is investigated. Concerning the second group of materials, the deposition by PLD

of IrO_2 on different substrates is also studied. Extensive characterization of each material supports their respective optimization process.

In **Chapter 4** the SSE in steady conditions is studied in γ-Fe_2O_3/Pt bilayers. Two different methods are employed: the external heater method and the current-induced SSE method. For the first one, the SSE efficiency in relation to the preparation conditions is addressed. A comparison with other FM/Pt structures reported in literature is provided, assuring maghemite's potential to be used in spintronics devices. Besides, maghemite thickness and temperature studies are presented. Concerning the current-induced SSE experiments, SSE and SMR contributions are extracted and analyzed. Finally, a thorough comparison is performed between both methods of triggering SSE in static conditions, showing their equivalence.

In **Chapter 5**, the ultrafast dynamics of the SSE is investigated in FM/NM structures using as FM three different materials, namely: insulating γ-Fe_2O_3, half-metallic Fe_3O_4, and metallic Fe. The objective of this chapter is to analyze, characterize and compare the dynamics of the thermal spin currents photoinduced in each material, which are expected to be of different nature (electronic and/or magnonic) as a function of their electrical conductivity.

Chapter 6 focuses on the ISHE spin-to-charge current conversion using IrO_2. For this, thermal spin currents are generated in γ-Fe_2O_3/IrO_2 bilayers. Influence of the IrO_2 thickness and of the temperature are studied, and, finally, the SOC mechanism governing ISHE is discussed. Besides, the multilayer approach to enhance the ISHE voltage is explored.

Finally, the **Conclusion and Outlook** section presents an overview of the key results and concluding remarks of this thesis, some future perspectives of this work being also briefly discussed.

Chapter 2

Experimental techniques

This chapter comprises an overview of the main experimental techniques used in the course of this thesis. First, we describe the sample preparation technologies, followed by a presentation of the characterization techniques, including structural, chemical, magnetic and electrical ones. Optical lithography, necessary in some of the further experiments for obtaining well-defined geometries, is also explained. Finally, more specific techniques such as those used for thermomagnetic and heat transport experiments, as well as Terahertz spectroscopy for time-evolution analysis, are discussed.

Most of the employed experimental equipment is located at the University of Zaragoza, either at the Institute of Nanoscience of Aragón or at Servicio de Medidas Físicas (Physical Measurements Service). Polymer Assisted Deposition and 3ω method for thermal conductivity determination of thin films were available through collaboration with Prof. Francisco Rivadulla at University of Santiago de Compostela. Terahertz spectroscopy was performed during a three-month research stay with the group of Prof. Tobias Kampfrath from Freie Universität in Berlin; the used spectrometer is located at the facilities of the Fritz Haber Institute, part of the Max Planck Society.

2.1 Thin film growth

Thin film fabrication constitutes an essential part of this work; not only as a mandatory step to obtain the media in which experiments are performed, but also as a —not minor— piece of research itself.

Several growth techniques have been used depending on the characteristics of the desired materials accordingly to their pursued functionality:

- **Pulsed Laser Deposition** was used to stabilize γ-Fe_2O_3 and IrO_2 as thin films. $\alpha-Fe_2O_3$, Fe_3O_4 and $Y_3Fe_5O_{12}$ thin films were also fabricated by means of this technique. Preparation of $Y_3Fe_5O_{12}$ was also optimized by **Polymer Assisted Deposition** in order to show the capabilities of this technique.
- **Sputtering** was the technique employed for Pt and Fe thin films growth.

2.1.1 Pulsed Laser Deposition

Pulsed Laser Deposition belongs to the family of Physical Vapor Deposition (PVD) processes. The technique is based on the focusing of a pulsed laser beam on a target of the material to be deposited, which is in turn placed facing a substrate holder. Both the target and the substrate holder are housed in a vacuum chamber. If the laser energy density exceeds a threshold, laser-target interaction results in the process of laser ablation and the creation of a so-called plasma plume, normal to the target surface. After propagation, this vaporized material condenses as thin film on the substrate after propagation.

Efficient vaporization of the material requires a short pulse duration, high energy density and high absorption of a small volume of material, meaning that the process cannot be explained within a thermodynamic equilibrium frame. This is easy to intuit considering that typical pulse duration of excimer lasers operating in the ultraviolet are 10 to 30 ns, and the fluence around 5 $J \cdot cm^{-2}$ is absorbed by a volume $\sim$ 3 mm $\times$ 1 mm $\times$ 100 nm (focused laser spot size times a typical oxide material absorption length) resulting in an almost instantaneous heating (rates as high as 10^{11} $K \cdot s^{-1}$ have been reported [102]) and rapid material removal. Consequently, nucleation process on the substrate is dominated by the kinetics of the plume

particles. This favors epitaxial growth of thin films by induction of compressive or tensile strain.

Mechanisms involved in the different steps of the process (i.e., ablation and plasma formation, plume propagation, and nucleation and growth) are numerous and complex. To begin with, photon absorption leads to electronic, thermal, chemical and mechanical excitation. All of them contribute to the plume formation, which is highly directed towards the direction normal to the target surface, following an angular distribution $\propto \cos^n \theta$, with $n = 1$ for thermal evaporation and in the range between $n = 4-14$ for non-thermal components [103]. Besides, a precise description must take into account not only the laser-target interaction but also the plume-laser interaction, as part of the beam energy is absorbed by the ejected material.

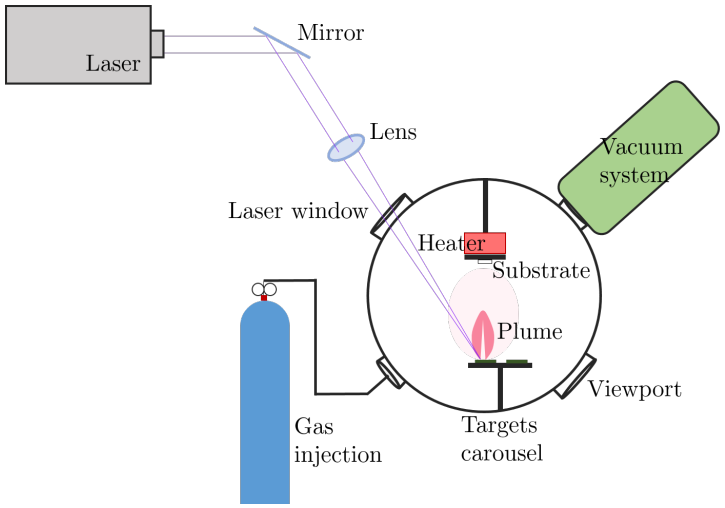

Figure 2.1 Sketch of a PLD experimental setup.

From a practical point of view, PLD has become an attractive technique for thin film growth due to some remarkable advantages over other techniques:

- First, its simplicity of implementation. A PLD setup consists of a pulsed laser, an optical path and a vacuum chamber. By means of the external optics, the laser beam is directed to a quartz window in the chamber —transparent to the laser wavelength— and focused on the target surface. The target usually

carries rotation and raster motion to improve the uniformity of the film and the erosion of the target. In addition to the laser window, the vacuum chamber must be equipped with the usual ports (pumping ports, gas inlets, pressure gauges, viewports) as well as ports for the targets and substrate holder. A schematic view of a PLD system is depicted in Figure 2.1.

- Secondly, the fact that the energy source —the laser— is external and thus independent of the vacuum hardware. This allows to carry out processes both in vacuum or under controlled atmosphere. Gas-assisted depositions are thus enormously facilitated, since a large range of working pressures can be used (essentially any pressure born by the vacuum system). In addition, it also enables combined use together with another type of (internal) evaporation source or even *in situ* characterization techniques.
- Arguably, the most remarkable feature of PLD is the capability of stoichiometric transfer from the target to the film. This is fostered by the non-equilibrium nature of the ablation process: as a consequence of the absorption of high energy by a small volume of material, the vaporization process becomes independent on the vapor pressures of the constituent ions [104].

Of course, PLD also shows some limitations. One of the main identified drawbacks is its *a priori* failure at homogeneously covering large areas, given the highly directional nature of the plume. In fact, the lateral thickness of deposited films reflects the $\cos^n \theta$ distribution, as can be seen from Figure 2.2(a) and (b). However, there is currently an active field of research devoted to the development of large-area PLD, based on different relative movements of target, beam and substrate [104–106]. A second issue historically attributed to PLD is the ejection of micron-sized solid particles in the ablation process, especially for large penetration depths of the laser pulse into the target. This phenomenon is known as *splashing* and can be triggered by different causes that shall not be discussed here as they are extensively analyzed in literature; see for example the review in reference [107].

The quality of the crystal structure of deposited films is influenced by tuning the

next relevant parameters:

- Topology, density and optical **properties of the target**, as well as laser wavelength [107].
- Target and substrate **positioning**. In particular, the separation between both of them will affect the material growth rate and thus the required energy [104, 108].
- **Laser parameters** (i.e., wavelength, fluence, pulse duration, pulse frequency and spot size) will determine the properties of the plasma, such as kinetic energy, flux, and ionization degree of the transported species [109].
- **Substrate temperature** during deposition represents another source of energy which provides adatoms with enough surface mobility for a sufficient diffusion length to promote crystalline and epitaxial growth [108].
- A good **level of vacuum** before the process start is desirable since it will reduce the contamination by impurities.
- A **background gas** can be used either as reactive species (e.g., molecular oxygen for oxides deposition) or to reduce the kinetic energy of the species in the plume [104].
- Lastly, the smallest the mismatch between **lattice constants** of substrate and thin film materials, the most favored epitaxial growth will be.

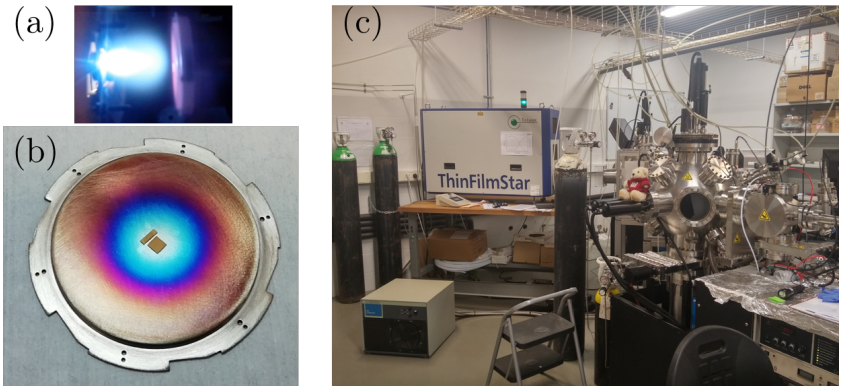

Figure 2.2 PLD experimental setup used in this thesis. **(a)** Plume of ablated material from a target. **(b)** Appearence of the substrate holder after a deposition: radial color profile mimics thickness variation. **(c)** Excimer laser and vacuum chamber PLDI.

The experimental setup used in this thesis is located at the INA. It is a system by *Neocera LLC* comprising a KrF excimer laser from *TuiLaser* (wavelength $\lambda = 248$ nm and pulse duration of 20 ns) and two vacuum chambers. The laser beam can be selectively directed to either of the chambers by means of two mirrors. One of the chambers (denoted PLDII) reaches vacuum levels $\sim 10^{-7}$ Torr by action of a turbomolecular pump and it is mainly used for deposition in oxygen atmosphere. The second chamber (denoted PLDI) is evacuated by a cryopump to a base pressure as low as $\sim 10^{-9}$ Torr. In addition, this chamber is equipped with a sputtering system, allowing for *in situ* combined use. The system is presented in Fig. 2.2(c).

2.1.2 Magnetron sputtering

Sputtering is another PVD technique. In this case, atoms from a solid target are ejected by its bombardment with energetic positive ions (usually Ar^+) and the consequent momentum exchange. The target is placed at the cathode of a glow discharge pair, whereas the substrate is located at the anode. The high voltage generated in this region ionizes the gas (usually argon), initiating the discharge. The plasma is then maintained by the emitted secondary electrons [110].

Magnetron sputtering is the most used variant of DC sputtering. It was developed to overcome one of the drawbacks of sputtering: its relatively slow deposition rate due to low ionization efficiency in the plasma [110]. In magnetron sputtering, a magnetic field is created parallel to the target surface, so that the electrons movement will be confined to the vicinity of the target, increasing the probability of ionization events. In addition to enlarge deposition rates, plasma stability is favored, meaning that lower operating pressures and voltages are granted [111].

Among the parameters affecting a deposition of a thin film by sputtering, we will name the following as the most relevant:

- **Power of the discharge**: it must be high enough so that the impact of accelerated ions on the cathode surface produces secondary electrons with enough energy to ionize new gas atoms and sustain the plasma [112].

Throughout the work described in this thesis, the value of the power was set at 10 W for most of the growths.

- **Inert gas (usually argon) pressure** should be high enough to maintain the discharge, meaning that enough ionizing electron-gas atom collisions must happen before electrons reach the anode (i.e., mean free path of electrons should not be over-enhanced). However, an excessive pressure will in turn increase the scattering between the gas atoms and the sputtered particles, preventing the latter from reaching the anode and condensing on the substrate [111]. The value used in most depositions within this thesis was $P_{\mathrm{Ar}} = 0.5$ mTorr.
- **Substrate-target distance and geometry** will influence the deposition rate and the arising of anisotropies in the microstructure of the sample, respectively.
- A good level of **base vacuum** before the process start to reduce contamination is even more desirable than in PLD due to slower deposition rates [111].
- In a similar fashion as in PLD, **substrate temperature** will affect the crystallinity of the thin film.

During this thesis, a sputtering system sharing an ultra-high vacuum (UHV) chamber with a PLD system was used: the combined PLD-sputtering system by *Neocera LLC* described in the PLD section. It is equipped with three magnetron sputtering guns and also with an RF power source in order to sputter insulating materials. RF sputtering has not been used in the course of this thesis.

2.1.3 Polymer Assisted Deposition

Physical vapor deposition technologies such as PLD or sputtering have the disadvantage of requiring expensive high-vacuum hardware that rockets up the cost of building such a facility. In addition to this, some of these techniques (for example, as we have seen, PLD) lack the desired scalability to be exploited by industry. In the search for alternatives, big efforts have been devoted to the development of chemical deposition methods from a starting solution to prepare epitaxial thin films. The main challenges were the achievement of nanometric control of thickness and roughness,

which for years have hampered the chemical production of high-quality functional oxides thin films thinner than $\sim$ 20 nm [113].

In this thesis, some samples were obtained by a water-based chemical method named Polymer Assisted Deposition (PAD) [114] that has proved itself capable of producing high-quality continuous functional epitaxial thin films of different oxides (featuring diverse structures such as perovskites [114, 115], rutiles [114], spinels [116] or garnets [117]) with well-controlled thicknesses below 20 nm. These samples were prepared through collaboration with the group of Prof. Francisco Rivadulla from Centro Singular de Investigación en Química Biológica y Materiales Moleculares (CIQUS) at University of Santiago de Compostela.

The steps followed in the preparation of an oxide thin film by PAD are listed here [113]:

(1) Stabilization of the cations in an aqueous precursor solution. For this, they are coordinated to an adequate polymer, which controls the viscosity of the solution. For multicationic oxides, these precursor solutions are mixed in the stoichiometric proportions. The total cation concentration controls the final thickness of the sample.

(2) Homogeneous covering of the substrate surface by the solution using spin-coating.

(3) Annealing at the appropriate temperature and atmosphere, optimized for the desired material. In this step, the solvents and polymers evaporate and the crystallization of films takes place.

In contrast to techniques in which growth is a non-equilibrium process, such as PLD, PAD can be more adequate in the stabilization as thin films of materials that are favored by thermodynamic conditions in their growth. This is most likely to happen in, for example, synthesis of complex phases (meaning complex cationic ordering) and, also, the mechanism found by the films to accommodate epitaxial stress, which can in turn influence the functional properties of the material, is affected [116, 118].

2.2 Structural and chemical characterization

The structure of the produced films was characterized to assess the crystal properties and, in some cases, to confirm the growth of the desired phase. Certain cases, (e.g., oxidation state discrimination) required further chemical analysis.

2.2.1 High resolution X-ray diffraction

Diffraction occurs when electromagnetic radiation impinges on a periodic structure with period on the length scale of its wavelength. The lengths of interest in this thesis are the interatomic distances, which extend to the order of angstroms, i.e., $\sim 10^{-10}$ m. Therefore, X-ray radiation has the appropriate wavelength for the study of crystal structures: $\lambda_{\text{X-ray}} = 10^{-11} - 10^{-8}$ m.

X-ray Diffraction (XRD) is indeed a widely used technique due to its huge potential in analyzing the crystal structure and quality of films without requiring elaborate preparation of samples (they can in fact be measured as-grown). In addition, it is a nondestructive technique. A great deal of information can be extracted from XRD measurements applied to thin films; for example lattice parameter, present crystalline phases, grains size, epitaxial strain or thickness of films.

The basic principle of XRD can be visualized from simple geometrical considerations, as sketched in Fig. 2.3: when a set of crystallographic planes (hkl) with interplanar distance d_{hkl} is struck by an incoming radiation of wavelength λ, a relative phase shift is induced between radiation scattered by atoms in one plane and the plane beneath, as a result of their path difference 2Δ. Interference between scattered beams will then be maximum —giving maximum detected intensity— when $2\Delta = n\lambda$. Recalling $2\Delta = 2d_{\text{hkl}} \sin\theta$ yields the Bragg's condition:

$$2d_{\text{hkl}} \sin\frac{2\theta}{2} = n\lambda \tag{2.1}$$

An XRD setup comprises an X-ray source, a monochromator, the holder placed in an eulerian cradle and the detector, aside from the required optics to ensure a

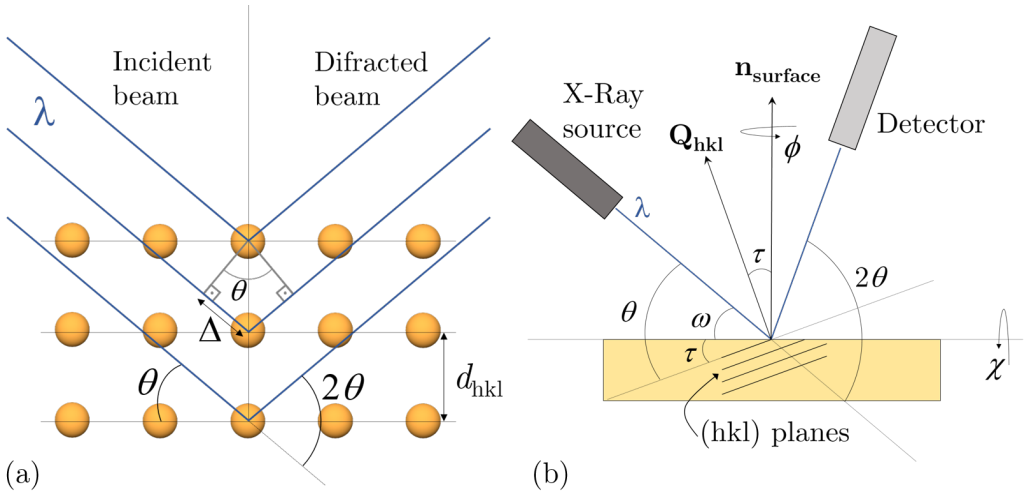

Figure 2.3 Geometry of measurement in XRD. **(a)** Visualization of the Bragg's condition in XRD. **(b)** Definition of angles in XRD measurements.

highly collimated beam. The equipment used during this thesis is a *Bruker D8 Advance* high-resolution diffractometer located at INA. In this system, the X-ray beam is emitted by a copper anode and passes through a four-crystal Ge (220) monochromator which selects the Cu $K_{\alpha 1}$ wavelength ($\lambda = 1.54056$ Å). This level of monochromacity enables the necessary precision to determine interplanar spacings [119], and it is the reason why this kind of XRD setup is branded as High-Resolution X-ray Diffraction (HRXRD).

The eulerian cradle allows for geometrical positioning by translation along the three Cartesian axes and rotation around four different angles:

- ϕ refers to the rotation of the sample around the axis normal to its surface.
- χ is the angle between the axis normal to the sample surface and the diffraction plane (the plane containing both the incident and diffracted beams).
- ω is the angle described by the incident beam and the intersection between the plane of the sample surface and the plane of diffraction. It corresponds to the angle between the incoming beam and the sample surface when $\chi = 0$. It is changed by rotation of the sample holder around the axis perpendicular to the diffraction plane.

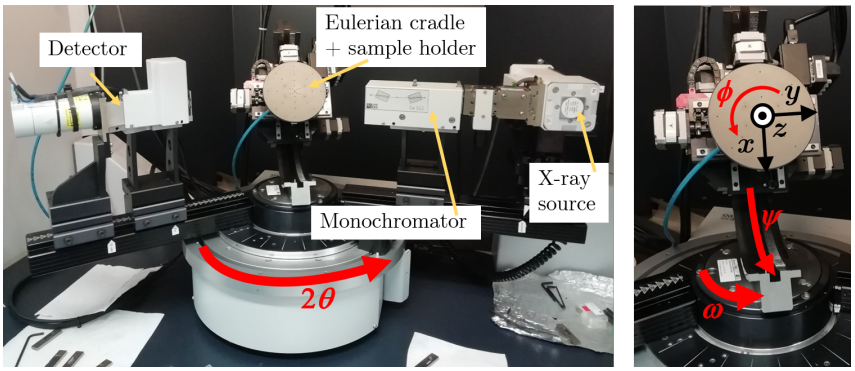

Figure 2.4 (a) Bruker D8 Advanced high-resolution XRD system at INA. (b) Zoom of the eulerian cradle showing the reference vectors.

- 2θ denotes the angle between the incoming and scattered beams. It is modified by rotation of the detector. This means that θ is the angle defined by the incident beam and the (hkl) plane responsible for the collected scattered radiation. A scan geometry that keeps $\theta = \omega$ and $\chi = 0$ (i.e., the atomic planes responsible for the detected scattered beam are those parallel to the surface of the sample) is called *symmetric*.

Acquirement of detected intensity while tilting one —or several— of these angles defines several types of scans that provide different information. In the following the scans of interest within this thesis are briefly described:

- In $2\theta/\omega$-scans the detector position 2θ and the sample position ω are concomitantly rotated keeping $\tau = \theta - \omega$ constant. In the symmetric variety ($\theta = \omega$) the dispersing planes are those parallel to the surface and thus the out-of-plane lattice parameter is obtained. In order to get information about the in-plane lattice parameters, asymmetric scans (either $\theta \neq \omega$ or $\chi \neq 0$) are demanded. The breadth of $2\theta/\omega$ diffraction peaks provides, in addition, useful information about the average size of the coherently diffracting domains through the Scherrer's empirical formula [120]:

$$D_{\text{hkl}} \approx \frac{0.9\lambda}{\beta_{2\theta} \cos\theta_{\text{hkl}}} \tag{2.2}$$

where $\beta_{2\theta}$ is the full width at half maximum (FWHM) of the diffraction peak at 2θ corresponding to the (hkl) plane and D_{hkl} is the size of the crystalline domain in the [hkl] direction scattering the incoming radiation coherently. In the case of epitaxial thin films, D_{hkl} can be approximated by the layer thickness.

- In the so-called *rocking curve*, also known as ω-scan, ω tilt is decoupled from the detector movement, so that 2θ is fixed fulfilling the Bragg's condition for a particular (hkl) plane and ω is rotated within a short range. This kind of scan is used for quantification of the dispersion in the crystalline growth with respect to the preferred [hkl] direction. A high misalignment will result in a broad distribution of the ω peak called *mosaic spread*. Thus, the FWHM of the *rocking curve* peak constitutes a figure of merit of the crystal quality of the thin films.
- ϕ-scan is likewise a tool for assessment of in-plane texture. 2θ and ω are fixed satisfying Bragg's condition for a asymmetric reflection with $\chi \neq 0$, so that the chosen (hkl) planes are taken to the diffraction plane. Then, intensity is collected while rotating ϕ angle 360°. By performing this scan for both the substrate and the film, the in-plane orientation of the latter with respect to the former can be inferred. Additionally, χ angle can be tilted within a slight range around the required χ, so that a ϕ-scan is measured for each value of χ and thus a 2D-diffraction map known as *pole figure* is obtained.
- Finally, Reciprocal Space Maps (RSM) or *Q-plots* can be performed in order to quantify the value of the in-plane and out-of-plane lattice constants of the film and the substrate. This allows to evaluate the mismatch between the in-plane parameters and compute the epitaxial strain (compressive or tensile) of the film. RSM are obtained by combination of $2\theta/\omega$ and *rocking curves* around an asymmetric diffraction peak of the film. Diffraction peak at position 2θ and $\omega = \theta \pm \tau$ is searched, where τ is the angle between the diffracting planes (hkl) and the plane parallel to the sample surface. Usually the useful transformation between 2θ and ω and the more convenient $\mathbf{Q}$ coordinates is performed [119].

$\mathbf{Q}_{\mathrm{hkl}}$ is the scattering vector:

$$\mathbf{Q}_{\mathrm{hkl}} = \mathbf{K} - \mathbf{K}' \tag{2.3}$$

where $\mathbf{K}$ and $\mathbf{K}'$ are the wave vectors of the incoming and diffracted radiation, respectively. For a crystal with primitive vectors of the lattice $\mathbf{a}$, $\mathbf{b}$ and $\mathbf{c}$, $\mathbf{Q}_{\mathrm{hkl}}$ satisfies

$$\begin{aligned} \mathbf{a} \cdot \mathbf{Q}_{\mathrm{hkl}} &= 2\pi \cdot h \\ \mathbf{b} \cdot \mathbf{Q}_{\mathrm{hkl}} &= 2\pi \cdot k \\ \mathbf{c} \cdot \mathbf{Q}_{\mathrm{hkl}} &= 2\pi \cdot l \end{aligned} \tag{2.4}$$

This set of relationships, known as Laue conditions, is equivalent to the Bragg's law, as shown in literature [119]. The transformation between both representations, in terms of the in-plane ($Q_{\parallel}$) and out-of-plane ($Q_{\perp}$) components of $\mathbf{Q}_{\mathrm{hkl}}$, is as follows:

$$\begin{aligned} Q_{\mathrm{hkl}} &= 2 \cdot \frac{2\pi}{\lambda} \sin\theta \\ Q_{\parallel} &= Q \sin\tau \\ Q_{\perp} &= Q \cos\tau \end{aligned} \tag{2.5}$$

The position of the diffraction spots in the RSM allows the calculation of in-plane and out-of-plane lattice parameters by using the Laue conditions in Eq. 2.4

2.2.2 X-ray reflectivity

The same diffractometer used for HRXRD can be operated to perform X-ray reflectivity or reflectometry (XRR). The defining point of XRR with respect to XRD is a low angle of incidende $\omega \approx \theta$ between the higly collimated primary beam and the sample surface. In this configuration, a combination of reflection and refraction phenomena rather than diffraction is used to study structural properties of the sample. XRR $2\theta/\omega$-scans yield quantitative information about density, surface and

interface roughness, and thickness of thin films. Since this technique does not rely on diffraction, crystallinity does not play a role and thus can be used to study not only crystalline but also amorphous samples.

A $2\theta/\omega$ pattern in XRR is originated as follows: incident beam is transported though air, with refractive index $n = 1$, towards the sample, with refractive index for X-ray frequencies slighty lower than 1. This means that X-rays travel from a higher refractive index medium to a lower refractive index medium; therefore, total reflection will take place for incident angles lower than a a critical angle θ_c. This θ_c depends on the electron density of the material and typically ranges between 1° and 10°.

Above θ_c, radiation is partially reflected and partially transmitted through the sample. If the sample is composed by a stack of layers (at least two layers –substrate and one film– are always present), above θ_c each interface partially reflects the incoming beam and trasmits part to the layer below. Note that the surface is considered as the interface between air and the sample. Reflected beams travel a different path depending on the different refractive indexes and thicknesses of their travelled media, what introduces a phase difference between them, as sketched in Fig. 2.5. As a result, constructive and destructive interference between individual beams reflected back to air from each interface will give rise to oscillations in the collected intensity known as Kiessig fringes. Each present layer will contribute with a period in the oscillation pattern. The higher the incidence angle, the lower the reflected intensity is, till signal finally evanesces with increasing θ.

The as-generated $I(2\theta)$ pattern will be affected by structural parameters of the sample as follows: the density of every layer modifies the value of the critical angle and the amplitude of the interference oscillations; thickness of layers will inversely affect the period of the oscillations; and roughness of interfaces and surface will damp the amplitude of oscillations and the evanescense angle: the higher the roughness, the lower the angle at which oscillation will be hidden by background.

The raw data obtained from measurement are analyzed using the software *Leptos* from Bruker. It simulates the sample structure and, by means of a simulated

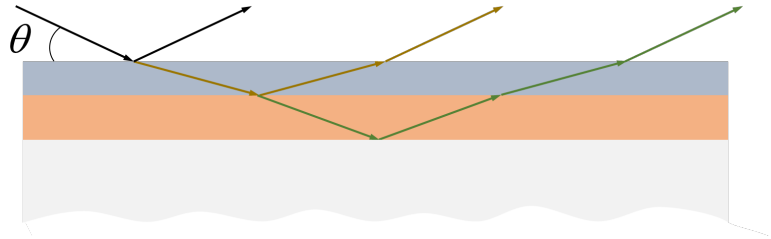

Figure 2.5 Paths of the refracted and reflected beams in a multilayer structure comprised of two layers (blue and orange) and a substrate (grey layer). Beam reflected by the surface is shown in black, beam reflected by the interface between both blue and orange layers is yellow colored and beam reflected by the interface between the first layer and the substrate is green colored.

annealing algorithm, which uses thicknesses and roughnesses as fitting parameters, the values of these quantities for each constituent layer are obtained.

2.2.3 X-ray photoelectron spectroscopy

X-ray photoelectron spectroscopy (XPS) is a technique for quantitative chemical analysis of surfaces. It is sensitive to the elements, oxidation state and coordination of the atoms below the surface of the sample.

The working mechanism, represented in Fig. 2.6(a), is based on the photoelectric effect: X-ray radiation is targeted on the surface of the sample and excites electrons from the core levels of its atoms. These electrons are then emitted with a kinetic energy defined by their binding energy E_{B} and chemical environment, following the expression:

$$E_{\mathrm{B}} = h\nu - K - \phi \tag{2.6}$$

where K is the kinetic energy of the electron and ϕ denotes the photoelectron work function. The detected energies can be referenced to the Fermi energy of the spectrometer, so that an "absolute" energy scale can be established and thus the work function of the sample does not need to be known.

$$E_{\mathrm{B}} = h\nu - K^{*} - \phi_{\mathrm{det}} \tag{2.7}$$

Therefore, energy-filtering of emitted electrons and subsequent recording of the intensity for a defined energy will provide the aforementioned chemical information. Relative concentration of the present species can be determined within 10% accuracy.

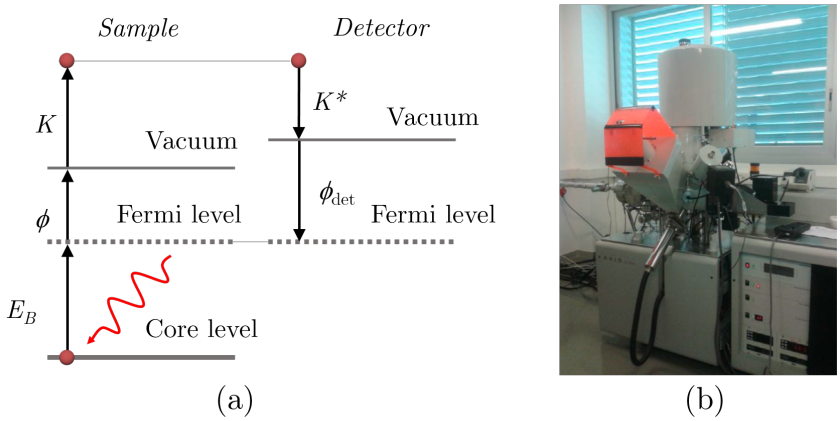

Figure 2.6 (a) Depiction of the XPS process. (b) XPS *Kratos AXIS UltraDLD* equipment at INA.

Electrons have a low inelastic mean free path, meaning those excited in atoms deeper than a few (typically 3 to 10) nanometers from the surface will not leave the sample without undergoing an energy loss event: that is the reason why XPS is a surface-sensitive tool. However, some equipments are capable of performing *in situ* etching with Ar^+, enabling depth profile analysis.

The system used in this thesis, shown in Fig. 2.6(b), is a *Kratos AXIS UltraDLD* with an Al K_α monochromatic source, operated at background pressure $< 10^{-9}$ Torr.

2.2.4 Transmission electron microscopy

Transmission Electron Microscopy (TEM) is a highly powerful technique that allows microstructural inspection of samples down to atomic scale, granting access to an enormous variety of information. A highly-accelerated electron beam (using accelerating voltages from 60 to 300 kV) is directed towards an ultrathin specimen. The different signals generated by the transmitted electrons (either non-scattered

electrons, elastically scattered electrons or inelastically scattered electrons) can be analyzed to determine structure and/or chemical composition of the studied sample.

The image resolution of any microscope is limited, among other factors, by the wavelength of the used radiation. Thus, with an associated wavelength substantially less than visible light, electrons can substantially increase resolution. Acceleration of electrons using a high voltage gives the possibility to tune their wavelength, according to:

$$\lambda = \frac{\mathrm{h}}{(2\mathrm{m}_e \mathrm{e} V)^{1/2}} \tag{2.8}$$

This expression easily comes from the De Broglie relation, ignoring relativistic effects. This means that, under this approximation, the wavelength of an electron accelerated using 300 kV voltage is $\sim$ 2 pm, enough to achieve atomic resolution [121].

However, the resolution of an electronic microscope is also lowered by other factors, especially aberrations introduced by magnetic lenses. Nonetheless, some modern microscopes are equipped with newly developed aberration correctors that allow spatial resolutions down to 0.5 Å.

Sample preparation is another critical point: specimens (usually cross-sections) extracted from the original thin film need to be thinned down to a few tens of nm, in order to enable transmission of electrons through them. The so-called *lamellae* (thin film foils) of the samples analyzed in this thesis were prepared by the clean room service of the Laboratorio de Microscopías Avanzadas (LMA) using the Focused Ion Beam facility inside a dual-beam Helios Nanolab 600 or 650 from FEI.

In general, a TEM instrument is composed of (1) an **illumination system** that comprises the electron source and the condenser lenses system, (2) the objective lenses system and specimen holder that together constitute the **stage**, and (3) an **imaging system** which uses magnification lenses, different detectors and screens, and the recording system [121]. A schematic representation of a TEM column can be found in Fig. 2.7(a).

TEM actually comprises a range of different techniques that can be implemented within the same instrument or, on the contrary, dedicated instruments can be

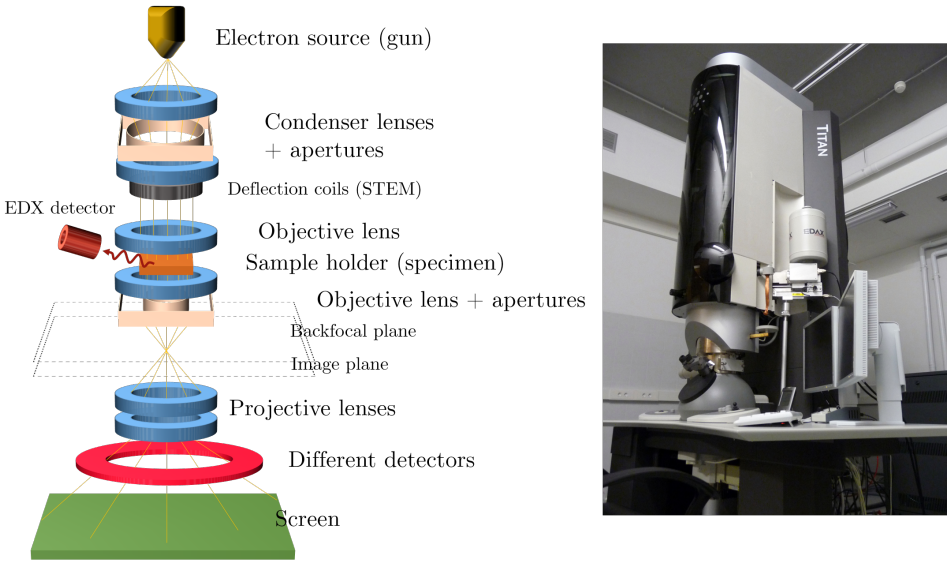

Figure 2.7 (a) Simplified scheme of a TEM column. (b) FEI Titan 60-300 *Low Base* TEM at INA.

designed for the optimal implementation of one specific technique.

In this thesis, high resolution TEM (HRTEM), scanning TEM (STEM), and electron diffraction will be the most relevant modes.

Electron diffraction is complementary to X-ray diffraction. Electrons are scattered more strongly than electromagnetic radiation, and thus, very tiny volumes of material can be studied (few to hundreds of nm in extension) [122]. In addition, TEM offers the capability to observe the real and reciprocal space for the very same region: the spatial distribution of scattering is translated into the image contrast (real space) in the imaging plane and the angular distribution will form diffraction patterns (reciprocal space) in the backfocal plane.

In HRTEM the objective lenses use both transmitted and elastically scattered beams to create an interference image of the crystal structure. The sample is illuminated with a parallel beam, forming approximately a plane wave.

In STEM, a strongly focused beam is used to form a convergent probe down

to $\sim$ 1Å which scans across the sample. Different electron-sample interactions will scatter electrons at different angles; thus, there are different detectors available for electron collection depending on the kind of information we are interested in. STEM is most often used in combination with high-angle annular dark field detection (HAADF), mainly because it results in "$Z-$contrast" imaging (Z represents the atomic number) as the high-angle electron scattering cross-sections scale as $\sim Z^2$ [123].

We will finally comment that the energy losses underwent by inelastically scattered electrons can be analyzed to get chemical information in the so-called analytical techniques, such as Electron Energy Loss Spectroscopy (EELS) or Energy-dispersive X-ray spectroscopy (EDX).

The experiments in this thesis were performed in a FEI Titan 60-300 *Low Base* TEM (picture in Fig. 2.7(b)), located at LMA-INA, and equipped with a spherical aberration corrector from CEOS for the probe in STEM mode. This corrector allows for resolutions as high as $\sim$ 0.09 nm, that, together with a high brightness Schottky field emission gun (XFEG), a monochromator and a Gatan Tridiem 866 energy filter for EELS enables 2D chemical compositional mapping with atomic resolution.

2.3 Magnetic characterization

Magnetic properties of the samples were studied by Vibrating Sample Magnetometry (VSM) and Superconducting Quantum Interference Device (SQUID)

2.3.1 Vibrating Sample Magnetometry

VSM measurement of magnetic properties is based on an induction method, i.e., it monitors a voltage induced in an electric circuit by a changing magnetic flux.

The sample is placed between the poles of an electromagnet that creates a uniform magnetic field and also between two identical pickup coils. A vibrating movement generated by a transductor is transmitted to the sample by means of a rod, perpendicular to the uniform magnetic field. The resulting oscillating magnetic

moment generates an electromotive force in the pickup coils according to:

$$V = -NS\frac{\mathrm{d}\left[H_{ext} + r(t)m\right]}{\mathrm{d}t} \propto -m\sin\left(\omega t\right) \tag{2.9}$$

$r(t) = A\cos\left(\omega t\right)$ represents the position of the sample around the center. This voltage V is measured by a lock-in amplifier. In order to determine the constant of proporcionality relating it to the magnetic moment m of the sample, a Ni calibration sample of known magnetic moment is measured.

The VSM system employed in this thesis is a model from ADE Technologies, located at INA.

2.3.2 Superconducting Quantum Interference Device

Superconducting Quantum Interference Device magnetometry uses Josephson effect phenomena to measure extremely small variations in magnetic flux and, thereby, in associated magnitudes [124]. A typical SQUID sensor consists of one (RF SQUID) or two parallel (DC SQUID) Josephson junctions in a superconducting ring. A bias current is maintained in the SQUID sensor and, in this situation, the variation of magnetic flux through the ring —which is quantizied— will result in a periodic variation of the voltage across the junctions. Alternatively, the induced screening current along the ring, with the period of the magnetic flux quantum is detected (RF SQUID). Based on this, the magnetic moment of a sample can be determined by moving it through the SQUID ring.

In this thesis a MPMS-XL SQUID from Quantum Design was used in the RSO mode that increases the sensitivity up to 1×10^{-8} emu. It is accessible through the Servicio de Medidas Físicas (Physical Measurements Service) at the University of Zaragoza. The maximum magnetic field created by the superconducting magnet is 5 T. Operation temperature ranges from 2 K to 400 K.

2.4 Optical lithography

Optical lithography was used in this thesis to define micro-sized patterns in the samples when necessary, following the top-down approach of nanotechnology.

The used optical lithography facility is located at INA in a 100-class clean room (meaning that the density of particles of size bigger than 0.1 µm is maintained below 100 particles/m^3) and reaches a spatial resolution of $\sim 2\,\mu m$.

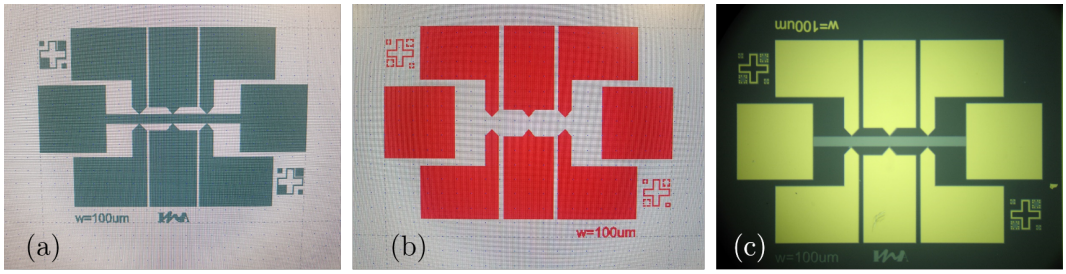

Figure 2.8 (a) Pattern transferred in the first lithography step, in which material of the thin film stack outside the green-colored areas is removed. (b) Pattern transferred in the second lithography step, which results in the deposition of metallic contacts in the red-colored areas. (c) Optical image of a 100 µm-wide Hall bar obtained by optical lithography from a γ-Fe_2O_3/Pt stack of thin films grown on an MgO subtrate.

In general, five basic elements are required for optical lithography: a light source, a mask showing the desired pattern to be transferred, a photoresist (a photosensitive material), the developer and an etching procedure. In addition, we might be interested in growing some material in an intermediate stage of the overall procedure, a process known as lift-off.

In this thesis, samples were patterned into Hall bar structures of 100 µm in width and 1600 µm in length. Two different lithography stages were required. In the first lithography process, the pattern was transferred to the sample. The goal of the second lithography process was the growth of metallic contacts. Therefore, two complementary transparent quartz photomasks with the designed motifs in chromium (which absorbs UV light) were used. The designs for the first and second lithography steps are shown in Fig. 2.8(a) and (b), respectively.

The result of the first lithography stage is the removal of all material in the sample

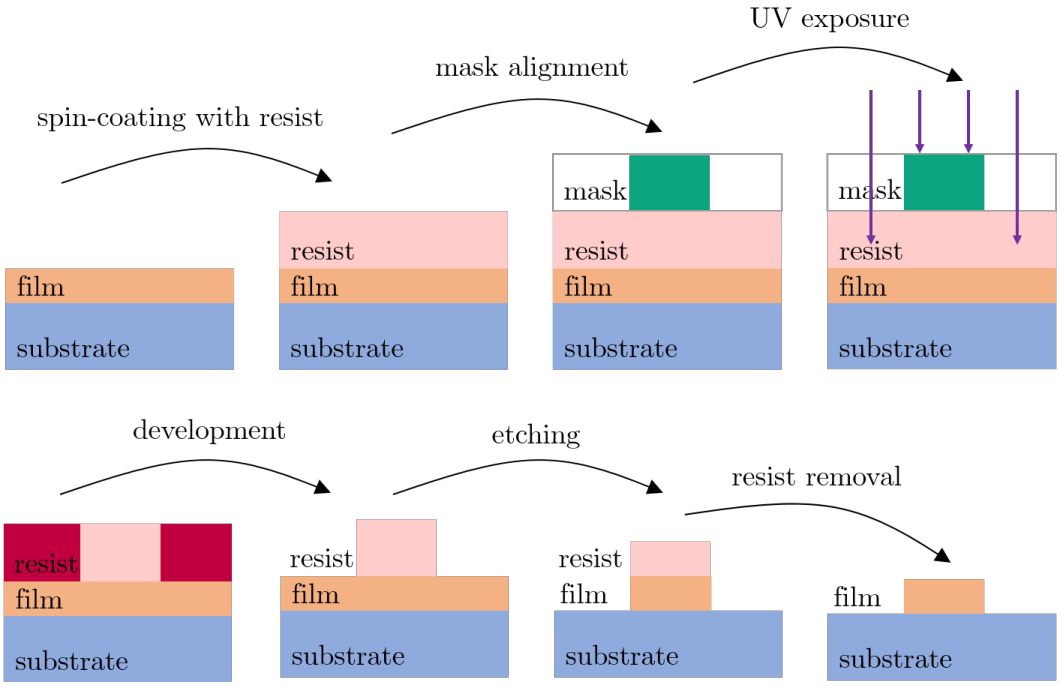

Figure 2.9 Diagram of the fist lithography stage, using positive photoresist.

except the colored areas in Figure 2.8(a). For this, several steps were needed: (1) first, the sample is cleaned and a positive photoresist is spin-coated on top of it to create a layer between 2 and 4 µm of thickness. (2) Subsequently, it is soft-baked at 100°C during 1 minute to eliminate the solvents and improve adhesion. (3) Next step is the exposure to the source of light after placing the mask on top of the sample and aligning the desired pattern. For this, we used UV radiation provided by a Hg lamp. The mask aligner and the lamp are integrated in the same equipment. The areas of the resist which are under the transparent parts of the mask become sensitized by the UV light. As a result, they become soluble in the appropriate developer. (4) After exposure, a post-exposure bake at 120°C of 1 minute of duration is carried out. (5) As a consequence, during the development the sensitized parts of the resist are dissolved and only a pattern of resist in the shape of the design remains on top of the sample. (6) The sample is then subjected to a hard-bake again at 120°C during

another minute. (7) Finally, the sample is etched by ion milling with accelerated Ar^+ ions. As a result of this, the material in the sample which is not protected by resist will be removed and the pattern will be transferred to the sample. The rests of resist are eliminated, usually with acetone. This first lithography stage is sketched in Fig. 2.9.

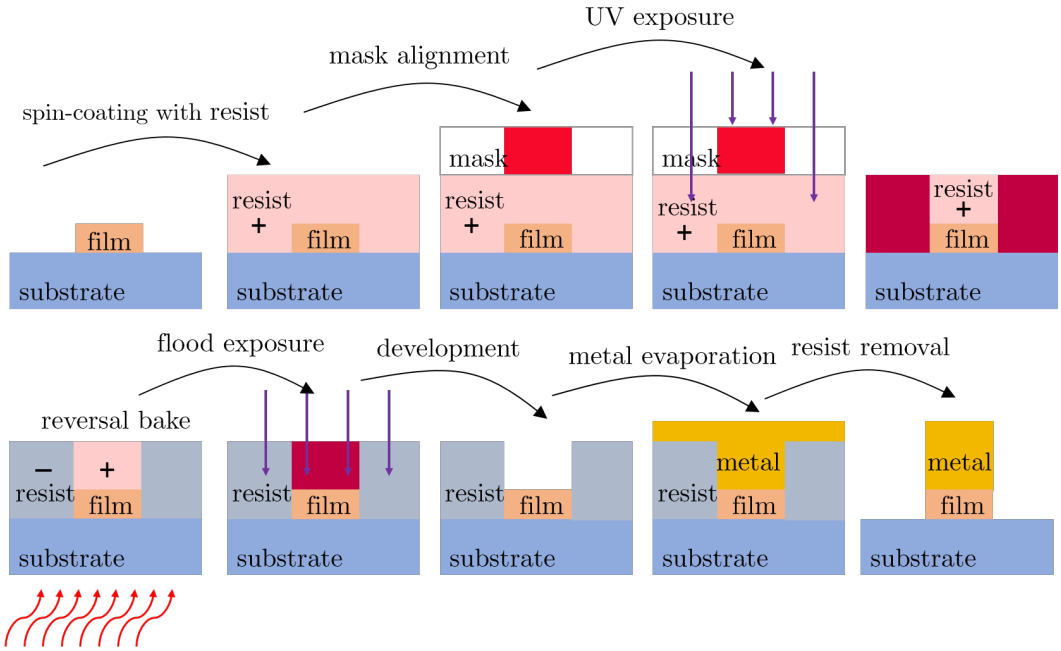

Figure 2.10 Scheme of the second lithography stage, which is a lift-off process using a reversible photoresist.

The objective of the second stage is the deposit of metallic pads by a lift-off process, and is schematically depicted in Fig. 2.10. In this case, a reversible photoresist is spinned on top of the sample and soft-baked. This resist will act as negative resist, which means that the areas of resist that will remain are those under the transparent parts of the mask. After mask alignment and exposure, another bake of 2 minutes at 120°C is performed. This one is called reversal bake because its effect is hardening and making the exposed resist insoluble in the developer (it becomes negative), while the unexposed areas will remain positively photoactive. After this, a

short flood exposure of 15 seconds without any mask will sensitize the non-hardened and thus photoactive parts of the resist, which retains its positive behavior and can subsequently be removed by the development process. Finally, the resists remains only in the areas that were not covered by chromium in the mask. Then, 2 nm of Cr (for adhesion improvement) and 10 nm of Au are evaporated in an e-beam evaporator. The very last step is the immersion in acetone to remove the remaining resist and, consequently, the metals grown on it. The result of the overall described process is shown in Fig. 2.10.

2.5 Transport measurements

Studying of transport phenomena is at the very core of this thesis. The phenomena under inspection are governed by the transport mechanisms of different quantities under different conditions, so access to the parameters that characterize them was paramount.

2.5.1 Electrical and thermomagnetic transport

Electrical and thermomagnetic transport measurements were performed within the same home-made setup using a set of compatible sample holders and probes. Aside from those, the main components of this system are (see Fig. 2.11):

- An *Oxford* continuous Helium flow cryostate with a flux controller and heating power controller that provide a range of temperatures from 4 K to 400 K for measurements.
- The sample inside the cryostate is placed between the pole pieces of an electromagnet powered by a *TDK Lambda* power supply and achieving up to 1 T field.
- A *Keithley* 236 source-meter unit (SMU) for current injection in the range between 100 fA to 100 mA.
- A *Keithley* 2000 multimeter, with a maximum input resistance of 10 GΩ and $6\frac{1}{2}$ digits precision.

- A *Keithley* 2182a nanovoltmeter. This instrument has a resolution down to a few nanovolts in the smallest voltage range and using high enough integration times (several seconds in this range). The input is terminated with a two-channel LEMO socket connector.

Figure 2.11 Transport measurement system components. (a) *Keithley* 2182a nanovoltmeter. (b) *Keithley* 2000 multimeter. (c) *Keithley* 236 SMU. (d) Electromagnet *TDK Lambda* power source. (e) Temperature controller. (f) Cryostate. (g) Electromagnet.

All these instruments can be remotely controlled by means of customized software developed in LabVIEW platform from *National Instruments*.

Depending on the nature of the measurements to be performed, different sample holders and probes are available. Some of these sample holders were preexisting in the set-up stock and some of them were specifically developed during this thesis.

In the following, a detailed description of the sample holder and set-up configuration for each type of measurement is provided.

(a) Electrical resistivity measurement

Four-probe geometry was utilized to measure electrical resistivities. Depending on the sample shape, a Van der Pauw [125] or instead a lineal geometry was chosen.

Van der Pauw geometry is appropriate for square-shaped samples. An ohmic contact is made in each corner on the sample. In this way, current is injected along one edge and voltage drop is measured between the contacts in the opposite edge

(see Fig. 2.12(a)). The measured resistances are averaged and the obtained R value is used to calculate the sheet resistance, R_s

$$R_s = \frac{\pi R}{\ln 2} \tag{2.10}$$

The resistivity ρ is computed as $\rho = t \cdot R_s$ where t is the thickness of the sample.

Lineal geometry is more suitable for elongated-shape samples. In this case, the four contacts are linearly placed, typically equally separated, as shown in Fig. 2.12(b). Current is injected between the outer contacts and voltage is measured between the inner contacts.

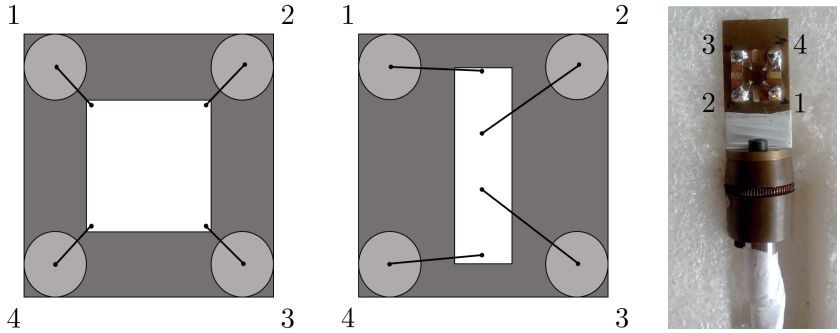

Figure 2.12 Electrical resistivity measurement. (a) Van der Pauw geometry. (b) Linear geometry. (c) Sample mounted in the four-pins chip carrier, which is inserted to the compatible probe.

In either case, the *Keithley* 236 SMU is used for current injection, whereas the *Keithley* 2000 multimeter measures the voltage. The sample holder is a four-pin chip carrier, which is inserted into a compatible probe driving four cables to a connection box where the electronics are conveniently wired. Electrical contacts from the sample to the pin pads were made with Al wire of 25 μm diameter, using silver paste in the sample end and tin solderings to the pin. An example of this assembly is pictured in Fig. 2.12(c).

(b) Longitudinal Spin Seebeck effect measurement using a heater

For Longitudinal Spin Seebeck effect study, a thermal gradient must be created across the sample ($\hat{z}$ direction) and the transverse voltage ΔV_y ($\hat{y}$ direction) must be detected. In this thesis, we used two different experimental setups to do so.

Here we describe the first option, which makes use of an external resistive heater for the generation of the thermal gradient. The samples are mounted in a preexisting sample holder which consists of two Aluminium Nitride (AlN) pieces attached together by two insulating Teflon screws and laying on a copper cold reservoir (heat sink). The sample is placed sandwiched between the AlN plates, material that was chosen attending to its insulating behavior [126] and yet high thermal conductivity up to 285 $\mathrm{Wm^{-1}K^{-1}}$ [127] which ensures minimum heat losses and electrical insulation of the sample. On top of the upper AlN piece, the thermal gradient is created by passing a current through a heater with $R = 2$ KΩ (heat

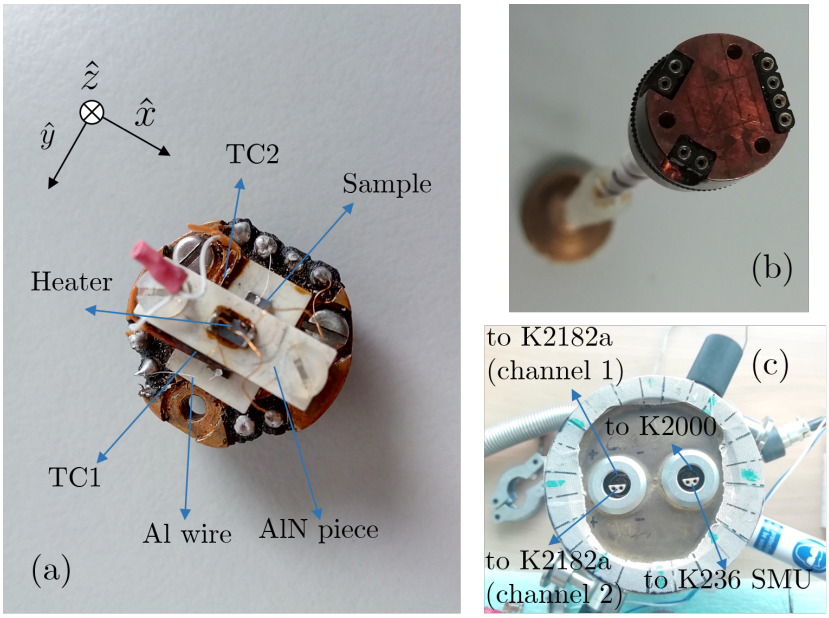

Figure 2.13 (a) Sample holder for LSSE measurement using a resistive heater. (b) Probe for this holder, showing the end where it is inserted. (c) Opposite end of the probe, showing the LEMO connections for the electronics.

source), attached using GE-varnish. The thermal drop ΔT established between both AlN plates is monitored by means of two T-type thermocouples. Constantan endings of the thermocouples are soldered together to allow differential measurement.

In this experiment, the *Keithley* 236 SMU injects current to the heater to establish the thermal gradient; the *Keithley* 2000 multimeter collects the signal from the thermocouples and thus provides the value of ΔT; and finally the output transverse voltage ΔV_y is measured by the *Keithley* 2182a nanovoltmeter. The sample holder, shown in Fig. 2.13(a), possesses eight pins: two for current injection, two for the thermocouples and two for each of both measurement channels available in the nanovoltmeter. The probe, shown in Fig. 2.13(b), is designed for in-plane measurements with respect of the magnetic field and features two socket LEMO connections in the outer ending (see Fig. 2.13(c)): one for the heater and thermocouples connection and the other for both channels of the *Keithley* 2182a nanovoltmeter.

In order to exclude parasitic effects which may contribute to ΔV_y (e.g., a ground offset or an ordinary Seebeck effect due to misalignment of contacts), the odd parity of the LSSE as a function of magnetic field is exploited as follows: the magnetic field is swept twice (from $H = -8$ kOe to $H = +8$ kOe and *vice versa*) for every ΔT, and the antisymmetric $\Delta V^{\mathrm{anti}}(H)$ component of ΔV_y is extracted. Then, the values of $\Delta V^{\mathrm{anti}}(H)$ at positive and negative saturated magnetic fields ($+H_{\mathrm{S}}$ and $-H_{\mathrm{S}}$) are used to calculate the output voltage $\Delta V_{\mathrm{ISHE}} = \left[\Delta V^{\mathrm{anti}}(+H_{\mathrm{S}}) - \Delta V^{\mathrm{anti}}(-H_{\mathrm{S}})\right]/2$.

(c) Spin Hall Magnetoresistance and Joule-Spin Seebeck effect simultaneous measurement

Another experimental approach for the study of the LSSE was examined in this thesis, as mentioned in the previous heading. In this case, the NM layer also plays the role of the heater, in addition to its original role as spin current detector by ISHE. For this, a large dc current I_{d} is driven along NM and the transverse voltage ΔV_y is recorded [128, 129]. This method has been referred to as current-induced LSSE or Joule-heating induced LSSE (JSSE).

The contribution of ISHE voltage ΔV_{ISHE} will be proportional both to the sine of the angle between the magnetic field and the direction in which ΔV_y is measured, and to the dissipated electrical power in NM by Joule effect (since the spin current is excited by the thermal gradient arisen as a consequence of this dissipation). In literature typically the in-plane angle α is rather defined as the angle between the directions of magnetic field and I_{d} —complementary to the aforementioned. Thus:

$$\Delta V_{\mathrm{ISHE}} \propto I_{\mathrm{d}}^2 R_{\mathrm{NM}} \cos\alpha \tag{2.11}$$

The fact to be highlighted here is that the contribution of SSE to ΔV_y is expected to be even in I_{d}, i.e., $\Delta V_{\mathrm{ISHE}}(I_{\mathrm{d}}) = \Delta V_{\mathrm{ISHE}}(-I_{\mathrm{d}})$.

Other effects may contribute to the output signal ΔV_y, mainly magnetoresistive phenomena such as the recently discovered SMR. A slight misalignement of the contacts could also rise a resistive contribution. These other effects, however, are odd in I_{d}: $\Delta V_{\mathrm{MR}}(I_{\mathrm{d}}) = -\Delta V_{\mathrm{MR}}(-I_{\mathrm{d}})$.

This means that we can disentangle both contributions by driving I_{d} in the opposite direction and adding or subtracting both signals. Therefore, we will have, on the hand:

$$\begin{aligned}
&\Delta V_y(I_{\mathrm{d}}) + \Delta V_y(-I_{\mathrm{d}}) = \\
&\quad = \Delta V_{\mathrm{ISHE}}(I_{\mathrm{d}}) + \Delta V_{\mathrm{MR}}(I_{\mathrm{d}}) + \Delta V_{\mathrm{ISHE}}(-I_{\mathrm{d}}) + \Delta V_{\mathrm{MR}}(-I_{\mathrm{d}}) = \\
&\quad = \Delta V_{\mathrm{ISHE}}(I_{\mathrm{d}}) + \Delta V_{\mathrm{MR}}(I_{\mathrm{d}}) + \Delta V_{\mathrm{ISHE}}(I_{\mathrm{d}}) - \Delta V_{\mathrm{MR}}(I_{\mathrm{d}}) = \\
&\quad = 2\Delta V_{\mathrm{ISHE}}(I_{\mathrm{d}})
\end{aligned} \tag{2.12}$$

While, in the other hand:

$$\begin{aligned}
&\Delta V_y(I_{\mathrm{d}}) - \Delta V_y(-I_{\mathrm{d}}) = \\
&\quad = \Delta V_{\mathrm{ISHE}}(I_{\mathrm{d}}) + \Delta V_{\mathrm{MR}}(I_{\mathrm{d}}) - \Delta V_{\mathrm{ISHE}}(-I_{\mathrm{d}}) - \Delta V_{\mathrm{MR}}(-I_{\mathrm{d}}) = \\
&\quad = \Delta V_{\mathrm{ISHE}}(I_{\mathrm{d}}) + \Delta V_{\mathrm{MR}}(I_{\mathrm{d}}) - \Delta V_{\mathrm{ISHE}}(I_{\mathrm{d}}) + \Delta V_{\mathrm{MR}}(I_{\mathrm{d}}) = \\
&\quad = 2\Delta V_{\mathrm{MR}}(I_{\mathrm{d}})
\end{aligned} \tag{2.13}$$

For the purposes of noise reduction, heating enhancement and accuracy in geometry, samples to be measured with this technique were optically lithographed into Hall bars of 1.6 mm length and 100 µm width. The procedure of optical lithography was described in the previous section.

The experimental setup was configured as follows: the *Keithley* 236 SMU drove the I_{d} current and we used the nanovoltmeter for ΔV_y recording. A specific chip carrier was designed to perform these JSSE and SMR measurements. This holder is compatible with the probe for the in-plane measurements with eight pins, so that the α angle can be varied.

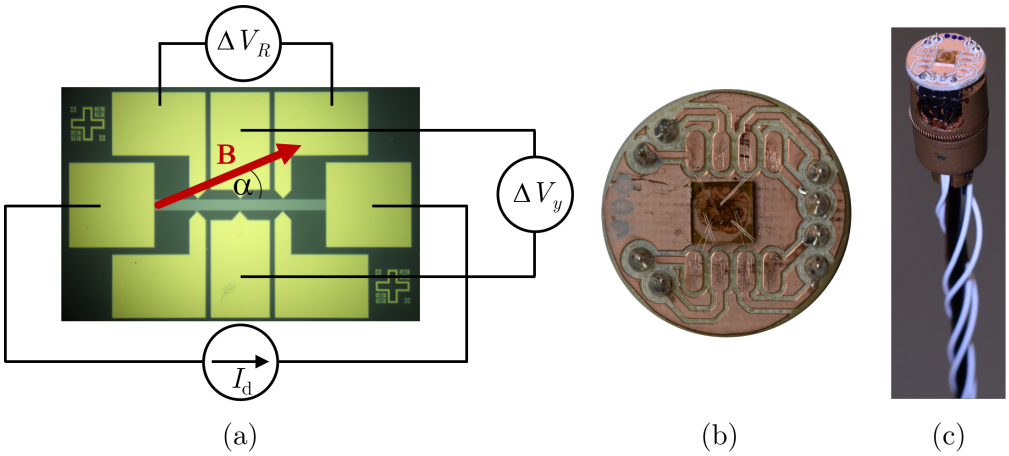

Figure 2.14 (a) Optical microscope image of a lithographed sample showing the electrical contacts geometry used for JSSE and SMR measurements. (b) Picture of the sample holder with a sample contacted to its pads. (c) Chip carrier inserted in the compatible probe.

Besides acting as resistive heater and spin-to-charge converter, the NM metalic layer (or strip, after lithography process) is also used as thermometer. For this purpose, its resistivity ρ_{NM} is systematically determined with varying the cryostate base temperature. This is done measuring longitudinal $V_{\mathrm{R}}(I)$ characteristics with significantly lower intensities than I_{d} at each temperature, using for V_{R} the extreme free pads of the Hall bars (see Fig. 2.14(a)). With this $\rho_{\mathrm{NM}}(T)$ calibration, temperature of the NM stripe during the further JSSE and SMR experiments can be thereby assessed.

The electrical connections from the lithographed sample to the chip carrier were performed using a wire bonding equipment available in the clean room at INA, specifically a *K&S Kulicke & SOFF* 4526 system (see Fig. 2.15). This instrument micro-welds aluminum wires of 25 µm of diameter by locally applying ultrasounds with a tiny tip, which results in the local heating, force and vibration that forms the bond. It allows to establish the connections between micrometer-sized regions of the sample and the millimeter-sized pads of the chip carrier, with the aid of an optical microscope.

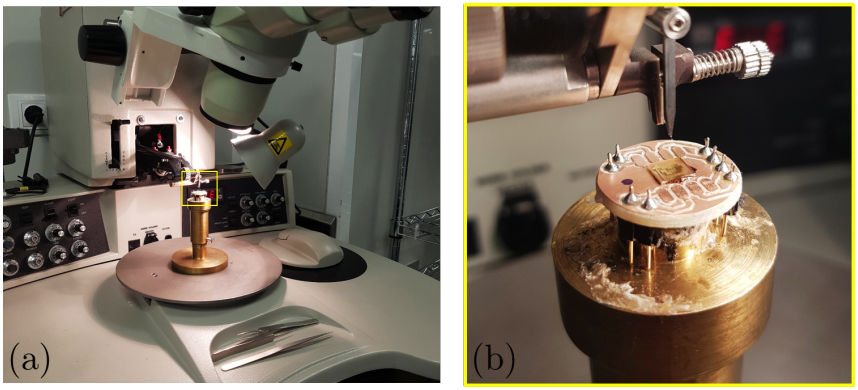

Figure 2.15 (a) Equipment used for wire bonding. (b) Detail showing the lithographed sample glued to the sample holder where the pads to be connected are visible.

2.5.2 Heat transport: 3ω determination of thermal conductivity

The knowledge of thermal conductivities of thin films and substrates is key for the quantitative discussion of the SSE. However, thermal transport properties of thin films differ from those of the bulk materials and are not handily characterizable [130]. In this work, the cross-plane thermal conductivity of thin films as well as substrates were determined by the 3ω method, firstly introduced by Prof. Cahill in 1990 [131] for bulk materials and later in 1997 extended for thin films [132].

In this method, a thin metallic stripe is deposited onto the sample to act as both a heater and a thermometer; an ac current at frequency ω is driven through the stripe to heat the surface of the sample, giving rise to an oscillating thermal

response ΔT at a frequency 2ω, due to Joule heating. In addition, the electrical resistance of the stripe, R, will oscillate accordingly to the temperature at 2ω frequency. As a consequence, the voltage drop across the stripe will have a 3ω component, following Ohm's law. This means that detection of this third harmonic signal $V_{3\omega}$ (usually accomplished by lock-in amplification) can be used to measure the thermal oscillations ΔT [131, 133]:

$$\Delta T_{2\omega} = \frac{V_{3\omega}}{V_{\omega}} \cdot \frac{2R}{(dR/dT)} \tag{2.14}$$

In our case, the voltage drop at 3ω is measured with a Stanford Research Systems SR830 lock-in amplifier, and a Keithley 6221 AC source is employed for applying current. As can be noticed from equation 2.14, a careful calibration of the resistance of the metallic line, R, and its variation with temperature, is required in order to implement this method.

It is shown that the real part of $V_{3\omega}$ decays logarithmically with twice the excitation frequency, according to [131, 133]:

$$\frac{V_{3\omega}}{V_{\omega}} = -\frac{dR}{dT}\frac{P}{4\pi l \kappa_{\mathrm{s}} R}\ln 2\omega \tag{2.15}$$

where P is the power applied to the metallic heater; l, its length and κ_{s} the thermal conductivity of the substrate, which can therefore be extracted from this expression by computing the slope of the linear dependence of $V_{3\omega}$ on $\ln 2\omega$.

Furthermore, thermal conductivity κ_{f} of a thin film deposited on a substrate can be obtained provided that a previous measurement in a bare portion of the substrate is also performed. This is necessary in order to determine the thermal oscillation produced by the AC excitation both in absence (ΔT_S) and in presence (ΔT_{S}) of the film. If $\kappa_{\mathrm{f}} << \kappa_{\mathrm{s}}$ the thin film contribution to ΔT is frequency-independent [134]. Therefore, the thermal response coming from the thin film itself can be computed as:

$$\Delta T_{\mathrm{f}} = \Delta T_{2\omega}(\ln 2\omega) - \Delta T_{\mathrm{S}}(\ln 2\omega) \tag{2.16}$$

From this, thermal conductivity of the film, κ_{f}, can be calculated using the following

expression [132, 134]:

$$\kappa_{\mathrm{f}} = \frac{tP}{wl\Delta T_{\mathrm{f}}} \tag{2.17}$$

where t is the thickness of the thin film and w the width of the metallic stripe. This expression is valid if the heater/thermometer stripe is wide enough compared to t so the heat flow through the film can be approximated to be one-dimensional. In this thesis, film thicknesses are in a range between a few and some tens of nanometers, whereas the width of the used stripes was $w = 60\,\mu\mathrm{m}$, three orders of magnitude bigger.

2.6 Terahertz Emission Spectroscopy

Terahertz Emission Spectroscopy (TES) detects and analyzes electromagnetic radiation at THz frequencies emitted by a sample. The THz emission is generated at the sample as response to an excitation; the THz waveform/transient is analyzed to gather information about the process responsible for the emission. Measures are done in the time domain and afterwards Fourier-transformed to obtain the spectrum (frequency domain).

THz spectral window is sometimes defined to cover the frequency range from ∼0.1 to 100 THz [135], but other authors restrict the range up to 10 THz [136, 137]. This more limited window between the infrared and the microwave spectral regions constitutes the so-called "THz gap" (because of the lack of efficient emitters and sensors), and it is often branded as a "bridge" between conventional electronics and optics or photonics [138]. This frequency window, however, is of great interest in condensed matter physics since many fundamental modes lay on this electromagnetic regime, e.g., vibrations of molecules and crystal lattices, density oscillations of carrier plasmas or free-carrier absorption in semiconductors, superconducting energy gaps, spin excitations such as spin waves, etc. [135, 138].

Spintronics is no exception. In the past two decades, application of THz techniques to this field has resulted in a spectacular development of ultrafast spintronics. The observation of subpicosecond light-induced demagnetization

in ferromagnetic nickel in 1996 [139] is usually considered as the triggering milestone. Since then, a rapid development has evolved through the study of Giant Magnetoresistance [140], Anomalous Hall effect [141, 142] and, most notoriously for the framework of this thesis, of ISHE, in the THz regime [143]. In regard to applications, in 2016 it was demonstrated that photo-induced spin currents and ISHE are powerful tools to develop conceptually new efficient sources in this elusive range [144]. The baptized as *spintronic emitter* presented in reference [144] outperforms the commonly used THz emitter in terms of amplitude and bandwidth, covering the whole 1 to 30 THz gap. This represents an increase of up to one order the magnitude with respect to standard emitters.

Experimental setup

In brief, in this setup THz emission from the sample is triggered by the incidence of a pump femtosecond optical pulse, as sketched in Fig. 2.16. The sample is for this purpose placed in one of the two focus positions available. Detection is accomplished by electro-optic sampling based on the electro-optic linear effect, also

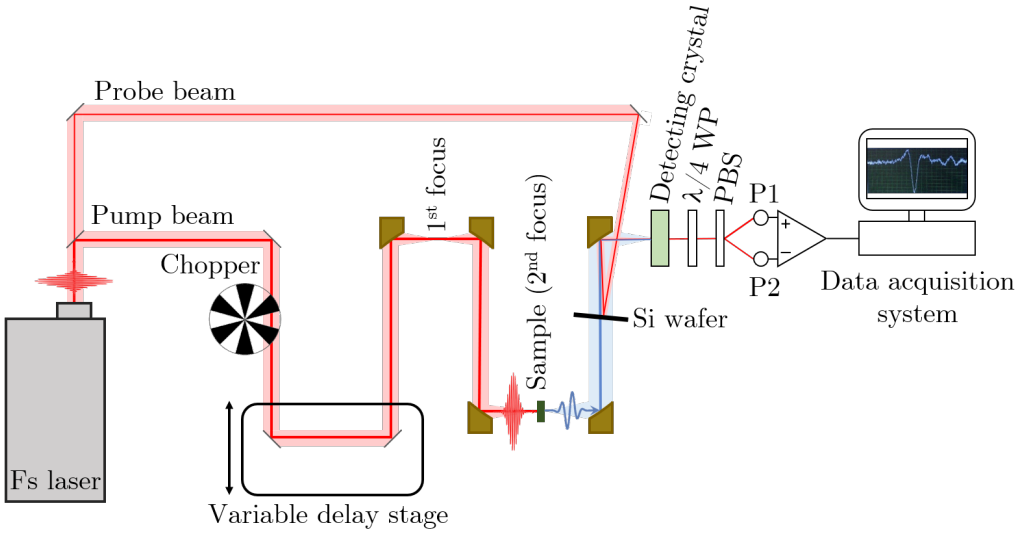

Figure 2.16 Simplified scheme of the experimental setup used for TES.

known as Pockels effect.

The **femtosecond laser system** utilized in this thesis was a high-repetition-rate laser oscillator (Femtosource M1, *Spectra-Physics*). It delivers pulses with a duration of 10 fs, central wavelength of 800 nm, energy of 2.5 nJ and a repetition rate of 80 MHz. The light amplification medium is a titanium-doped sapphire crystal that is pumped by a continuous-wave Nd:YVO_4 laser at a wavelength of 532 nm. The generation of pulsed radiation in the optical cavity is achieved by a process called mode-locking. For more details about how this process is induced in this setup, the reader is referred to the accurate descriptions in [145–147].

As we mentioned above, detection of the THz transients emitted by the sample is performed taking advantage of the **electro-optical linear effect** or Pockels effect, which enables a technique known as electro-optic sampling. This effect describes the phenomenon whereby the refractive index of a crystal changes (birefringence) linearly to an applied electromagnetic field (for example, a THz pulse $\mathbf{E}_{\mathrm{THz}}$). The proportionality between the change in the refractive index Δn and the field is the reason why this effect receives the name of *linear* electro-optic effect. The crystal must be non-centrosymmetrical; usually ZnTe or GaP crystals are used as detectors.

Electro-optic sampling takes advantage of the Pockels effect by making use as probe of a second visible laser pulse $\mathbf{E}_{\mathrm{vis}}$ that travels through a detection crystal collinearly to the THz pulse, as follows: when THz pulse reaches the detection crystal transiently changes the refractive index for that co-propagating visible probe pulse. As a consequence, the polarization of the visible pulse changes from linear to elliptical. This ellipticity is then analyzed using a **balanced detection** scheme. Since the birefringence is proportional to the intensity of $\mathbf{E}_{\mathrm{THz}}$ at the position of the sampling pulse, varying time-delay of the read-out pulse with respect to the THz pulse allows to step-by-step trace the time-domain waveform of the THz pulses, by mapping step-by-step the temporal evolution of the THz electromagnetic field, as pictured in Fig. 2.17. This is usually achieved by a moving time-delay mechanical stage (see Fig. 2.16).

The induced probe ellipticity is analyzed as follows: first, a $\lambda/4$-waveplate

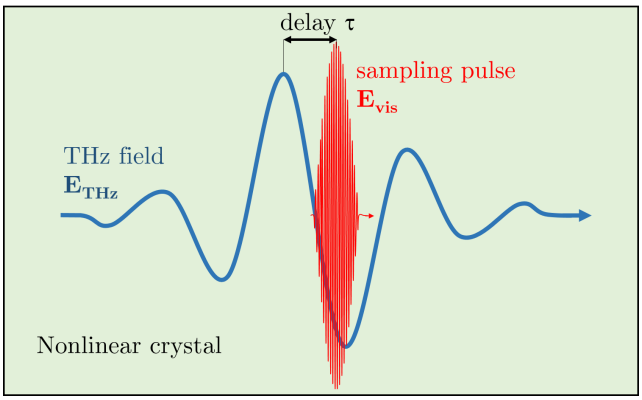

Figure 2.17 Electro-optic sampling of a THz waveform $\mathbf{E}_{\mathrm{THz}}$ using a short visible pulse $\mathbf{E}_{\mathrm{vis}}$. Both pulses co-propagate in a nonlinear crystal in which Pockels effect can be observed.

introduce a phase difference or "optical bias" of $\pi/2$, transforming the incoming $\mathbf{E}_{\mathrm{vis}}$ linear polarization into circular. A subsequent polarizing beam splitter separates the perpendicular components sending them to a pair of photodiodes, giving rise to equally-sized signals on both of them. The presence of the $\mathbf{E}_{\mathrm{THz}}$, however, induces an ellipticity in $\mathbf{E}_{\mathrm{vis}}$ polarization that will result in an unbalance in the photodiodes proportional to this ellipticity.

As pictured in Fig. 2.16, the probe pulse comes from the same oscillator as the pump beam: the output of the laser is split at a ratio of 80:20 to seed the THz generation and detection path, respectively.

Finally, two major strategies are combined in this setup to increase **signal-to-noise ratio**: on the one hand, a mechanical chopper running at 30 kHz modulates the pump laser beam for phase sensitive detection by lock-in amplification; on the other, a fast delay stage (so-called "shaker") varies the time delay up to 40 ps at a frequency of 25 Hz, allowing rapid-scanning.

More thorough details than provided in the description above are gathered in the PhD thesis of Dr. Lukas Braun and Dr. Tom S. Seifert, who during their work designed, built and developed the setup to its current form [146, 147].

A bit more on the electro-optic effect

Despite the name of *linear* electro-optic effect, it is the second-order polarization the responsible for the change in the refractive index of the detector for the visible pulse $\mathbf{E}_{\text{vis}}$ induced by the (in this case) THz electric field $\mathbf{E}_{\text{THz}}$; in fact, electro-optic effect is explained in terms of a nonlinear coupling between the low frequency $\mathbf{E}_{\text{THz}}$ pulse and the visible pulse $\mathbf{E}_{\text{vis}}$ in the sensor crystal. Let us study this process more formally.

In a classical light-matter interaction picture, electronic charges in a medium get displaced as a result of the application of an electric field $\mathbf{E}(\omega)$. This induced charge displacement can be viewed as an oscillating dipole that itself emits radiation at the oscillation frequency. This is macroscopically described by the induced polarization $\mathbf{P}$ (total electric dipole per unit volume). For studying nonlinear optical phenomena, polarization is expanded into a power series of $\mathbf{E}$:

$$\mathbf{P} = \epsilon_0 \sum_{i=1}^{\infty} \chi^{(i)} \mathbf{E}^i, \tag{2.18}$$

where the constants of proportionality χ are known as optical susceptibility tensors and ϵ_0 is the vacuum permittivity. We assume plane waves for the electromagnetic field [148]:

$$\mathbf{E}(\omega, \mathbf{k}) \propto \mathbf{E}(\omega) \mathrm{e}^{i\mathbf{k}\cdot\mathbf{r}} \tag{2.19}$$

$\mathbf{E}(\omega)$ can be written as a discrete sum of its frequency components, those included in the spectral bandwidth of the electromagnetic radiation at play:

$$\mathbf{E}(\omega) = \sum_n \mathbf{A}_n \mathrm{e}^{-i\omega_n t} \tag{2.20}$$

As a first observation, we note that the spectral components of $\mathbf{E}(\omega)$ interact with each other through the nonlinear interaction with matter as expressed in Eq. 2.18.

We are here interested in the second-order nonlinear term of the polarization, quadratic in $\mathbf{E}$. Combining Eq. 2.18 and Eq. 2.20, this second-order polarization is

given by:

$$P_i^{(2)}(\omega) = \epsilon_0 \sum_{j,k} \sum_{n,m} \chi_{ijk}^{(2)}(\omega; \omega_n, \omega_m) E_j(\omega_n) E_k(\omega_m), \tag{2.21}$$

where $i = x$, y and z and $\chi_{ijk}^{(2)}$ denotes the spatial components of the susceptibility third-rank tensor. Clearly, factors of the form $\mathrm{e}^{i(\omega_n \pm \omega_m)t}$ appear in $\mathbf{P}^{(2)}(\omega)$, yielding $\omega = \omega_n \pm \omega_m$. These terms are responsible for the "sum-frequency generation" and "difference-frequency generation" processes.

Difference-frequency generation is of great relevance in the field of THz photonics, since it is on the basis of the electro-optic rectification, one of the existing THz emission methods. In this process, both mixing components come from the pump optical laser, mix in a noncentrosymmetrical crystal such as ZnTe or GaP, and result in the emission of pulses at the THz frequencies.

Reciprocally, sum-frequency generation is the responsible term for the linear electro-optic effect we are discussing here. As we have already explained, it allows the detection of THz pulses with the help of a second visible pulse that co-propagates in a detecting crystal. The total present field is of the form $\mathbf{E} = \mathbf{E}_{\mathrm{THz}} + \mathbf{E}_{\mathrm{vis}}$; THz and visible frequencies are the inputs for sum-frequency generation. The relevant terms in Eq. 2.21 are the cross terms $P_i^{(2)} \propto \epsilon_0 \sum_{jk} \chi_{ijk}^{(2)} E_j^{\mathrm{THz}} E_k^{\mathrm{vis}}$. They represent a polarization component that is linear in $\mathbf{E}_{\mathrm{vis}}$ and accounts for a change in the linear optical properties of the medium with respect to $\mathbf{E}_{\mathrm{vis}}$ modulated by $\mathbf{E}_{\mathrm{THz}}$.

Chapter 3

Thin film growth and characterization

This chapter reports on the growth of different oxides as thin films. We will study the effect of the experimental parameters during deposition on the functional properties of the obtained films.

We will focus on two groups of materials: (1) insulating materials with long-range magnetic order (MOIs), and (2) metallic materials with high strong SOC and no magnetic long-range ordered ground state (which we denote NM).

The first group of materials constitutes by itself a relevant field of work within spintronics development. With the charge current-based devices seeming to be approaching their limit, spin current-based technologies represent a promise for power dissipation reduction [27, 36]. For this purpose, capability to generate and manipulate pure spin currents (with no concomitant charge currents) becomes an essential requirement, as we discussed in the introduction. Among MOIs candidates, throughout this thesis we have been interested mainly in the performance of maghemite (γ-Fe_2O_3) thin films. In addition, growth and properties of three other MOI materials have been addressed: yttrium iron garnet ($Y_3Fe_5O_{12}$, YIG for short), $LaCoO_3$ and $CoFe_2O_4$.

Within the second group of compounds (NM and high SOC oxides), IrO_2

deposition conditions as thin film were studied in this thesis. We have sought for the convenient properties to be used for spin-to-charge conversion. Besides, prototypical Pt has been used in the experiments in which the matter of study was the LSSE rather than the ISHE.

3.1 Iron oxides

3.1.1 Introduction: the family of iron oxides

Iron oxides family (which includes oxides, hydroxides and oxide-hydroxides) comprises sixteen different compounds displaying a variety of properties, from the structural, magnetic and electric points of view [149]. These properties have been exploited in a broad number of applications of great technological significance. As the most ancient of them, we can name pigments (which go from as back in time as ochre paintings by prehistoric men to modern colorants) and early Chinese compasses (see Fig. 3.1). Modern uses spread over different industries, technologies and scientific disciplines, from steel production to medicine or art. For a complete review of these applications we point the reader to Chapter 19 of reference [150].

(a) (b)

Figure 3.1 (a) Prehistoric cave art using ochre preserved in the Cave of Altamira, north of Spain, executed during Upper Paleolithic. Altamira has been declared a World Heritage Site by UNESCO. (b) Model of a south-pointer carved in lodestone as spoons from the Chinese Han Dynasty period (206 BC - 220 AC); such devices were used for divination purposes.

Four of the iron oxides can be found in nature in mineral forms; sorted by

oxidation state of iron these compound are FeO (wüstite), Fe_3O_4 (magnetite), γ-Fe_2O_3 (maghemite) and α-Fe_2O_3 (hematite). In this thesis, we will study magnetite and maghemite, so a brief description of each is provided below.

Magnetite Fe_3O_4

Magnetite is intrinsically linked to magnetism history from its very beginning. In fact, the word *magnet*, as *magnetite*, is thought to come from *Magnesia*, a region in Asia Minor abundant in sources of lodestone (a rock rich in magnetite). Naturally magnetized lodestones constituted the first known magnets [20]. However, we still lack a complete understanding of its magnetic and electronic properties.

Fe_3O_4 is a half-metallic ferrimagnet, with a Néel temperature of 860 K. Half-metallic character of Fe_3O_4 is acquired by the existence of a gap in the majority spin band, meaning that at Fermi level there are electrons with only the minority spin polarization. The consequent ideal spin polarization of 100% at Fermi level, together with the high T_C, makes magnetite an attractive material for spintronic applications.

Fe_3O_4 crystallizes at room temperature in an inverse cubic spinel structure, space group $Fd\bar{3}m$, with lattice parameter of 8.397 Å [20]. This crystal structure features two types of cation sites embedded in a cubic face-centered (fcc) lattice of O^{2-} anions: tetrahedrally coordinated by oxygen (or A sites) and octahedrally coordinated (or B sites). In the unit cell containing 32 O^{2-} anions, 1/8 (8) of the tetrahedral sites are occupied by ferric ions Fe^{3+} (electronic configuration $3d^5$ with orbital occupations $t_{2g}^{3\downarrow}e_{2g}^{2\downarrow}$), whereas 1/2 (16) of the octahedral sites are equally shared by ferric and ferrous ions, Fe^{3+} ($t_{2g}^{3\uparrow}e_{2g}^{2\uparrow}$) and Fe^{2+} ($3d^6$ distributed as $t_{2g}^{3\uparrow}e_{2g}^{2\uparrow}t_{2g}^{1\downarrow}$) [20]. Thus, the unit formula is $(Fe^{3+})_A(Fe^{3+}Fe^{2+})_BO_4^{2-}$.

However, the sixth $3d$-electron associated with Fe^{2+} is delocalized in a narrow $t_{2g}^{\downarrow}$ band; i.e., every B-site orbital occupation can be actually represented as $t_{2g}^{3\uparrow}e_{2g}^{2\uparrow}t_{2g}^{0.5\downarrow}$ rather than by a picture with half of the sites featuring a localized $t_{2g}^{1\downarrow}$ electron and half of the sites lacking it. These itinerant $t_{2g}^{\downarrow}$ electrons (with $\downarrow$ minority spin polarization) provide electrical conduction along this band, and are thus responsible

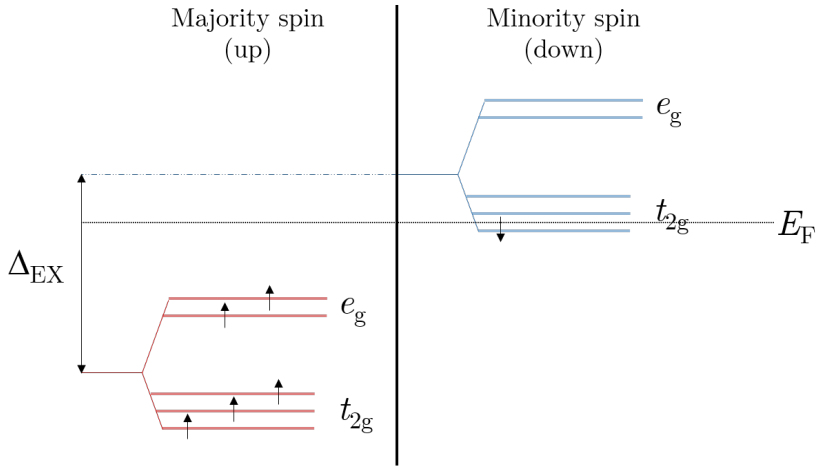

Figure 3.2 Schematic representation of the $d-$energy levels of the Fe^{2+} in the octahedral coordination (B) sites. The majority and minority spin bands are splitted by the exchange energy Δ_{EX}, with the Fermi level E_F located in the t_{2g} levels of the minority spin band.

for the half-metallicity [151], as sketched in Fig. 3.2. As a consequence of the existence of this narrow band, magnetite is considered to be in the limit between semiconductor and metallic behavior, with a small gap of 0.1 eV and a electrical resistivity of $10 - 100\,\mu\Omega{\cdot}$m [20, 150].

It must be pointed that nowadays it is generally accepted that electron transport in magnetite obeys not only to this band conduction of delocalized electrons but also to a mechanism based on thermally activated hopping of polarons [152].

The two types of coordination sites define two magnetic Néel sublattices. As can be anticipated in view of the chosen $\uparrow$ and $\downarrow$ notation for orbital occupations, the sublattices are ferromagnetically ordered within, but strongly antiferromagnetically coupled with each other via the Fe_A-O-Fe_B superexchange interaction. Both sublattices have uncompensated magnetic moments, therefore giving ferrimagnetic behavior, see Fig. 3.3. Application of Hund's rule assigns magnetic moment of 5 μ_B to Fe^{3+}, and magnetic moment of 4 μ_B to Fe^{2+}, yielding a resulting magnetic moment per formula unit of $\mu_B - \mu_A = (5 + 4 - 5)\mu_B = 4\,\mu_B$ at $T = 0$ K. Preferred direction of magnetization (easy axis) is along $\langle 111 \rangle$.

A remarkable characteristic of Fe_3O_4 is the undergoing of the Verwey transition

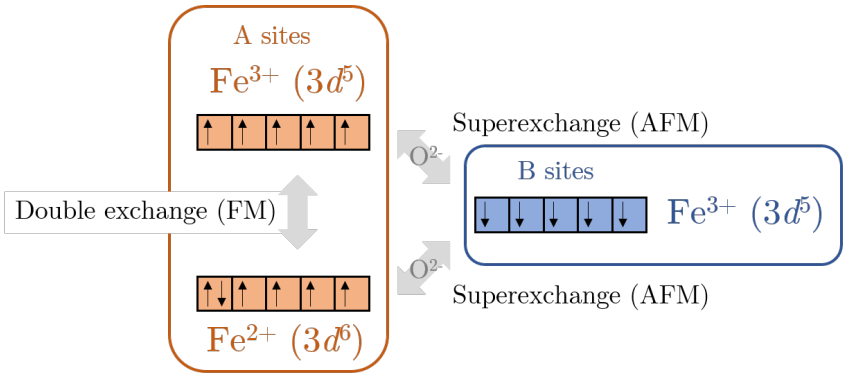

Figure 3.3 Simple scheme of the spin configuration of $3d$ orbitals of iron cations in magnetite and magnetic interaction between them.

at $T_V = 119 - 125$ K [153]. It is a first-order metal-insulator transition accompanied by a structural transition. Below T_V, electrical conductivity drops by two orders of magnitude and crystal symmetry decreases to a Cc space group monoclinic structure, with $\sqrt{2}a$, $\sqrt{2}a$ and $2a$ lattice parameters (where a is the lattice constant of the cubic phase above T_V). A discontinuous change in magnetization and an anomaly in specific heat (a peak) are other important manifestations of this Verwey transition.

Although first measurements were done almost 90 years ago [154], there is still no consensus on the precise nature of this transition, the mechanism behind it. A careful and exhaustive review of evolution of experimental and theoretical advances and discussion about the Verwey transition in magnetite can be found in reference [155]. Here, we will only briefly say that two major interpretations have been developed. One of them relies on charge ordering below T_V due to Fe^{2+}–Fe^{3+} ion ordering in the B sites, what results in a localization/delocalization transition, in the line of the original explanation proposed by Verwey in 1939 [153] (for a recent publication supporting this interpretation, see for example reference [156]). The other interpretation claims that the transition cannot be of purely electronic origin, and that phonons also play a role in it. In this cooperative scenario, electron-phonon coupling induces local lattice distortions enhanced by on-site Coulomb interactions and finally opens a gap at the Fermi level when temperature is below T_V [157–160].

Maghemite γ-Fe_2O_3

Maghemite is another iron oxide with attractive properties to be used in spintronics applications: it is an insulating ferrimagnetic material with an estimated Néel temperature of $T_N \approx 985$ K [20]. This T_c cannot be easily checked experimentally because above $T = 700 - 800$ K γ-Fe_2O_3 transforms into the isostoichiometric compound α-Fe_2O_3 (hematite) [150].

The name of *maghemite* was formed probably as a combination between *magnetite*, which exhibits the same structure, and *hematite*, which has the same stoichiometry. This name was proposed after recognition of maghemite's natural occurrence, subsequently to its in-lab production by oxidation of magnetite [161]. History of this naming along with other denominations among the community that did not crystallize can be found in [149] or [162]. Regarding current and historic applications, maghemite is an important magnetic material, as gathered by R. Dronskowski in his review [163]. For example, in the 20th century it was extensively used as the magnetic pigment in recording media of magnetic tapes for audio information (e.g., cassettes and studio or broadcasting tapes) or computer tapes (diskettes and hard drives); its use in synthetic pigments for the brown color range is worth mention as another relevant application of maghemite [150, 163].

Maghemite phase is metastable at ambient conditions and tends to transform into the more stable and isostoichiometry hematite, α-Fe_2O_3, upon heating. Hematite is a tilted antiferromagnet with hexagonal structure (isostructural with corundum) [150]. It shows weak ferromagnetism at room temperature and undergoes the Morin transition to a collinear antiferromagnetic state at $T_M = 260$ K.

γ-Fe_2O_3 shows the same crystal structure that Fe_3O_4: a spinel. However, in the case of γ-Fe_2O_3 only the trivalent state of iron, Fe^{3+}, is present. As a consequence, charge neutrality in the cell is kept by the presence of cation vacancies in the octahedral interstitial positions (B sites) [150, 162, 165], forming what is called a *defective* spinel. Depending on the synthesis process, these vacant sites can either be randomly distributed within the crystal or follow an ordered pattern [149, 150, 162, 163]. In the disordered case, the structure can be approximated

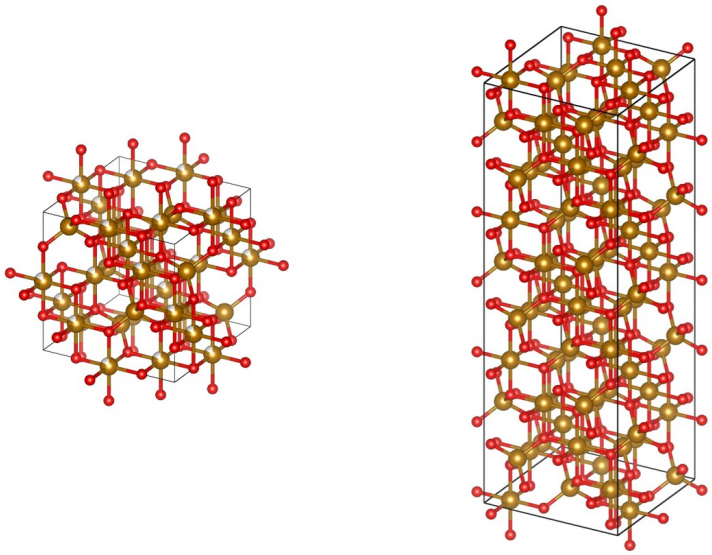

Figure 3.4 Unit cell of the two possible structures featuring maghemite. Left: disordered cubic inverse spinel. Right: ordered three-fold tetragonal inverse spinel. Red balls represent oxygen anions and yellow balls represent iron cations. Structures created using VESTA software [164].

to a cubic unit cell with formula $(Fe^{3+})_8^A\,[Fe^{3+}_{5/6}\otimes_{1/6}]_{16}^B\,O^{2-}_{32}$. The space group corresponds to a cubic inverse spinel, same as magnetite ($Fd\bar{3}m$). This structure was observed by X-ray diffraction in epitaxially grown single crystals of maghemite in [166]. In the ordered vacancies case, there is a decrease in the symmetry to the space group $P4_12_12$. This group corresponds to a tetragonal spinel structure which contains three cubic spinels stacked one on top of each other in the c direction (commonly referred to as *three-fold tetragonal structure* or *tetragonal superstructure*) [150]. The formation of this three-fold superstructure is a necessary condition for vacancy ordering, considering that in the cubic $Fd\bar{3}m$ structure a fractional number of vacancies per unit cell would be required —therefore not possible. Thus, tetragonal lattice parameters keep the relation $c = 3a$ ($a = 8.347$ Å and $c = 25.042$ Å). The superstructure has been examined by X-ray [167, 168], neutron [169] and electron diffraction [170, 171]. Additionally, an intermediate cubic and partially ordered state, spacial group $P4_332$, has been observed and described [150, 163, 172].

The randomly distributed and totally ordered in the three-fold structures are both represented in Fig. 3.4.

The most remarkable difference between γ-Fe_2O_3 and Fe_3O_4 may be the following: in the case of maghemite, there are only localized $3d^5$ electrons in both types of interstitial sites, with orbital distribution $t_{2g}^3 e_{2g}^2$; therefore, electrical conduction is hindered and maghemite becomes an electrical insulator with a bandgap of 2.03 eV [150].

Magnetic structure is similar to that of magnetite: the A and B sites feature two Néel sublattices. Ferromagnetic coupling inside each sublattice and superexchange interaction between the A and B sublattices (antiferromagnetic order with spin polarizations $(t_{2g}^{3\downarrow} e_{2g}^{2\downarrow})_A$ and $(t_{2g}^{3\uparrow} e_{2g}^{2\uparrow})_B$) give rise to ferrimagnetism. Application of Hund's rules yields net magnetic moment per unit formula $5 \times \left(\frac{5}{3} - 1\right) \mu_B = \frac{10}{3} \mu_B$. Again, magnetization lies along the cube diagonals, $\langle 111 \rangle$ direction [20].

3.1.2 Maghemite growth and iron oxide discrimination

Maghemite synthesis can be achieved by dry oxidation of magnetite [150, 162, 163]:

$$2\,Fe_3O_4 + \frac{1}{2}O_2 \rightarrow 3\,\gamma\text{-}Fe_2O_3 \tag{3.1}$$

This is a topotactic transition that implies a composition transformation with no alteration of structure. However, in order to avoid the formation of the most stable phase α-Fe_2O_3 (what entails both composition and structure transformations), temperature during oxidation must be maintained *low enough*, since on heating γ-Fe_2O_3 transforms irreversibly to α-Fe_2O_3 [162]. In air, this happens at approximately 800 K [20], although depending of samples and atmosphere lower temperatures have been pointed out [162, 173]. In general, T below $\sim$ 700 K can be considered to be *low enough*. When preparing γ-Fe_2O_3 as thin film, the use of an appropriate substrate with small lattice mismatch will also favor the stabilization of γ-Fe_2O_3 phase against α-Fe_2O_3.

All in all, Fe_3O_4 transformation to γ-Fe_2O_3 could be considered an intermediate

step in the formation of α-Fe_2O_3, as summarized in next equation:

$$2\,Fe_3O_4 + \frac{1}{2}O_2 \xrightarrow{T\geq 400-500\,K} 3\,\gamma\text{-}Fe_2O_3 \xrightarrow{T\geq 700-800\,K} 3\,\alpha{-}Fe_2O_3 \tag{3.2}$$

In between of proposed temperatures, nucleation of hematite starts.

In this thesis, preparation of maghemite thin films of nanometric thickness is approached by phase transformation via post-annealing of magnetite thin films. In order to optimize growth parameters, commercial (*Crystal GmbH*) magnesium oxide (MgO) single-crystal substrates of 0.5 mm of thickness and (001) surface crystal orientation were chosen. MgO crystallizes in the face-centered cubic rocksalt (NaCl) structure [174]. This choice of substrate responds to the small mismatch between MgO and Fe_3O_4 or γ-Fe_2O_3 atomic spacing: its lattice parameter of $a_{MgO} = 4.211$ Å [174] is in ∼1:2 relation with those of magnetite and maghemite. Specifically, defining the misfit as [111, 175]

$$f = \frac{a_f - a_s}{a_f} \tag{3.3}$$

where a_f and a_s denote film (as bulk material) and substrate lattice constants, we see that the produced lattice mismatch is as low as $\sim +0.3\%$ in Fe_3O_4 and $\sim +0.9\%$ in γ-Fe_2O_3. These positive f mean that accommodation of the interface will result in small tensile strain in magnetite and maghemite thin films.

The know-how about PLD fabrication of Fe_3O_4 thin films is well established in our lab [176]. We use a homemade target of Fe_3O_4 and deposit in ultra high vacuum, using the parameters listed in Table 3.1.

Parameter	Value
Nominal heater temperature	600°C
Background pressure at room temperature	$\sim 10^{-9}$ Torr (ultra high vacuum)
Laser pulse frequency	10 Hz
Deposition rate	~ 3 nm $\cdot$ min^{-1}

Table 3.1 PLD deposition parameters of magnetite.

The use of deposition rate as control parameter is a better choice than pulse energy, since the latter is measured *outside* the vacuum chamber, while the important quantity is the intensity that *reaches* the target inside. These two values differ because transmission through the laser access window changes in time due to deposition of material (from previous processes). Therefore, since a specific transmitted intensity (in given environmental conditions and for a fixed pulse frequency) will produce a specific deposition rate, using this rate as deposition control parameter is equivalent to using laser energy *inside* the chamber, after going through the window.

The produced Fe_3O_4 thin films were annealed in different conditions to optimize the quality of the obtained γ-Fe_2O_3. Discrimination of iron oxides will be of great relevance in order to rule out the presence in our sample of any parasitic phases other than the desired one.

Atmosphere, temperature and annealing duration

We start studying the influence of temperature and duration of the post-annealing of magnetite thin films in two different atmospheres: air and oxygen pressure. Annealing in air is *ex situ* carried out in a furnace, whereas annealing in oxygen atmosphere is executed *in situ* inside the PLD vacuum chamber.

In the case of samples annealed *ex situ* in air, temperature is decreased down to room temperature after the deposition of the magnetite thin film at 600°C (nominal temperature measured at the PLD heater). Cooling rate is set at 10°C/min. Magnetite thin film is then removed from the deposition chamber and sample holder and taken to the furnace. In the case of samples annealed *in situ*, temperature is decreased to the annealing point and the desired oxygen pressure is then set in the chamber. After the stipulated process duration, the sample is cool down at 10°C/min, in the oxygen atmosphere, to room temperature. Only then is the oxygen pumped out the chamber before removing the sample from it.

In Table 3.2 we specify the annealing conditions to optimize γ-Fe_2O_3 preparation from magnetite thin films.

Duration t (min)	30	60	90	150	240	150	240	150	180	240
Atmosphere	air							0.1 Torr O_2		
Temperature (°C)	250					350		450 (PLD heater)		

Table 3.2 Annealing conditions tested for the optimization of Fe_3O_4 to γ-Fe_2O_3 transformation.

After thin film growth, samples were structurally characterized by means of XRD. We show in Fig. 3.5 the $2\theta/\omega$-scans around the (002) Bragg peak of the MgO substrate; the diffraction pattern from a Fe_3O_4 sample (not annealed) is also shown as reference. The annealing process has a visible effect of shifting the (004) Bragg peak of the film to higher 2θ positions. This is an indication of the degradation of Fe_3O_4 phase and formation of γ-Fe_2O_3, since γ-Fe_2O_3 out-of-plane lattice parameter is smaller than that of Fe_3O_4 (recall the Bragg condition given in Eq. 2.1).

Due to in-plane tensile strain, Fe_3O_4 accommodates its in-plane lattice parameter to (twice) the MgO parameter, making it larger than in bulk Fe_3O_4. As a consequence, the out-of-plane lattice parameter is lower (compressively strained), and the (004) Bragg peak from Fe_3O_4 thin film is slightly shifted to higher 2θ values with respect to that of the bulk material. The same happens in the case of γ-Fe_2O_3 thin films. In Fig. 3.6 the out-of-plane lattice parameters $a_\perp$ obtained from the (004) Bragg peak positions are plotted together with the out-of-plane lattice parameters calculated for a perfectly elastic (i.e., unit cell volume-conserving) growth of the thin film.

We start by examining the effect of annealing duration in samples annealed in air at 250°C. We see that 30 min of annealing are clearly not enough: the peak of magnetite has disappeared, but the peak of maghemite is barely incipient and still centered very close to magnetite position. Both 60 and 90 minutes of annealing produce a much more defined peak, closer to maghemite position. However, longer processes produce samples of better crystal quality as they show Laue oscillations (indicating crystal coherence) and higher peak positions (or, conversely, lower $a_\perp$). No difference is observed in the XRD spectra between maintaining the annealing

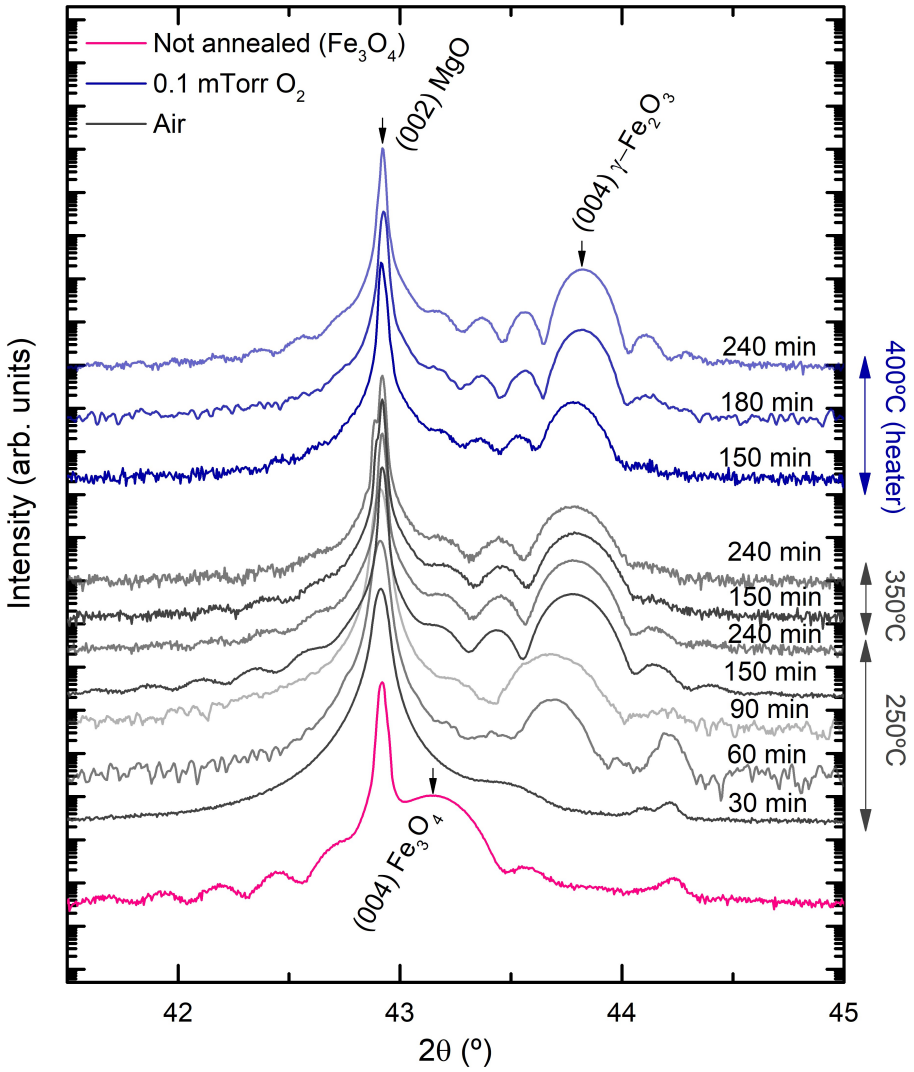

Figure 3.5 XRD spectra measured around the (002) MgO substrate Bragg peak for the samples annealed at different temperatures and for different duration.

150 or 240 minutes. We conclude that annealing duration > 90 minutes is needed to complete the Fe_3O_4 to γ-Fe_2O_3 transformation. Concerning the annealing temperature, we observe no difference in the XRD spectra of 250°C and 350°C for the same annealing durations; the value of $a_\perp$ saturates at ~ 8.26 Å, as illustrated

in Fig. 3.6.

As for *in-situ* annealed samples at 450°C, the obtained lattice parameter is the same as those of samples annealed in air during longer than 90 minutes (Fig. 3.6). Besides, the XRD patterns also feature Laue oscillations indicating high crystal quality. Finally, no perceptible difference is found between the tested annealing durations (150, 180 and 240 minutes).

Magnetic characterization is also helpful in order to trace the completeness of the transformation from Fe_3O_4 to γ-Fe_2O_3. We will focus on samples annealed during $t > 90$ minutes, as we saw by XRD structural characterization that duration lower than that is not enough to get good crystal quality (thus suggesting that more time is needed to complete the oxidation).

In Fig. 3.7(a) we show the behavior of magnetic moment as a function of temperature, $m(T)$, measured with an applied magnetic field of 500 Oe in a SQUID magnetometer. We include the measurement corresponding of a pure magnetite thin film for comparison. First thing to note is that every sample exhibits significant magnetic moment, strongly suggesting that formation of α-Fe_2O_3 can be discarded.

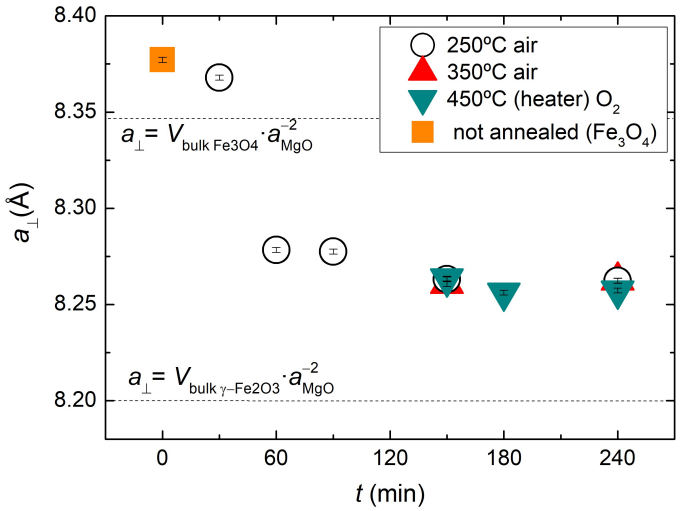

Figure 3.6 Out-of-plane lattice parameters $a_\perp$ obtained for the samples annealed at different temperatures and along different durations.

This will be confirmed by the magnetic hysteresis loops. Secondly, we focus on the possible presence of remaining Fe_3O_4 after the annealing. To elucidate this, we look for any noticeable and sudden decrease in magnetic moment around the Verwey transition temperature; we can see from the reference Fe_3O_4 sample that this transition comports a very abrupt decrease in that magnitude. The abruptness and critical temperature of Verwey transition are indicators of deviations δ from ideal stoichiometry ($Fe_{3(1-\delta)}O_4$, $\delta > 0$) [177–181]. Beyond a critical nonstoichiometry $\delta_c \approx 0.0039$ [177], the transition is inhibited due to the destruction of long-range order [181]; δ_c acts as a percolation limit. Instead, a domain state with finite-range correlations is set [181] and the transition changes from first to second or higher order [177–179, 181]. Accordingly, the variation of magnetization on temperature becomes much smoother, until the total transition extinction at $\delta > 3\delta_c \approx 0.012$ [179].

On account of this, we can use the behavior of magnetization around T_V as

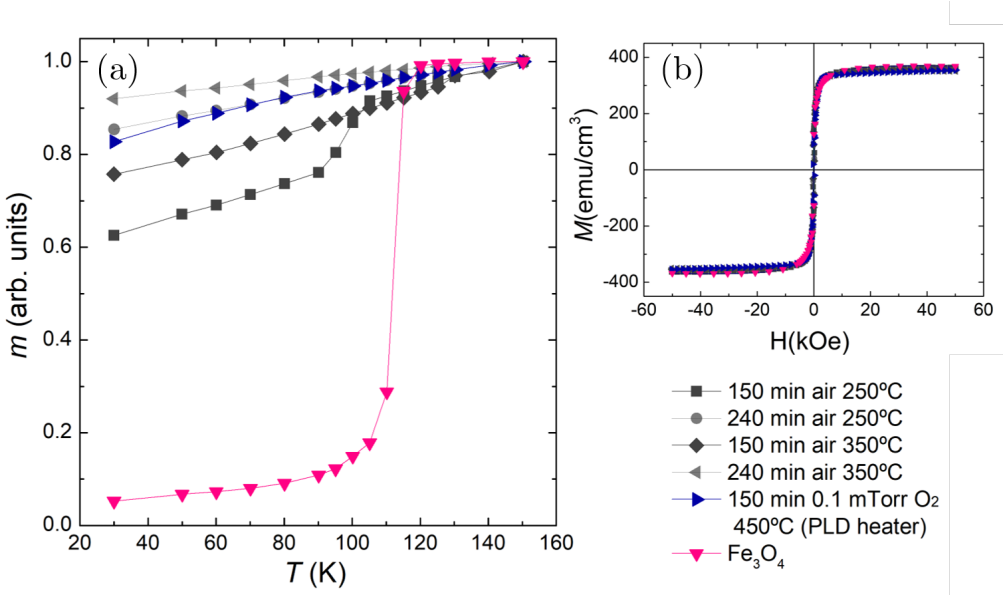

Figure 3.7 Magnetic characterization of the samples annealed at temperatures > 150°C as well as a reference magnetite thin film. (a) Magnetic moment dependence on temperature. (b) Hysteresis magnetic loops.

indication of the phase transformation from Fe_3O_4 to γ-Fe_2O_3. The sample annealed at 250°C during 2.5 hours in air displays a pronounced decrease on magnetic moment around $T \sim 100$ K, entailing that a significant proportion of magnetite is still remaining. On the contrary, upon 4 hours of annealing, such a step is not observed, suggesting that the transformation is completed. The rest of the annealed samples do not show any sudden decrease either, although a very slight step at $T \sim 120$ K is also visible in the data corresponding to the sample annealed at 350°C during 2.5 hours.

In addition, in-plane magnetic hysteresis loops measured at $T = 300$ K show volume magnetizations from $M \sim 360$ emu/cm^3 in the case of samples annealed in air at 250°C to $M \sim 350$ emu/cm^3 in the case of those annealed in air at 350°C or in oxygen atmosphere (Fig. 3.7(b)). The former are closer to Fe_3O_4 value of $M = 368$ emu/cm^3. In all cases, the formation of spurious α-Fe_2O_3 can be ruled out from the saturation values, which are in accordance with reported values for γ-Fe_2O_3 [182–184], whereas the presence of α-Fe_2O_3 phase would have caused a significant decrease in the saturation values.

From this section we extract the following conclusion: on the one hand, if the post-annealing of magnetite thin films to obtain maghemite is performed in air, the process duration must be longer than 2.5 hours, both at 250°C or 350°C (although at 250°C the contribution of remaining magnetite is much more significant).

On the other hand, if the process is carried out in oxygen atmosphere, at nominal 450°C, the process is more efficient and 2.5 hours seem to be enough. This, together with other clear advantages (e.g., in order to *in situ* fabricate heterostructures with interfaces of great quality), makes *in situ* annealing in oxygen atmosphere the most suitable option.

Effect of oxygen pressure

Once the atmosphere, temperature and duration of the annealing were chosen, the effect of the oxygen partial pressure was studied. For this, four different annealing pressures P_{O_2} (1, 10, 50 and 100 mTorr) were tested. The produced samples

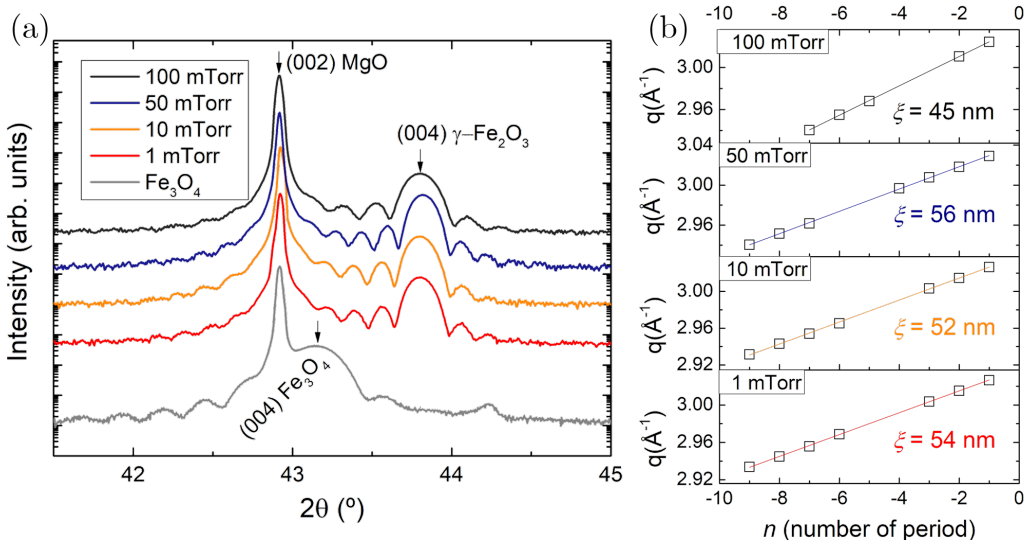

Figure 3.8 (a) XRD $2\theta/\omega$ scans around the MgO substrate (002) Bragg peak of the samples annealed with different oxygen pressures P_{O_2}. (b) Position of the Laue oscillations maximums in q-space. The corresponding coherence lengths ξ can be obtained from the slope Δq of the linear fit.

were structurally, chemically, magnetically and electrically characterized in order to identify the optimal P_{O_2}.

We start by analyzing the symmetric XRD diffraction patterns around the (002) MgO Bragg peak, shown in Fig. 3.8(a). The (004) Bragg peak of the four samples is considerably shifted from the Fe_3O_4 position to 43.80° (1, 10 and 100 mTorr) and 43.82° (50 mTorr), the latter being the closest to ideal maghemite position. The four of them show Laue oscillations up to eighth order. As these oscillations have their origin in the finite number of diffractive layers, a crystal coherence length $\xi = 2\pi/\Delta q$ can be extracted from their periodicity Δq in the q-space. The fits and the obtained coherence lengths ξ are depicted in Fig. 3.8(b). In the four cases, the periodicity of the Laue oscillations yield a ξ which is closer than 90% to the thin film thickness, indicating the that crystalline coherence is maintained essentially along the full thickness of the films.

In Fig. 3.9 we summarize the values for the out-of-plane lattice parameters $a_\perp$

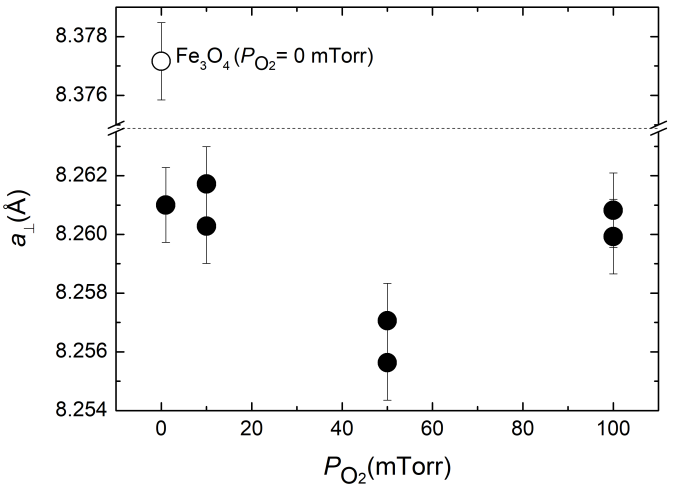

Figure 3.9 Out-of-plane lattice parameters $a_\perp$ obtained for the samples annealed at different oxygen pressures P_{O_2}.

calculated from the XRD spectra. We fabricated a second batch of samples using annealing pressures P_{O_2} = 10, 50 and 100 mTorr in order to confirm the obtained values. As shown in Fig. 3.9, their $a_\perp$ reproduce those of the first series of samples. According to these results, P_{O_2} = 50 mTorr seems to be the optimal annealing pressure with regard to lattice parameter, the one that pushes the (004) Bragg peak further from that of magnetite.

We performed XPS measurements at the Fe 2p core level energy edge in order to determine the oxidation state of Fe cations in our samples. C 1s binding energy (BE) of C at 284.9 eV was used for calibration. The results are plotted in Fig. 3.10, within the survey range of BE of the Fe 2p electrons (700 to 740 eV). The Fe 2p spectrum shows the Fe $2p_{1/2}$ and Fe $2p_{3/2}$ components. It is possible to qualitatively distinguish iron oxide state using satellite features to those two peaks [185–189]. As we see in Fig. 3.10(a), in the case of Fe_3O_4 only Fe $2p_{1/2}$ and Fe $2p_{3/2}$ peaks are visible. On the contrary, all the annealed samples show in their Fe 2p XPS spectra not only both main peaks but also a satellite structure at higher BE, which appears

when only Fe^{3+} cations are present. In the case of pure magnetite, Fe^{3+} and Fe^{2+} satellite structures compensate each other and, as a result, no satellite accompanies the main $2p_{1/2}$ and $2p_{3/2}$ peaks. Therefore, from Fig. 3.10(b), (c) and (d) we can conclude that Fe^{3+} is at least highly dominant over Fe^{2+} in annealed samples.

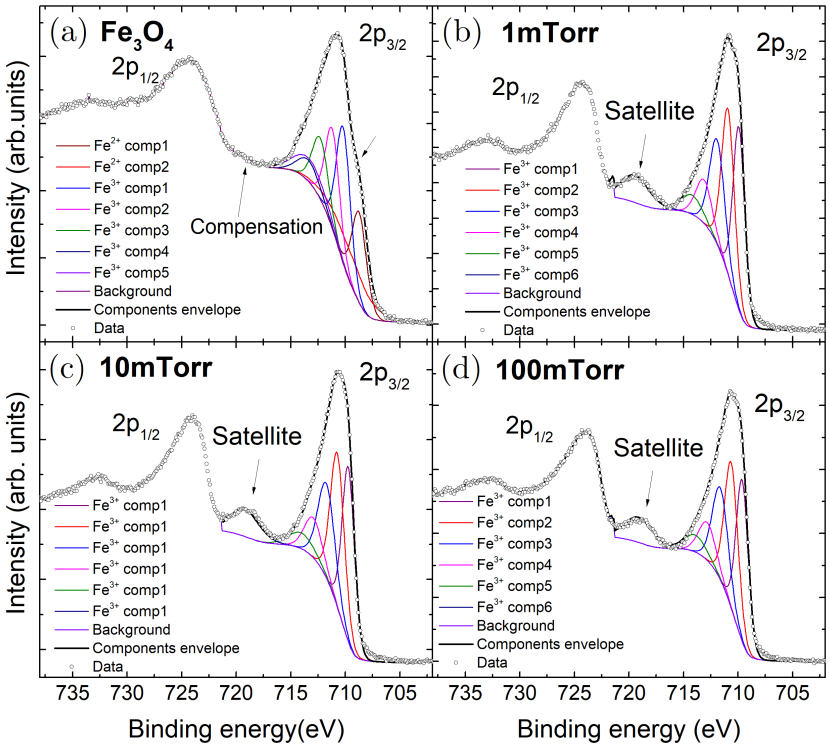

Figure 3.10 XPS spectra of the samples annealed at different P_{O_2}.

We fit the Fe $2p_{3/2}$ peak —which is actually a complex lineshape rather than a single peak— to the multiplet structure calculated by Gupta and Sen [190], which allows us to determine the parameters of the peak (BE and FWHM) and estimate the stoichiometry of the sample [191]. In the case of magnetite, the fit provides a BE of ~ 710.8 eV, which is in between the 711 eV corresponding to the presence of only Fe^{3+}, and the 710 eV for only Fe^{2+}, as reported in literature [186, 188, 192, 193]. In addition, the FWHM is found to be ~ 4.3 eV. As visible in Fig. 3.10, this FWHM

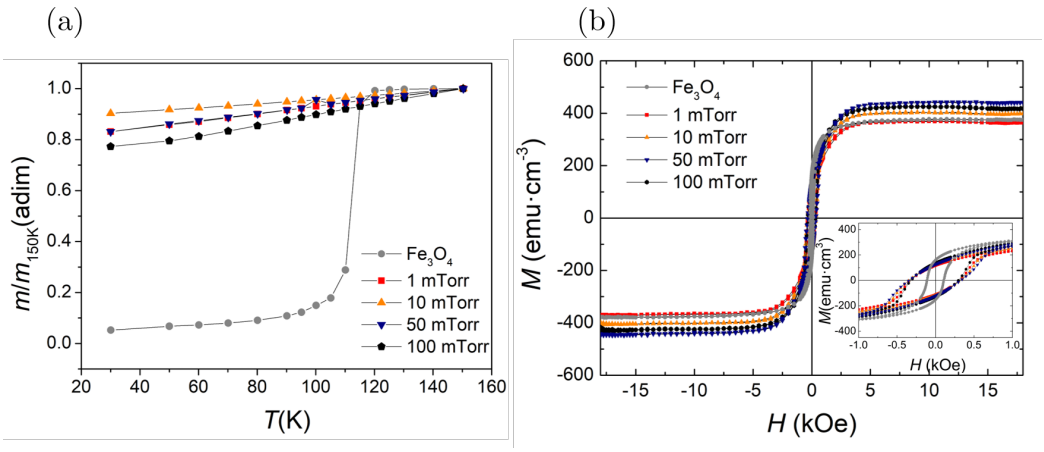

Figure 3.11 Magnetic characterization of the samples annealed at different P_{O_2}.

is broader than that of Fe_2O_3 (only Fe^{3+}) or FeO (only Fe^{2+}), due to its origin at the convolution of both cations peaks. This value is also consistent with previous reports. Lastly, the Fe:O atomic ratio extracted from the fitting is 0.72(7), which adequately matches Fe_3O_4 stoichiometry.

In the case of annealed samples, the satellite peak is located at energy $\Delta \sim 8.0$ eV higher than that of the main peak BE, in agreement with previous reports for maghemite [182, 186, 187]. In addition to the presence of the satellite structure, the spectra show other differences with respect to the magnetite reference sample: a shift of the BE to 711.1 eV and a narrowing of the peak down to FWHM ~ 3.0 eV, which are characteristic values for Fe^{3+} [187, 193, 194]. Finally, quantification yields Fe:O $\sim 0.64(6)$, compatible with γ-Fe_2O_3 stoichiometry.

Magnetization as a function of temperature was measured by SQUID magnetometry in an applied magnetic field of 500 Oe. The absence of the Verwey transition is patent in Fig. 3.11(a), which evidences the destruction pf the magnetite phase in the four annealed samples. In-plane hysteresis magnetic loops $M(H)$ were measured using VSM at room temperature. No loss of magnetization with respect to expected values are observed in Fig. 3.11(b), as the saturations values are close to bulk values of ~ 390 emu $\cdot$ cm^{-3}. Coercivity of annealed samples is slightly wider

than for reference Fe_3O_4 (see inset in Fig. 3.11(b)), around $H_C \sim 300$ Oe. This value is similar to that of other thin films grown by PVD methods on MgO substrates [182–184].

As explained in section 3.1.1, a main difference between magnetite and maghemite can be found in their electrical conductivity: at room temperature, magnetite exhibits a resistivity in the range from 10^{-3} to $10^{-2}\,\mu\Omega\cdot$cm, whereas maghemite is insulating. Therefore, we aimed at measuring electrical resistivity of the four thin films using the Van der Pauw method. For the three samples annealed at $P_{O_2} \geq 10$ mTorr, resistivity was beyond the range of the measurement system: 50 k$\Omega\cdot$cm for the dimensions of the films, thus confirming their insulating character. Moreover, the sample annealed at $P_{O_2} = 1$ mTorr showed a resistivity of $\rho = 7.7\times10^3\,\Omega\cdot$cm, five orders of magnitude larger that that of magnetite, indicating that 10 mTorr is the minimum pressure required.

Electron diffraction and imaging in TEM can also provide information about the iron oxide phases present in a sample. However, one must be careful about two issues: first, the local character of the attained information using this technique; the absence of a specific iron oxide in the examined region of the specimen prepared by FIB (the *lamella*) does no entail that it might not be present in other region of the thin film. Secondly, the scan of the electron beam onto the specimen may have a reducing effect that can lead to misinterpretation; this makes it necessary to work as fast as possible.

In Fig. 3.12, we present the diffraction pattern and High Angle Annular Dark Field Scanning TEM (HAADF-STEM) images for reference magnetite (Fig. 3.12(a) and (d)) and for some of the annealed samples. The annealed samples show a different short range order structure; this order is represented by the diffraction spots $\pm(011)$ and $\pm(01\bar{1})$ that are permitted in the diffraction pattern of maghemite spinel (see Fig. 3.12(b) and (c) but not in the magnetite spinel [195]. Electron diffraction and TEM images also allows us to differentiate whether cation vacancies are ordered or not. As we see in the Fig. 3.12(e) and (f), one can differentiate both configurations just by looking at the TEM images, because the superstructure along

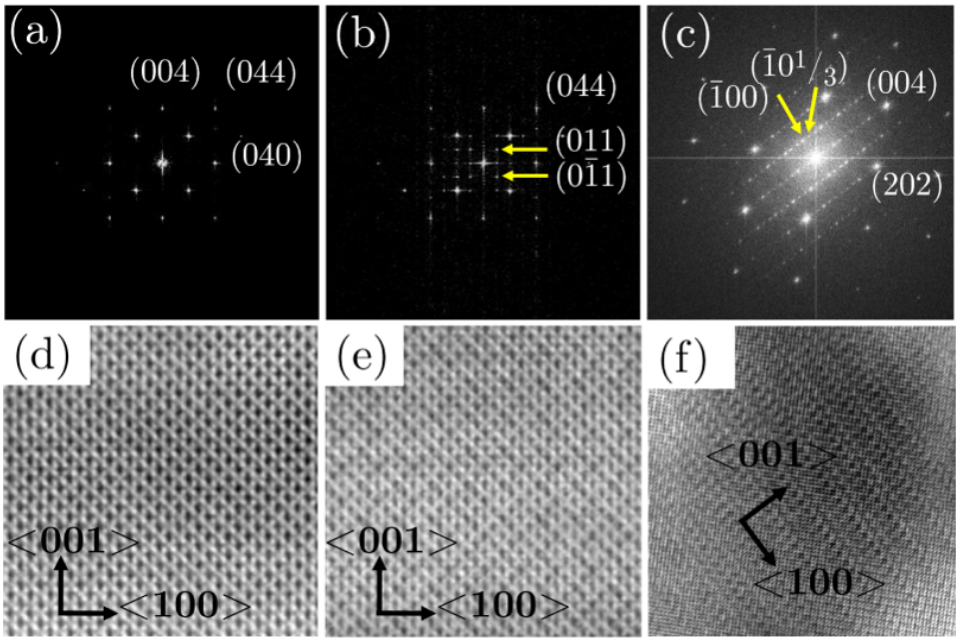

Figure 3.12 (a) Electron diffraction pattern of the reference Fe_3O_4. (b) Electron diffraction pattern of one annealed sample that shows spots $\pm(011)$ and $\pm(01\bar{1})$. This specimen exhibits the vacancies-disordered configuration. (c) Electron diffraction pattern of one annealed sample which shows the superstructure along c axis, due to an ordering of the vacancies. (d), (e) and (f) HAADF-STEM images corresponding to the diffraction patterns above.

c direction can be easily sensed. Anyway, we can unambiguously infer whether Fe vacancies follow an ordered pattern or not by means of the diffraction pattern. For the three-fold tetragonal structure, the $(ab\frac{n}{3})$ spots will appear, as we see in Fig. 3.12(c).

3.1.3 Conclusions

The fabrication of epitaxial γ-Fe_2O_3 thin films by means of PLD has been optimized. The first step was the deposition of Fe_3O_4 thin films and their subsequent subjection to a post-annealing process. We therefore carried out a thorough characterization (structural, chemical, magnetic and electrical) of the effect of the annealing parameters, finding the values that provide the best γ-Fe_2O_3 films quality. This characterization proved that a 2.5 hours *in-situ* annealing of PLD-grown Fe_3O_4

thin films at (nominal) 450°C in O_2 atmosphere at 50 mTorr-pressure succeed in totally completing the $Fe_3O_4 \rightarrow \gamma$-$Fe_2O_3$ transformation, yielding high-quality epitaxial γ-Fe_2O_3 thin films.

All the γ-Fe_2O_3 samples presented in this thesis have been fabricated using these optimized deposition conditions.

3.2 Iridium(IV) oxide

3.2.1 Introduction

Iridium(IV) oxide, IrO_2 belongs to the family of the transition metal dioxides that crystallize in the tetragonal rutile structure and exhibit metallic conductivities at room temperature; besides IrO_2, this family includes RuO_2, OsO_2 or RhO_2, for example. Their interesting transport properties arise from the presence of an incomplete *d*-shell in the band structure of the transition metal. In particular, IrO_2 has become a widely used material in applications as thin film due to its low electrical resistivity [196, 197] (which makes it the best conductor of the rutile transition metal dioxides family), excellent performance as diffusion barrier even at high temperatures [198, 199], attractive electrochemical properties [200–205] and biological compatibility [206]. The applications are widespread in diverse areas and include its use in electrodes for chlorine or oxygen evolution [200, 201], as sensing material in pH sensors [202, 207], as optical switching layers in electrochromic devices [204, 205] or as coating in minimally invasive devices such as stents for treating coronary heart disease [206, 208, 209]. More applications have been proposed in the field of integrated circuits, such as electrodes in ferroelectric capacitors for non-volatile memories [198, 210].

More recently, the search for materials with good performance as spin current detectors via the ISHE has led the interest of the scientific community to the 5*d* transition metal oxides (TMOs), because of their strong SOI [211] and moderate electrical conductivities [212, 213]. From a wider perspective, a variety of exotic phases has been described in TMOs [214]. Such phases emerge from the complex

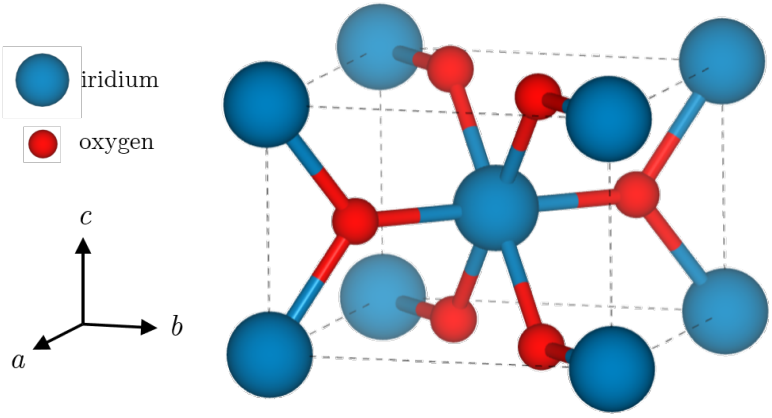

Figure 3.13 Unit cell of IrO_2. The representation has been created using VESTA software [164].

interplay between charge, orbital, spin and lattice degrees of freedom in their strongly correlated d electrons, as a result of which a delicate balance is achieved by the energy scales of the competing interactions. In particular, in the family of iridates Hund's coupling, crystal-field splitting, bandwidth, SOI energy and on-site Coulomb repulsion become comparable [215, 216]. As a consequence, this family displays a rich diversity of intriguing phenomena such as metal-insulator transitions [217, 218], exotic magnetic ground states [219, 220] or novel topological phenomena [218, 221, 222].

IrO_2, a metallic material with no long-range magnetic order, has been targeted as a highly valid spin current detector by Fujiwara and coworkers. They studied the performance of polycrystalline and amorphous samples of IrO_2 in spin absorption experiments carried out with non-local spin-valve structures [213], finding a value for ρ_{SH} one order of magnitude larger than those of noble metals. In contrast, Qiu *et al.* studied the performance of IrO_2 in a longitudinal spin Seebeck effect (LSSE) device and found it to be significantly lower than that of Pt [223]. Authors attributed the small signal of ISHE found in IrO_2 in their experiment to a low spin mixing conductance, a parameter that quantifies the efficiency in the transmission of spin across the interface between both layers.

The electronic band structure of IrO_2 has been theoretically [224–229] and experimentally [211, 226, 229–234] addressed since as early as 1977 [235]; nevertheless, it was the experimental evidence of very efficient spin-to-charge conversion [213] that renewed the interest in this fascinating material and triggered a good number of works dedicated to explain the large SHE/ISHE. However, the precise role of different SHE and ISHE mechanisms in IrO_2 is yet to be clearly elucidated.

IrO_2 crystallizes in the tetragonal rutile structure ($P4_2/mnm$ space group), with lattice constants $a = b = 4.498$ Å and $c = 3.154$ Å. The unit cell contains two formula unit, as depicted in Fig. 3.13. Each Ir^{4+} cation (electronic configuration $5d^5$) is surrounded by six O^{2-} anions in a slightly distorted octahedral environment. These octahedra share edges along y direction and apexes along x and z; this feature has as consequence an enhancement of of IrO_2 bandwidth and therefore of its metallic nature of with respect other iridates displaying different IrO_6 octaheda-based structures as, for example, perovskites or pyrochlore structures (in which IrO_6 basic blocks share only corners).

3.2.2 Growth optimization on MgO al Al_2O_3 substrates

In this section, we describe the conditions to fabricate IrO_2 thin films on (001) MgO and (0001) Al_2O_3 substrates with the desired properties: good morphology (low roughness) and good electrical conductivity. We were particularly interested in using these substrates because, as explained in the previous section, the iron oxide maghemite, γ-Fe_2O_3, can be deposited on them as epitaxial thin film of high crystal quality. The final purpose of the optimization of IrO_2 is the fabrication of γ-Fe_2O_3/IrO_2 heterostructures for spin-to-charge conversion by ISHE in IrO_2, using spin currents thermally excited by SSE in the maghemite layer (see Chapter 6).

Target preparation

To fabricate IrO_2 as thin films by PLD an IrO_2 target was used. In literature, there are examples of growth of IrO_2 by ablation of pure iridium targets under reactive O_2

atmosphere [236–239] and, alternatively, using polycrystalline IrO_2 targets [234]. In this work, a solid target of 18 mm of diameter was prepared by solid-state sintering using 5 g of iridium (IV) oxide powder of 99.9% purity. The powder was compacted, taken to 990°C in air and maintained in those conditions during 30 hours. After cooling, the sintering process in air at 990°C was repeated throughout additional 30 h in order to improve the compactness and density of the target.

Laser frequency

El Khakani and coworkers found that deposition temperature has a significant impact on the room-temperature resistivity of the obtained samples [236]. Temperatures below 400°C, resulted in resistivities larger than that of the bulk single-crystal IrO_2, whose value was reached for deposition temperatures > 400°C. We accordingly established a nominal deposition temperature of 450°C with a ramp of 10°C/min. When the deposition temperature is reached, we stabilized an O_2 atmosphere in order to avoid reduction of the iridium and subsequent nucleation of metallic iridium. As reported by Kim *et al.* [234] we set $P_{O_2} = 50$ mTorr. Both MgO and Al_2O_3 $5 \times 5 \times 0.5$ mm^3 substrates were simultaneously loaded in the chamber. After deposition, the samples were cooled down at 5°C/min.

The first attempt was performing a deposition setting a laser repetition rate of 10 Hz. However, XRR characterization revealed that the obtained ~ 80 nm-thick samples exhibited roughness values higher than desired. Besides, an additional very slow period-oscillation can be appreciated in the spectra; this suggests the existence of a spurious phase which prevents the proper fitting of a simulated curve to the XRR data, as illustrated in the left panels of Fig. 3.14. This fact is indicative of the need to slow the growth rate. Therefore, a second deposition process was carried out setting a laser repetition rate of 3 Hz. With this, the roughness of the produced samples was noticeably improved, and the measured XRR spectra could then be adequately fitted to a simulation of the samples, yielding a thickness of 33 nm and roughness in the subnanometer range. The density values provided by the fits are ~ 11.7 g/cm^3, similar to IrO_2 nominal density (11.66 g/cm^3). This rules out the

presence of pure metallic iridium in the samples.

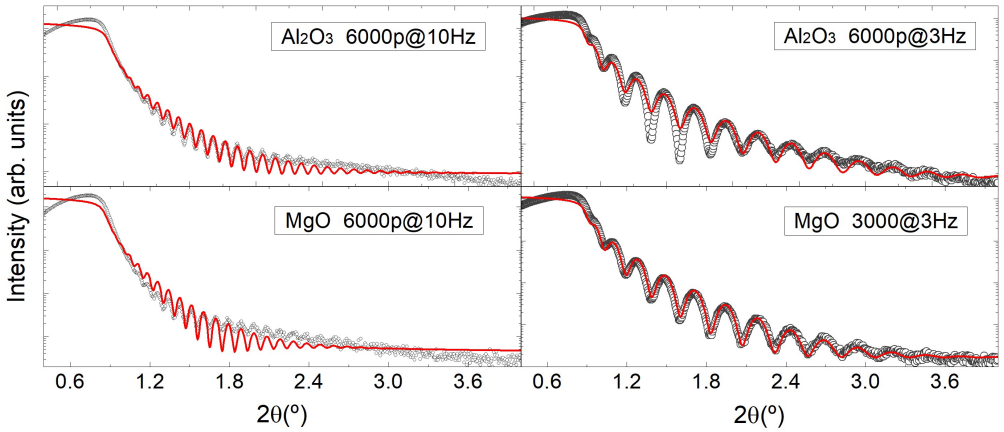

Figure 3.14 XRR patterns measured for IrO_2 thin films deposited on different substrates and using different laser repetition rates.

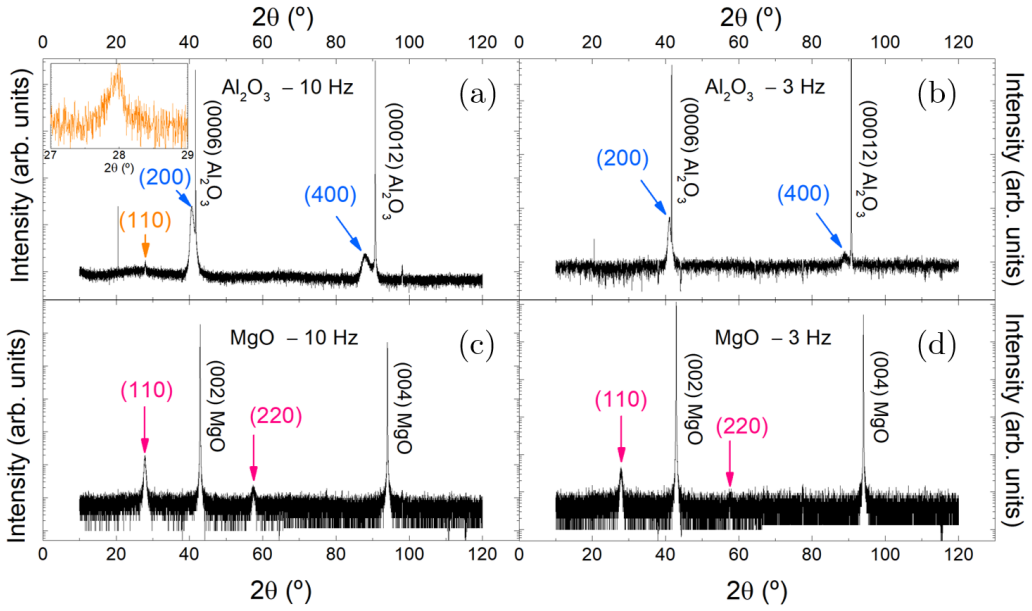

Figure 3.15 XRD $2\theta/\omega$ scans measured for IrO_2 thin films deposited on different substrates and using different laser repetition rates: on Al_2O_3 at 10 Hz (a), on Al_2O_3 at 3 Hz (b), on MgO at 10 Hz (c), and on MgO at 3 Hz (d).

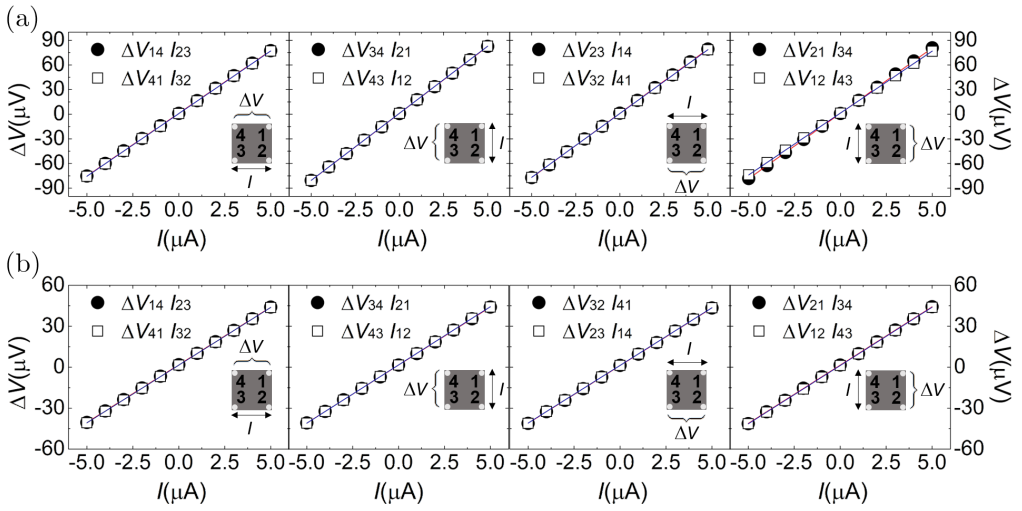

Figure 3.16 Van der Pauw measurements: the $I(\Delta V)$ characteristics showed ohmic nature in all cases. (a) Measurements at every different edge of the square sample deposited on Al_2O_3 using a 3 Hz laser repetition rate. (b) Measurements at every different edge of the square sample deposited on MgO using a 3 Hz laser repetition rate.

The four samples crystallinity was probed by means of XRD. The wide-range patterns are depicted in Fig. 3.15. The diffractograms of samples deposited on Al_2O_3 (Fig. 3.15(a) and (b)), in addition of the (0006) and (00012) Al_2O_3 reflections, showed the (200) and (400) Bragg peaks of IrO_2. Besides, as highlighted in the inset of Fig. 3.15(a), (110) plane of IrO_2 is also slightly diffracting in the sample deposited at 10 Hz frequency, evidencing the presence of grains with different crystal orientations. Relative intensity of the peaks suggest however that {100} orientation is dominant. Moreover, the (110) peak is no longer present in the pattern of the sample grown using a repetition rate of 3 Hz (Fig. 3.15(b)), suggesting a strongly textured growth.

As for the samples deposited on (001) MgO substrates, only the {110} family peaks are visible, besides the (002) MgO and (004) MgO reflections (Fig. 3.15(c) and (d)), which is also indicative of textured structure.

Electrical conductivity is a crucial parameter given the purpose of IrO_2 layers in SSE experiments. The metallic nature of IrO_2 was therefore asserted by

room-temperature electrical transport measurements using the Van der Pauw method. In Fig. 3.16 we show the detailed electrical measurements performed in the samples deposited at 3 Hz. The same measurements (not shown) were carried out in the samples grown at 10 Hz. The provided values of the room-temperature electrical resistivity ρ are summarized in Table 3.3. These values compare well with those gathered in literature for single-crystal [197, 234, 238, 240] and polycrystalline [236, 241, 242] IrO_2, which cover a range from $\sim 10^{-7} - 10^{-8}$ $\Omega \cdot m$.

Interestingly, longitudinal resistivity in IrO_2 is an anisotropic property. In other words, its value depends on the growth direction, as in-detail measured in ref. [240]. This could be the reason behind two observations from our results: first, resistivity of samples deposited on Al_2O_3 are different from those of samples deposited on MgO. Secondly, 3 Hz- and 10 Hz-grown samples on MgO display identical resistivities, whereas they differ in the case of Al_2O_3 substrate. Regarding the anisotropic nature of ρ, both facts seem reasonable given that in MgO {110} direction is preponderant for both frequencies whilst in Al_2O_3 a mixture of {110} and {100} is shown in samples deposited at 10 Hz but only {100} is present for 10 Hz. Indeed, the resistivity measured in the 10 Hz case is in between of those measured for the samples textured in the {110} and {100} directions.

Therefore, it can be concluded that laser repetition rate has non-negligible impact on the crystal and electrical properties of IrO_2, as a slower rate provides samples of better crystal quality and smoother surfaces. Hence, we chose 3 Hz was established as preferred frequency for IrO_2 growth.

Laser rep. rate / Substrate	10 Hz	3 Hz
Al_2O_3	198(3) $\mu\Omega \cdot$ cm	234(7) $\mu\Omega \cdot$ cm
MgO	128(2) $\mu\Omega \cdot$ cm	127(4) $\mu\Omega \cdot$ cm

Table 3.3 Room-temperature resistivity values measured by the Van der Pauw method for different substrates and laser repetition rates.

Laser operation voltage

The laser high-voltage operation level has a great influence on energy distribution, i.e., on the laser spot profile. Lower voltages produce more uniform spots, and this could positively affect the growth of some materials with a narrow window of optimal energy values. Thus, it is advisable to check whether reducing the voltage results in any improvement in IrO_2 growth. To this end, we carried out two depositions setting two different laser voltage values, namely, 20 kV and 30 kV.

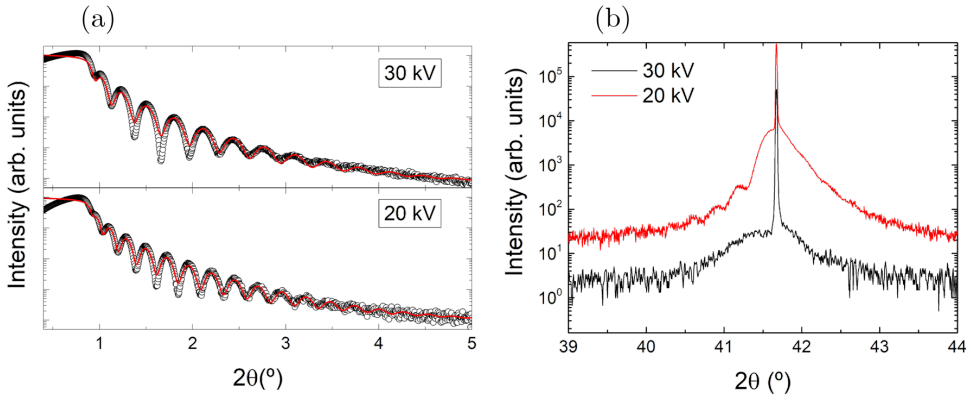

Figure 3.17 Structural characterization of IrO_2 thin films deposited on Al_2O_3 substrates by PLD using two different values of laser voltage. (a) XRR patterns: experimental data (open circles) and a simulated annealing fit (red solid line) are shown. The fit yielded density values of 11.7 g/cm^3, assuring that pure iridium is not present in the samples. (b) XRD $2\theta/\omega$ scans around the (0006) Al_2O_3 Bragg peak.

The samples were structurally characterized by means of XRR and XRD. No significant difference was revealed by XRR, as similar values of density ($\approx$ 11.7 g/cm^3) and roughness ($\approx$ 0.3 for 30 kV and $\approx$ 0.2 nm for 20 kV) were provided by the respective fits. Nevertheless, XRD patterns show clear differences. If we focus on the range of Al_2O_3 (0006) Bragg peak, we can see that IrO_2 (200) Bragg peak is surrounded by Laue oscillations only in the sample grown using a laser voltage of 20 kV. Peak is also sharper and narrower, in better agreement with the thickness determined by XRR (25 nm for the 30 kV-sample and 33 nm for the 20 kV-sample). In conclusion, crystal coherence of IrO_2 thin films grown by PLD is favored by using

lower values of the laser high voltage.

Deposition rate

A study of the deposition rate influence on the IrO_2 thin films quality was also performed in order to find its optimal growth rate in our PLD system.

First, the number of laser pulses was adjusted at 6300 at 3 Hz (i.e., a process duration of 35 minutes) and different energy values were selected. We performed 3 depositions on top of (0001) Al_2O_3 substrates, whose corresponding growth rates were 1.2, 0.95 and 0.75 nm/min, using XRR-estimated thicknesses (not shown). The samples were structurally characterized by XRD. The $2\theta/\omega$ scans around the (0006) Al_2O_3 Bragg peak are shown in Fig. 3.18(a). The three of them show the (200) IrO_2 Bragg peak, but only the sample deposited at 0.75 nm/min displays Laue oscillations in its diffractogram, entailing its higher crystal quality.

A second experiment was performed in order to test the effect of an even more pronounced reduction of the deposition rate. To this end, two more samples were grown. In the first one, laser energy was adjusted to get a rate of ≈ 0.75 nm/min, and it was substantially reduced in the other one. Concerning the number of pulses, 2160 pulses were shot (12 minutes) in the first case, and they were increased in the second case to 4500 (25 minutes) in order to get similar thicknesses. XRR measurement and fit, displayed in Fig. 3.18(b), provided thicknesses values of 9.2 nm and 7.7 nm, respectively, yielding deposition rates of 0.77 nm/min and 0.31 nm/min. Concerning roughness and density, some differences were found: the sample grown at 0.31 nm/min showed a roughness of 0.6 nm according to the fit, which relatively to thickness is as large as $\approx 8\%$; this represents a far more pronounced roughness than the $\approx 3\%$ (0.2 nm) obtained in the case of the sample grown at 0.77 nm/min. Besides, density converge to greater values (≈ 13.3 g/cm^3, far from the nominal 11.66 g/cm^3) for the sample grown at 0.31 nm/min. This might be indicative of a deficient stoichiometry transference between target and sample.

In brief, we finally determined that the optimal parameters to deposit IrO_2 in our PLD system are: laser repetition rate of 3 Hz, laser voltage of 20 kV, and a

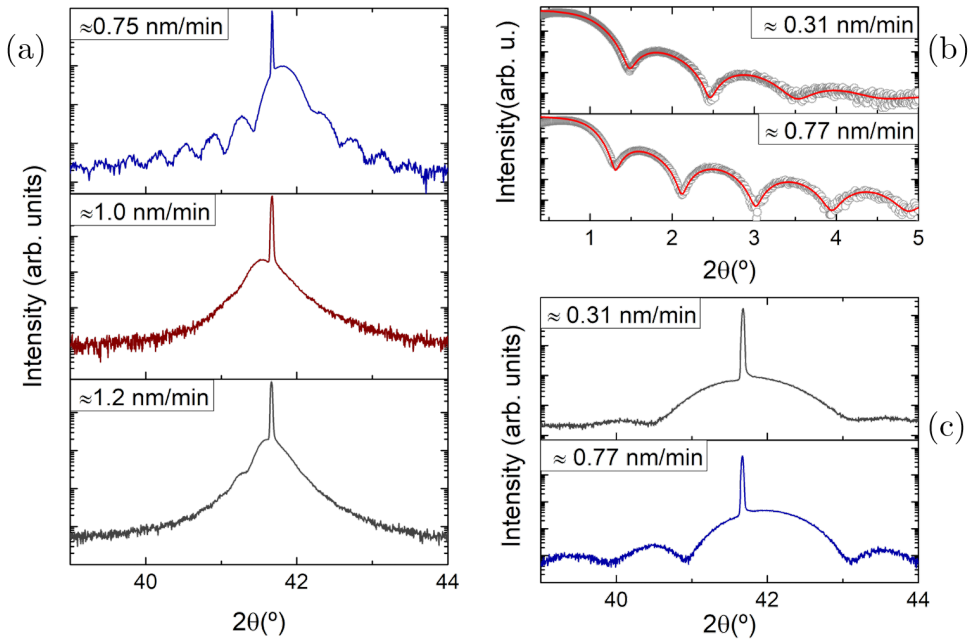

Figure 3.18 Structural characterization of IrO_2 thin films deposited on Al_2O_3 substrates by PLD at different deposition rates. (a) XRD $2\theta/\omega$ scans around the (0006) Al_2O_3 Bragg peak for samples deposited at 0.75, 1.0 and 1.2 nm/min. (b) XRR measurement and fit of samples deposited at low deposition rates. (c) XRD $2\theta/\omega$ scans around the (0006) Al_2O_3 Bragg peak of the same samples as in (b).

deposition rate of ~ 0.75 nm/min.

3.2.3 Epitaxial growth of IrO_2 on TiO_2 and SnO_2 substrates

In this section, we report on the fabrication of epitaxial thin films of IrO_2 on TiO_2 substrates cut in different crystallographic orientations, namely: (110), (001) and (100). Besides, IrO_2, thin films of different thicknesses were prepared on top of each substrate, in the range from 2 to 100 nm. Additionally, one sample was prepared on top of a (001) SnO_2 substrate.

Motivation

The objective of the deposition of IrO_2 in different orientations and thicknesses was within a collaboration with Dr. María Ángeles Laguna-Marco and Dr. Eduardo Arias-Egido to study the effect of those parameters together with epitaxial strain on the conduction mechanisms and magnetic properties of IrO_2 thin films. They complemented this research with non-epitaxial samples showing amorphous, textured and non textured structures, deposited by other methods (e.g., sputtering).

The study was triggered by the theoretical suggestions about the possibility of tuning the ground state of IrO_2 through structural modifications [226, 243, 244]. More specifically, Panda *et al.* proposed that tuning the ratio between Coulomb interactions and bandwidth energies may result in a metal-to-insulator transition accompanied by a magnetic phase change [243]. On the other hand, Kahk *et al.* results suggest that epitaxial strain along *c* axis could lead to changes in the metallic behavior of IrO_2 as a result of its effect on the relative properties of t_{2g} orbitals [226]. Finally, Ming and coworkers have drawn attention to the relevance of IrO_2 layer thickness, predicting a thickness-controlled metal-to-insulator transition [244]. However, such predictions are yet to be confirmed experimentally.

Structural characterization

Using the optimal parameters found in the previous section (3 Hz-laser repetition rate, 20 kV-laser voltage and ≈ 0.75 nm/min-deposition rate), the following samples were prepared by means of PLD:

- On (100) TiO_2 substrates: 2 nm-thick, 5 nm-thick, 20 nm-thick and 100 nm-thick IrO_2.
- On (001) TiO_2 substrates: 5 nm-thick, 7 nm-thick, 20 nm-thick and 100 nm-thick IrO_2.
- On (110) TiO_2 substrates: 5 nm-thick, 7 nm-thick, 20 nm-thick and 100 nm-thick IrO_2.
- On (100) SnO_2 substrate: 5 nm-thick IrO_2.

TiO_2 crystallizes in the same rutile structure as IrO_2, being $a = b = 4.59$ Å

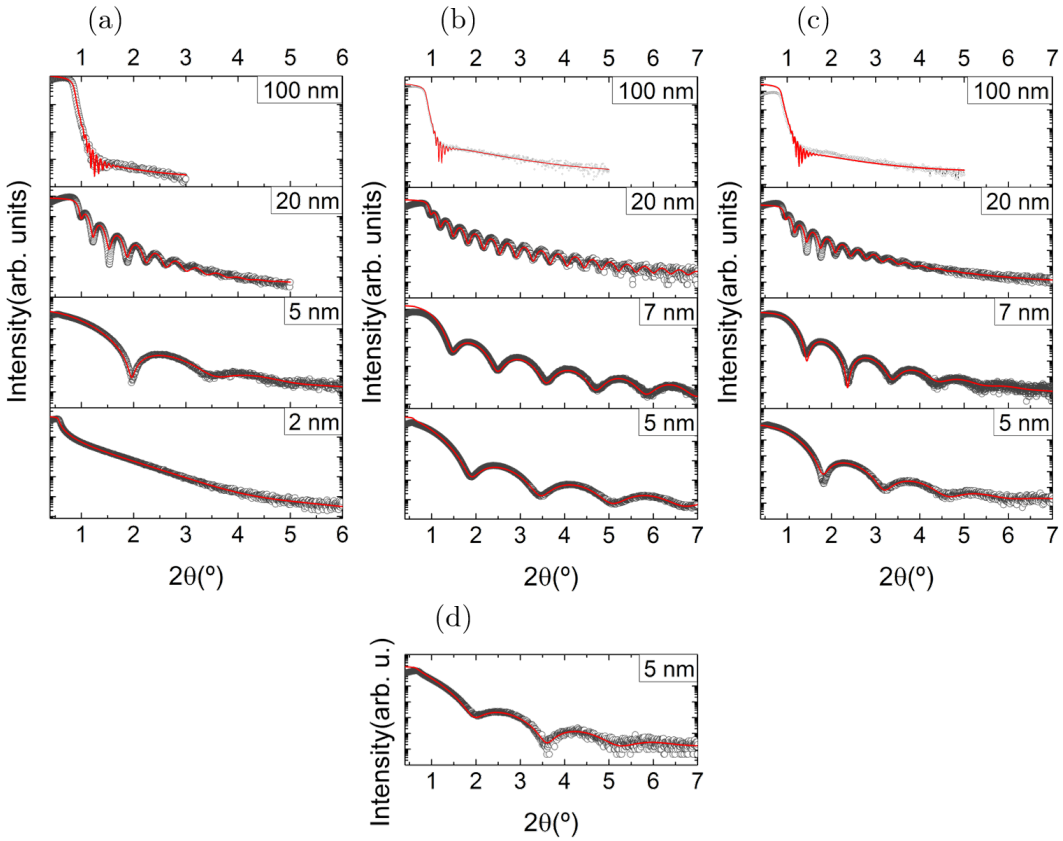

Figure 3.19 XRR $2\theta/\omega$ scans measured for epitaxial thin films of IrO_2 deposited on (a) (100) TiO_2, (b) (110) TiO_2, (c) (001) TiO_2 and (d) (100) SnO_2.

and $c = 2.96$ Å, its lattice parameters. With respect to IrO_2, this represent a -2.0% (compressive) in-plane strain and $+6.0\%$ (tensile) strain along the c axis (Eq.3.3). Concerning SnO_2 (which also shares rutile-like crystal structure), its lattice constants are $a = b = 4.74$ Å and $c = 3.19$ Å. Accordingly, mismatches with respect to those of IrO_2 are -5.4% and -1.3%, respectively.

The first step was the precise determination of each sample thickness by means of XRR fitting; no significant deviations from the nominal values were found. Concerning roughness, samples grown on (110) TiO_2 substrates display a smoother surface than the others, as evidenced by the longer-lasting oscillations. In all cases

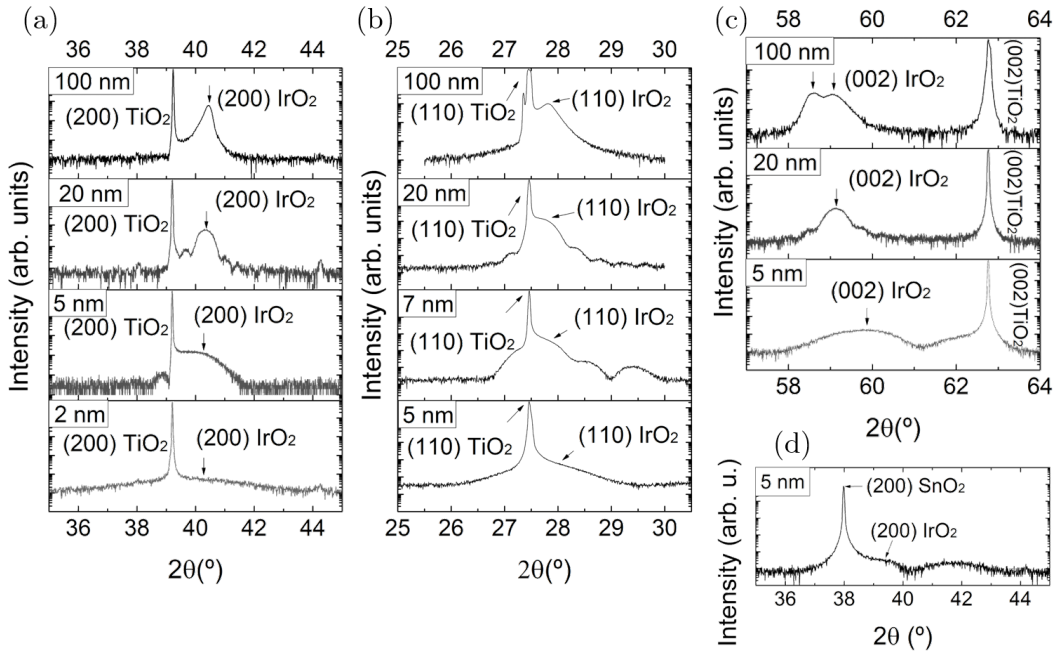

Figure 3.20 XRD $2\theta/\omega$ scans measured for epitaxial thin films of IrO_2 deposited on (a) (100) TiO_2, (b) (110) TiO_2, (c) (001) TiO_2 and (d) (100) SnO_2.

(except fot 100 nm-thick samples), roughness remains below 1 nm. For 100 nm-thick sample, it reaches ≈ 3 nm (3% of total thickness). These are very acceptable values for the intended use.

Next, XRD $2\theta/\omega$ patterns of the samples were recorded. Fig. 3.20 gathers the diffractograms around a corresponding Bragg peak of each substrate. Only peaks corresponding to the substrate orientation were observed in all the samples, proving their epitaxial growth. Regarding the effect of thickness, the film peaks suffer a small displacement as the thickness is increased, revealing a very slight relaxation of the cell; the only notorious effect is observed in the 100 nm-thick film on (001) TiO_2: the IrO_2 diffraction clearly features a double peak. This could suggest an abrupt relaxation of the cell from a specific thickness.

Finally, reciprocal space maps (RSM) for selected thicknesses were collected in order to precisely determine the two in-plane and the out-of plane lattice parameters

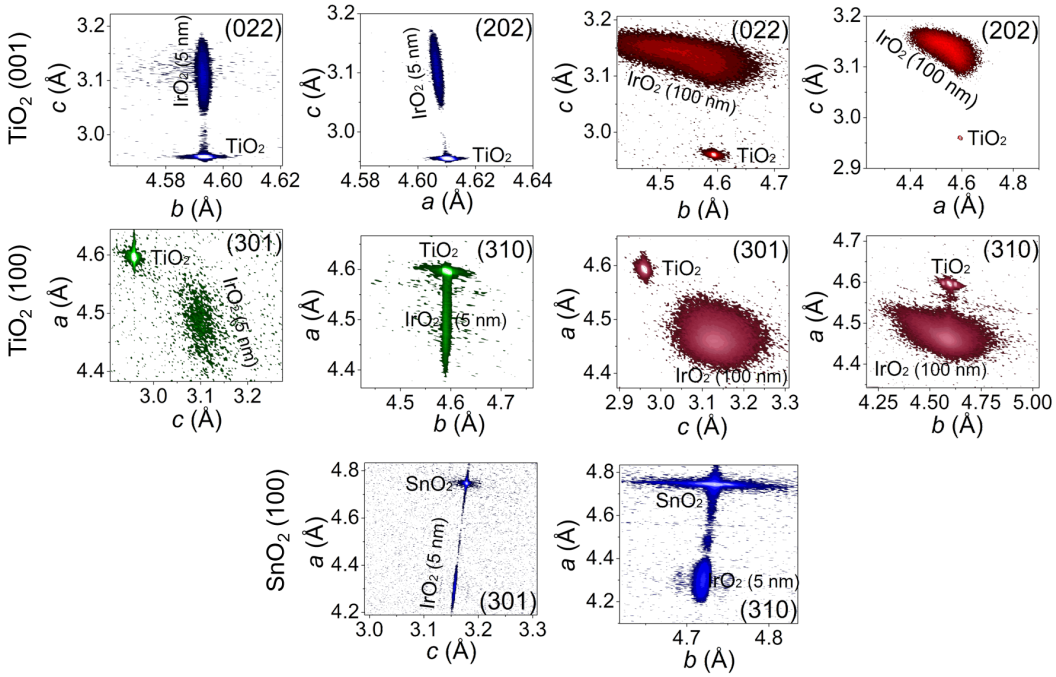

Figure 3.21 RSM around asymmetric reflections measured for epitaxial thin films of IrO_2 deposited on (001) TiO_2 (top row), (100) TiO_2 (middle raw), and (100) SnO_2 (bottom raw).

of the deposited films. Specifically, we measured them for the 5 and 100 nm-thick samples in the (001) and (100) orientations. With respect to the (110) direction, we could not find a proper reflection intense enough to be detected with our equipment. The measured RSM are represented in Fig. 3.21.

Concerning the (001) orientation on TiO_2, it is clearly discerned that IrO_2 grows fully strained as a 5 nm-thick thin film: its a (from the (202) reflection) and b (from the (220) reflection) lattice constants are 4.59 Å, perfectly matching the substrate's lattice parameter (+2% tensile strain). The out-of-plane $c = 3.11$ Å is slightly smaller than that of bulk IrO_2, in order to compensate the in-plane tensile strain, representing a -1.3% of compressive strain. The epitaxial strain is however relaxed along the thickness of the 100 nm-thick sample: as wee see in the upper line of Fig. 3.21, the films spots spread in the in-plane-direction from the substrate value (4.59 Å) to bulk IrO_2 value (4.50 Å). In the case of the 5 nm-thick sample, the unit cell

volume can be computed as the lattice parameter display precise values: a volume of ≈ 65.5 Å^3, bigger than that of the bulk, is obtained.

The situation is different in the (100) IrO_2 thin films: the $b = 4.59$ Å parameter matches perfectly that of the substrate, indicating that the film is fully strained in that direction (see the (310) reflection); however, according to the (301) reflection, the other in-plane lattice parameter, c, is compressed with respect bulk IrO_2 (3.09 Å against 3.15 Å, meaning that -1.9% of compressive strain is imposed) but without reaching the substrate value (2.96 Å). The out-of-plane a is $a = 4.48$ Å, extremely close to the bulk 4.50 Å(-0.4%). This out-of-plane strain is such that the unit cell volume is conserved with respect to the bulk material (≈ 63.8 Å^3) in this case. A similar situation is found in the 100 nm-thick sample: $b = 4.59$ Å is fully strained, while c is compressed down to 3.13 Å(-0.6% of compressive strain), less than the 5 nm-thick sample. Concerning the out-of-plane parameter, it is $a = 4.46$ Å, similar to that of the thinner sample.

Finally, as for the 5 nm-thick sample deposited on (100) SnO_2, the film holds a nearly perfect in-plane match with the substrate, which imposes a -0.5% of compressive strain in c direction and $+4.9\%$ tensile strain in the b direction; meanwhile, the out-of-plane lattice parameter is -4.70% compressed. It is worth mentioning the remarkable deformation underwent by a and b parameters, which in bulk have the same value but differ 0.5 Å in this sample.

3.2.4 Conclusions

In this section we have described the process conducted in order to optimize the growth of IrO_2 thin films in our PLD system, finding the appropriate value of different paramenters (laser voltage, laser repetition rate and deposition rate). Besides, we successfully implemented this acquired knowledge to the fabrication of epitaxial thin films of IrO_2 of several thicknesses and crystallographic orientations.

3.3 $Y_3Fe_5O_{12}$

3.3.1 Introduction

Yttrium Iron Garnet belongs to the family of magnetic ceramic garnets. These compounds have important applications in microwave and magneto-optical devices, thanks to their exceptional magneto-optical properties [245, 246]. Among these properties, we can highlight the combination of a net magnetic moment with insulating electrical properties, low dielectric losses, narrow ferromagnetic resonance (FMR) linewidth related to small spin-wave damping, optical transparency in a wide range and pronounced Faraday effect [247].

In cubic iron garnets of general formula $A_3Fe_5O_{12}$ (O_h^{10} space group $Ia\bar{3}d$), Fe^{3+} cations occupy the different octahedral:tetrahedral sites in a precise 2:3 distribution [248]. In the particular case of $Y_3Fe_5O_{12}$ (YIG), the Fe^{3+} sublattices order antiferromagnetically, whereas Y^{3+} ions located at the dodecahedral sites are nonmagnetic. Therefore, there is uncompensated magnetic moment from Fe^{3+} at tetrahedral sites which gives rise to a ferrimagnetic state at room temperature, up to a Néel temperature of ~ 560 K [248, 249]. Moreover, YIG exhibits the narrowest FMR (ferromagnetic resonance) linewidth and smallest damping parameter among magnetic garnets, which makes it an outstanding synthetic material for microwave and magneto-optical applications such as filters and resonators [247, 250–253].

The development of spintronics, magnonics, and spin caloritronics in the last years has led to a renewal of the interest in magnetic garnets [250, 254–256]. In these areas, the availability of epitaxial thin films with low magnetic damping is essential for most studies and applications. In this regard, the standard method for YIG single-crystal fabrication, liquid phase epitaxy (LPE) [247], and other bulk synthetic methods cannot be used due to the difficulties in controlling the layer thickness down to the nanometer range [257]. On the other hand, the development of physical techniques such as pulsed PLD or sputtering allowed to overcome this problem, producing high-quality epitaxial thin films of YIG of a few nanometers with low values of magnetization damping [251, 254, 258, 259]. However, as explained in

Section 2.1.3, chemical solution deposition offers important advantages in terms of affordability and scalability for thin-film fabrication. This is why the development of simpler, cheaper, and more versatile techniques to chemically synthesize high-quality epitaxial YIG thin films has become a scientific and technological challenge of considerable relevance in the field.

In this section we address the chemical synthesis of YIG by means of Polymer Assisted Deposition (PAD). We obtain the optimum deposition parameters to produce high-quality thin films with chemical, crystalline and magnetic properties comparable to those of films produced by PVD methods.

3.3.2 Growth

The YIG samples were synthesized on top of 0.5 mm-thick (111) $Gd_3Ga_5O_{12}$ (GGG) commercial substrates by PAD from an aqueous solution. Lattice parameter of GGG ($a = 12.383$ Å) displays with lattice parameter of YIG ($a = 12.376$ Å) a mismatch as low as 0.06%. The synthesis procedure involved the following steps:

1. Individual solutions of the cations were prepared. First, the corresponding nitrate (yttrium or iron) was solved in water together with adequate polymers to stabilize the cations. In this case, we used ethylenediaminetetraacetic acid (EDTA, 1:1 molar ratio) and polyethylenimine (PEI) (in 1:1 mass ratio to EDTA).
2. Both solutions were mixed according to the desired stoichiometry (3:5). The resulted solution was then concentrated; the value of this final concentration controls the thickness of the synthesized films. We used a total cation concentration of $\sim$ 170 mM; with this value, we expected to obtain films in the 15-20 nm-thick range.
3. We spin-coated 35 µL of solution on (111) GGG substrates (5×5 mm^2 of surface area). The spin-coating was maintained during 20 s at 4000 rpm, with acceleration/deceleration ramps of 250 rpm/s^2.
4. In order to evaporate solvent and polymers and favor the crystallization of the films, samples were then annealed in air at different temperatures and

subsequently slowly cooled down at 3°C/min to avoid cracks formation.

In the first place, we evaluated the annealing temperature effect on one of the most remarkable characteristics of YIG (its narrow FMR linewidth), as test of films quality. For this, FMR experiments were performed in a Bruker EMX spectrometer operating at 9.4 GHz (X band) and equipped with an ER 4102ST resonant cavity (TE102 mode). The obtained FRM spectra depending on the annealing temperature are plotted in Fig. 3.22(a). A single sharp line is observed for samples annealed at 750°C. Fitting to a Lorentzian derivative function provides a peak-to-peak linewidth of $\Delta H_{\mathrm{pp}} \approx 20$ Oe. As evidenced in Fig. 3.22(b), moving away from this temperature results in a broadening of the FMR line and a shift of the resonant fields H_{r}, as well as the emergence of additional peaks which are likely associated to the formation of secondary phases.

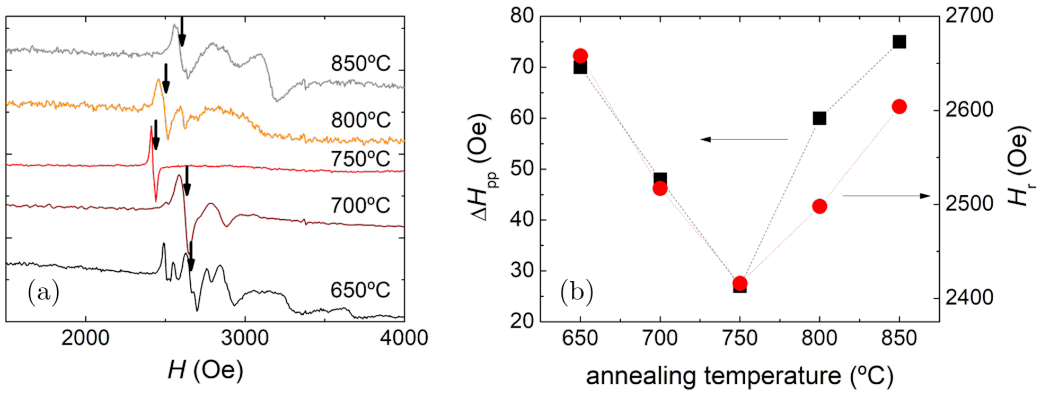

Figure 3.22 (a) FMR spectra for different YIG samples depending on the annealing temperature. (b) FMR linewidth ΔH_{pp} and resonant field H_{r} as a function of annealing temperature.

Therefore, according to these results, annealing at 750°C in air is the optimum condition for the preparation of YIG films by PAD, in terms of FMR linewidth. In order to compare the achieved ΔH_{pp} with the values obtained by a PVD technique, a reference 15 nm-thick YIG sample was deposited by PLD on a (111) GGG substrate. The comparison is shown in Fig. 3.23. In the case of the PLD-grown sample, the

fit to a Lorentzian derivative function yields $\Delta H_{pp} \approx 4$ Oe. The broader linewidths of PAD-grown samples ($\Delta H_{pp} \approx 20$ Oe in the case of sample with annealing temperature of 750°C) are likely attributable to a larger surface porosity of these films, with respect to samples prepared by PLD.

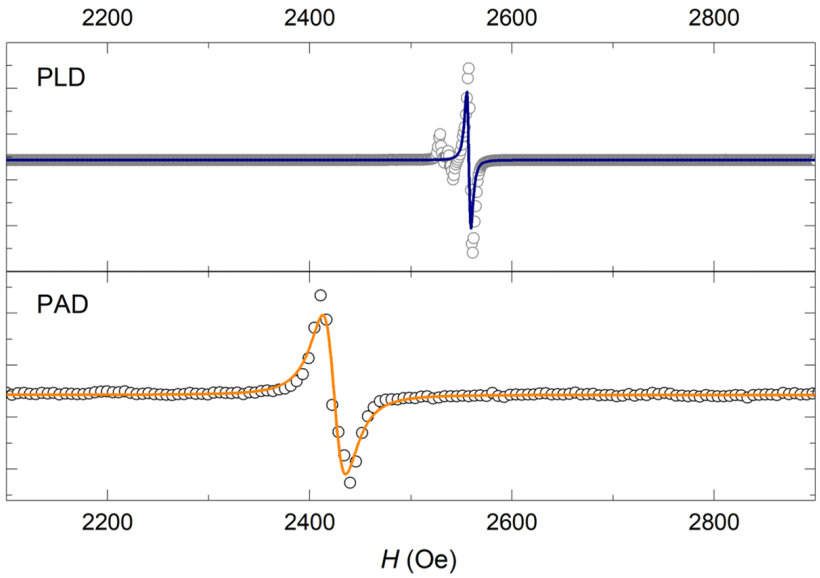

Figure 3.23 FRM spectra at X band (9.4 GHz) measured at room temperature for samples deposited using PLD (top panel) and PAD (bottom panel). Experimental data (open circles) and fit to a derivative Lorentzian function (solid line) are shown.

Additionally, a comparison between the results for chemically synthesized YIG nanometric thin films with those found in literature for films fabricated by PVD methods is provided. A widespread variety of values have been reported: Hauser *et al.* obtained ΔH_{pp} between 1.5 and 4 Oe in films grown by PLD at room temperature and postannealed under O_2 at high temperature for recrystallization [253], being the most similar to YIG single crystals, for example those reported by Dubs *et al.* ($\Delta H_{pp} \approx 1.5$ Oe) [257]; Onbasli and coworkers reported a $\Delta H_{pp} \approx 3-4$ Oe on films grown on top of (100) GGG by PLD [251]; Sun *et al.* found $\Delta H_{pp} \approx 5-17$ Oe in their films synthesized by PLD [260]; the sputtering-grown films in work of Liu and coworkers showed ΔH_{pp} values between 6 and 8 Oe [261].

3.3.3 Characterization

Once the optimal conditions for the PAD growth of YIG were established, we prepared a sample and performed an exhaustive characterization. Structural and chemical quality were assessed by XRD and TEM, and after that, static and dynamic magnetic properties were evaluated by SQUID magnetometry and FMR.

Thickness of the sample was determined my XRR (Fig. 3.24(a)), which provided a value of 15.1(9)nm, with a roughness $\sigma \sim 1$ nm. XRD diffraction pattern, shown in Fig. 3.24(b), confirms the oriented growth and good epitaxial matching to the substrate, as well as the absence of secondary phases, i.e., only the (hhh) Bragg peaks from YIG and GGG are visible in the range $2\theta = 15°\text{C}$ - $130°\text{C}$. Epitaxial relationship between GGG substrate and YIG film is also evidenced by the high-resolution RSM around the (664) Bragg reflection in Fig. 3.24(c), in which a nearly perfect match between the in-plane lattice parameters of substrate and film is observed.

STEM experiments were performed in order to further ascertain the good structural quality of the film. HAADF imaging in STEM revealed a very sharp interface with coherently strained structures (see Fig. 3.25(a)). In addition, the local chemical composition was studied by atomic resolution EELS analysis (Fig. 3.25(b)). This analysis displayed the expected $Y_3Fe_5O_{12}$ atomic arrangement with no significant amount of vacancies or defects, asserting the good homogeneity of the film. Finally, Geometrical Phase Analysis (GPA) was applied to the HAADF-STEM images to quantitatively evaluate the lattice mismatch between substrate and film. As shown in Fig. 3.25(c), we found practically zero in-plane and out-of-plane lattice mismatch: $\epsilon_{xx} = 0.1(8\%)$ and $\epsilon_{zz} = 0.5(7\%)$. This result provided further proof of the fully strained growth of YIG.

This complete structural and compositional analysis proved the good structural quality of the YIG film grown by PAD usin $750°\text{C}$ as annealing temperature. Next step was the characterization of magnetic behavior. Static magnetic properties were assessed by SQUID magnetometry; in particular, the magnetic hysteresis loop at room temperature as well as the dependence of magnetization on temperature were

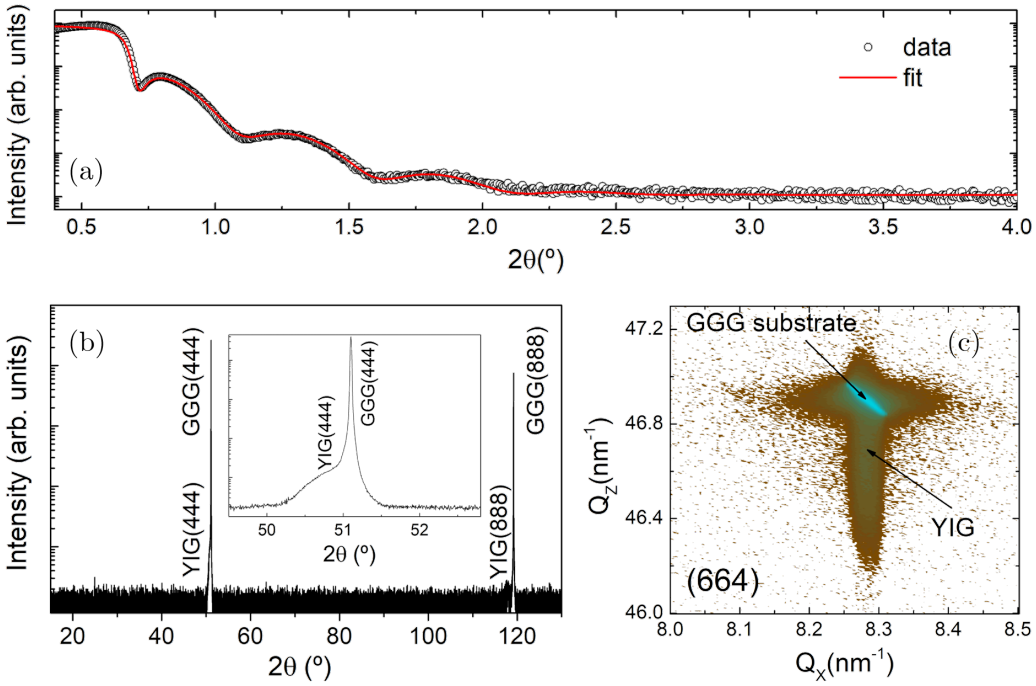

Figure 3.24 (a) XRR measurement of a YIG thin film synthesized by PAD at 750°Con top of (111) GGG, yielding thickness $t = 15.1(8)$ nm and surface roughness $\sigma \sim 1$ nm. (b) XRD $2\theta/\omega$ pattern of this sample. The pattern presents only the (444) and (888) Bragg peaks of YIG and GGG. The inset presents a refined scan around the (444) Bragg peak. (c) High-resolution reciprocal space map around the (664) Bragg reflection.

measured (3.26). The $M(H)$ loop shows a coercivity as low as $H_C \approx 2 - 3$ Oe and a saturation magnetization similar to that of the bulk material, i.e., $M_S \approx 140$ emu $\cdot$ cm^{-3}. Meanwhile, dependence of M on temperature shows a Néel order temperature around $T_N \sim 500$ K. As illustrated in 3.26(b), the $M(T)$ reproduces well the dependence described by the Brillouin function using $J = 5/2$ (iron) and magnetization and Curie temperature close to those of bulk YIG. These values are close to those reported for high-quality crystals of YIG [249, 251, 258].

Dynamic magnetic properties of the 750°C-optimized thin films were broadband characterized by FMR, between 2 and 10 GHz. The dependence of the peak-to-peak linewidth ΔH_{pp} on the excitation frequency f is presented in Fig. 3.27. The data follow a linear dependence, as expected within the frame of the

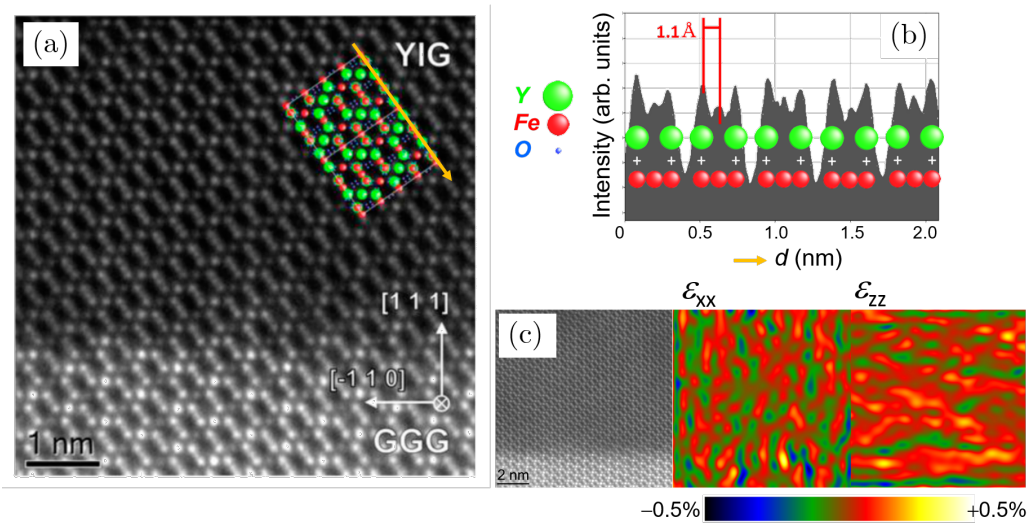

Figure 3.25 (a) HAAFD-STEM image of a cross-sectional specimen extracted from a YIG thin film synthesized by PAD at 750°C on top of (111) GGG, showing the detail of the interface between film and substrate. The sketch of the atomic structure of YIG is superimposed green, red, and blue balls representing Y, Fe, and O atoms, respectively. (b) EELS analysis taken along the yellow arrow in (a). (c) Geometrical Phase Analysis (GPA)pParallel (middle picture) and perpendicular (right picture) to the film plane, corresponding to the HAADF-STEM image in the left picture.

Landau-Lifshitz-Gilbert equation; linear fitting allows for the determination of the intrinsic Gilbert damping coefficient α according to [262]

$$\Delta H_{\mathrm{pp}} = \Delta H_{\mathrm{pp}}(0) + \frac{2\alpha}{\sqrt{3}\,(|\gamma|2\pi)} f \tag{3.4}$$

where $|\gamma|$ denotes the gyromagnetic ratio and $\Delta H_{\mathrm{pp}}(0)$ is the extrinsic broadening of the linewidth associated with the magnetic inhomogeneities inside the material. However, in order to carry out this fit, we first need to know the value of γ. This can be achieved by means of the Kittel formula, which relates resonant frequency and magnetic field:

$$f = \left|\frac{\gamma}{2\pi}\right| \sqrt{H_{\mathrm{r}}\left(H_{\mathrm{r}} + 4\pi M_{\mathrm{s}}\right)} \tag{3.5}$$

where M_{s} is the magnetization saturation of the YIG thin film. Therefore, we

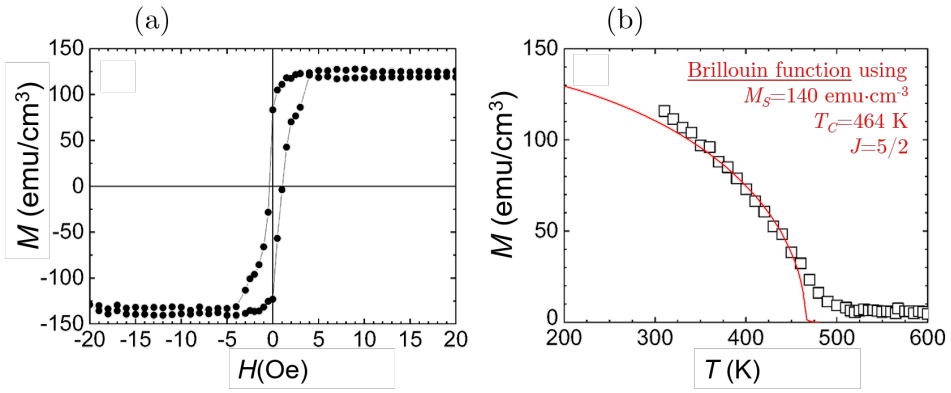

Figure 3.26 (a) In-plane magnetic hysteresis loop of a YIG thin film synthesized by PAD at 750°C on top of (111) GGG, measured at room temperature. (b) Magnetization of the YIG film as a function of temperature.

represent f against H_r and fit these data to Eq. 3.5, obtaining $M_s = 144.2$ emu $\cdot$ cm^{-3} and $|\gamma|/2\pi = 2.89$ MHz/Oe. These values are extremely comparable to those of bulk YIG ($M_s = 140$ emu $\cdot$ cm^{-3} and $|\gamma|/2\pi = 2.80$ MHz/Oe).

Once we determined the value of $|\gamma|$, we proceed to the linear fit of ΔH_{pp} dependence on f according to Eq. 3.4, which provides a Gilbert damping parameter $\alpha = 5.50 \times 10^{-3}$. In addition, the inhomogeneous broadening obtained from the fitting is $\Delta H_{pp}(0) \approx 0$, suggesting that magnetic inhomogeneities are not significant in YIG thin films grown by PAD.

These values of damping parameter α and FMR linewidth ΔH_{pp} are comparable to those reported for some of the best samples of YIG thin films prepared by sputtering. In Table 3.4, we compare our results of PAD-grown samples with some of the best values reported in literature using other methods of deposition.

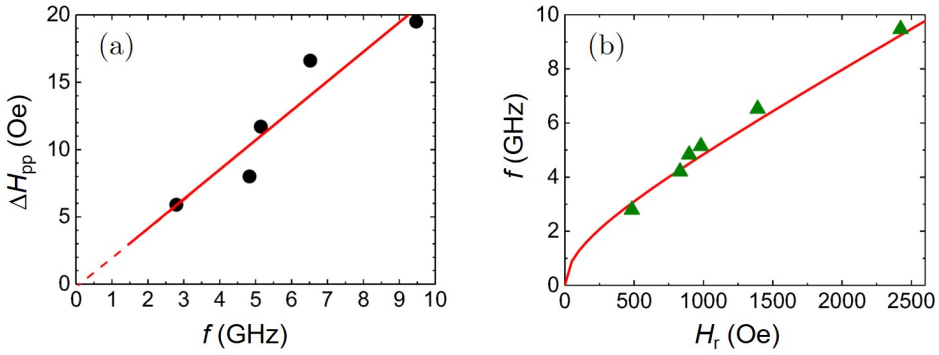

Figure 3.27 (a) Peak-to-peak linewidth ΔH_{pp} against excitation frequency for a YIG film grown by PAD at 750°C. The solid line is the linear fit. (b) Magnetic field dependence of the resonant frequency for the same sample. Solid line is the fit to the data using the Kittel formula.

Deposition method	Thickness (nm)	M_s (emu · cm^{-3})	Gilbert damping α
PAD (this work)	15	144.2	$\sim 5 \times 10^{-3}$
PLD + recryst. [253]	20 - 56	146	~ 6 - 8×10^{-5}
PLD [251]	17 - 190	120 - 137	~ 2 - 7×10^{-4}
PLD [260]	5 - 32	133 - 149	~ 2 - 3.2×10^{-4}
sputtering [258]	40	145	$\sim 7 \times 10^{-4}$
sputtering [261]	7 - 26	140	$\sim 1 \times 10^{-3}$
LPE [257]	83 - 113	142 - 145	~ 1.2 - 1.7×10^{-4}
LPE [263]	100	144	$\sim 2.8 \times 10^{-4}$

Table 3.4 Comparison of magnetic data of YIG films synthesized by PAD with other YIG films deposited by different methods.

3.3.4 Conclusions

In this section, it has been shown that PAD is a suitable method to fabricate YIG thin films with the thickness, crystal and magnetic quality required by applications in emerging fields such as spintronics. This is a relevant result from the technological point of view as, on the one hand, PAD offers affordability and scalability when

compared to physical methods; and, on the other hand, PAD allows to synthesize films of a few nm of thickness (as required for current spintronics and magnonics applications), unlike other chemical synthetic methods such as LPE.

We have determined the optimal conditions for PAD synthesis of YIG on (111) GGG substrates, and then performed and exhaustive structural and magnetic characterization on the optimized samples. We have found that PAD-deposited films exhibit properties comparable to those of some of the films grown by PVD methods. In particular, we highlight the fully strained growth, low coercivity of ~ 2 Oe and small magnetic Gilbert damping $\alpha = 5.50 \times 10^{-3}$.

Chapter 4

Static spin Seebeck effect in γ-Fe_2O_3/Pt bilayers

MOI are ideal platforms for LSSE experiments, because they ensure that other (essentially, thermoelectric) sources linked to mobile charge and spin carriers, such as ANE or SDSE, are not contributing to the measured output. In this regard, YIG has been the recurrent choice in experiments studying LSSE and other spintronic effects, becoming a reference. However, when focusing on one particular effect, diversity in materials is needed in order to improve the devices performance and assure universality of the attained results. Deeper insight into the fundamentals of the phenomenon is also benefited from the use of other materials.

In this chapter, we present the results of LSSE experiments performed using γ-Fe_2O_3 as FM layer, in static experimental conditions (i.e., under a steady ΔT) and using electrical detection by ISHE. Maghemite, which already owns a long history of applications in several fields (as mentioned in Chapter 3), stands as a promising material for SSE —and, in general, spintronic— devices due to its insulating nature combined with a high magnetic ordering temperature.

We start by a description of the basic LSSE experiment in γ-Fe_2O_3/Pt thin films using an external heater (as described in section 2.5.1(b)), followed by a comparison to the results previously reported in Fe_3O_4/Pt bilayers. Next, we present the relative

quantification of both sources of LSSE (interfacial and bulk magnon accumulation, as explained in Chapter 1). The strategy followed to this end was based on the study of LSSE and thermal conductivities for maghemite thin films of different thicknesses. Temperature dependence of LSSE is also presented. Secondly, we provide the results attained in experiments performed following the current or Joule heating SSE method (JSSE, section 2.5.1(c)). In this case, not only LSSE but also SMR is studied. We conclude with a comparative discussion of the LSSE results provided by both methods.

Maghemite layer in all samples was prepared using the optimized process reported in Chapter 3. Pt layer was straightway *in situ* sputtered at room temperature using an argon pressure of $P_{\mathrm{Ar}} = 5 \times 10^{-4}$ Torr and a sputtering power $P = 10$ W.

4.1 Static experiment using a heater

In the following, the results of LSSE experiments in γ-Fe_2O_3/Pt bilayers using the technique described in section 2.5.1(b) are presented. A preliminary step to approach the study of LSSE in γ-Fe_2O_3/Pt bilayers was to rule out the presence of ANE on bare γ-Fe_2O_3 layers. For this, we prepared a γ-Fe_2O_3 thin film on an MgO substrate and performed a measurement in the LSSE geometry and conditions, using the same setup. We applied different thermal differences ΔT across the sample ($\hat{z}$ direction) in the presence of a magnetic field in $\hat{x}$ direction and measured the transverse voltage in $\hat{y}$. In every case, we obtained an open-circuit response which saturated the voltmeter (not shown): maghemite insulating behavior prevents the excitation of a thermoelectric current generating a transverse electric field $\mathbf{E}_{\mathrm{ANE}}$ (see Eq.1.37) by spin-dependent scattering of conduction electrons (itinerant spins).

Additionally, proximity magnetism induced in the Pt layer could be a second source of ANE in the experimental geometry of LSSE. It has been shown that this magnetic proximity effect (MPE) is originated by interdiffusion of Fe which results in the induction of magnetic moment in Pt around Fe; consequently, deposition of Pt at low temperatures minimizes MPE down to a negligible magnitude [264, 265].

In sight of this, Pt was deposited at room temperature to avoid this possible ANE contribution.

Therefore, it can be concluded that in these experimental conditions any voltage which is (1) antisymmetric in magnetic field and (2) measured in $\hat{y}$ direction is originated in the Pt layer by ISHE spin-to-charge conversion of the spin current excited by LSSE, both at the γ-Fe_2O_3/Pt interface and the γ-Fe_2O_3 bulk thickness.

4.1.1 Experimental results

As described in Chapter 3, maghemite epitaxial thin films were prepared by post-annealing of magnetite thin films. In that chapter, the optimization of maghemite fabrication as a function of the annealing oxygen pressure P_{O_2} was presented. Here, we report on the influence of this same parameter on LSSE experiments. Three samples annealed at different P_{O_2} were prepared: 10, 50 and 100 mTorr. Besides, a not-annealed Fe_3O_4 thin film was also prepared in a Fe_3O_4/Pt bilayer, as reference. For all samples, thickness of the FM layer was $t_{FM} \approx 50$ nm, whereas Pt layer thickness was $t_{Pt} \approx 7$ nm. The films were deposited on (001) MgO substrates with dimensions of $2 \times 7 \times 0.5$ mm^3.

The ISHE voltage ΔV_{ISHE} was extracted for every thermal difference ΔT and sample as explained in 2.5.1(b): for every ΔT, the magnetic field was swept twice (i.e., from $H = -8$ kOe to $H = +8$ kOe and *vice versa*) and we extracted the antisymmetric $\Delta V^{anti}(H)$ ISHE signal (Fig. 4.1(a)-(d)). Then, we denote ΔV_{ISHE} to the value calculated for every ΔT from ΔV^{anti} taking the saturation values at positive and negative fields ($+H_S$ and $-H_S$) as $\Delta V_{ISHE} = \left[\Delta V^{anti}(+H_S) - \Delta V^{anti}(-H_S)\right]/2$. In Fig. 4.1(e), ΔV_{ISHE} for every sample is represented as a function of ΔT. We see that the expected linear dependence is kept; the standard spin Seebeck coefficient, S_{zy}, is finally computed as defined in Eq. 1.32 from the linear fits of $\Delta V_{ISHE}(\Delta T)$ data.

The thereby determined S_{zy} as a function of the annealing pressure P_{O_2} are plotted in Fig. 4.1(f). The coefficient obtained for $P_{O_2} = 10$ mTorr is very similar to that of the reference magnetite (which corresponds to the $P_{O_2} = 0$ mTorr point

in Fig. 4.1(f)). It is enhanced for $P_{O_2} = 50$ mTorr and $P_{O_2} = 100$ mTorr, reaching the maximum for $P_{O_2} = 50$ mTorr. This is in line with the results attained in the optimization process in section 3.1.2. There, we found that the samples annealed at $P_{O_2} = 50$ mTorr showed the best structural properties and the highest values of saturation magnetization; it was therefore fairly reasonable to also expect the greatest S_{zy} for this annealing pressure.

Henceforth in this dissertation, the raw measurements of the antisymmetric component ΔV^{anti} voltage as a function of magnetic field will not be shown, although they were always performed for different values of ΔT at every temperature T in order to extract the $\Delta V_{\text{ISHE}}/\Delta T$ slope.

We note in Fig. 4.2(a) that the shape of the obtained ΔV^{anti} field dependence

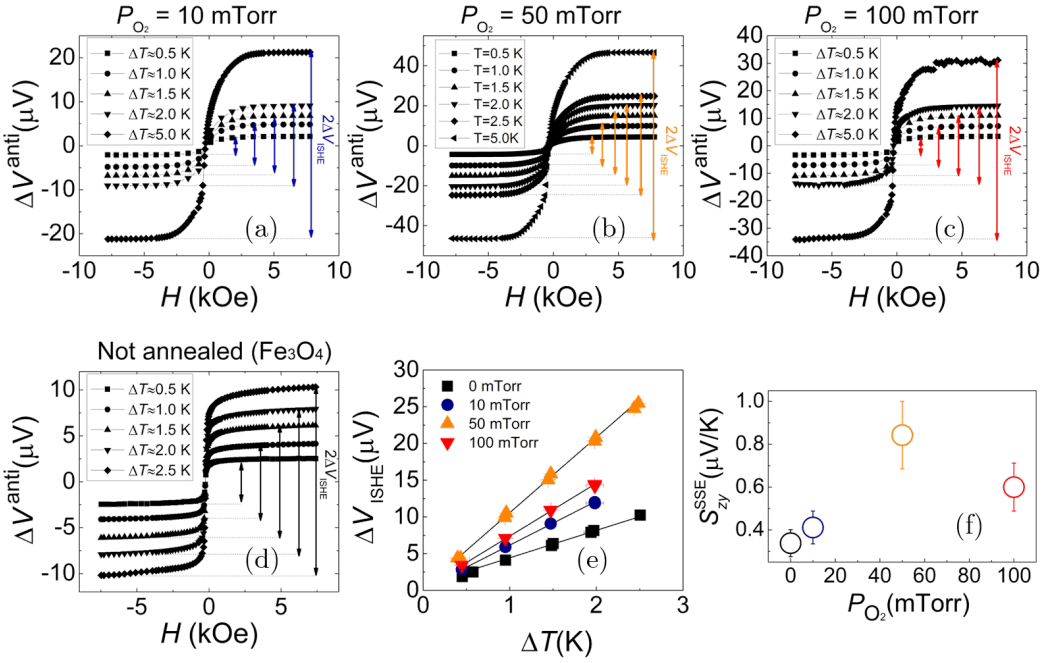

Figure 4.1 (a)-(d) Magnetic-field dependent ΔV^{anti} signals measured γ-Fe_2O_3/Pt bilayers at various applied ΔT for different annealing pressures P_{O_2}: (a) $P_{O_2} = 10$ mTorr, (b) $P_{O_2} = 50$ mTorr, (c) $P_{O_2} = 100$ mTorr and (d) not annealed. The depicted arrows mark the magnitude of $2\Delta V_{\text{ISHE}}$. (e) Linear dependence and fit of measured ΔV_{ISHE} as a function of ΔT. (f) Computed S_{zy} as a function of annealing pressure P_{O_2}.

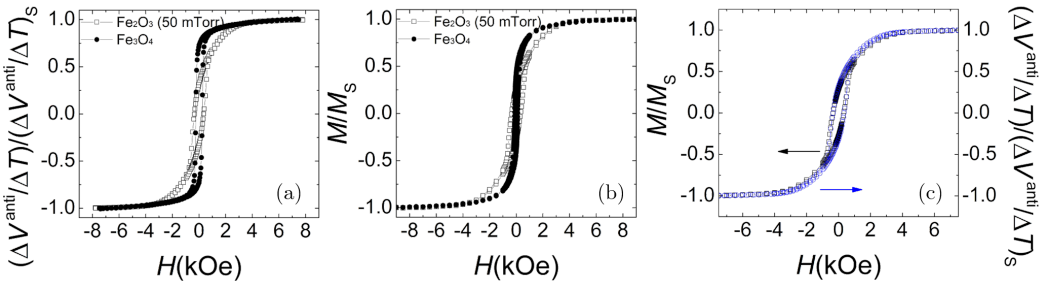

Figure 4.2 (a) Comparison of the hysteresis loops described by the antisymmetric ISHE voltage as a function of magnetic filed for γ-Fe_2O_3/Pt (open squares) and Fe_3O_4/Pt bilayers (closed circles). (b) Comparison between the corresponding magnetic hysteresis loops. (c) Scaling of the LSSE/ISHE (open circles) and magnetic signals (open squares) for γ-Fe_2O_3/Pt.

differs from maghemite to magnetite; the differences are equivalent to those found between the respective magnetization, M, hysteresis loops: remanence is larger in magnetite, whereas coercive field is lower, although saturation magnetizations are highly similar (see Fig. 4.2(b) or results in section 3.1.2). In other words, ΔV^{anti} hysteresis loops qualitatively track the respective in-plane M loops, since the ISHE field depends on the polarization of the spin current injected in the Pt layer. This is clearly illustrated in Fig. 4.2(c) for maghemite, where $M(H)$ and $\Delta V^{\mathrm{anti}}(H)$ are superimposed.

As inferred from discussion in Chapter 1, one needs to be cautious in order to compare the S_{zy} reported for other materials with the result in maghemite, even in the most comparison-friendly case in which SSE has been detected also by ISHE in Pt: a rigorous comparison would require comparable interface quality and identical Pt thickness, because minor variations affect the output voltage through spin decay due to spin diffusion length. Besides, Pt thin film electrical resistivity ρ_{c} could also be thickness dependent, leading to changes in the measured voltage for the same spin current I_{s}; as expressed in Eq. 6.1, the spin Hall resistivity ρ_{SH} would be affected by two channels: first, directly by the different value of the electrical conductivity ρ_{c}, and, secondly, by the ρ_{c}-dependence of θ_{SH}. Additionally, if the variation in ρ_{c} is significant enough to imply a transition in the conduction regime, this would involve

FM layer (t_{FM})	NM layer (t_{NM})	S_{zy} (V/K)	Exp. conditions	Ref.
γ-Fe_2O_3(thin film, 50 nm)	Pt (7 nm)	$8.4(9) \times 10^{-7}$	300 K	This work [266]
Fe_3O_4(thin film, 50 nm)	Pt (7 nm)	$3.4(6) \times 10^{-7}$	300 K	This work [266]
Fe_3O_4(thin film, 50 nm)	Pt (5 nm)	7.4×10^{-8}	300 K	[267]
Fe_3O_4(thin film, 23 nm)	Pt (7 nm)	$\approx 5 \times 10^{-7}$	300 K	[268]
YIG (bulk, 1 mm)	Pt (15 nm)	$\approx 1.1 \times 10^{-7}$	300 K	[68]
YIG (bulk, 1 mm)	Pt (10 nm)	$\approx 2 \times 10^{-7}$	300 K	[269]
YIG (thin film, 4.5 μm)	Pt (10 nm)	$\approx 1 \times 10^{-7}$	300 K	[269]
YIG (thin film, 8 μm)	Pt (6 nm)	$\approx 3 \times 10^{-8}$	300 K	[73]
YIG (thin film, $\geq 10\,\mu m$)	Pt (6 nm)	$\approx 1.5 \times 10^{-6}$	300 K	[270]
YIG (thin film, 50 nm)	Pt (6 nm)	$\approx 2.2 \times 10^{-7}$	300 K	[270]
(Mn,Zn)Fe_2O_4 (bulk, 1 mm)	Pt (15 nm)	$\approx 3 \times 10^{-8}$	300 K	[271]
$NiFe_2O_4$ (thin film, 1.2 μm)	Pt (10 nm)	$3(2) \times 10^{-8}$	300 K	[96]
$ZnFe_2O_4$ (bulk, 0.5 mm)	Pt (8 nm)	2.8×10^{-8}	300 K	[272]
$CoFe_2O_4$ (thin film, 168 nm)	Pt (5 nm)	$9.41(32) \times 10^{-8}$	300 K	[273]
$CoFe_2O_4$ (thin film, 20 nm)	Pt (5 nm)	$\approx 4.6 \times 10^{-8}$	300 K	[273]
$La_{0.7}Sr_{0.3}MnO_3$ (thin film, 100 nm)	Pt (5 nm)	$\approx 2.5 \times 10^{-8}$	300 K	[274]
$La_{0.7}Sr_{0.3}MnO_3$ (thin film, 100 nm)	Pt (3 nm)	$\approx 4.5 \times 10^{-8}$	300 K	[274]
MnF_2 (thin film, 30 nm)	Pt (4 nm)	4.5×10^{-6}	35 K, 14 T	[77]
Cr_2O_3 (bulk, 0.5 mm)	Pt (10 nm)	$\approx 1.3 \times 10^{-8}$	40 K, 14 T	[76]

Table 4.1 Comparison of the spin Seebeck coefficient S_{zy} of γ-Fe_2O_3/Pt thin film bilayers with other different FM/Pt structures.

a replacement of the main mechanism behind ISHE, resulting in an alteration of the magnitude and ρ_c-scaling of θ_{SH}. Moreover, thickness of the FM can also strongly modify the magnitude of the SSE spin current, as we will discuss in the next section, both because of the magnon propagation length scale and because of thickness effect on the thermal gradient along the FM layer (∇T_{FM}). Finally, other issues such as thin film crystallinity or, especially, the quality of the FM/NM interface may strongly affect the magnitude of the effects (LSSE through the interfacial contribution and ISHE through the efficiency of spin angular momentum transmission across the interface, which is characterized by the spin mixing conductance $g_{\uparrow\downarrow}$).

With this in mind, in Table 4.1 we summarize some of the results for LSSE at room temperature (exception is made for the antiferromagnetic materials in which SSE in only detected below Néel temperatures) gathered in literature along with the description of the utilized samples. We restrict ourselves to experiments based in electrical detection by ISHE with Pt as NM detector layer.

S_{zy} of γ-Fe_2O_3/Pt compares very well with the highest of those reported for other materials, being indeed the largest of all of them, except that of antiferromagnetic

MnF_2 measured at low temperature and high magnetic field. In particular, we highlight that it is ≈ 4 times bigger than S_{zy} of the most comparable YIG/Pt experiment in terms of YIG and Pt thicknesses, which is reported in Ref. [270]. All in all, maghemite has proved itself a very suitable material also for spin caloritronics applications.

4.1.2 Thickness dependence

In Chapter 1 we explained that there are two sources of thermal spin currents contributing to LSSE: thermal propagation of magnons in the bulk of the FM layer (bLSSE) and interface contribution due to the temperature difference between both sides of the interface (iLSSE). Nevertheless, most previous studies on the matter only take into account one of the contributions, frequently neglecting or disregarding the other one. Whilst time-resolved optical approaches of SSE measurements have been able to selectively excite only interfacial LSSE (iLSSE) [82, 83, 275], the relative contributions in a standard DC measurement in which the whole sample is subjected to a thermal gradient have yet to be addressed. In this section, we quantify the relative contribution of each source in our experimental conditions —electrical detection by ISHE in a static experiment— and show that within the usual range of tens of nanometers neither of both components can be neglected.

Our approach to the quantification of iLSSE and bLSSE contributions was based on the study of the LSSE as a function of t_{FM}. To this end, a series of samples consisting of γ-Fe_2O_3/Pt bilayers deposited on (001) MgO substrates with x, y and z dimensions of $2 \times 7 \times 0.5$ mm^3 was prepared. XRD patterns around the (002) Bragg peak of MgO substrate are provided in Fig. 4.3.

A thorough analysis of Eqs. 1.34 and 1.33 leads us to identify three sources of modulation of the thermally excited LSSE spin current J_{s} by t_{FM}:

(1) Directly, due to the existence of a magnon propagation length scale Λ_{m} comparable to the samples dimensions: only magnons from distances smaller than it reach the interface with the spin-to-charge NM layer and contribute to the signal, which leads to a saturation behavior as t_{FM} increases (see Fig.

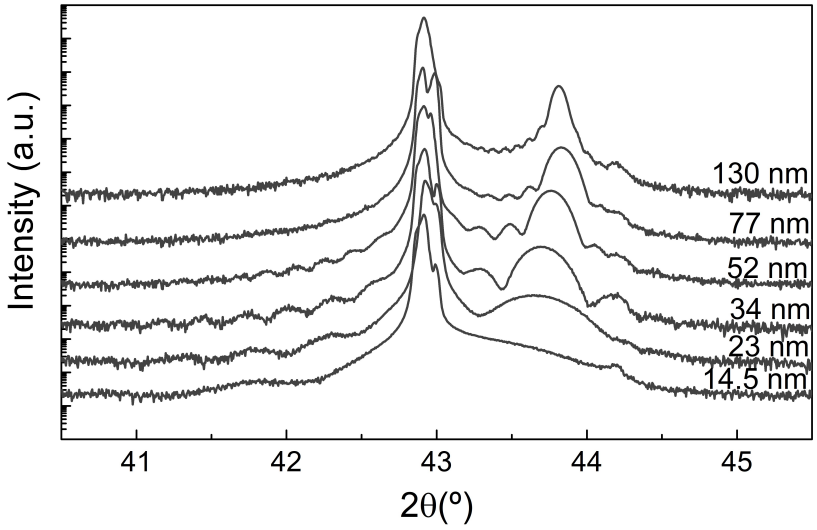

Figure 4.3 XRD patterns around the (002) Bragg peak of MgO substrate of γ-Fe_2O_3/Pt samples with different thickness of the γ-Fe_2O_3 layer.

4.4). This source is contained in the $\frac{\cosh(t_{FM}/\Lambda_m)-1}{\sinh(t_{FM}/\Lambda_m)}$ factor in Eq. 1.34

(2) The change of the involved thermal drops due to the variation of the FM layer thickness in relation to the rest of the stacked layers under the same ΔT.

(3) A possible dependence of the thermal conductivity of the FM layer on its thickness.

Concerning the second possibility we must consider that in the used setup, as detailed in Section 2.5.1, the temperature difference between the hot and cold reservoirs (i.e. the temperature drop ΔT across the whole sample including the substrate) is the controlled and measured magnitude (temperature difference method). The temperature profile shows two main features: (1) a change in its slope from layer to layer because of the different thermal conductivities and (2) a discontinuity at the interfaces due to the interfacial thermal resistance, also known as Kapitza resistance. Therefore, as illustrated in Fig. 4.5, the total temperature difference can be split into the consecutive thermal drops along the sample:

$$\Delta T = \Delta T_{Pt} + \Delta T_i^{Pt/FM} + \Delta T_{FM} + \Delta T_i^{FM/S} + \Delta T_S \tag{4.1}$$

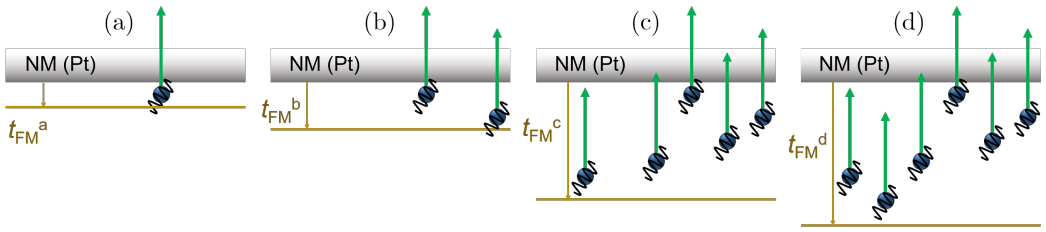

Figure 4.4 Influence of the thermal magnon propagation length (Λ_m, represented by the green arrows) in LSSE depending on the FM thickness (t_{FM}). (a)-(b) While $t_{FM} < \Lambda_m$, all excited magnons propagate to the FM/NM surface and contribute to the spin-to-charge conversion by ISHE in NM. (c)-(d) However, once that $t_{FM} > \Lambda_m$, ISHE signal saturates because magnons which are farther than Λ_m to surface do not reach it and consequently do not contribute to the spin current injected in NM; i.e., **for the same exciting thermal gradient along FM layer**, measured ISHE voltage would behave like $\Delta V_{ISHE}^{a} < \Delta V_{ISHE}^{b} < \Delta V_{ISHE}^{c} = \Delta V_{ISHE}^{d}$

which accounts for the temperature drop in the Pt layer, at the Pt/FM interface, in the FM layer, at the FM/substrate interface, and across the substrate. According to a simple thermal model the heat flux is constant through the whole sample:

$$\begin{aligned} J_Q &= \left(\frac{t_{Pt}}{\kappa_{Pt}} + \frac{t_{FM}}{\kappa_{FM}} + \frac{t_S}{\kappa_S} + R_i^{Pt/FM} + R_i^{FM/S} \right)^{-1} \Delta T = \\ &= \frac{1}{R_T} \Delta T = \frac{\kappa_{FM}}{t_{FM}} \Delta T_{FM} = \frac{1}{R_i^{Pt/FM}} \Delta T_i^{Pt/FM}, \end{aligned} \tag{4.2}$$

where t's denote thicknesses and κ's denote thermal conductivities; $R_i^{Pt/FM}(R_i^{FM/S})$ is the thermal resistance coming from the Pt/FM (FM/substrate) interface; and R_T represents the thermal resistance of the system as a whole, i.e., the composition of the thermal resistances of each layer and interfaces.

It must be highlighted that, for the same total ΔT, the thermal drops across the FM layer thickness and at the NM/FM interface (ΔT_{FM} and $\Delta T_i^{Pt/FM}$) change upon changing t_{FM}, as expressed in Eq. 4.2. Consequently, J_s^b and J_s^i change as well, since they are driven by those thermal differences (recall Eqs. 1.33 and 1.34), a fact that should be taken into account in a rigorous interpretation of LSSE experiments. However, this issue has been omitted in previous studies about the t_{FM} dependence of LSSE, although it represents a source of modulation of the contribution of both

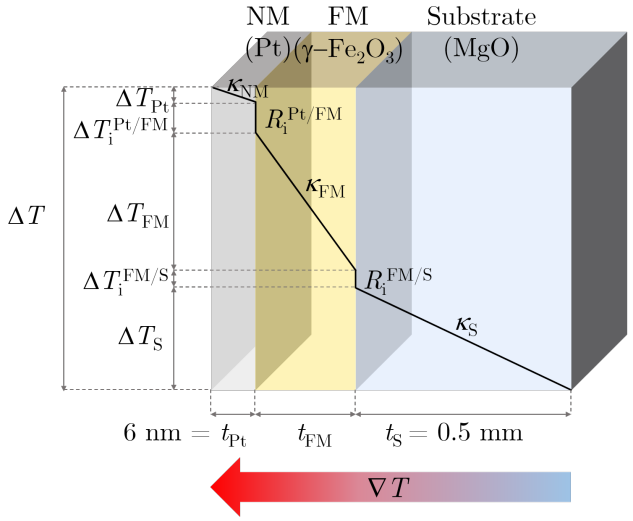

Figure 4.5 Depiction of the thermal differences established in the LSSE experiment through the studied sample, as expressed in Eq. 4.1. The graded arrow shows the direction of the thermal gradient.

LSSE mechanisms. Typically, only the dependence related to Λ_m is addressed, whereas the influence of t_{FM} in ΔT_{FM} has not been considered so far. For this accurate analysis, knowledge on the cross-plane thermal conductivities is needed in order to perform the required calculations to quantify the gradients. Therefore, a key point in our work was the assessment of the thermal conductivities for thin films of different thicknesses.

Thermal conductivity of maghemite thin films

As indicated above, in order to quantify the thermal drops along the sample, the thermal conductivity of maghemite thin films with different thickness need to be determined. The cross-plane thermal conductivity of the samples were measured by the 3ω technique, detailed in Section 2.5.2. As explained there, in this method a thin metal resistor serves as a heater and a thermometer simultaneously. The resistors used were made of Au or Pt (100 nm thick, 10 µm width, 1 mm length) and fabricated by evaporation and optical lithography. Additional 10 nm of Cr were

used underneath the resistor for adhesion improvement. The measurements were performed by applying current with a Keithley 6221 AC source at frequencies from 56 to 2120 Hz to produce a heat dissipation of 30 mW for all samples.

Five samples with thicknesses ranging from 50 to 90 nm were prepared. Lower thicknesses were not included because they would approach the limit of the technique resolution.

As a requirement for 3ω measurement, γ-Fe_2O_3, samples were deposited only on half the MgO substrate. Thus, a reference resistor can be placed on the other half onto bare substrate. This way, the determination of the thermal conductivity κ_{FM} of the thin films gains in precision as errors coming from slight differences between substrates are avoided. As a result of this precaution, the temperature rise $\Delta T_{2\omega}$ for both parts (bare substrate and thin film-covered substrate) is perfectly parallel, allowing for a straight extraction of ΔT_{f} by subtraction (recall Eq. 2.16). An example is provided in Fig. 4.6.

It is important to note that the thereby determined thin film conductivity is not the intrinsic κ_{FM} but an effective κ'_{FM} which also accounts for the thermal loss at

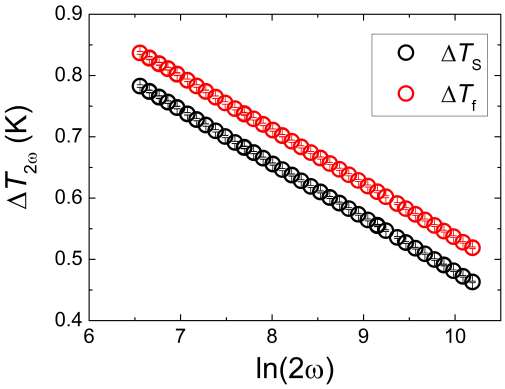

Figure 4.6 Temperature rise on a sample with a 50 nm thick γ-Fe_2O_3 thin film and on the bare MgO substrate.

the MgO/γ-Fe_2O_3 interface $R_i^{FM/S}$ [132].

$$\kappa'_{FM} = \frac{\kappa_{FM}}{1 + R_i^{FM/S}\kappa_{FM}/t_{FM}} \tag{4.3}$$

We used this effective κ'_{FM} to calculate ΔT_{FM} in the LSSE experiments. This means that hereafter, $\Delta T_i^{FM/S}$ will be contained in ΔT_{FM}. It is a good approximation to take $\kappa'_{FM} \approx \kappa_{FM}$, i.e. $R_i^{FM/S} \ll t_{FM}/\kappa_{FM}$. This is supported by the time domain thermoreflectance (TDTR) measurements of stacked repetitions of (Fe_3O_4/Pt) units on MgO substrates reported in reference [268]. Authors obtain the effective thermal conductivity of the $(Fe_3O_4/Pt)_n$ multilayer, but this effective conductivity includes the contribution of MgO/Fe_3O_4 interface, as in 3ω method. In their data, no difference is observed for different values of the period n (effective *thickness* of the multilayer). From this, we can infer that the thermal resistance of MgO/Fe_3O_4 is negligible with respect to the conductance of the layer, since otherwise the dependence expressed by Eq. 4.3 would be expected. MgO/Fe_3O_4 epitaxial interface is highly similar to that of MgO/γ-Fe_2O_3, especially since both sets of samples (those in this study and those in reference [268]) were grown by PLD in the same PLD system and given the approach to prepare epitaxial thin films of maghemite based on the post-annealing of PLD-grown epitaxial magnetite thin films, as explained Chapter 3.

Thermal conductivities κ'_{FM} were determined for different temperatures, except for one of the samples. The results are displayed in Fig. 4.7(a)-(d). Data measured at room temperature as a function of the thin film thickness t_{FM} are plotted in Fig. 4.7(e). They follow a rather complex dependence, which may be attributed to the presence of defects rapidly changing with the film thickness; a possible candidate are the antiphase boundaries (APBs) which are usually shown by spinel structures (such as maghemite) and whose density decrease with thickness [176, 276].

Concerning MgO substrate, we measured $\kappa_S = 44.2(5)$ W m^{-1}K^{-1} at $T = 300$ K, in agreement with reported values for MgO single crystals [277, 278].

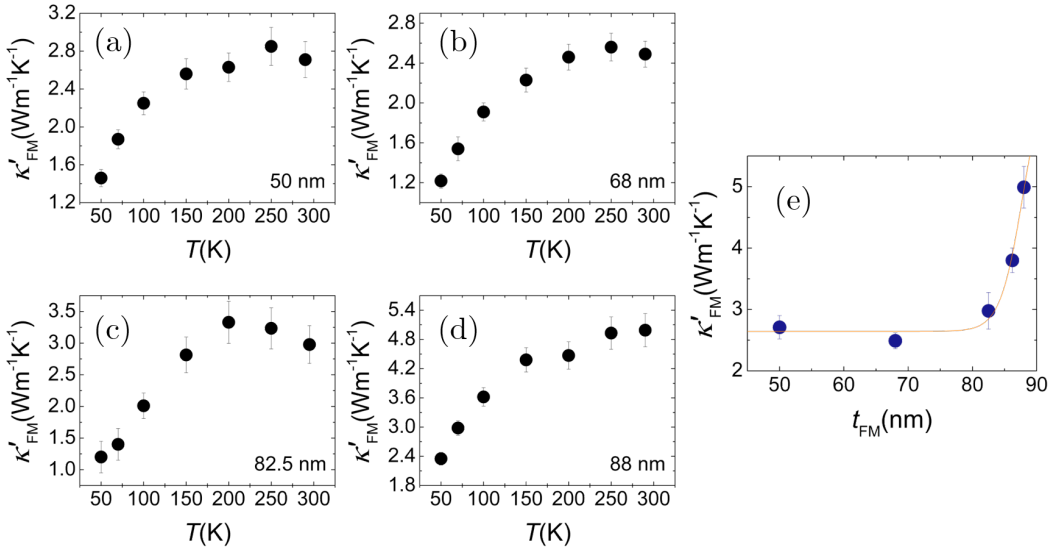

Figure 4.7 (a)-(d) Measured temperature dependence of the (effective) thermal conductivity of maghemite epitaxial thin films of different thicknesses. (e) Measured temperature dependence of the (effective) thermal conductivity of maghemite epitaxial thin films as a function of the thickness. Solid line represents an experimental fit to a sigmoid function used for interpolation of κ'_{FM} at the desired t_{FM}.

Quantification of the bulk and interfacial contributions to LSSE

From the obtained experimental t_{FM} dependence of κ'_{FM} shown in Fig. 4.7, the values of κ'_{FM} at the t_{FM} of the samples studied in the LSSE experiments can be interpolated, as displayed in Fig. 4.7(e). The estimation of thermal conductivities of maghemite allowed us to write every temperature drop of interest (i.e., those ones driving both sources of LSSE) in terms of the known ΔT from Eq. 4.2:

$$\begin{aligned} \Delta T_{\mathrm{FM}} &\approx \frac{\kappa_{\mathrm{S}} t_{\mathrm{FM}}}{\kappa_{\mathrm{S}} t_{\mathrm{FM}} + \kappa'_{\mathrm{FM}} t_{\mathrm{S}}} \Delta T \\ \Delta T_{\mathrm{i}}^{\mathrm{Pt/FM}} &\approx \frac{\kappa_{\mathrm{S}} \kappa'_{\mathrm{FM}} R_{\mathrm{i}}^{\mathrm{Pt/FM}}}{\kappa_{\mathrm{S}} t_{\mathrm{FM}} + \kappa'_{\mathrm{FM}} t_{\mathrm{S}}} \Delta T, \end{aligned} \tag{4.4}$$

where two approximations have been taken:

- The thermal resistance contribution of the Pt layer in Eq. 4.2, $t_{\mathrm{Pt}}/\kappa_{\mathrm{Pt}}$, and the corresponding temperature drop in Eq. 4.1, Δt_{Pt}, have been neglected:

Pt thermal resistance is two orders of magnitude lower than the rest of the terms, due to its small thickness $t_{\mathrm{Pt}} = 6$ nm and large thermal conductivity $\kappa_{\mathrm{Pt}} = 64$ $\mathrm{Wm^{-1}K^{-1}}$[279]. The thermal resistances of the stacked layers are $R_{\mathrm{MgO}} \sim 10^{-5}$ $\mathrm{W^{-1}m^2K}$, R_{FM} ranges from $\sim 10^{-9}$ to 10^{-8} $\mathrm{W^{-1}m^2K}$, and from literature $R_{\mathrm{i}} \sim 10^{-9}$ $\mathrm{W^{-1}m^2K}$ [279, 280]; all of them exceed $R_{\mathrm{Pt}} \sim 10^{-11}$ $\mathrm{W^{-1}m^2K}$ by at least two orders of magnitude.

- Besides, we have considered $\kappa_{\mathrm{S}}\kappa_{\mathrm{FM}}R_{\mathrm{i}}^{\mathrm{Pt/FM}} \ll \kappa_{\mathrm{FM}}t_{\mathrm{S}}$, which is reasonable, given the substrate thickness as well as the typical values of R_{i}.

In Fig. 4.8(a) the measured dependence of transverse voltage ΔV_{ISHE} on t_{FM} is shown. Following a widespread practice in line with the standard definition of the SSC in Eq. 1.32 [281, 282], these quantities have been normalized by the established total thermal difference ΔT, which is the same for every t_{FM}. However, this means that according to Eq. 4.4 ΔT_{FM} and ΔT_{i} depend on t_{FM}. To rigorously take into account both effects, the scaling with the corresponding temperature drops must be used instead. For this, we express Eqs. 1.33 and 1.34 it in terms of the measured total ΔT, using Eq. 4.4:

$$\begin{aligned} J_{\mathrm{s}}^{\mathrm{i}} &\propto \frac{\kappa_{\mathrm{S}}\kappa'_{\mathrm{FM}}R_{\mathrm{i}}^{\mathrm{Pt/FM}}}{\kappa_{\mathrm{S}}t_{\mathrm{FM}} + \kappa'_{\mathrm{FM}}t_{\mathrm{S}}}\Delta T \\ J_{\mathrm{s}}^{\mathrm{b}} &\propto \frac{\cosh\left(t_{\mathrm{FM}}/\Lambda_{\mathrm{m}}\right) - 1}{\sinh\left(t_{\mathrm{FM}}/\Lambda_{\mathrm{m}}\right)}\frac{\kappa_{\mathrm{S}}}{\kappa_{\mathrm{S}}t_{\mathrm{FM}} + \kappa'_{\mathrm{FM}}t_{\mathrm{S}}}\Delta T \end{aligned} \tag{4.5}$$

This pair of equations make clear that only a small fraction of the thermal energy is actually converted into electrical energy, i.e., only a small fraction of ΔT participates in generating the output ISHE voltage ΔV_{ISHE} through the LSSE. To be consistent with this fact, we propose the use of the following spin Seebeck coefficients:

$$S^{\mathrm{i}} = \frac{\Delta V_{\mathrm{ISHE}}^{i}}{d_y \Delta T^{\mathrm{NM/FM}}} \quad \text{and} \quad S^{\mathrm{b}} = \frac{\Delta V_{\mathrm{ISHE}}^{b}}{d_y \Delta T_{\mathrm{FM}}}, \tag{4.6a}$$

where d_y is the distance between the transverse contacts to measure ΔV_{ISHE}. These definitions make use of the temperature difference actually driving each effect, rather than the overall temperature difference, contrary to the standard S_{zy} in Eq. 1.32.

Likewise, we write them in terms of the measured ΔT by using 4.4:

$$S^{\mathrm{i}} \approx \frac{\Delta V^{i}_{\mathrm{ISHE}}}{d_y \Delta T} \frac{\kappa_{\mathrm{S}} t_{\mathrm{FM}} + \kappa_{\mathrm{FM}} t_{\mathrm{S}}}{R_{\mathrm{i}}^{\mathrm{Pt/FM}} \kappa_{\mathrm{S}} \kappa_{\mathrm{FM}}} \quad \text{and} \quad S^{\mathrm{b}} \approx \frac{\Delta V^{b}_{\mathrm{ISHE}}}{d_y \Delta T} \frac{\kappa_{\mathrm{S}} t_{\mathrm{FM}} + \kappa_{\mathrm{FM}} t_{\mathrm{S}}}{\kappa_{\mathrm{S}} t_{\mathrm{FM}}} \tag{4.6b}$$

ISHE transverse voltage ΔV_{ISHE} and the exciting spin current density J_{s} are related by $\Delta V_{\mathrm{ISHE}} \propto \theta_{\mathrm{SH}} \rho_{\mathrm{c}} J_{\mathrm{s}}$ [49], where θ_{SH} is the so-called spin Hall angle accounting for the efficiency of the spin-to-charge conversion, and ρ_{c} is the longitudinal electrical resistivity of the NM ISHE medium (Pt in our case). Depending on the mechanism governing ISHE, θ_{SH} can be either independent or proportional to ρ_{c} [47, 52, 283], as reviewed in Chapter 1. However, in this experiment, Pt layer thickness is the same for all samples, which means ρ_{c} is also constant. Therefore, the transverse ISHE voltage ΔV_{ISHE} becomes proportional to the exciting spin current in the employed experimental conditions: $\Delta V_{\mathrm{ISHE}} \propto J_{\mathrm{s}}$. Accordingly, from this and Eq. 4.5, the contribution to ΔV_{ISHE} of both sources of

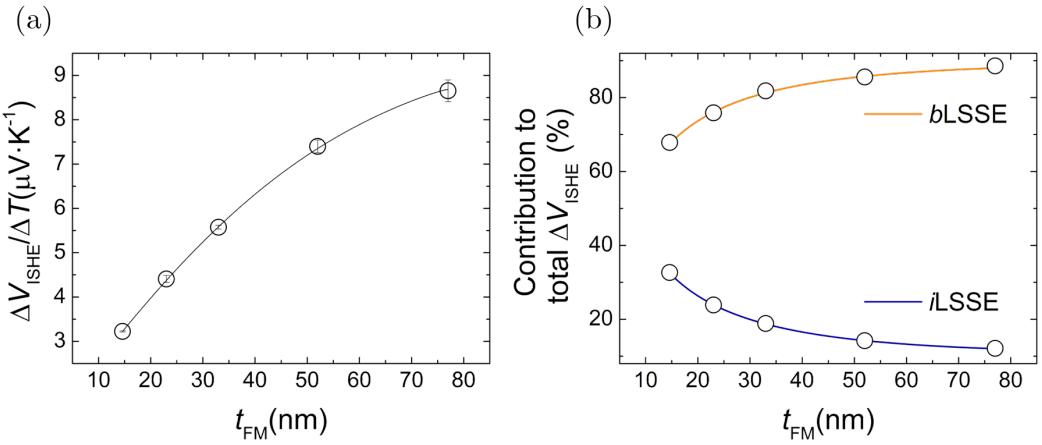

Figure 4.8 (a) Transverse voltage ΔV_{ISHE} measured for every different t_{FM}, normalized by the total temperature difference ΔT (open circles) and fit of Eq. 4.10 to the experimental data (solid line). (b) Relative contribution of each LSSE source to the total ISHE voltage.

LSSE can be written as:

$$\begin{aligned}\Delta V_{\mathrm{ISHE}}^{\mathrm{i}} &\propto \frac{\kappa_{\mathrm{S}}\kappa'_{\mathrm{FM}}R_{\mathrm{i}}^{\mathrm{Pt/FM}}}{\kappa_{\mathrm{S}}t_{\mathrm{FM}}+\kappa'_{\mathrm{FM}}t_{\mathrm{S}}}\Delta T \\ \Delta V_{\mathrm{ISHE}}^{\mathrm{b}} &\propto \frac{\cosh\left(t_{\mathrm{FM}}/\Lambda_{\mathrm{m}}\right)-1}{\sinh\left(t_{\mathrm{FM}}/\Lambda_{\mathrm{m}}\right)}\frac{\kappa_{\mathrm{S}}}{\kappa_{\mathrm{S}}t_{\mathrm{FM}}+\kappa'_{\mathrm{FM}}t_{\mathrm{S}}}\Delta T\end{aligned} \tag{4.7}$$

Finally, in sight of the definition of the corresponding spin Seebeck coefficients in Eq. 4.6, we obtain:

$$\begin{aligned}\Delta V_{\mathrm{ISHE}}^{\mathrm{i}} &\approx S^{\mathrm{i}}\cdot d_y\cdot\frac{\kappa_{\mathrm{S}}\kappa'_{\mathrm{FM}}R_{\mathrm{i}}^{\mathrm{Pt/FM}}}{\kappa_{\mathrm{S}}t_{\mathrm{FM}}+\kappa'_{\mathrm{FM}}t_{\mathrm{S}}}\Delta T \\ \Delta V_{\mathrm{ISHE}}^{\mathrm{b}} &\approx A\cdot d_y\cdot\frac{\cosh\left(t_{\mathrm{FM}}/\Lambda_{\mathrm{m}}\right)-1}{\sinh\left(t_{\mathrm{FM}}/\Lambda_{\mathrm{m}}\right)}\frac{\kappa_{\mathrm{S}}}{\kappa_{\mathrm{S}}t_{\mathrm{FM}}+\kappa'_{\mathrm{FM}}t_{\mathrm{S}}}\Delta T\end{aligned} \tag{4.8}$$

where the coefficient A is defined by:

$$S^{\mathrm{b}} = A\cdot\frac{1}{t_{\mathrm{FM}}}\frac{\cosh\left(t_{\mathrm{FM}}/\Lambda_{\mathrm{m}}\right)-1}{\sinh\left(t_{\mathrm{FM}}/\Lambda_{\mathrm{m})}\right.} \tag{4.9}$$

Note that, unlike S^{i} and A, S^{b} depends on t_{FM} through the $\frac{\cosh\left(t_{\mathrm{FM}}/\Lambda_{\mathrm{m}}\right)-1}{\sinh\left(t_{\mathrm{FM}}\right.}$ factor.

Altogether, the measured transverse voltage ΔV_{ISHE} is

$$\begin{aligned}\Delta V_{\mathrm{ISHE}} &= \Delta V_{\mathrm{ISHE}}^{\mathrm{i}} + \Delta V_{\mathrm{ISHE}}^{\mathrm{b}} = \\ &= S^{\mathrm{i}}\cdot d_y\cdot\Delta T_{\mathrm{i}}^{\mathrm{Pt/FM}} + A\cdot d_y\cdot\frac{\cosh\left(t_{\mathrm{FM}}/\Lambda_{\mathrm{m}}\right)-1}{\sinh\left(t_{\mathrm{FM}}/\Lambda_{\mathrm{m}}\right)}\frac{\Delta T_{\mathrm{FM}}}{t_{\mathrm{FM}}} \approx \\ &\approx \left(S^{\mathrm{i}}\cdot d_y\cdot\frac{\kappa_{\mathrm{S}}\kappa'_{\mathrm{FM}}R_{\mathrm{i}}^{\mathrm{Pt/FM}}}{\kappa_{\mathrm{S}}t_{\mathrm{FM}}+\kappa'_{\mathrm{FM}}t_{\mathrm{S}}} + A\cdot d_y\cdot\frac{\cosh\left(t_{\mathrm{FM}}/\Lambda_{\mathrm{m}}\right)-1}{\sinh\left(t_{\mathrm{FM}}/\Lambda_{\mathrm{m}}\right)}\frac{\kappa_{\mathrm{S}}}{\kappa_{\mathrm{S}}t_{\mathrm{FM}}+\kappa'_{\mathrm{FM}}t_{\mathrm{S}}}\right)\Delta T\end{aligned} \tag{4.10}$$

The fit of this expression to the experimental data shown in Fig. 4.8(a) provided $\Lambda_{\mathrm{m}} = 29(1)$ nm, $S^{\mathrm{i}}R_{\mathrm{i}}^{\mathrm{Pt/FM}} = 1.83(6)\times10^{-9}$ $(\mathrm{Vm^{-1}K^{-1}})\cdot(\mathrm{W^{-1}m^2K})$ and $A = 40.8(9)\times10^{-9}$ $\mathrm{V\cdot K^{-1}}$.

Given the reported order of magnitude of interfacial thermal resistances $R_{\mathrm{i}} \sim 10^{-9} - 10^{-8}$ $\mathrm{W^{-1}m^2K}$, we can establish from the fit that S^{i} order of magnitude

lies between 0.1 and 1 $\mathrm{Vm^{-1}K^{-1}}$, in agreement with previous estimations in other systems [81, 83, 270]. Concerning S^{b}, A value provides from $S^{\mathrm{b}} = 0.065(6)$ $\mathrm{Vm^{-1}K^{-1}}$ for the thinnest sample up to $S^{\mathrm{b}} = 0.46(4)$ $\mathrm{Vm^{-1}K^{-1}}$ for the thickest one.

In literature, Λ_{m} at room temperature corresponding to other ferrimganetic oxides can be found: $\Lambda_{\mathrm{m}} = 17$ nm for half-metal Fe_3O_4 [284] or $\Lambda_{\mathrm{m}} \sim 100$ nm for insulating YIG [270]. This values are similar to the one obtained for maghemite, reassuring this material's potential in spin-caloritonics applications. However, one must be cautious in this comparison, because those works only considered the influence of the thermally excited magnon propagation length on the thickness dependence of LSSE; *i*LSSE, thickness dependence of thermal conductivity and variation of thermal drops on thickness were not addressed.

All in all, the relative contribution of each source —*b*LSSE and *i*LSSE— to the total ΔV_{ISHE} output in a typical range of FM thicknesses for an experiment in which a total ΔT is established, could finally be calculated. For this, $\Delta V_{\mathrm{ISHE}}^{\mathrm{i}}$ and $\Delta V_{\mathrm{ISHE}}^{\mathrm{b}}$ generated per Kelvin of total thermal drop ΔT were calculated from Eq. 4.6b (i.e., the two addends between brackets in Eq. 4.10). The result is shown in figure 4.8(b). As one could expect, the influence of $R_{\mathrm{i}}^{\mathrm{Pt/FM}}$ is greater for thinner samples and consequently *i*LSSE contribution to the overall signal reduces as t_{FM} is increased, and reversely for *b*LSSE. We found that bulk component dominates in the range of thickness of the samples, due to the reduced value of the interfacial thermal resistance compared to that of the FM layer. Despite this, the interfacial contribution is by no means negligible against *b*LSSE, as it represents from $\approx 33\%$ to $\approx 12\%$ of the total voltage.

4.1.3 Temperature dependence

LSSE dependence on temperature brings up fundamental issues about the mechanisms controlling the effect; it comprises the corresponding variation with temperature of several parameters that characterize the process at three levels: (a) heat current to spin current conversion efficiency, both in the FM layer and at FM/NM interface; (b) spin angular momentum transference efficiency at the

FM/NM interface; and (c) spin current to charge current conversion efficiency in the NM layer. The main parameters to be included in the analysis of the LSSE temperature dependence are:

1. The involved thermal conductivities: their evolution with temperature plays a major role as it determines the active temperature differences ΔT_{FM} and $\Delta t_{\mathrm{i}}^{\mathrm{Pt/FM}}$. In other words, they determine the fraction of the thermal energy which is actually transferred to the spin current, and, in the end, converted into electrical energy.
2. Resistivity of the NM layer and conduction regime, which determine the main ISHE mechanism and thus the scaling of the spin Hall angle θ_{SH}, i.e., the efficiency in the spin-to-charge conversion at NM.
3. Spin diffusion length of the NM material λ_{NM}: at the FM/Pt interface, the spin polarization is maximum and diffuses away inside NM layer. The value of this mechanism length scale in relation with NM thickness strongly influences the measured charge current.
4. In the FM, the competition between magnon propagation length Λ_{m}, which increases on decreasing temperature (enhancing the LSSE), and magnon population, which decreases on decreasing temperature as it is given by the Bose-Einstein distribution (reducing the LSSE).
5. Spin mixing conductance $g_{\uparrow\downarrow}$, determined by the exchange interaction at the interface: it quantifies the efficiency in the transference of spin angular momentum across the NM/FM interface. However, it has been reported that temperature has little influence on this paramenter in ferrimagnetic/Pt structures such as YIG/Pt or Fe_3O_4/Pt. [285]

As we see, temperature dependence is quite complex, not readily analyzable in quantitative o even qualitative terms. In this work, this dependence was measured for a 40 nm-thick sample of γ-Fe_2O_3 covered by a 6.5 nm-tick layer of Pt for spin-to-charge detection by ISHE. The sample was deposited on an MgO (001) substrate.

The obtained $\Delta V_{\mathrm{ISHE}}/\Delta T$ is displayed in Fig. 4.9(a); it increases with

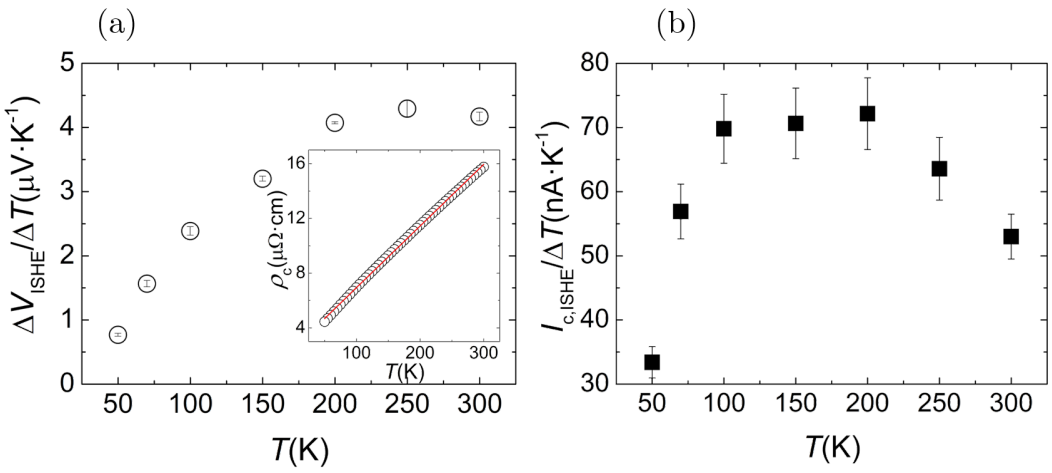

Figure 4.9 (a) Experimental data of $\Delta V_{\mathrm{ISHE}}/\Delta T$ dependence on temperature of γ-Fe_2O_3(40nm)/Pt(6nm) bilayers. The inset shows the temperature dependence of Pt thin film resistivity. (b) ISHE charge current per Kelvin ($I_{\mathrm{c,ISHE}}/\Delta T$) dependence on temperature.

temperature until $T \approx 250$ K, when it reaches a local maximum. This kind of dependence has been ascribed in other ferrimagnetic insulators to the dominance of the increase of magnon population over the decrease of magnon diffusion length until the maximum, when the trend inverts [92, 286]. Besides, this behavior points out that the magnon diffusion length in maghemite must be in the same order of magnitude of the thickness of the measured sample, i.e., tens of nanometers, as already known from the thickness dependence study.

In order to separate the Pt electrical resistivity ρ_{c} contribution to the dependence by Ohm's law, we measured ρ_{c} in the same range of temperature. The data, plotted in the inset of Fig. 4.9(a), followed a linear dependence on T. Using this measurement we calculated the ISHE charge current per Kelvin $I_{\mathrm{c,ISHE}}/\Delta T$, as illustrated in 4.9(c). Three different regions can be identified: the current increases from low temperature up to ~ 100 K, it remains around a balance value in the range from $\sim 100K$ to $\sim 200K$ when it start decreasing. Those regions can be assigned to the three scenarios previously indicated, namely: the dominance of the magnon population rise with temperature over the decrease of Λ_{m} at low temperatures, the

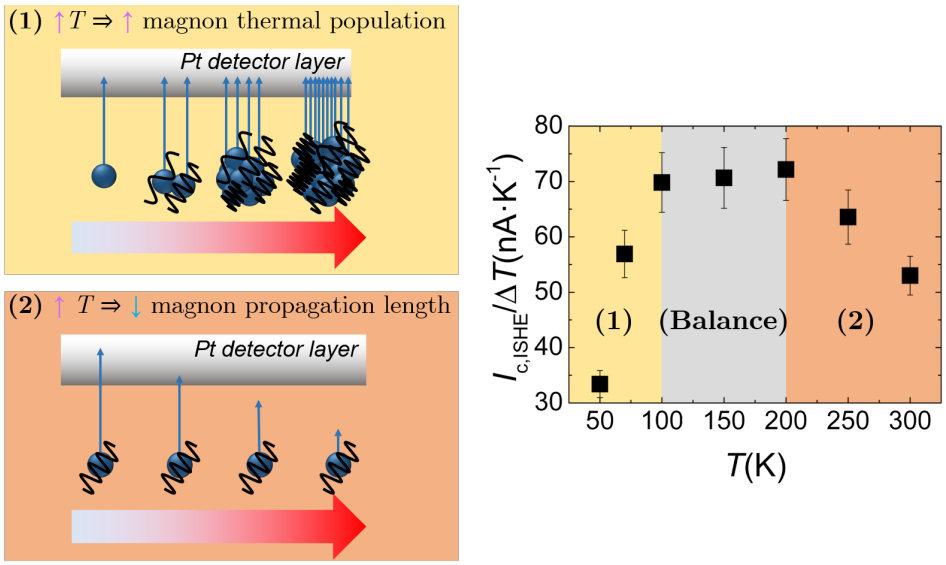

Figure 4.10 Magnon mechanisms modulating the thermal dependence of LSSE and their influence on $I_{\mathrm{c,ISHE}}/\Delta T$ at different temperature regions.

attainment of a balance between both mechanisms, and the predominance of Λ_{m} decrease at higher temperatures. Both mechanisms as well as their influence in measured $I_{\mathrm{c,ISHE}}/\Delta T$ are sketched in Fig. 4.10.

A more accurate analysis takes into account the variation of the thermal differences ΔT_{FM} and $\Delta T_{\mathrm{i}}^{\mathrm{Pt/FM}}$ driving LSSE due the change of κ'_{FM} with temperature. In other words, in order to compare ISHE voltage and charge current at different temperatures it is advisable to do so at the same exciting conditions, i.e., same ΔT_{FM} and $\Delta T_{\mathrm{i}}^{\mathrm{Pt/FM}}$ [287, 288]. To this end, we calculate Δt_{FM} for the different temperatures employing the $\kappa'_{\mathrm{FM}}(T)$ values measured in the previous section for the thinnest sample, and use it for normalization of the ΔV_{ISHE} measured at each temperature, obtaining $\Delta V_{\mathrm{ISHE}}/\Delta T_{\mathrm{FM}}$. Additionally, we also calculate $I_{\mathrm{c,ISHE}}/\Delta T_{\mathrm{FM}}$. Both curves are shown in Fig. 4.11. Note that *i*LSSE contribution in still neglected by doing is, which for a 40 nm-thick maghemite thin film is a rough approximation (see 4.8(b)).

Using this scaling, identification of three regions is also possible, as illustrated

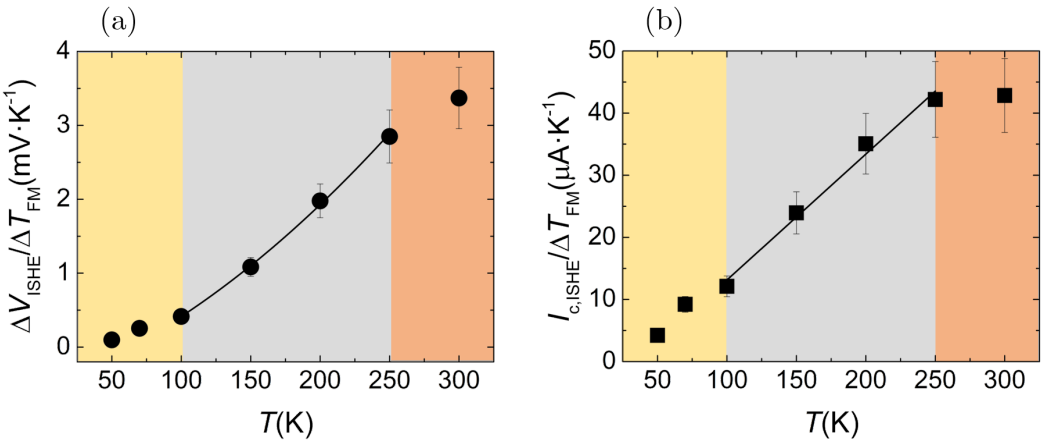

Figure 4.11 (a) Experimental data of $\Delta V_{\mathrm{ISHE}}/\Delta T$ dependence on temperature of γ-Fe_2O_3(40nm)/Pt(6nm) bilayers. Solid line is a quadratic fit in the intermediate range of temperature. The inset shows the temperature dependence of Pt thin film resistivity. (b) ISHE charge current per Kelvin ($I_{\mathrm{c,ISHE}}/\Delta T$) dependence on temperature. Solid line is a linear fit in the intermediate range of temperature.

in Fig. 4.11: inside each one, the ISHE current dependence on temperature can be approximated to a linear behavior, featuring different slopes for different regions. This can be explained in terms of the SOC mechanism governing the ISHE in Pt combined with the already mentioned magnon-related mechanisms: according work of Sagasta *et al.* and given the measured range of resistivities, the conduction regimen of the Pt layer changes from super-clean at $T = 50$ K to intermediate at $T = 300$ K; ISHE dominant mechanism changes accordingly from intrinsic (with $\theta_{\mathrm{SH}} \propto \rho_{\mathrm{c}}$) to skew-scattering ($\theta_{\mathrm{SH}}$ independent of ρ_{c}) [47, 52, 283]. Hence, at low temperature the ISHE current increases due mainly to increase in magnon population (first region, yellow color in Fig. 4.11); when Pt enters the intrinsic regimen, θ_{SH} scales linearly with ρ_{c}, which in turn increases linearly with temperature, giving the observed linear dependence of ISHE current (see Fig. 4.11(b), grey-colored region). Accordingly, the ISHE voltage follows meanwhile a parabolic dependence on T ($\propto \rho_{\mathrm{c}}^2$), as shown in Fig. 4.11(a), grey-colored region. Gradually, both magnon-related mechanisms equilibrate reducing the slope until a point in which the decrease of magnon diffusion length dominates over the increase

of magnon population and also counteracts the effect of increasing θ_{SH} at the highest temperature (orange-colored region in Fig. 4.11).

4.2 Static experiment using the current-heating spin Seebeck effect approach

In this section, the results of the study of LSSE in γ-Fe_2O_3/Pt bilayers by means of an alternative method are reported. This method is often referred to as current-heating or Joule spin Seebeck effect (JSSE), explained in Section 2.5.1. In this technique, NM material (Pt in the case described here) holds a triple role: (1) spin current detector by ISHE spin-to-charge conversion, (2) heater, and (3) thermometer. All the experiments were performed at base temperature of $T = 300$ K.

4.2.1 Sample preparation

The samples to be studied by this method were prepared following a top-down approach, i.e., first, thin film were deposited and after that optical lithography was carried out to get the desired geometry. Two twin thin films were deposited at the same time, in order to use the second one for comparison with the heater method (results of the comparison are presented in Section 4.3).

γ-Fe_2O_3/Pt bilayers were deposited on (001) MgO substrates by PLD and *in situ* sputtering, as described in previous sections. Dimensions of the substrates were $5\times5\times0.5$ mm^3. Thickness of maghemite layer was $t_{FM} = 55$ nm, and Pt layer was 3.5 nm thick. γ-Fe_2O_3 thickness was determined from the period of Laue oscillations (see Fig. 4.12(a) for the XRD pattern around (002) MgO substrate Bragg peak and Fig. 4.12(b) for the fit of Laue oscillations positions), whilst Pt thickness was obtained from the fit of a simulation to the XRR measurement (Fig. 4.12(c)).

One of the samples —the one in which JSSE was studied— was patterned into a Hall bar of 100 μn in width and 1.6 mm in length by the optical lithography procedure described in Section 2.4. Metallic pads were deposited by a lift-off process.

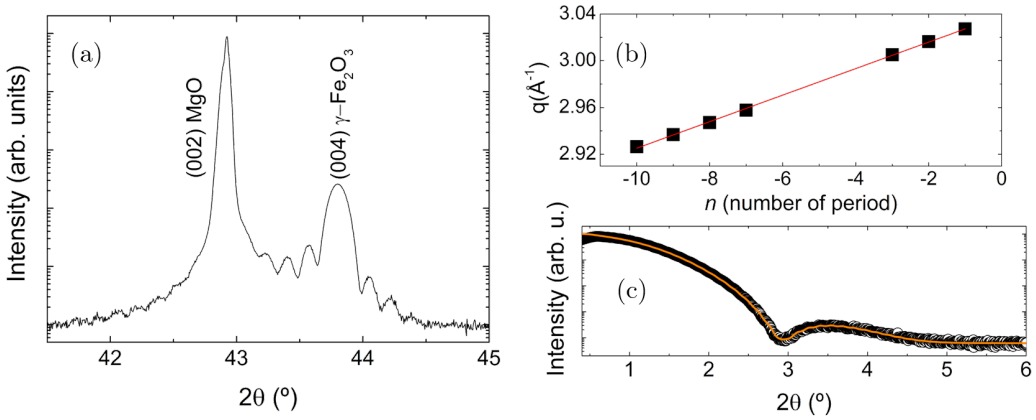

Figure 4.12 Structural characterization by XRD and XRR of the γ-Fe_2O_3/Pt sample which was studied by the JSSE method, as deposited as thin films, i.e., prior to optical lithography process. (a) XRD pattern around the (002) Bragg peak of the MgO substrate. (b) Position of the Laue oscillations maximums in q-space an linear fit. (c) XRR measurement and fit of the simulated pattern.

4.2.2 Pt thermometer calibration

Next step was the calibration of the Pt strip to be used as thermometer. To this end, its electrical resistance as a function of temperature was measured: different temperatures were carefully stabilized and $I(V)$ curves (not shown) were recorded at each one, by measuring the longitudinal voltage ΔV_{R} established by the injection of an electrical current. For this calibration, the injected electrical current must be significantly lower to that later used for driving the LSSE; in other words, it must be low enough to ensure that Joule heating is negligible. We used intensity ramps between $I_{\mathrm{d}} = \pm 50\mu\mathrm{A}$.

Linear fit to the $R_{\mathrm{Pt}}(T)$ data, shown in Fig. 4.13, provided the next expression for the calibration curve:

$$R_{\mathrm{Pt}} = 0.747(4)T_{\mathrm{Pt}} + 484(2) \;\Rightarrow\; T_{\mathrm{Pt}} = \frac{R_{\mathrm{Pt}} - 484(2)}{0.747(4)} \tag{4.11}$$

This calibration enables the assessment of Pt temperature during JSSE experiments by determination of the strip resistance of Pt, through the measurement

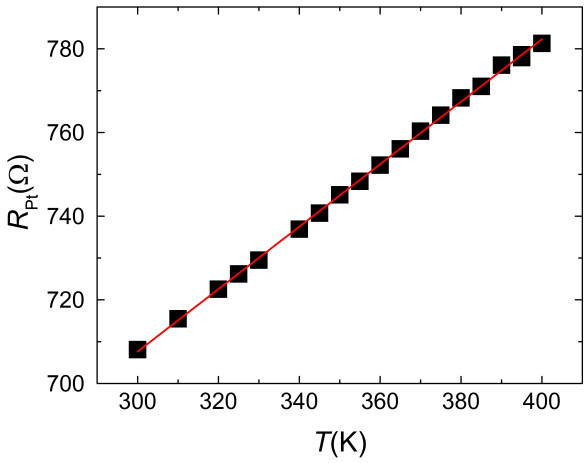

Figure 4.13 $R_{\mathrm{Pt}}(T)$ dependence of the Pt strip, to be used as thermometer calibration.

of the voltage drop between the longitudinal contacts, calculation of $R_{\mathrm{Pt}} = \Delta V_{\mathrm{R}}/I_{\mathrm{d}}$ and introduction of R into the expression 4.11. The thermal drop across the sample can be therefore determined by

$$\Delta T = T_{\mathrm{Pt}} - T \tag{4.12}$$

4.2.3 Intensity dependence of the transverse voltage

As explained in Section 2.5.1, in the employed geometry LSSE and resistive effects behave differently under oppositely directed currents: the ΔV_{ISHE} voltage is even in the dc current responsible for the Joule heating of the Pt strip, I_{d}, whilst (magneto)resistive effects are odd in I_{d}. Therefore, both phenomena can be disentangled by driving $+I_{\mathrm{d}}$ and its opposite $-I_{\mathrm{d}}$, and then adding or subtracting the respective signals. This was in detail shown in Eqs. 2.12 and 2.13.

The first experiment was the current intensity dependence of the measured transverse voltage ΔV_y, setting the angle between I_{d} and magnetic field to $\alpha = 0°$. After the application of I_{d}, a time elapse of 30 minutes was observed in order to reach the steady state. During that time, the longitudinal R_{Pt} resistance was monitored to ensure that a steady state was achieved; only then the measurement did start.

The stable value of R_{Pt} was recorded in order to determine T_{Pt}. The as-measured raw data for $\alpha = 0°$ are shown in Fig. 4.14(a). The extracted even ΔV_{ISHE} and odd ΔV_{MR} signals are plotted in Fig. 4.14(b) and (c), respectively.

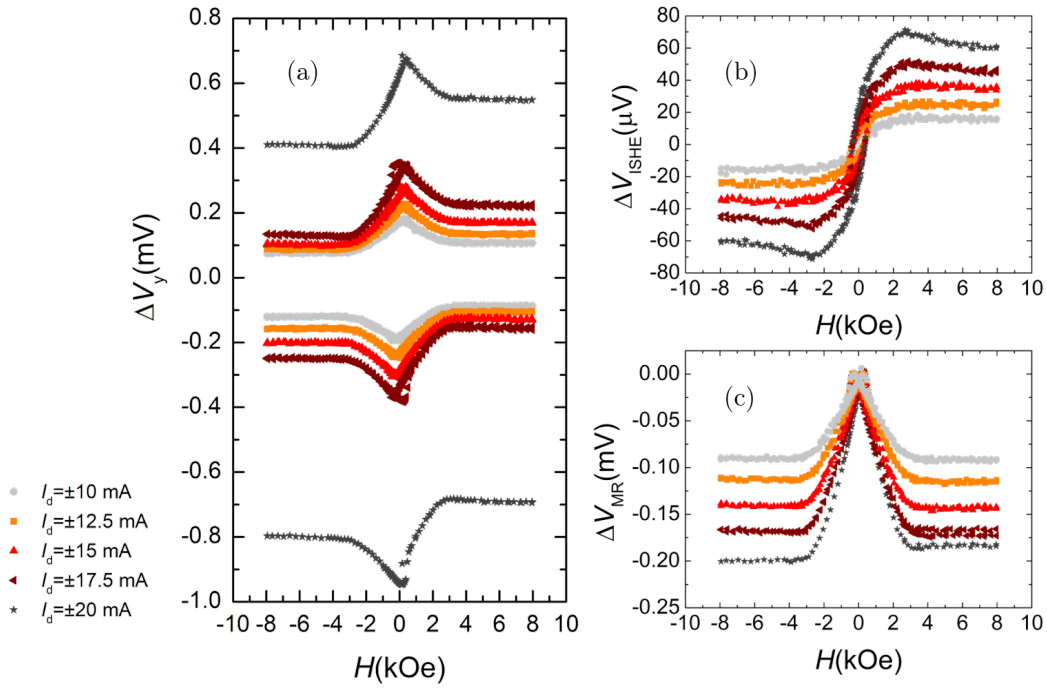

Figure 4.14 (a) Recorded transverse voltage ΔV_y on the MgO//γ-Fe_2O_3(55 nm)/Pt(3.5nm) lithographed sample upon Joule heating of the Pt strip with different intensities I_{d} in $\alpha = 0°$ configuration. (b) Addition of $+I_{\mathrm{d}}/2$ and $-I_{\mathrm{d}}/2$ to get the ISHE signal originated from LSSE. (c) Subtraction of $-I_{\mathrm{d}}/2$ from $+I_{\mathrm{d}}/2$ to get the odd signal originated from (magneto)resistive effects. The background level, which increase with I_{d} due to the consequent increase of the transverse resistance, has been removed in (b) and (c).

The Longitudinal spin Seebeck effect

As LSSE is proportional to the thermal gradient through the sample, the expected ΔV_{ISHE} dependence will be quadratic in I_{d}, given that ΔT is proportional to the heating power $R_{\mathrm{d}} I_{\mathrm{d}}^2$. For the sake of comfort in reading, we copy here Eq. 2.11, which accounts for ΔV_{ISHE} dependence on I_{d} and α, defined as the angle between

I_d flow direction and the applied magnetic field:

$$\Delta V_{ISHE} \propto I_d^2 R_d \cos\alpha = 2 I_d^2 R_{Pt} \cos\alpha \tag{4.13}$$

Note that the electrical resistance along the total length of the strip (R_d) is twice the calibration resistance R_{Pt}, because the former is established between the outermost contacts between which I_d is injected, and the latter is measured between inner contacts, separated by half the distance. Thus, $R_d = 2R_{Pt}$. In Fig. 4.15(a) a scheme with the definitions of the different resistances is provided.

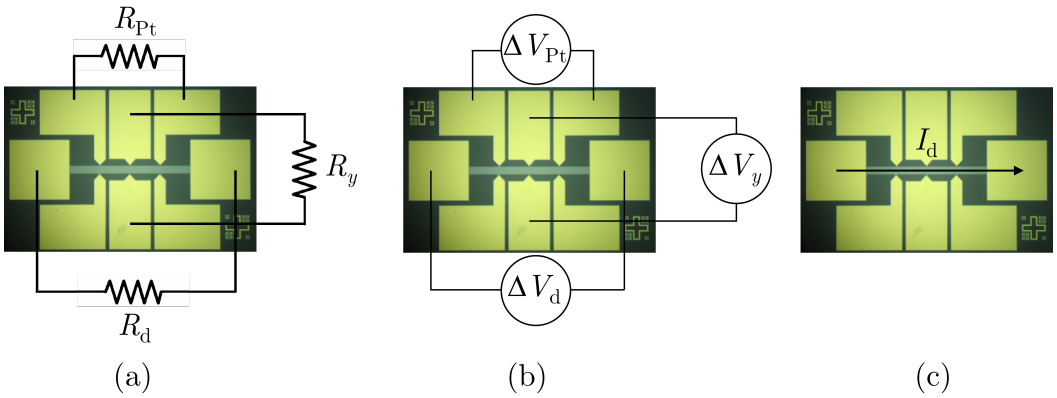

Figure 4.15 Definition of the electrical magnitudes involved in the JSSE experiments: (a) resistances, (b) voltages, and (d) charge current.

In this experiment, we set $\alpha = 0°$ for every I_d. Therefore, ΔV_{ISHE} scales as $\propto I_d^2 R_{Pt}$. It must be noted that R_{Pt} changes upon heating the strip, i.e., $R_{Pt} = R_{Pt}(I_d^2)$. In fact, this is the effect that allows the simultaneous use of Pt for on-chip thermometry, besides heating and spin-to-charge current conversion.

Besides, although the transverse resistance R_y will also increase upon heating as $R_y(I_d^2)$, its influence will be contained in odd powers of I_d^2 [128], since

$$V \propto I_d R_y \propto I_d I_d^2 \tag{4.14}$$

Thus, this contribution will be canceled in the even signal $\Delta V_{ISHE} = 1/2[\Delta V_y(I_d) +$

$\Delta V_y(-I_\mathrm{d})]$.

As evidenced in Fig. 4.14(b), addition of $+I_\mathrm{d}$ and $-I_\mathrm{d}$ signals to obtain the even ΔV_ISHE reveals the hysteretic dependence on magnetic field expected from LSSE/ISHE phenomena. To confirm the origin of this even signal on thermal effects, in Fig. 4.16 we plot the $\Delta V_\mathrm{ISHE}(I_\mathrm{d})$ and $\Delta V_\mathrm{ISHE}(I_\mathrm{d}^2 R_\mathrm{d})$ dependences. There, $\Delta V_\mathrm{ISHE}(I_\mathrm{d})$ magnitude has been calculated from ΔV_ISHE values at saturated fields $+H_\mathrm{S}$ and $-H_\mathrm{S}$ as $= 0.5[\Delta V_\mathrm{ISHE}(+H_\mathrm{S}) - \Delta V_\mathrm{ISHE}(-H_\mathrm{S})]$. As evidenced in Figs. 4.16(a) and (b), ΔV_ISHE follows a parabolic dependence on I_d and linear on $R_\mathrm{d} I_\mathrm{d}^2$, which asserts its thermal origin on the Joule heating (Eq. 4.13).

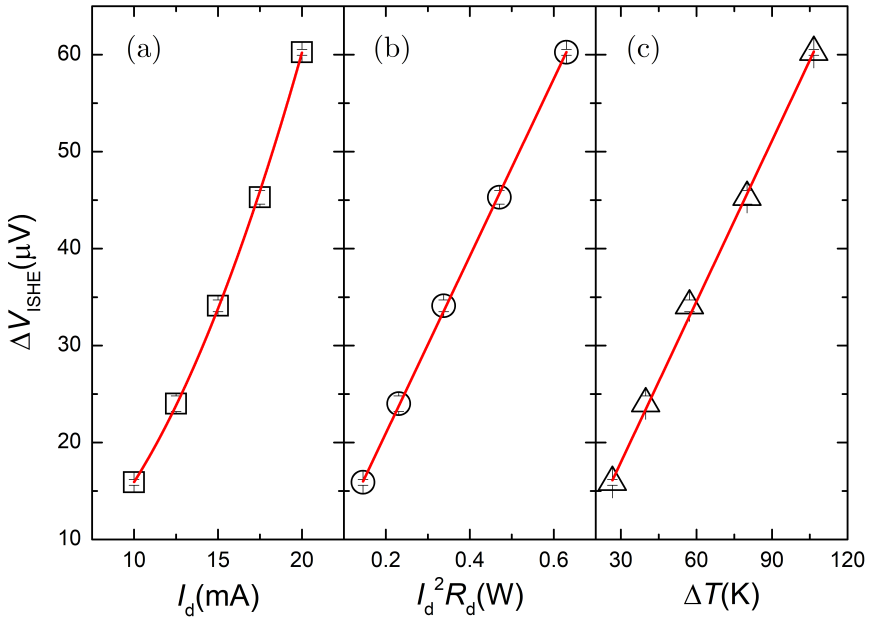

Figure 4.16 (a) ΔV_ISHE magnitude dependence on the heating current I_d and second power fit in a γ-Fe_2O_3(55 nm)/Pt(3.5 nm) heterostructure. (b) ΔV_ISHE magnitude dependence on the heating power $I_\mathrm{d}^2 R_\mathrm{d}$ and linear fit. (c) ΔV_ISHE magnitude dependence on the thermal drop across the sample ΔT, calculated as expressed in Eq. 4.12 as the difference between Pt and environment temperatures.

Thanks to the calibration performed in the previous section, the Pt strip can be

also used as temperature sensor, which enables the plot of ΔV_{ISHE} as a function of ΔTa, alternatively to the ΔV_{ISHE} representation against $I_{\mathrm{d}}^2 R_{\mathrm{d}}$. Since the temperature rise is caused by the Joule heating, ΔT is proportional to $I_{\mathrm{d}}^2 R_{\mathrm{d}}$, meaning that both dependences must be equivalent. As explained before, the longitudinal resistance R_{Pt} is monitored from the moment that I_{d} is applied. After half an hour, R_{Pt} reaches an steady value, meaning that the Joule heating is also steady and the measurement can be performed. This final value of R_{Pt} is recorded and then introduced into the calibration curve (Eq. 4.11), thereby obtaining the Pt temperature T_{Pt}. In this experiment, the ambient temperature is set to $T = 300$ K, so we estimate the thermal rise across the sample as $\Delta T = 300 - T_{\mathrm{Pt}}$. Note that the assumption that MgO bottom side is at $T = 300$ K was made. In 4.16(c), ΔV_{ISHE} magnitude is depicted as a function of the thermal rise ΔT. As expected from LSSE phenomena and already checked with $I_{\mathrm{d}}^2 R_{\mathrm{d}}$, the ΔV_{ISHE} depends linearly on ΔT.

From the value of the $\Delta V_{\mathrm{ISHE}}(\Delta T)$ linear fit slope, the standard spin Seebeck coefficient defined in Eq. 1.32 can be computed. Using the sample thickness t_z and distance between transverse pads ($l_y = 100$ μm), the calculated coefficient was $S_{zy} = 2.76(3)\mu\mathrm{V\,K}^{-1}$.

The Spin Hall Magnetoresistance

Let us now turn into the odd signal, attributed to resistive effects. ΔV_{MR} features a peak around each coercive field of γ-Fe_2O_3, thus showing hysteresis for the increasing and decreasing field operation (4.14(c)). Above saturation field of γ-Fe_2O_3, it remains constant. There are three possible sources that may contribute to this signal [99, 128, 129]:

1. The recently discovered spin Hall magnetoresistance (SMR).
2. The conventional anisotropic magnetoresistance originated in Pt due to an hypothetical magnetic proximity effect (MPE).
3. A contribution from the longitudinal voltage due to a possible misalignment of the transverse contacts.

Thanks to the accurate geometry achieved by optical lithography process, with sharp

contacts between pads and strip, the cross coupling influence can be neglected. Concerning, AMR stemmed from MPE, it has been already mentioned that MPE reduces to insignificant values if Pt is deposited at room temperature [264, 265]. Moreover, it has been shown in similar YIG/Pt and γ-Fe_2O_3/Pt heterostructures that in this kind of experiment the influence of MPE triggered AMR in the observed behavior can be excluded, while SOC (SHE and ISHE) plays the crucial role [99, 129, 289, 290]. All in all, the phenomena observed in Fig. 4.14(c) is legitimately ascribed to the SMR.

It is convenient to introduce now the definitions of transverse and longitudinal resistivities employed in the used geometry to parametrize the SMR [36]. The longitudinal resistivity, denoted as ρ_{xx}, is:

$$\rho_{\text{long}} \equiv \rho_{xx} = \frac{\Delta V_x w t_{\text{Pt}}}{l_x I_{\text{d}}}, \tag{4.15}$$

where l_x is the separation between the contacts to measure ΔV, w is the width of the Hall bar, and t_{Pt} denotes the Pt thickness. As for the transverse resistivity ρ_{xy}

$$\rho_{\text{trans}} \equiv \rho_{xy} = \frac{\Delta V_y t_{\text{Pt}}}{I_{\text{d}}} \tag{4.16}$$

where $\Delta V_x \equiv \Delta V_{\text{Pt}}$ as defined in Fig. 4.15(b).

The SMR ratio is here calculated as

$$\frac{\Delta\rho_{xy}}{\rho} = \frac{\rho_{xy}(H = H_{\text{S}}) - \rho_{xy}(H = 0)}{\rho} = \frac{\rho_{xy}(H = H_{\text{S}})}{\rho}, \tag{4.17}$$

where ρ is the intrinsic resistivity of the NM (Pt), and plotted against I_{d}, $I_{\text{d}}^2 R_{\text{Pt}}$ and T_{Pt} in Fig. 4.17. The obtained curves do not follow a monotonic behavior, but show a local maximum instead.

According to theory there are three parameters that may potentially contribute to this variation: the spin Hall angle θ_{SH}, the Pt spin diffusion length λ_{Pt} and the spin mixing conductance $g_{\uparrow\downarrow}$ [100, 289]. The observed trend of the curve is the result of the competition between them. On the one hand, the range of resistivities

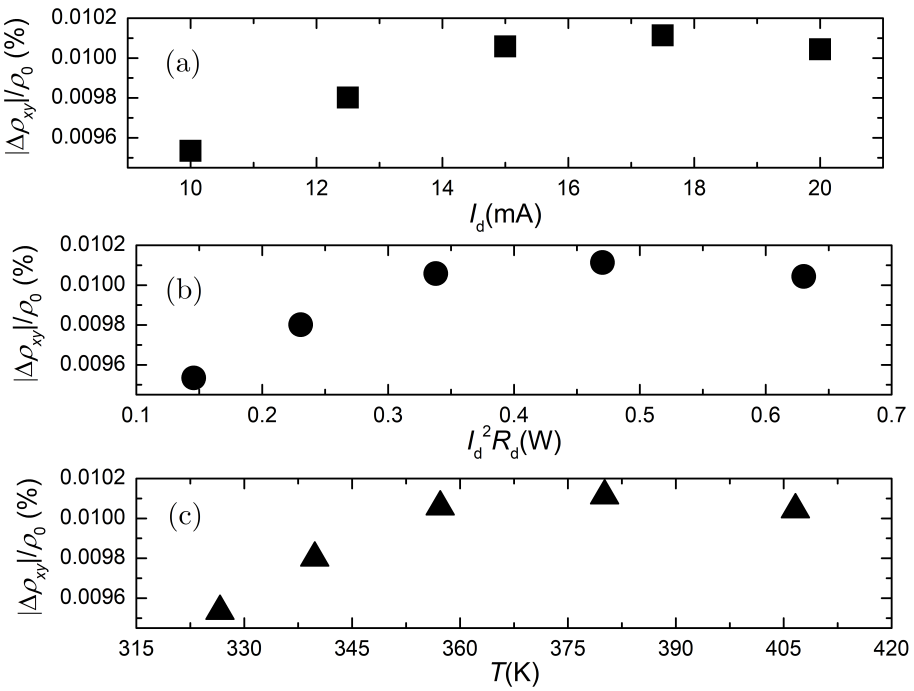

Figure 4.17 (a) Dependence of the SMR ratio of the transverse resistivity, $\Delta\rho_{xy}/\rho$, on heating current I_d in a γ-Fe_2O_3(55 nm)/Pt(3.5 nm) heterostructure. (b) $\Delta\rho_{xy}/\rho$ dependence on the heating power $I_\mathrm{d}^2R_\mathrm{d}$. (c) $\Delta\rho_{xy}/\rho$ on the Pt temperature.

exhibited by the Pt corresponds to the intrinsic regime of ISHE [63], entailing that the spin Hall angle scales as $\theta_\mathrm{SH} \propto \rho$. In the calibration it was determined that Pt resistivity increases linearly with temperature. On the other hand, it has been shown in Ref. [289] that this dependence in YIG/Pt structures is mainly governed by the variation of λ_Pt with temperature as $\lambda_\mathrm{Pt} \propto T^{-1}$, according to Elliot-Yafet mechanism of spin relaxation by spin-orbit scattering [289], which is the predominant mechanism for spin diffusion in Pt [63]. Finally, respecting $g_{\uparrow\downarrow}$, Czeschka *et al.* showed by spin-pumping experiments that temperature has little influence on it in other ferrimagnetic/Pt structures such as YIG/Pt or Fe_3O_4/Pt [285].

4.2.4 Angular dependence of the transverse voltage

In-plane angular dependence of the transverse odd and even voltages brings insight into the mechanisms triggering them. In particular, it allows to assure their respective origins in LSSE and SMR. We study this dependence by setting $I_d = 10$ mA and varying α by 30°-steps. Both polarizations of I_d were recorded for each angle value before moving to the next one, in order to avoid deviations of α between both directions of I_d.

The LSSE angular dependence

We start with the study of the in-I_d even signal, which is attributed to the ISHE voltage arising from the LSSE triggered by Joule heating. Due to the detection geometry of ISHE, ΔV_{ISHE} voltage is proportional to the sine between the applied magnetic field (which determines the spin polarization in Eq. 1.26) and the direction in which the voltage is measured. As we are detecting the transverse voltage (with respect the heating current I_d), this angle is complementary to the in-plane angle α. Hence, we expect $\Delta V_{ISHE} \propto \cos\alpha$, as reflected in Eq. 4.13.

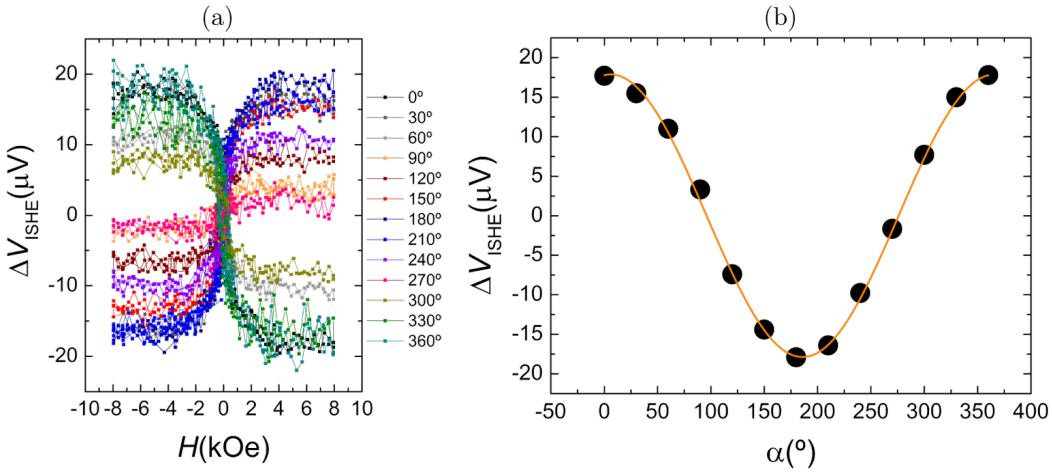

Figure 4.18 (a) ΔV_{ISHE} measured in a γ-Fe_2O_3(55 nm)/Pt(3.5 nm) structure by current heating induced SSE using $I_d = \pm 10$ mA. (b) Dependence of ΔV_{ISHE} magnitude on the angle between I_d direction and the applied magnetic field: data and fit to a cosine function.

In Fig. 4.18(a) the measured $\Delta V_{\mathrm{ISHE}}(H)$ loops for each value of α are displayed. As explained before, ΔV_{ISHE} values have been extracted as $\Delta V_{\mathrm{ISHE}} = 1/2[V_y(+I_{\mathrm{d}}) + V_y(-I_{\mathrm{d}})]$; the individual raw measurement for each I_{d} direction and angle are not shown. The magnitude of ΔV_{ISHE} (calculated as half the difference between the saturation voltages) as a function of α is depicted in Fig. 4.18(b). It perfectly follows the cosine dependence, as evidenced by the presented fit. This fact further ensures the ISHE origin of the measured voltage and, together with the even behavior in I_{d}, asserts its thermal root in LSSE.

Finally, it might be worth mentioning that a slight mispositioning of α can be detected in Fig. 4.18(b); from the fit, it is quantified to be $\Delta\alpha = 6.0(8)^{\circ}$. This is due to a misalignment of the sample in the holder and probably also to a slight deviation in the calibration of the angular position of the holder itself.

The SMR angular dependence

Next, we focus on the in-I_{d} odd signal. In Fig. 4.19(a) we represent, for each α value, the field dependence of the transverse resistivity, which has been calculated as defined in Eq. 4.16 from the odd voltage $\Delta V_{\mathrm{MR}} = 1/2[V_y(+I_{\mathrm{d}}) - V_y(-I_{\mathrm{d}})]$, the individual raw measurement for each I_{d} direction and angle are not shown. The saturated ρ_{xy} values are depicted in Fig. 4.19(b) as a function of α.

The observed in-plane angular dependence can be explained from the SMR relation with the magnetic order parameter, in this case, the magnetization orientation unit vector, $\mathbf{m}$. In the transverse configuration, this relation can be fully described as [100]:

$$\rho_{\mathrm{trans}} \equiv \rho_{xy} = \Delta\rho_1 m_x m_y + \Delta\rho_2 m_z, \tag{4.18}$$

where m_x, m_y and m_z are the projections of $\mathbf{m}$ onto the I_{d} direction (x), onto the in-plane transverse direction (in which ρ_{trans} is measured, y) and onto the out-of-plane direction (z). According to this expression, $\Delta\rho_1$ and $\Delta\rho_2$ are the maximum SMR achievable. In the experimental geometry employed here, $m_z = 0$,

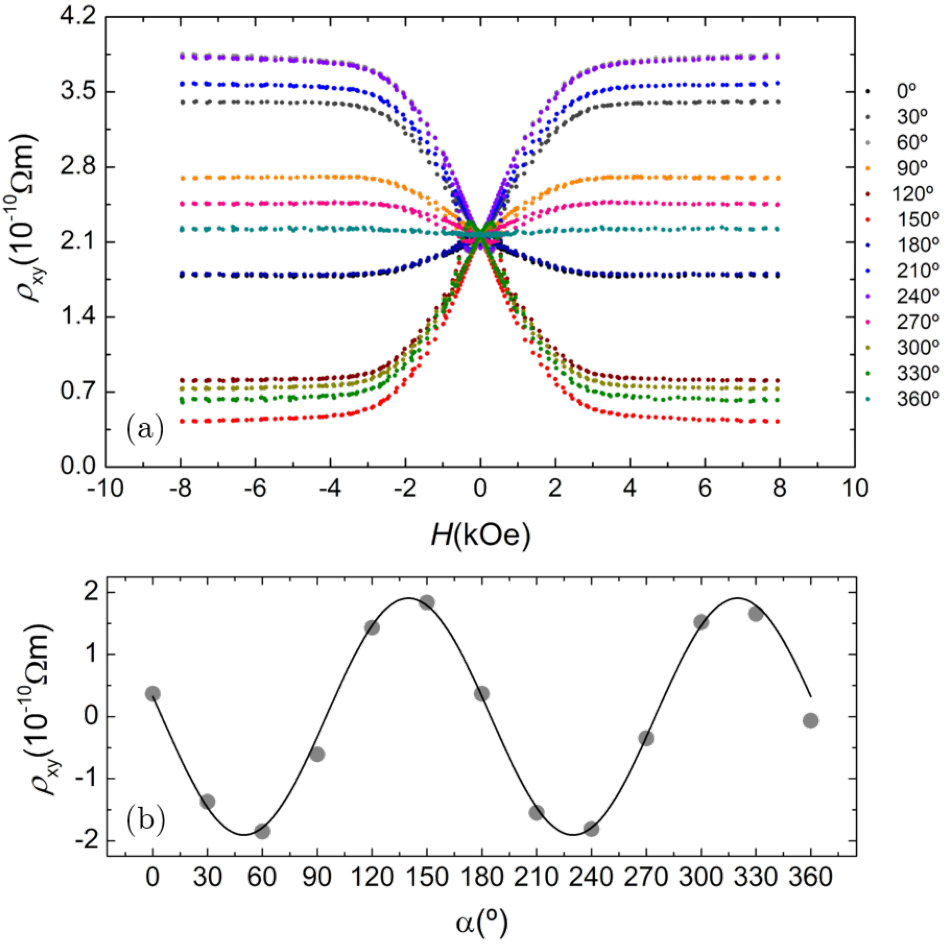

Figure 4.19 (a) Transverse resistivity ρ_{xy} as a function of the magnetic field measured in a γ-Fe_2O_3(55 nm)/Pt(3.5 nm) structure using $I_d = \pm 10$ mA. (b) Dependence of the saturation ρ_{xy} on the angle between I_d direction and the applied magnetic field: data and fit to a $1/2\sin(2\alpha)$ function (Eq. 4.19).

$m_x = \cos\alpha$ and $m_y = \sin\alpha$. Therefore, it yields

$$\rho_{\text{trans}} \equiv \rho_{xy} = \Delta\rho_1 \cos\alpha \sin\alpha = \frac{1}{2}\Delta\rho_1 \sin 2\alpha. \tag{4.19}$$

Accordingly, expression in Eq. 4.19 is fitted to the experimental data in Fig. 4.19(b), which follows the expected $\sin 2\alpha$ dependence. The fit provides a value for

the SMR $\Delta\rho_1 = -3.8(2) \times 10^{-10}\Omega\,\mathrm{m}$. The slight mispositioning already detected in the JSSE fit is quantified to be $\Delta\alpha = 9(2)°$. This mispositioning is the reason why, in the previous section, we observed a nonzero SMR signal even though $\alpha = 0°$ (nonimal).

4.2.5 Angular dependence of the longitudinal voltage

Longitudinal detection —i.e., ΔV is measured in I_d direction— is also possible; with respect to LSSE/ISHE, it is equivalent to transverse detection upon rotation of $\alpha = 90°$. However, given the geometry of the Hall bar, signal-to-noise ratio is expected to be worse due to larger background level V_d. In our setup, both ΔV_y and ΔV_x are indeed simultaneously recorded using the two channels of the *Keithley* 2182a nanovoltmeter. For completeness, here I present the results measured in the longitudinal channel.

The LSSE angular dependence

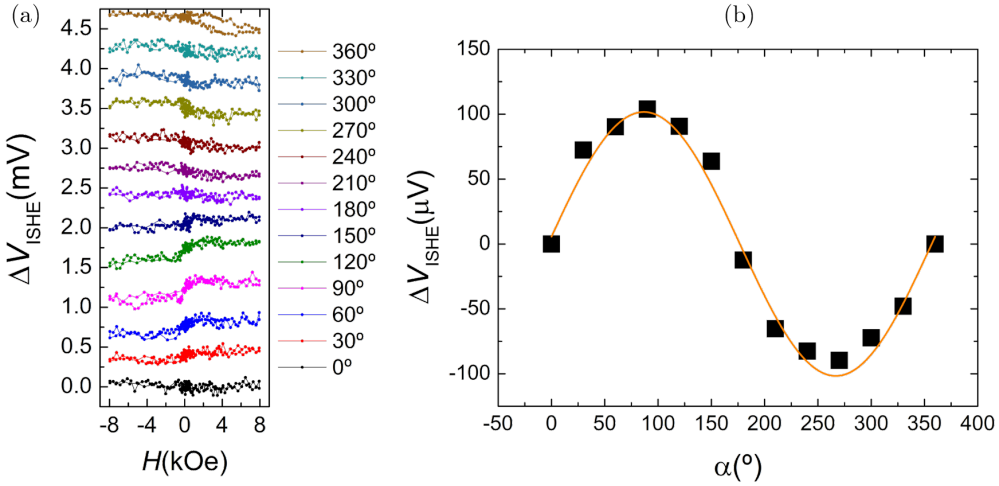

Figure 4.20 (a) ΔV_ISHE measured in a γ-Fe_2O_3(55 nm)/Pt(3.5 nm) structure by current-heating SSE using $I_\mathrm{d} = \pm 10$ mA in the longitudinal configuration. (b) Dependence of ΔV_ISHE magnitude on the angle between I_d direction and the applied magnetic field: data and fit to a cosine function.

As anticipated, signal-to-noise ratio is quite high, and thus, for the sake of clarity, in Fig. 4.20(a) the even voltages $\Delta V_{\mathrm{ISHE}} = 1/2[V_y(+I_{\mathrm{d}}) + V_y(-I_{\mathrm{d}})]$ are depicted as a function of the field one on top of each other, uniformly spaced by vertical offsets for each value of α.

In agreement to the ISHE geometry, the ΔV_{ISHE} magnitude follows a cosine dependence on α 90° out of phase, i.e., a sine dependence, as shown in Fig. 4.20(b).

The SMR angular dependence

With regard to the SMR component, in Fig. 4.21(a) the field dependence of the longitudinal resistivity, which has been calculated as defined in Eq. 4.15 from the odd voltage $\Delta V_{\mathrm{MR}} = 1/2[V_y(+I_{\mathrm{d}}) - V_y(-I_{\mathrm{d}})]$, is depicted for each α value. The individual raw measurement for each I_{d} direction and angle are not shown. The ρ_{xx} values at saturation fields are depicted in Fig. 4.21(b) as a function of α.

In the longitudinal configuration, the SMR in-plane angular dependence is formulated with respect to the magnetization unit vector, **m**, as [100]:

$$\rho_{\mathrm{long}} \equiv \rho_{xx} = \underbrace{\rho + \Delta\rho_0}_{\rho_0} + (1 - m_y^2), \tag{4.20}$$

where m_y is the projection of **m** onto the in-plane transverse direction and ρ is the normal resistivity with zero field. According to this expression, $\Delta\rho_1$ and $\Delta\rho_0$ are the parameters that determine the observed SMR. Instead of $\Delta\rho_0$, usually $\rho_0 = \rho + \Delta\rho_0$ is employed. In the experimental geometry employed here, $m_y = \sin\alpha$, and, therefore,

$$\rho_{\mathrm{long}} \equiv \rho_{xx} = \rho_0 + \cos^2\alpha. \tag{4.21}$$

We fit this expression to the experimental data shown in Fig. 4.21(b), yielding $\rho_0 = 3.19(1)\times10^{-7}\,\Omega\,\mathrm{m}$ nd $\Delta\rho_1 = 3.4(2)\times10^{-10}\,\Omega\,\mathrm{m}$. This value of $\Delta\rho_1$ is compatible within the experimental error with the one obtained in the transverse configuration.

Moreover, both $\Delta\rho_1$ and ρ_0 compare very well with those reported in literature. In Table 4.2 a brief comparison with other reported values in which Pt thickness is the same as in this study is provided. As we see, the results in this work are utterly

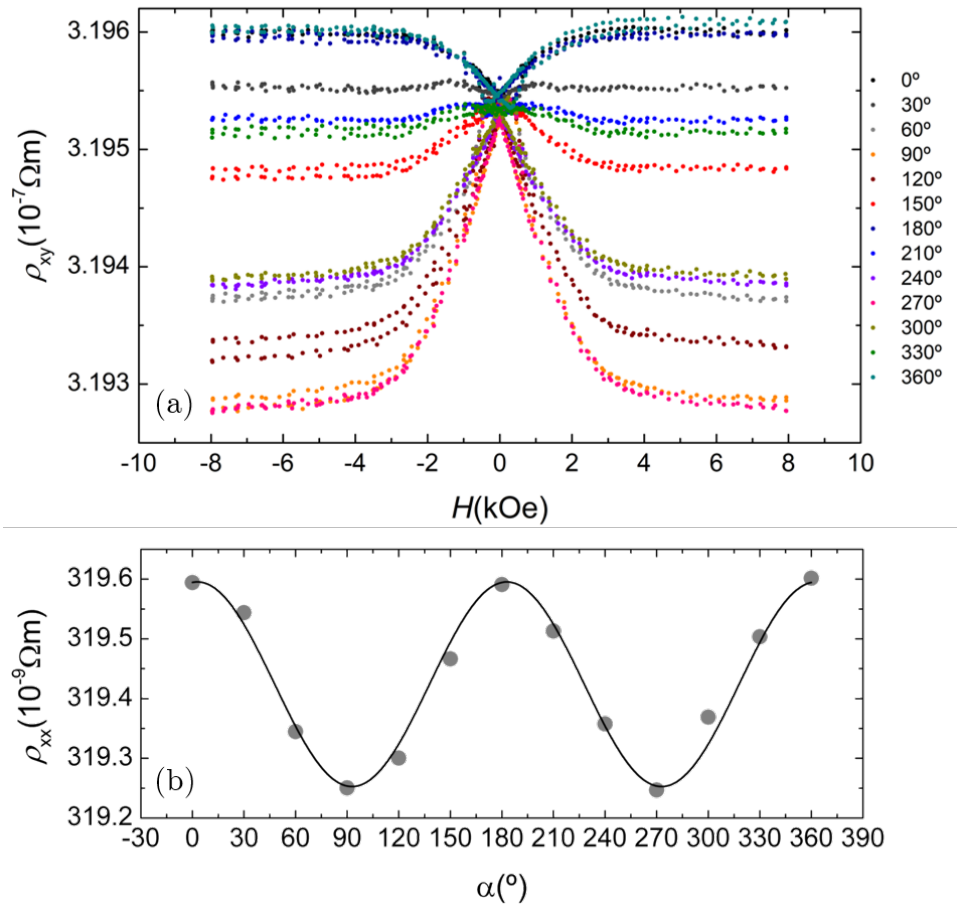

Figure 4.21 (a) Longitudinal resistivity ρ_{xx} as a function of the magnetic field measured in a γ-Fe_2O_3(55 nm)/Pt(3.5 nm) structure using $I_d = \pm 10$ mA. (b) Dependence of the saturation ρ_{xx} on the angle between I_d direction and the applied magnetic field: data and fit to a $\cos^2(\alpha)$ function (Eq. 4.21).

close to those found by Althammer *et al.* in YIG/Pt at the same temperature [101]. The comparison with the result of Dong *et al.* in Ref. [290] is less straightforward, because their experiment was performed at lower temperature. They obtain lower values of SMR in a γ-Fe_2O_3/Pt bilayer at $t = 250$ K, which is consistent with the result presented in Section 4.2.3, in which an increase of SMR upon increasing temperature was observed, until reaching a maximum at $T \approx 380$ K.

Structure	T(K)	ρ_0 (Ω m)	$\Delta\rho_1/\rho_0$	Ref.
γ-Fe_2O_3(55 nm)/Pt(3.5 nm)	300	$3.19(1) \times 10^{-7}$	1.06×10^{-3}	This work
YIG(46 nm)/Pt(3.5 nm)	300	3.066×10^{-7}	9.4×10^{-4}	[101]
γ-Fe_2O_3(40 nm)/Pt(3.5 nm)	250	-	3.8×10^{-4}	[290]

Table 4.2 Comparison of SMR result with literature.

4.3 Comparison between both methods of static heating

Finally, the comparison between both methods of triggering and detecting LSSE —external heater and heating current— is addressed. As mentioned in the previous section, a second sample was deposited simultaneously to that employed for the current heating induced LSSE; hence, both samples are identical. However, no lithography was performed out in this twin sample. The dimensions of this substrate were $2 \times 7 \times 0.5$ mm^3, adequate to the external heater method.

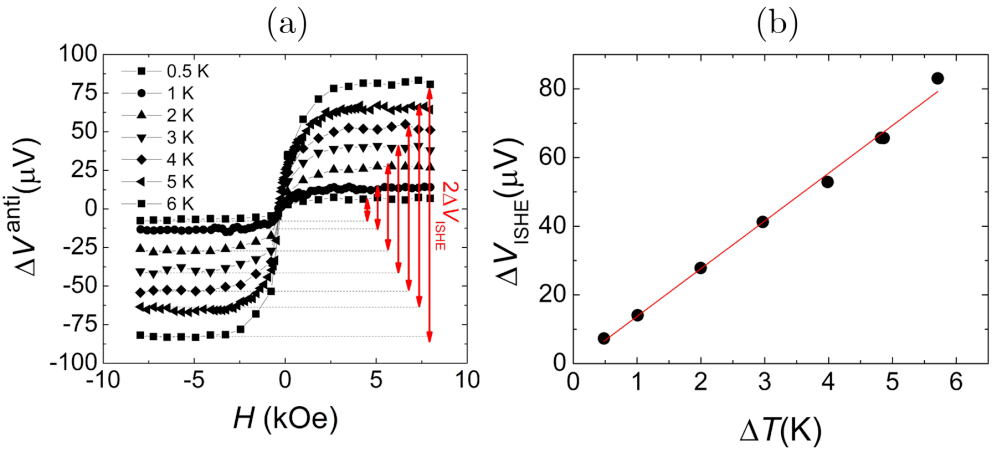

Figure 4.22 (a) Magnetic-field dependent ΔV^{anti} signals measured for a γ-Fe_2O_3(55 nm)/Pt(3.5 nm) bilayer at various applied ΔT. (b) Dependence of ΔV_{ISHE} on the applied thermal difference across the sample.

We carried out LSSE experiments using the external heater method in the second sample. Different thermal differences ΔT were established across the sample, and the output voltage in the y direction (recall the experimental geometry described in Section 2.5.1) was measured as a function of the magnetic field. The extracted

antisymmetric component is depicted in Fig. 4.22(a). The ΔV_{ISHE} magnitude is obtained from the saturation values and plotted as a function of ΔT in Fig. 4.22(b). From the linear fit, the spin Seebeck coefficient is calculated to be $S_{zy} = 1.07(9)\mu\mathrm{V\,K}^{-1}$.

This value substantially differs from the S_{zy} obtained using the current-heating approach, which was $S_{zy} = 2.76(3)\ \mu\mathrm{V\,K}^{-1}$. As it is not reasonable to accept that identical samples present different coefficients, the origin of this discrepancy must be found in some experimental issue. The most risky detail was the differences in the estimation of ΔT: in the ceramic heater approach, ΔT was directly measured by two thermocouples located at the closest-to-sample end of the heat reservoirs between which the sample is sandwiched, whilst in the Joule heating method it was estimated from the Pt resistance under the assumption that the opposite (with respect to Pt) side of the substrate was at room temperature.

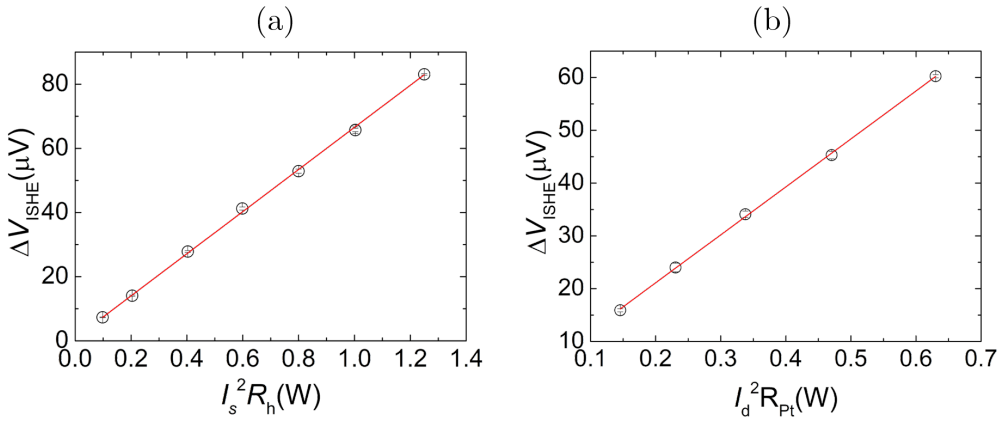

Figure 4.23 For twin γ-Fe_2O_3(55 nm)/Pt(3.5 nm) bilayers: (a) ΔV_{ISHE} as a function of the power dissipated by the ceramic heater in the external heater approach, and (b) ΔV_{ISHE} as a function of the power dissipated by the Pt strip in the current-heating method.

Given the difficulties for the determination of comparable ΔT, an alternative must be explored. In line with the heat flux measurement method [90, 287, 291], the heat flux scaling instead of thermal gradient scaling may be used in the calculation of the spin Seebeck coefficient. No mistake is made in doing so because both samples

are identical, and therefore the same applied heat flux generates identical thermal gradients (as thermal conductivities are the same). Thus, we calculate an alternative spin Seebeck coefficient which makes use of the heat flux normalization, and is defined as:

$$S'_{zy} = \frac{\Delta V_{\mathrm{ISHE}}}{d_y J_{\mathrm{Q}}} = \frac{\Delta V_{\mathrm{ISHE}}}{d_y} \frac{A}{P}, \tag{4.22}$$

where P is the power responsible for the heating; A, the area across which the heat flux flows; and d_y, the distance between contacts to measure ΔV_{ISHE}. In the external heater method, $P = I_{\mathrm{s}}^2 R_{\mathrm{h}}$, where I_{s} is the electrical current injected by the *Keithley* 236 source-meter unit and $R_{\mathrm{h}} = 2$ kΩ is the ceramic heater resistance. In the case of the heating current SSE method, $P = I_{\mathrm{d}}^2 R_{\mathrm{Pt}}$, as discussed in the previous section. In both cases, A is the Pt surface. Thus, ΔV_{ISHE} dependence on P is depicted for both methods in Fig. 4.23, and fitted to a linear dependence.

In Table 4.3 the obtained result alongside the geometrical parameters used for the computation of the alternative coefficient are gathered. As we see, using the heat flux normalization yields the same S'_{zy} coefficient for both samples, as one should expect for identical samples.

Method	$\Delta V_{\mathrm{ISHE}}/P$ ($\mu\mathrm{V W}^{-1}$)	A (mm^2)	d_y (mm)	S_{zy} ($\mu\mathrm{V K}^{-1}$)	S'_{zy} ($\mu\mathrm{V\,m\,W}^{-1}$)
External heater	65.0(7)	2×7	6.5(5)	1.07(9)	0.14(1)
Joule heating current	91(1)	1.6×0.1	0.1	2.76(3)	0.145(2)

Table 4.3 Comparison of LSSE results measured using two different methods.

This result entails that both methods are equivalent; it also demonstrates that the setup for the external heater approach is properly built in order to minimize heat leakages, validating this method.

4.4 Conclusions

In this section, LSSE under static heating in γ-Fe_2O_3/Pt bilayers has been studied using two different approaches.

First, the temperature difference making use of an external heater was employed.

A transverse voltage mirroring the hysteresis loop of magnetization was recorded upon heating the sample in the out-of-plane direction with an external ceramic heater. This voltage showed the features of ISHE phenomena an was proportional to the established thermal gradient, proving its origin on the LSSE. The obtained magnitude of the effect was maximum for maghemite preparation annealing pressure of 50 mTorr, in agreement with the optimal pressure with regards to the structural characteristics found in Chapter 3. The obtained spin Seebeck coefficient S_{zy} exceeds that of prototypical YIG, proving maghemite's potential to be used in spintronics devices.

Besides, the dependence of LSSE and thermal conductivity on maghemite thickness were studied. From the analysis of the results, the separate bulk magnon accumulation and purely interfacial contributions to the LSSE in static conditions were quantified. According to the obtained results, neither of both sources of thermal spin current can be neglected in the measured range of thicknesses (from ≈ 15 nm to ≈ 80 nm): although the bulk contribution dominates, the interfacial input represents from $\approx 33\%$ of the total voltage for the lowest thickness to $\approx 12\%$ for the thickest sample. This is a relevant result as it improves the accuracy in the interpretation of LSSE experiments, which may as well benefit the efficient design of spin caloritronic devices.

Temperature dependence of LSSE in γ-Fe_2O_3/Pt was also measured. Three different regimens were identified: domination of magnon population at low temperatures, balance at intermediate temperature, and decrease of magnon diffusion length influence at highest temperatures.

Next, LSSE and SMR were simultaneously detected using the current heating scheme. The equivalence between this method and the external heater approach was proved by using the heat flux scaling of the ISHE voltage. A heat flux-normalized spin Seebeck coefficient of $S'_{zy} = 1.4\ \mu\mathrm{V\,m\,W^{-1}}$ was obtained by both methods for twin samples, demonstrating the universality of the effect.

Chapter 5

Ultrafast Spin Seebeck effect dynamics

In this chapter, we report on the investigation of LSSE ultrafast dynamics using Terahertz Emission Spectroscopy (TES). FM/NM bilayers using FM materials with increasing degree of electrical conductivity were studied. Specifically, metallic iron, half metallic magnetite and insulating maghemite were used. The different electrical behaviors enabled the independent observation of different thermal phenomena. In all cases, Pt was employed for the NM layer.

The measurements of the ultrafast LSSE dynamics have been carried out at the Fritz Haber Institute in Berlin, in the group of Prof. Tobias Kampfrath from Berlin Freie Universität.

5.1 Introduction

Among the several methods available to generate thermal gradients in thin films, laser heating in combination with all-optical detection schemes has already provided substantial insights into the temporal evolution of the SSE with sub-picosecond resolution [82, 83]. In particular, terahertz (THz) emission spectroscopy (TES) represents both a powerful tool for time-resolved study of SSE and an opportunity

to identify new potentialities of spintronics in the elusive THz spectral window [144]. Heating on ultrafast time scales is straightforwardly achieved by illuminating the FM/NM bilayer with femtosecond laser pulses [147], as explained in Section 2.6.

In a recent work, Seifert *et al.* were able to obtain the ultrafast spin Seebeck current $J_s(t)$ from the THz signal emitted by a YIG/Pt bilayer upon photoexcitation with a femtosecond infrared laser pulse, revealing the femtosecond dynamics of the SSE [83]. They observed that thermalization of the available metal electrons determines the $\sim$ 100 fs time scale of J_s rising, and explained this in terms of a model in the frame of a sd-exchange-like coupling at the FM/NM interface. However, it must be noted that all studies of time-evolution of SSE so far utilized YIG as FM layer [81–83, 292], and thus further works with other insulating materials are necessary in order to generalize the obtained results.

Moreover, in this work the possibility of disentangling the spin-dependent Seebeck effect (SDSE) and the spin Seebeck effect (SSE) was explored. As discussed in Chapter 1, heating FM/NM bilayers may generate two differently originated spin currents depending on the electronic mobility of FM layer: SSE and SDSE spin currents, as sketched in Fig. 5.1 [24]. Whilst the SSE relies on transfer of spin angular momentun by interfacial spin torque between the magnetic moments in FM and the conduction electrons in NM, the SDSE is based on transfer across the FM/NM interface of spin-polarized electrons thermoelectrically excited [78]. In both cases, the spin flow can be detected by spin-to-charge current conversion in NM layers with sufficiently large ISHE. Thus, their separation is challenging in the steady conditions; this is the reason SSE study has been restricted to insulating FM. However, since the spin angular momentum transfer mechanisms present in the SSE and in the SDSE are different, one may expect that SSE and SDSE currents evolve very differently in time in dynamic experiments. Therefore, based on their distinctive dynamics, both effects may be separated. Additionaly, these differences should be especially pronounced when the heating stimulus is shorter than the characteristic relaxation time of each mechanism, which makes TES based on ultrafast photoexcitation a particularly promising tool for this purpose.

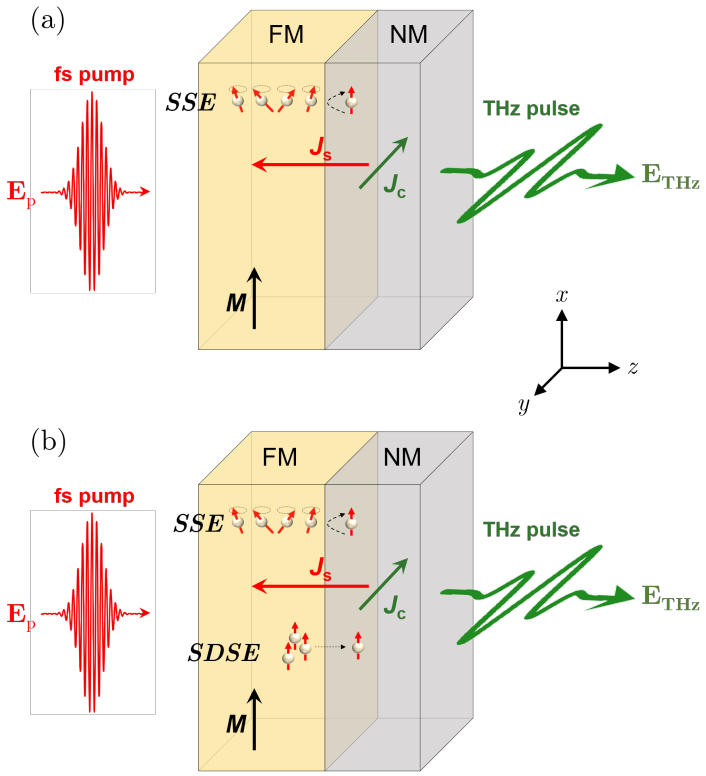

Figure 5.1 Generation of thermal spin currents upon ultrafast photoexcitation and ISHE detection by TES in a FM/NM bilayer. (a) FM is insulating, so only the magnonic contribution (SSE) is present. (b) FM is conductive, so both SSE and SDSE (conduction electrons contribution) are present.

Schematics of the TES experiment and the expected photoinduced currents using insulating and metallic FM layers are depicted in Fig. 5.1(a) and (b). The sample under study is illuminated with near-infrared femtosecond laser pulses (central wavelength of 800 nm, duration of 10 fs, energy of 2.5 nJ, repetition rate of 80 MHz) coming from a Ti:sapphire laser oscillator. The corresponding electric field is denoted as $\mathbf{E}_\mathrm{p}$. The absorbed energy from the pulses is deposited in the electronic system(s) present in the sample, exciting as a result a spin current $J_\mathrm{s}(t)$ at the FM/NM interface. This spin current is converted into a transverse charge current $J_\mathrm{c}(t)$ in the NM (Pt) by means of the ISHE, resulting in the emission of electromagnetic pulses, $\mathbf{E}_\mathrm{THz}$, with frequencies extending to the THz range (see Fig. 5.1). The THz signal is

detected by contact-free electro-optic sampling using a ZnTe crystal as detector (see Section 2.6 for details). During the experiments, sample magnetization is in-plane saturated by an external magnetic field of $\approx$ 190 mT and a dry environment is maintained by purging with a constant flow of nitrogen.

5.2 Samples structure

For the the long-range magnetically ordered material in the FM layer in the FM/NM stacks, metallic iron, half-metallic magnetite (Fe_3O_4) and insulating maghemite (γ-Fe_2O_3) were chosen. Samples were deposited on two-side polished (001) MgO substrates of dimensions $10 \times 10 \times 0.5$ mm^3.

Two samples were prepared: in the first one, 10 nm of γ-Fe_2O_3 were epitaxially

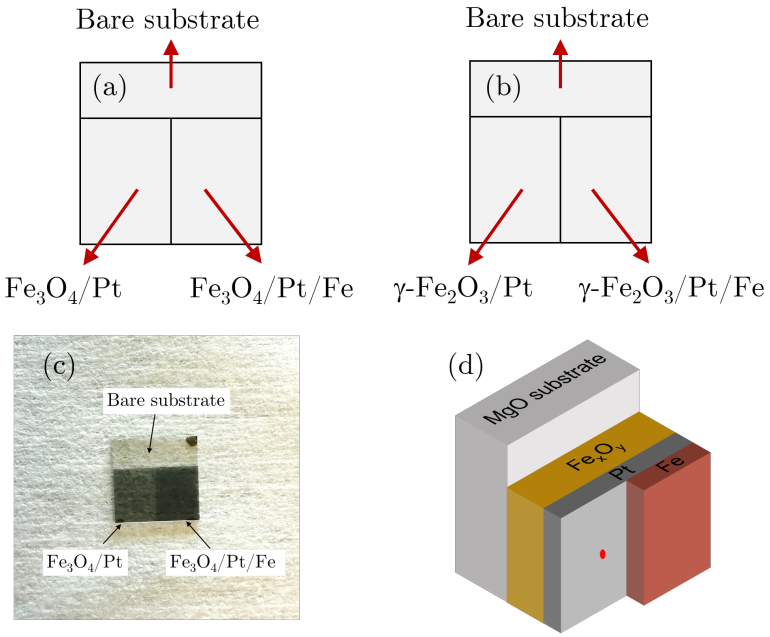

Figure 5.2 Structure of the samples used for TES: (a) Top-view distribution of the sample with Fe_3O_4. (b) Top-view distribution of the sample with γ-Fe_2O_3. (c) Top-view picture of the sample with Fe_3O_4. (d) Perspective-view of the samples structure. The red circle represents the optical laser focused on the surface.

grown covering approximately 2/3 of the substrate surface area; and, in the second one, 10 nm of Fe_3O_4 were epitaxially grown covering the same area. In both samples, a Pt film (thickness of 2.5 nm) was subsequently sputtered *in situ* onto the iron oxide region at room temperature inside the same vacuum chamber. Then, 2.5 nm-thick Fe was deposited by sputtering on half of the area covered by γ-Fe_2O_3/Pt and Fe_3O_4/Pt (approximately 1/3 of the total substrate surface area). As a result, we had adjacent γ-Fe_2O_3/Pt/Fe and γ-Fe_2O_3/Pt structures on the same one substrate; and adjacent Fe_3O_4/Pt/Fe and Fe_3O_4/Pt stacks on a second substrate. Iron was finally capped by a few nm of MgO using *in situ* PLD to prevent oxidation. As this MgO layer is not active in the experiments, it will be omitted in the sample notation.

In summary, the distribution on each substrate is indicated in Table 5.1 and schematically illustrated in Fig. 5.2(a) and (b). In Fig. 5.2(c) a picture of one of the actual samples is provided.

Substrate 1		Substrate 2	
Area	Structure	Area	Structure
1/3	Bare substrate	1/3	Bare substrate
1/3	Fe_3O_4/Pt	1/3	γ-Fe_2O_3/Pt
1/3	Fe_3O_4/Pt/Fe	1/3	γ-Fe_2O_3/Pt/Fe

Table 5.1 Distribution of the stacked layers on the samples.

The deposition of adjacent (iron oxide)/Pt/Fe and (iron oxide)/Pt stacks on the same substrate significantly simplifies the THz emission experiments. The two stacks can be easily placed into the focus of the femtosecond pump beam by lateral shifting, as illustrated in Fig. 5.2(d), with minimal changes of optical paths. The THz signal from the γ-Fe_2O_3/Pt/Fe and Fe_3O_4/Pt/Fe regions of each sample serves as an ideal reference that allows for accurate alignment of the setup and definition of the time-axis origin.

The pump field $\mathbf{E}_\mathrm{p}$ is approximately constant throughout the thin absorptive layers of the samples (substrate is transparent to it). Therefore, the locally absorbed

pump-pulse energy is proportional to $\mathrm{Im}(n_\mathrm{p}^2)$ where n_p is the complex value of the refractive index of the material at the pump wavelength (800 nm). While the Pt and Fe layers absorb the pump radiation strongly ($\mathrm{Im}(n_\mathrm{p}^2) = 28$ and 37, respectively) [293, 294], Fe_3O_4 is weakly absorbing ($\mathrm{Im}(n_\mathrm{p}^2) = 2.3$) [295], and YIG and γ-Fe_2O_3 are transparent to the pump beam. Therefore, the absorption of energy by Pt and Fe layers give rise to different phenomena:

- On the one hand, the absorption of energy by Pt electrons creates a thermal rise across the FM/NM interface, triggering the interfacial SSE (see Eq. 1.33) due to the difference between magnon temperature at the FM side and electron temperature at the NM side. This is the only effect expected in the case of a totally insulating FM layer.
- On the other hand, because the absorption of energy is different for Pt and Fe, a thermal difference across the Fe/Pt interface is produced. Consequently, a thermoelectric current is generated. As conduction electrons of Fe are strongly polarized in the majority-spin direction [296], this thermoelectric current is spin-polarized, and hence associated to a spin current (this is the interfacial version of SDSE). Note that the SSE also occurs at the Fe/Pt interface, but it is negligible with respect to the strong thermoelectric effect.

As mentioned above, the spin current $J_\mathrm{s}(t)$ generated across the interface is then converted into a charge current $J_\mathrm{c}(t)$ by means of the ISHE in the NM (Pt) layer. Consequently, electromagnetic pulses in the THz frequency range, $\mathbf{E}_\mathrm{THz}$, are emitted.

5.3 Experimental results

The thickness of the ZnTe crystal used as electro-optic sensor determines the range of frequency to which the detection is sensible. In this work, two ranges were explored: the lowest end of the THz window was detected using a 1 mm-thick ZnTe crystal, and a higher range was studied using a 10 μm-thick ZnTe crystal.

In all cases, The THz signal from the Fe_xO_y/Pt/Fe stack is strongly dominated by the signal from the Pt/Fe interface and more than one order of magnitude larger than the signal from the Fe_xO_y/Pt regions without Fe. In view of this, in the following

the THz signal from Fe_xO_y/Pt/Fe regions is labeled with Pt/Fe and accordingly displayed reversed.

5.3.1 Low frequency detection

As expected from ISHE phenomenology, the raw electrooptic signal $S(t)$ inverts when the in-plane FM magnetization **M** is reversed, as shown in Fig. 5.3 for γ-Fe_2O_3/Pt (a), Fe_3O_4/Pt (b) and one of the Fe/Pt samples (c).

To obtain the odd component in **M** originated by the SSE or SDSE currents, the difference $S_-(t)$ between signals for both magnetization directions is calculated: $S_-(t) = S(+M) - S(-M)$. In the following, we will always focus in this difference signal $S_-(t)$, since it contains the information of SSE or SDSE phenomena.

In Fig. 5.4(a) $S_-(t)$ is depicted for the three type of stacks. Compared to γ-Fe_2O_3/Pt bilayer, $S_-(t)$ for Fe_3O_4/Pt features a steeper initial rise and a sharp kink right before the first maximum is attained, followed by an additional sharp kink. Besides, the global minimum is shifted to later times, as indicated by the dashed vertical line. This trend is even more enhanced in the Fe/Pt $S_-(t)$.

By Fourier transformation of the time-domain signals $S_-(t)$ of Fig. 5.4(a), the normalized amplitude $|S(\omega)|$ as a function of frequency $\omega/2\pi$ is calculated and displayed by Fig. 5.4(b). As expected from the time-domain data in Fig. 5.4(a), Fe_3O_4/Pt amplitude spectrum is slightly blue-shifted relative to γ-Fe_2O_3/Pt, and additionally, its bandwidth is increased. Again, this trend is even more pronounced

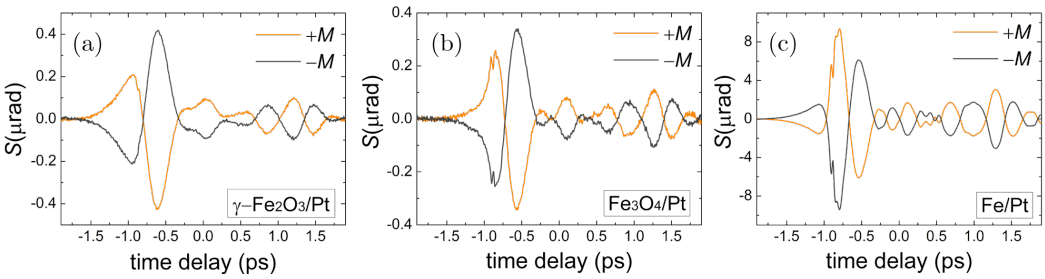

Figure 5.3 Raw electro-optic signal $S(t)$ measured for both in-plane magnetization directions in (a) γ-Fe_2O_3/Pt bilayer, (b) Fe_3O_4/Pt bilayer and (c) one of the Fe/Pt stacks.

in the Fe/Pt spectrum.

To provide a straighter comparison, the three spectra are normalized and plotted together in 5.4(c). γ-Fe_2O_3/Pt spectrum is composed of clearly slower frequencies in comparison to Fe/Pt. Interestingly, Fe_3O_4/Pt band covers those of the other two In fact, it tracks Fe/Pt spectrum at the highest end and that of γ-Fe_2O_3/Pt at the lowest end.

The different behaviors indicate that different processes occur in each material. In particular, the more complex behavior of magnetite suggests that the observed signal results from the composition of more than one mechanism.

To gain more insight into the mechanisms at play in each sample, the spin current that generates in the end the measured THz waveforms is extracted for each sample. In the frequency domain, the measured electro-optic signal $S(\omega)$ is related to the THz field $E_{\mathrm{THz}}(\omega)$ directly behind the sample by multiplication with a transfer function $h(\omega)$ which describes the propagation of the THz wave away from the sample and the response function of the electro-optic detector [83, 297]. The measurement of $h(\omega)$ using a reference emitter allows for an inversion procedure and the retrieval of $E_{\mathrm{THz}}(\omega)$. Finally, the knowledge of $E_{\mathrm{THz}}(\omega)$ enables the determination of the spin current $J_{\mathrm{s}}(\omega)$ through a generalized Ohm's law accounting for the spin-to-charge conversion via the ISHE [298]:

$$E_{\mathrm{THz}}(\omega) = eZ(\omega)\theta_{\mathrm{SH}}\lambda_{\mathrm{NM}}J_{\mathrm{s}}(\omega), \tag{5.1}$$

where $-e$ is the electron charge, $Z(\omega)$ denotes the sample impedance, θ_{SH} is the spin Hall angle of the NM layer, and λ_{NM} is the diffusion length of the spin-polarized current in the NM layer.

In Fig. 5.5 the normalized spin current extracted for the three materials are depicted.

We make the following observations: first, the spin current excited in the metallic structure (Fe/Pt) rises and decays in a faster time scale than the spin current excited in the γ-Fe_2O_3/Pt bilayer, where only the SSE is operative due to the insulating nature of γ-Fe_2O_3. This could be already anticipated from the spectra in Fig.

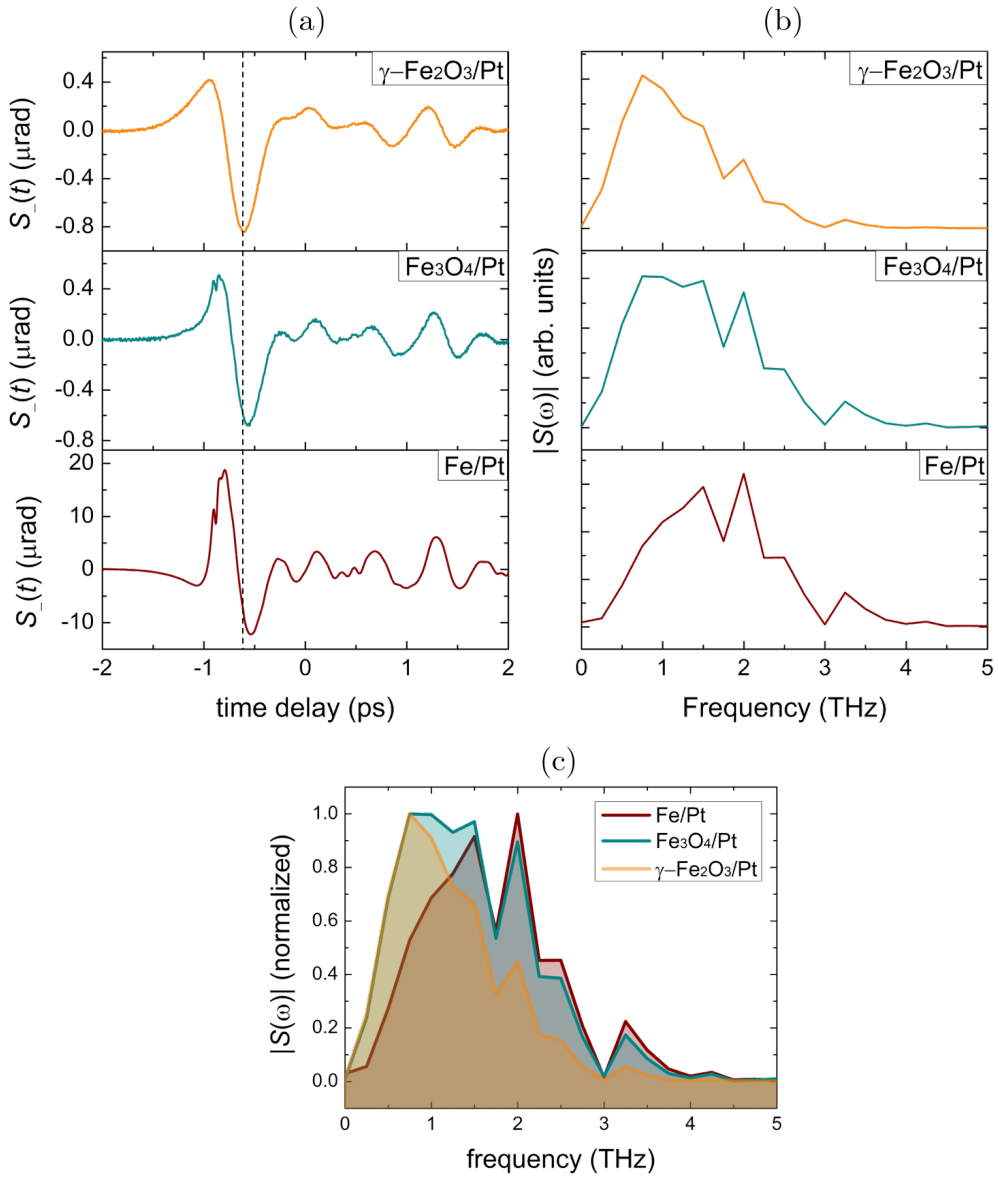

Figure 5.4 (a) Electro-optic signals of THz pulses emitted from FM/Pt bilayers with FM= γ-Fe_2O_3, Fe_3O_4 and Fe, detected with a 1 mm-thick ZnTe crystal. The dashed vertical line marks the minimum signal of γ-Fe_2O_3/Pt. (b) Fourier amplitude spectra corresponding to the signals in (a), normalized by their maximum values and vertically offset. (c) Same Fourier amplitude spectra as in (a), plotted together.

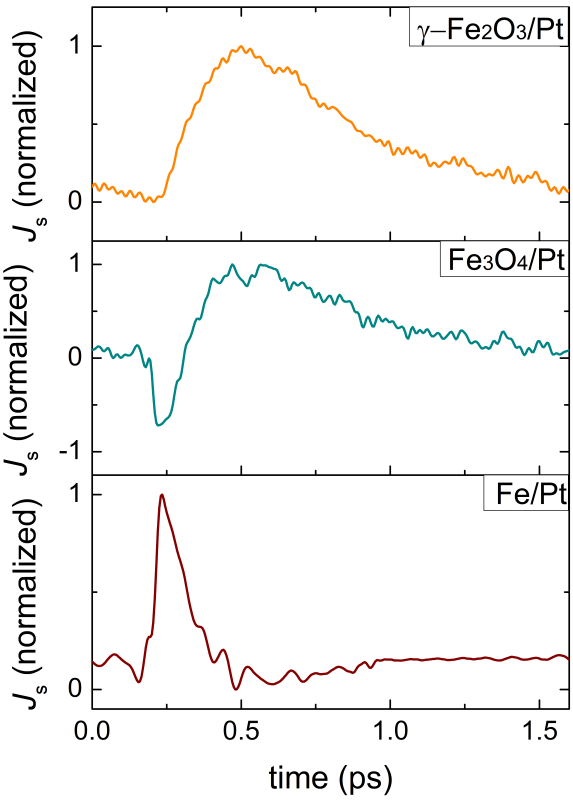

Figure 5.5 Normalized ultrafast photoinduced spin currents $J_s(t)$ extracted from the time-domain electrooptical signal for γ-Fe_2O_3/Pt, Fe_3O_4/Pt and Fe/Pt bilayers.

5.4(b). Thus, thermal spin-polarized currents (SDSE) proceed in a faster time scale than magnonic spin currents excited by SSE. Secondly, the spin current injected in the Fe_3O_4/Pt bilayer shows two clearly distinguishable features which proceed on different time scales and with opposite signs. The fast feature is comparable to the $J_s(t)$ of the Fe/Pt bilayer, while the slow one resembles the $J_s(t)$ of the γ-Fe_2O_3/Pt. In fact, the temporal evolution of spin current in magnetite can be very well reproduced by a linear combination of those measured in γ-Fe_2O_3/Pt and Fe/Pt, as shown in Fig. 5.6(a). Analogous agreement is also observed for the

corresponding THz electro-optic signals of Fig. 5.4(c) which is shown as well in Fig. 5.6(b). This remarkable result suggests that both type of spin currents (from magnons and from spin-polarized electrons) contribute to the spin current $J_s(t)$ in Fe_3O_4/Pt.

The opposite sign of the SDSE spin current excited in Fe_3O_4/Pt with respect to Fe/Pt can be explained by the minority spin polarization at Fermi level of Fe_3O_4, as detailed in Section 3.1.1; an experimental value for this spin polarization of -72% has been reported in literature for (001) Fe_3O_4 deposited on MgO (which is the orientation of the thin films used in this work) [299]. Note that the negative sign of the spin polarization indicates that it corresponds to the spin-down orientation. Thus, in Fe_3O_4 the electrons close to Fermi level are minority electrons (spin-down polarized), whose magnetic moment is atiparallely aligned to the total magnetization **M**. The gap in the majority-spin channel (spin-up polarization) is calculated to be larger than the pump photon energy of 1.55 eV [300]. The situation is different for ferromagnetic iron, in which conduction electrons show both spin polarizations, with a higher mobility of the majority channel and a spin-up polarization of the laser-excited spin current [296]. Consequently, electron-carried spin currents flowing

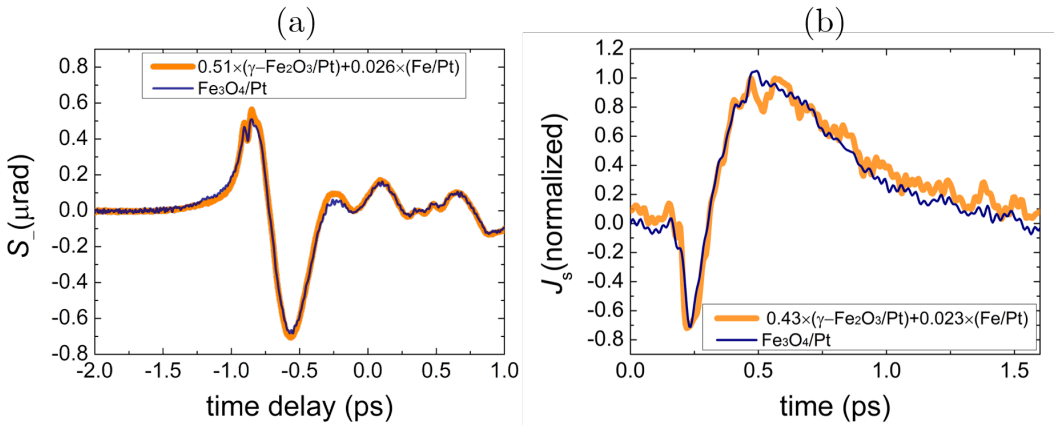

Figure 5.6 (a) The spin current generated in Fe_3O_4/Pt can be well described by a linear combination of the spin currents generated in γ-Fe_2O_3/Pt and Fe/Pt: overlap between both. (b) The same as in (a) using electro-optic signals $S_-(t)$.

in Fe/Pt and Fe_3O_4/Pt are indeed expected to have opposite sign, in agreement with the observed results.

Concerning the SSE (magnon) component of the spin current of Fe_3O_4/Pt, its amplitude is similar to that of γ-Fe_2O_3/Pt. Writing the temporal version of Eq. 5.3, the instantaneous spin current density follows

$$J_s(t) = S^i \Delta T_i^{NM/FM}(t). \tag{5.2}$$

Here, S^i is the interfacial spin Seebeck coefficient and $\Delta T_i^{NM/FM}(t)$ is the time-changing temperature difference between the NM and FM layers. The interfacial SSE coefficient is given by

$$S^i \propto J_{sd}^2 M_s a, \tag{5.3}$$

where J_{sd} is the exchange coupling constant across the FM/NM interface, M_s is the saturation magnetization of FM, and a is its lattice constant. γ-Fe_2O_3 and Fe_3O_4 exhibit almost identical M_s and a, which, given that the obtained SSE peaks in $J_s(t)$ also show similar intensity, means that exchange sd-coupling of γ-Fe_2O_3/Pt and Fe_3O_4/Pt interfaces is very similar.

5.3.2 High frequency detection

Here I present the analogous results obtained using a 10 μm-thick ZnTe crystal as electro-optic sensor. The measured $S_-(t)$ for each structure are presented in Fig. 5.7(a).

Similarly to the results for low frequency detection, the emitted THz waveforms show clear differences. First, in this case the detected signal $S_-(t)$ for γ-Fe_2O_3/Pt is remarkably less intense than for Fe_3O_4/Pt. This is contrast to the situation at low frequencies in which the amplitude for both structures was similar. This is already pointing to a reduced contribution of high frequency dynamics in spin currents excited in γ-Fe_2O_3/Pt, with respect to that excited in Fe_3O_4/Pt. Second, the waveforms hold distinct shapes: the initial decay is faster for magnetite, and,

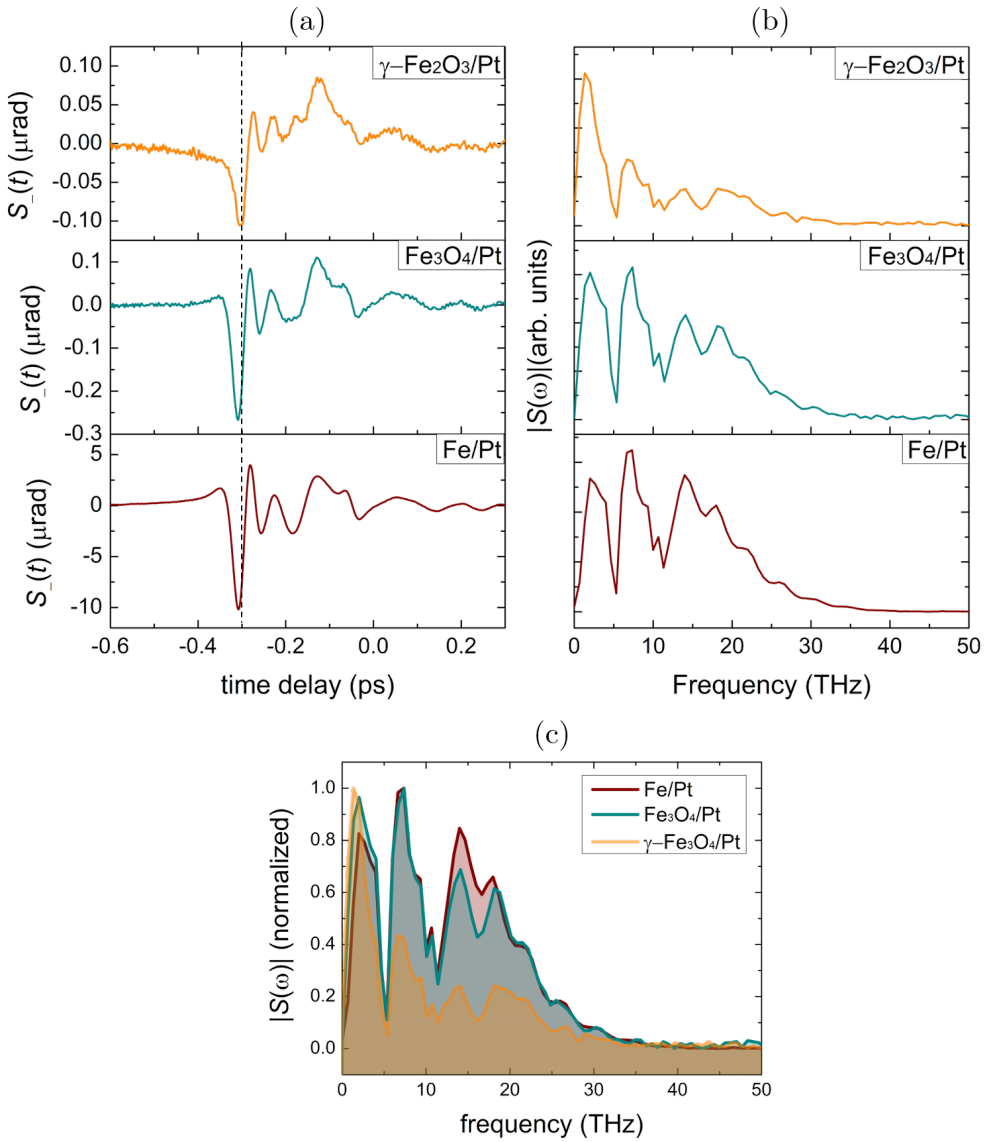

Figure 5.7 (a) Electro-optic signals of THz pulses emitted from FM/Pt bilayers with FM= γ-Fe_2O_3, Fe_3O_4 and Fe, detected with a 10 μm-thick ZnTe crystal. The dashed vertical line marks the minimum signal of γ-Fe_2O_3/Pt. (b) Fourier amplitude spectra corresponding to the signals in (a), normalized by their maximum values and vertically offset. (c) Same Fourier spectra as in (b), plotted together.

contrary to maghemite, preceded by a slight rise. The global minimum is again shifted. All these features are even more marked for iron.

Concerning the Fourier spectra depicted in Fig. 5.7(b), the $|S(\omega)|$ amplitude in γ-Fe_2O_3/Pt substantially decays beyond a frequency of $\approx$ 10 THz. In contrast, the spectra corresponding to Fe_3O_4/Pt and Fe/Pt covers a bandwidth up to $\approx$ 30 THz. The three spectra are plotted together in Fig. 5.7(c) for easier comparison. For γ-Fe_2O_3/Pt, $|S(\omega)|$ reaches its maximum at $\approx$ 1.5 THz, while that of Fe/Pt is maximum at $\approx$ 7 THz. $|S(\omega)|$ of Fe_3O_4/Pt features similar intensity for both maxima, again pointing to the composition of the other two behaviors.

Spin currents extraction was not performed at this frequency because the transference function of the 10 μm-thick ZnTe crystal was not been determined.

5.4 Comparison between γ-Fe_2O_3 and YIG

Finally, the SSE dynamics in γ-Fe_2O_3/Pt are compared to those reported by Seifert *et al.* in YIG/Pt bilayers, also accomplished by TES [83].

In their work [83], authors found that the SSE spin current instantaneously follows the dynamics of the generalized electronic temperature of the Pt layer: a rise on a time scale of 100 fs on which the electrons thermalize to Fermi-Dirac distribution, followed by a decay on a scale of several 100 fs on which the electrons cool down by energy transfer to the Pt crystal lattice. In addition, they developed a model based on sd-like exchange coupling across the FM/NM interface. This model predicts that the temporal evolution of the SSE current is totally determined by the electron dynamics of the metallic NM layer and independent of the insulating magnetic FM layer. To confirm and generalize this interpretation, studies with other FM materials other than YIG are required.

In Fig. 5.8(a) the THz electro-optic signal measured by Seifert *et at.* in a YIG(4 μm)/Pt(5 nm) bilayer is taken from the original publication. This waveform and that of γ-Fe_2O_3(10 nm)/Pt(2.5 nm) bilayer in this thesis exhibit the same shape to very good approximation. It must be noted that both works have been performed using the same experimental setup, and thus both data result from the same transference

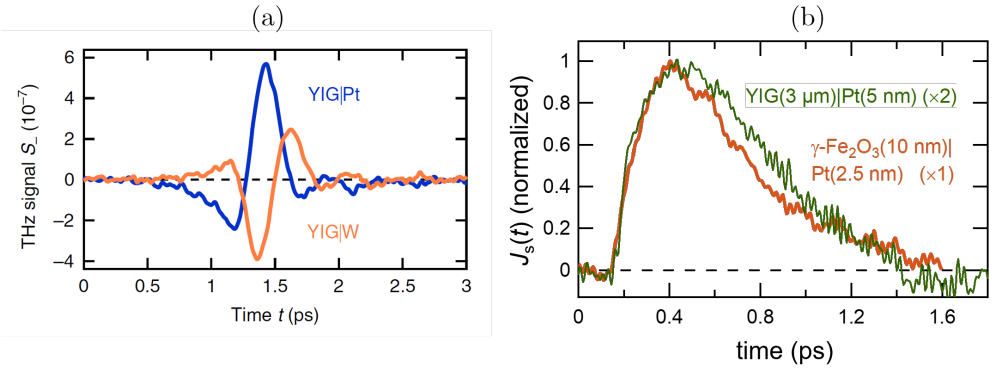

Figure 5.8 (a) Electro-optic signals of THz pulses emitted from a YIG(4 μm/Pt(5 nm) bilayer. Reproduced from Ref. [83]. (b) Ultrafast spin current $J_s(t)$ in YIG/Pt (Ref. [83]) and γ-Fe_2O_3/Pt (this work) as extracted from the THz emission signals of (a). Note the different amplitude scalings.

function of the detector, which implies that they are directly comparable.

Moreover, the extracted temporal evolution of the respective spin currents $J_s(t)$ are depicted together in Fig. 5.8(b). First, $J_s(t)$ have been normalized by pump energy per Pt thickness, to account for the difference in excitation density of Pt layer. The spin currents are then depicted normalized to their respective maximum value.

First, it must be noted that both spin currents follow almost the same temporal dynamics, even if they are excited in different insulating materials. In particular, the rise is essentially identical for both samples. Therefore, this observation confirms the prediction that the ultrafast dynamics of the optically induced spin Seebeck current are solely determined by the dynamics of the electrons in the NM layer.

With regards to the magnitude, the spin current in γ-Fe_2O_3/Pt sample is ~ 2 times higher than in the YIG/Pt sample for the same pump energy per Pt thickness. This enhanced response makes maghemite an interesting source of magnonic spin currents. To understand the origin of this difference in magnitude, we consider Eq.5.2. In both systems the pump energy is deposited in the same material (Pt of the NM layer), as both γ-Fe_2O_3 and YIG are transparent to the pump wavelength. Thus, the factor distinctively affecting the magnitude must be found in the spin

Seebeck coefficient. According to our measurements, the ratio of the Seebeck coefficients of γ-Fe_2O_3/Pt and YIG/Pt amounts to about 2. Therefore, Eq. 5.3 implies that

$$2 \approx \frac{S^{\mathrm{i}}(\gamma - Fe_2O_3)}{S^{\mathrm{i}}(YIF)} \approx 2\frac{J^2_{\mathrm{sd}}(\gamma - Fe_2O_3)}{J^2_{\mathrm{sd}}(YIG)}, \tag{5.4}$$

where the following values have been used: $a(YIG) = 12.376\,\text{Å}$ [20], $a(\gamma - Fe_2O_3) = 8.347\,\text{Å}$ [150], $M_{\mathrm{s}}(YIG) = 140$ emu·cm^{-3} [20], and $M_{\mathrm{s}}(\gamma - Fe_2O_3) = 400$ emu·cm^{-3} [266]. Therefore, the sd-exchange coupling constant J_{sd} of the γ-Fe_2O_3/Pt interface approximately equals that of the YIG/Pt interface [301]. However, it must be noted that quality of the interface can significantly affect the value of the exchange coupling strength at the interface between two given materials from one sample to another. Nevertheless, it can be concluded that γ-Fe_2O_3/Pt interface and YIG/Pt interface hold a at least comparable sd-exchange coupling constant.

5.5 Conclusions

In conclusion, in this chapter the ultrafast spin transport in FM/Pt bilayers was studied. As FM, different materials with different electrical behavior were used: metallic iron, insulating maghemite and half-metallic magnetite. Two relevant results were attained.

First, the ultrafast resolution of the experimental setup allowed us to simultaneously but separately observe SDSE and SSE in half-metallic magnetite, based on their different time scales and supported by measurements in insulating maghemite and metallic iron. Moreover, both contributions to the spin current showed opposite orientation: positive for the SSE spin current carried by magnons, and negative for the SDSE spin current carried by conduction electrons with minority-spin orientation. This is in agreement with the half-metallic nature of magnetite, in which only minority-spin direction is metallic resulting in a negative spin polarization at Fermi level.

Second, the results revealed that γ-Fe_2O_3/Pt SSE dynamics are identical to those of already reported YIG/Pt, only differing in magnitude, which is two times higher

in the case of γ-Fe_2O_3/Pt. This observation shows the universality of SSE behavior in the ultrafast time scale, confirming the prediction that the time evolution of the spin current is solely determined by the dynamics of the electronic system of the NM material. Besides, from the observed amplitude of the respective $J_s(t)$, it was found that YIG/Pt and γ-Fe_2O_3/Pt interfaces exhibit a comparable exchange-coupling constant.

Chapter 6

Inverse spin Hall effect in IrO_2 using thermally excited spin currents

Spin-to-charge conversion is a central process in the emerging field of spintronics. One of its main applications is the electrical detection of spin currents and, for this, the ISHE has become one of the preferred and convenient methods. Usually, heavy transition metals such as Au or Pt are employed for spin-to-current conversion by the SHE or ISHE. However, these noble metals show extremely low electrical resisitivity ρ_c, and whereas this fact represents an advantage when they are used for spin current injection (by the SHE), it degrades their performance in spin current detection (by the ISHE), since the generated voltage is proportional to ρ_c [49]:

$$\Delta V_{\mathrm{ISHE}} \propto \theta_{\mathrm{SH}} \rho_c I_s \approx \rho_{\mathrm{SH}} I_s. \tag{6.1}$$

As explained in Section 3.2, $5d$ transition metal oxides display promising properties for their use in spin-to-charge current conversion by ISHE: moderate electrical conductivities and high SOC. In particular, the work of Fujiwara *et al.* demonstrated the great potential of the iridium(IV) oxide (IrO_2) in spin absorption

experiments implemented in non-local spin-valve structures, finding a spin Hall resistivity ρ_{SH} one order of magnitude larger than that of noble metals. This work triggered a prolific research activity about IrO_2, especially on the theoretical side, aiming at explaining the observed results. On the experimental side, Qiu *et al.* studied spin-to-charge conversion by ISHE in LSSE experiments in YIG(4.5 μm)/IrO_2(30 nm) bilayers grown on a GGG substrate [223]. Surprisingly, their experiment yielded a very low performance of IrO_2, a fact they attributed to a poor efficiency in the spin angular momentum transference efficiency across the interface, i.e., a low spin mixing conductance $g_{\uparrow\downarrow}$. All in all, the role of the different SHE and ISHE mechanisms (discussed in Chapter 1) in IrO_2 has not been clearly elucidated yet.

In this chapter, the ISHE spin-to-charge current conversion by IrO_2 thin films is investigated. To this end, thermal spin currents were generated by LSSE in γ-Fe_2O_3/IrO_2 bilayers and, subsequently, converted into charge currents in the topmost IrO_2 layer. Influence of the substrate, IrO_2 layer thickness, temperature and number of repeated bilayers in multilayered structures were studied.

6.1 LSSE magnitude

First, the LSSE/ISHE experiment was performed in γ-Fe_2O_3/IrO_2 bilayers deposited on (0001) Al_2O_3 and (001) MgO substrates. Each material was deposited as thin film using the respective optimized procedures found in Chapter 3. Thickness of γ-Fe_2O_3 layer was $t_{FM} \approx 50$ nm and thickness of IrO_2 layer was $t_{NM} = t_{IrO_2} \approx 6$ nm.

As an example, the antisymmetric component of the transverse voltage versus magnetic field for a thermal difference of $\Delta T = 1$ K across the sample is shown in Fig. 6.1(a). These measurements were performed at $T = 300$ K.

Whilst the saturation value reached by the voltage is equal for both samples, the saturation field is much higher for that one deposited on Al_2O_3: due to ISHE phenomenology, the $\Delta V_{ISHE}(H)$ hysteresis loop mirrors maghemite's magnetic hysteresis loop on each substrate, as evidenced in Fig. 6.1(b) and (c).

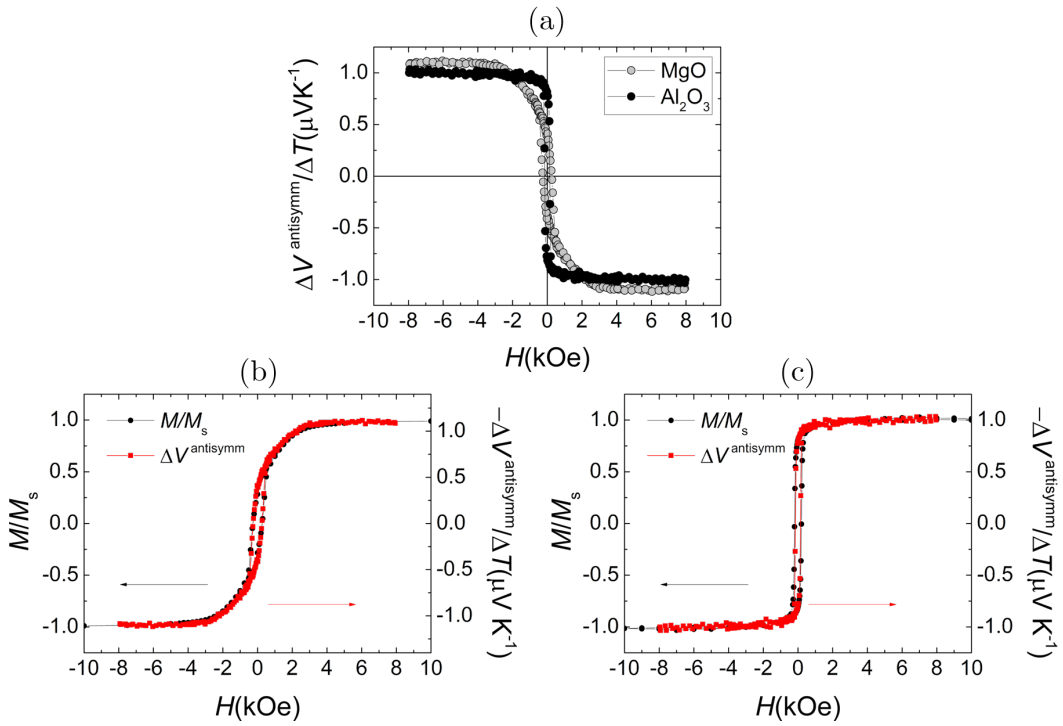

Figure 6.1 (a) $\Delta V_{\mathrm{ISHE}}/\Delta T$ as a function of the magnetic field measured in γ-Fe_2O_3(50 nm)IrO_2(6 nm) deposited on Al_2O_3 and MgO substrates. (b) Scaling of magnetization and $-\Delta V_{\mathrm{ISHE}}/\Delta T$ for the samples deposited on MgO. (c) Scaling of magnetization and $-\Delta V_{\mathrm{ISHE}}/\Delta T$ for the samples deposited on Al_2O_3.

Following the standard procedure, the experiment is repeated for different values of ΔT (not shown). Next, a linear fit of ΔV_{ISHE} dependence on ΔT was performed and the standard spin Seebeck coefficient, S_{zy}, is calculated as defined in Eq. 1.32. The following coefficients were obtained: $S_{zy} = -7.4(5) \times 10^{-8}$ VK^{-1} for the sample deposited on MgO, and $S_{zy} = -7.1(5) \times 10^{-8}$ VK^{-1} for the sample deposited on Al_2O_3.

Pt is the benchmark against which every other ISHE material is compared. In the case of IrO_2, a first important observation is the negative sign of the ISHE voltage with respect to Pt, implying $\theta_{\mathrm{SH}} < 0$. Besides, in order to compare the magnitude of the effect in both materials, a γ-Fe_2O_3/Pt bilayer was deposited on (001) MgO substrate, keeping $t_{\mathrm{FM}} \approx 50$ nm and $t_{\mathrm{NM}} = t_{\mathrm{Pt}} \approx 6$ nm. The direct

comparison of the antisymmetrical component of the measured transverse voltage is provided in Fig. 6.2(a). To check that both signals share a common origin and differ only in magnitude but not in nature, they are depicted scaled and superimposed in Fig. 6.2(b); finding that indeed one loop tracks the other.

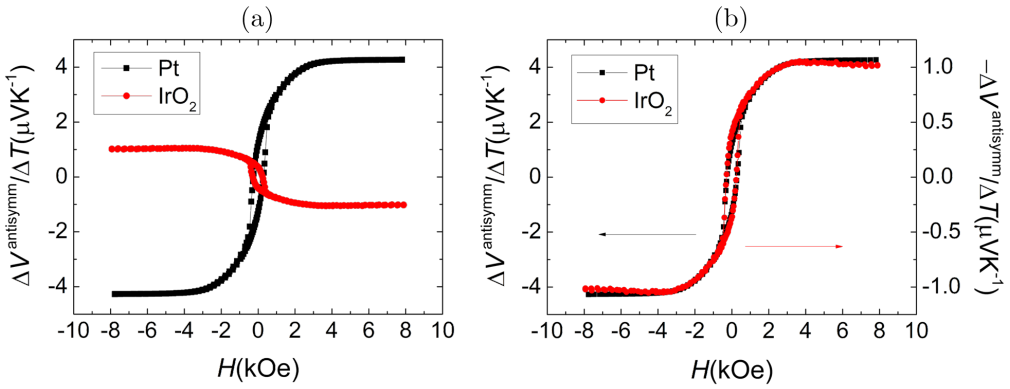

Figure 6.2 (a) Comparison of the $\Delta V_{\mathrm{ISHE}}/\Delta T$ signals measured using Pt and IrO_2 as NM metals in γ-Fe_2O_3($\approx$ 50 nm)/NM($\approx$ 6 nm) bilayers deposited on MgO. (b) Scaling of both signals.

The spin Seebeck coefficient of the γ-Fe_2O_3/Pt sample was $S_{zy} = 5.7(4) \times 10^{-7}$ VK^{-1}. This means that S_{zy} using IrO_2 ($S_{zy} \approx -7.25 \times 10^{-8}$ $\mathrm{VK}^{-}1$) compared with S_{zy} using Pt amounts to only 13%. This value is much greater than the $\approx$ 1.5% determined in Ref. [223]. This increase may be due to the smaller thickness of IrO_2 in a context of diffusive transport of spin polarization from the interface, and also to *in situ* deposition providing a high quality interface. Concerning the first reason, IrO_2 layer in this study had a thickness of 6 nm against the 30 nm used in Ref. [223]; in LSSE experiments spin polarization of conduction electrons is maximum at the interface and diffuses away with a length scale λ_{IrO_2}, which was determined to be $\lambda_{IrO_2} = 3.8$ nm for polycrystalline IrO_2 in Ref. [213]. A thickness of 30 nm is therefore far beyond this diffusion length scale, giving as a result an extremely reduced ΔV_{ISHE} measurement.

Nevertheless, the value of S_{zy} in IrO_2 obtained here is still surprising low considering the high spin Hall resistivity ρ_{SH} reported in Ref. [213]. The thickness

study presented in the next section aims at elucidating possible causes for this.

6.2 Thickness and temperature study

In order tho shed light on the behavior of ISHE in IrO_2 thin films, a systematic study of the ISHE detection of SSE in $\gamma-Fe_2O_3/IrO_2$ bilayer structures for different thickness of the IrO_2 layer was performed. The thickness of maghemite was kept at 50 nm throughout every sample, whereas the thickness of IrO_2, t_{IrO_2}, was varied from 2 to 22 nm. $\gamma-Fe_2O_3/IrO_2$ bilayers were *in situ* grown by PLD on $Al_2O_3(0001)$ substrates of dimensions $2 \times 7 \times 0.5$ mm^3, using the respective optimized procedures found in Chapter 3.

XRD characterization was carried out for every sample. In wide-range $2\theta/\omega$ scans, only the $\{100\}$ reflections of IrO_2 were present, indicating that this material is strongly textured in that direction. Regarding $\gamma-Fe_2O_3$, only the $\{111\}$ reflections of $\gamma-Fe_2O_3$ are visible, which confirms that it grows on Al_2O_3 in the [111] orientation. An example is provided in Fig. 6.3(a).

The shorter scans around the (0006) substrate Bragg peak are shown in Fig. 6.3(b). (200) IrO_2 peak is visible, increasing in intensity and narrowing as the layer thickness is increased, in accordance with Scherrer's formula (Eq. 2.2).

The Scherrer's formula (Eq. 2.2) is applied to the (200) Bragg peak Of IrO_2 of the two thickest samples ($t_{IrO_2} = 22$ nm and 16 nm), for which the peak is clearly visible, to determine the crystalline domain size of IrO_2 in the [100] direction. The peak positions and FWHM were determined to be $2\theta(21\,\text{nm}) = 41.96°$, $2\theta(16\,\text{nm}) = 42.067°$, $\beta_{2\theta}(21\,\text{nm}) = 0.66$ and $\beta_{2\theta}(16\,\text{nm}) = 0.744°$. These parameters yield crystalline domains of $D_{100}(21\,\text{nm}) \approx 13$ nm and $D_{100}(16\,\text{nm}) \approx 11.5$ nm. Note that the domain size is smaller than the thickness of the IrO_2 layer. Therefore, although no reflection from different crystallographic planes are visible in the diffraction patterns, it must be concluded that IrO_2 is strongly textured in the [100] direction.

Additionally, longitudinal resistivities ρ_c of the different IrO_2 layers were determined using an in-line four probe geometry, prior to LSSE experiments. The measured $V(I)$ characteristic curves displayed ohmic behavior, as shown in

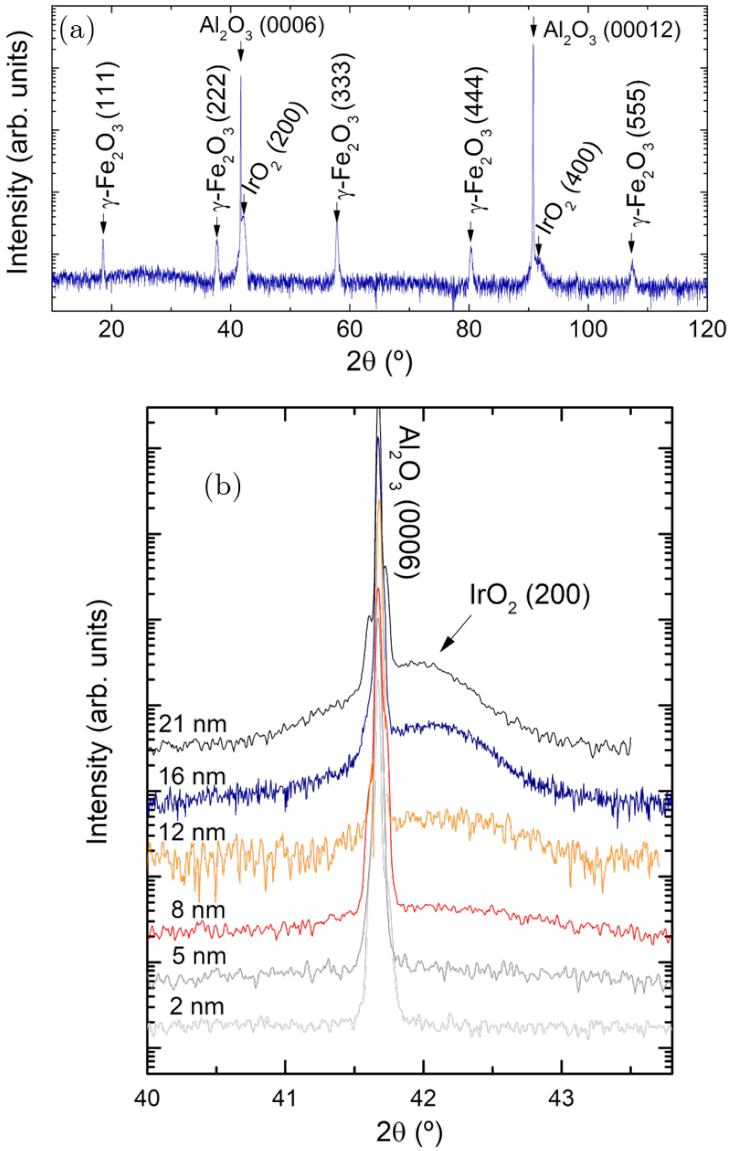

Figure 6.3 (a) Wide-range symmetric $2\theta/\omega$ XRD scan for the sample with a 16 nm-thick IrO_2 layer. (b) $2\theta/\omega$ diffraction patterns around the (0006) Al_2O_3 Bragg peak, showing the evolution of (200) IrO_2 peak with thickness.

Fig. 6.4(a), proving the metallic nature of IrO_2. The resistivity, shown in Fig. 6.4(b), increases on decreasing thickness. This behaviour is consistent with recent

theoretical works that predict changes in the metallic properties of IrO_2 through thickness variation [244] and epitaxial strain along the c axis [226].

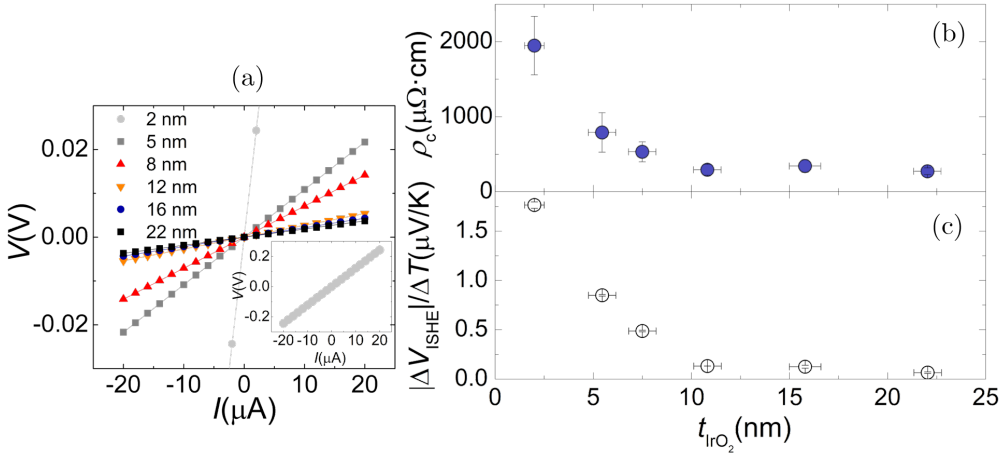

Figure 6.4 (a) $V(I)$ characteristic curves measured for different t_{IrO_2}. The $V(I)$ characteristic of the thinnest sample is zoomed out. (b) Thickness dependence of the longitudinal resistivity of IrO_2 [100] textured thin films. (c) Thickness dependence of $\Delta V_{ISHE}/\Delta T$ detected by ISHE from LSSE experiments in γ-Fe_2O_3/IrO_2 bilayers.

Finally, each sample was subjected to several temperature differences ΔT from 0.5 K to 2.5 K using the external heater method explained in Section 2.5.1. For each value of ΔT, the transverse voltage dependence on the magnetic field was recorded and the antisymmetric component, stemming from ISHE, was extracted. From the linear fit of ΔV_{ISHE} dependence on ΔT, the corresponding slopes were obtained and depicted in Fig. 6.4(c). The common behavior of $\Delta V_{ISHE}/\Delta T$ and ρ_c indicates that $\rho_c(t_{IrO_2})$ strongly dominates $\Delta V_{ISHE}/\Delta T$ dependence on t_{IrO_2} (recall Eq. 6.1). To extract the contribution of interest for this work —i.e., that of the spin-to-charge conversion process represented by $I_c = \theta_{SH} I_s$ in Eq. 6.1—, the charge density current per Kelvin is calculated as

$$\frac{J_c}{\Delta T} = \frac{1}{d_y \cdot \rho_c} \frac{\Delta V_{ISHE}}{\Delta T}, \tag{6.2}$$

where d_y refers to the distance between the electrical contacts to measure ΔV_{ISHE}. This way, the influence of ρ_c is removed from the thickness dependence and only the

spin-to-charge conversion effect remains. The obtained dependence of J_c on t_{IrO_2} is plotted in Fig. 6.5. We note that $J_c/\Delta T$ features indeed a peak at low values of t_{IrO_2} followed by a monotonic decrease for higher values. This behavior constitutes the fingerprint of a typical diffusion mechanism of spin polarization with a characteristic length, λ_{IrO_2} comparable to the layer thickness [46]. The obtained curve is similar to that reported for other ISHE media, such as the prototypical Pt [302, 303].

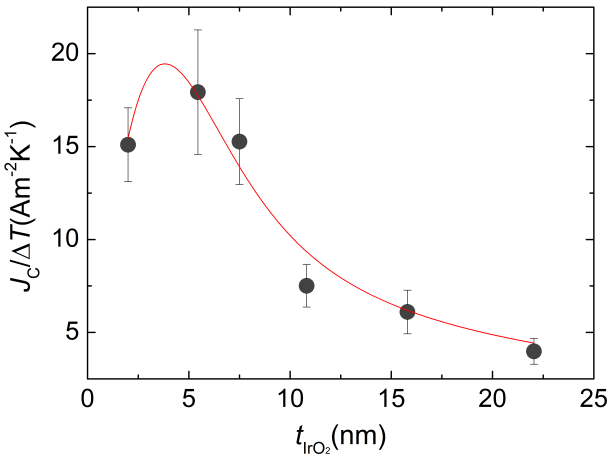

Figure 6.5 Symbols: ISHE charge current density per Kelvin generated by LSSE in γ-Fe_2O_3/IrO_2, bilayers deposited on Al_2O_3 substrates for different IrO_2 thickness. Line: Fit to eq. 6.4

The model developed by Castel *et al.* relates the thickness of a NM layer to the detected transverse ISHE voltage caused by a spin current [302]. According to it, NM thickness (t_{NM}) dependence of ΔV_{ISHE} can be expressed as:

$$\Delta V_{ISHE} \propto \frac{\theta_{SH}}{t_{NM}} \cdot \frac{g_{\uparrow\downarrow}}{g_{\uparrow\downarrow} + \frac{1}{\lambda_{NM}\rho_c} \cdot \frac{1-e^{-2t_{NM}/\lambda_{NM}}}{1+e^{-2t_{NM}/\lambda_{NM}}}} \cdot \frac{\left(1-e^{t_{NM}/\lambda_{NM}}\right)^2}{1+e^{2t_{NM}/\lambda_{NM}}} \tag{6.3}$$

where λ_{NM} denotes the spin diffusion length of the NM layer. Equivalently:

$$J_c \propto \frac{\theta_{\mathrm{SH}}}{t_{\mathrm{NM}}\rho_{\mathrm{c}}} \cdot \frac{g_{\uparrow\downarrow}}{g_{\uparrow\downarrow} + \frac{1}{\lambda_{\mathrm{NM}}\rho_{\mathrm{c}}} \cdot \frac{1-e^{-2t_{\mathrm{NM}}/\lambda_{\mathrm{NM}}}}{1+e^{-2t_{\mathrm{NM}}/\lambda_{\mathrm{NM}}}}} \cdot \frac{\left(1-e^{t_{\mathrm{NM}}/\lambda_{\mathrm{NM}}}\right)^2}{1+e^{2t_{\mathrm{NM}}/\lambda_{\mathrm{NM}}}} \tag{6.4}$$

This expression can be fitted to the set of data in Fig. 6.5 in order to attain the value of $\lambda_{\mathrm{IrO_2}}$. In their work [302], based on spin-pumping experiments with YIG/Pt bilayers, Castel and coworkers supposed that the ISHE was originated by extrinsic mechanisms due to skew scattering, which is characterized by the scaling $\sigma_{\mathrm{SH}} \propto \sigma_{\mathrm{c}}$, yielding a constant θ_{SH} [11, 47, 52]. However, such assumption does not work for the observed experimental results in IrO_2; a fit of Eq. 6.4 to the data only converges if taking $\theta_{\mathrm{SH}} \propto \rho_{\mathrm{c}} = \sigma_{\mathrm{c}}^{-1}$ (i.e., σ_{SH} independent of σ_{c} and $\rho_{\mathrm{SH}} \propto \rho_{\mathrm{c}}^2$). Admitting this scenario, a fit of Eq. 6.4 to the current density data converges providing a value for spin diffusion length of IrO_2 $\lambda_{\mathrm{IrO_2}} = 3.3(7)$ nm. Therefore, this result rules out a dominant role of skew scattering in the ISHE process in our textured IrO_2 thin films.

The behavior of the absolute ISHE charge current I_{c} above the spin diffusion length also provides information about the mechanism responsible for the ISHE. If skew scattering is the main term, assuming that the injected spin current I_{s} is the same for all samples (since t_{FM} is maintained constant), then θ_{SH} should be independent of ρ_{c} and, thus, of $t_{\mathrm{IrO_2}}$, which would make I_{c} saturate to a constant value for $t_{\mathrm{IrO_2}} > \lambda_{\mathrm{IrO_2}}$. In contrast, in the case that the spin Hall angle scales as $\theta_{\mathrm{SH}} \propto \rho_{\mathrm{c}}$, I_{c} also scales as $\propto \rho_{\mathrm{c}}$ for a given I_{s}. This means that the saturation behavior in the thickness dependence must be expected in $I_{\mathrm{c}}/\rho_{\mathrm{c}}$ instead of in I_{c}. As shown in Fig. 6.6, the experimental data follow this latter trend, supporting the $\theta_{\mathrm{SH}} \propto \rho_{\mathrm{c}}$ scaling and thus excluding skew scattering as the main ISHE mechanism in the experiment. The the spin-to-charge conversion (represented by θ_{SH}) increases linearly on increasing ρ_{c} and therefore, for the same I_{s}, the converted I_{s} will be smaller for lower ρ_{c} (bigger $t_{\mathrm{IrO_2}}$).

Therefore, these results entail that either the intrinsic mechanism or the extrinsic side jump must govern the ISHE in IrO_2 thin films with [100] preferential texture.

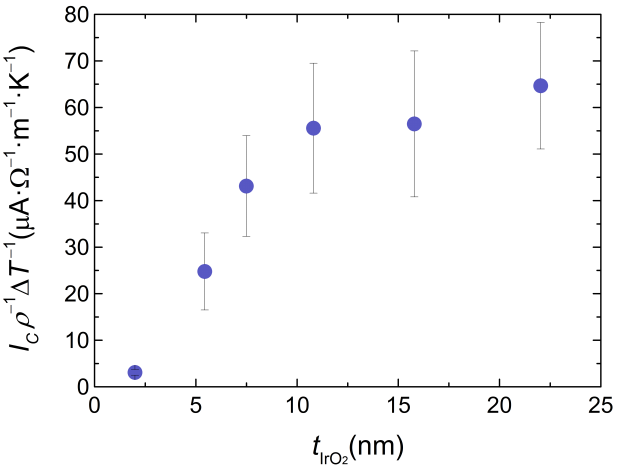

Figure 6.6 Evolution of ISHE charge current $I_c/(\rho_c \Delta T)$ with thickness of IrO_2.

Since both of them share the same θ_{SH} dependence on resistivity, the separation of intrinsic and side jump contributions has been a long-standing problem, also controversial from the theoretical point of view. Some authors [304] predicted that side jump is always negligible compared to skew scattering (by a factor of $1/Z^2$); in contrast, others concluded that both contributions can be comparable [305, 306]. In either case, the intrinsic contribution is the most likely candidate to play the dominant role in our experiment, as discussed in the following.

First, if we accept the result in reference [304] —side jump is generally negligible relative to skew scattering—, and considering that we have ruled out a predominant role of skew scattering, we can conclude that the intrinsic SOC governs the ISHE.

Alternatively, let us examine the situation that aligns with the results in [305–307] —side jump is not always negligible. The side jump contribution to θ_{SH} is proportional to the impurity concentration [11, 305], and therefore it may dominate the overall effect at sufficiently high concentrations. In other cases, its contribution to the spin Hall conductivity is smaller than those of skew scattering or the intrinsic mechanism [11]. As a consequence, side jump is usually manifested either in doped systems or alloys, or at low temperatures, where it gains importance

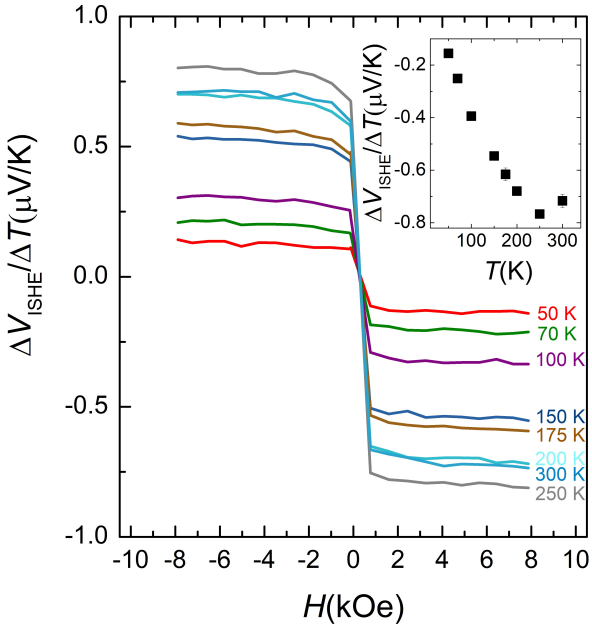

Figure 6.7 Evolution with temperature of the measured $\Delta V_{\mathrm{ISHE}}/\Delta T$ output excited by the LSSE in the sample with $t_{\mathrm{IrO_2}} = 5.5$ nm

and may become comparable to skew scattering even at low impurity concentrations [307–309]. Nevertheless, the experiments presented here were performed at room temperature in IrO_2 samples deposited by PLD with base vacuum of $P \sim 10^{-9}$ Torr and using a target of 99.9%-pure IrO_2. Thus, an impurity that could be expected would be metallic iridium due to reduction (although this is highly unlikely since the deposition of IrO_2 is performed in oxygen atmosphere). In this regard, Fert and Levy showed that for impurities at the beginning and end of the 5*d* series (Lu, Hf, Ir, Pt) the side jump contribution at impurity concentrations of $\approx 2\%$ is much smaller than the skew scattering contribution [305].

In view of all of the above, it seems reasonable to accept that the ISHE in [100] textured thin films of IrO_2 is most likely driven by the intrinsic SOC.

As previously pointed, another relevant observation concerns the sign of ΔV_{ISHE}: it is negative, entailing $\theta_{\mathrm{SH}} < 0$. In the pioneering work with polycrystalline IrO_2 of Fujiwara and coworkers [213], they observed a change in the sign of the ISHE

signal with decreasing temperature (from positive at $T > 90$ K to negative at $T < 90$ K). They ascribed this to the coexistence of different SOC mechanisms with opposite signs. We also performed the LSSE experiment at different temperatures for the sample in which the largest room-temperature value of $J_c/\Delta T$ was measured ($t_{IrO_2} = 5.5$ nm). The results are plotted in Fig. 6.7. As shown, such reversal in the signal with respect to the magnetic field is not observed here; rather, it is negative for every measured temperature. This suggests that the same ISHE mechanism dominates over the entire temperature range.

Regarding this, it was also recently shown that the intrinsic spin Hall conductivity σ_{ij}^{k} in IrO_2 is remarkably anisotropic, changing not only in magnitude but also in sign depending on the directions of the spin current (i direction), spin polarization (k direction) and electric field (j direction) [228]. As a result, the sign of the induced ISHE electric field $\mathbf{E}_j$ depends not only on the sign of the vector product $\mathbf{J_s}^i \times \hat{\mathbf{s}}$, but also on the direction in which the spin-to-charge conversion process is occurring. Accordingly, the preferred direction (if any) of growth with respect to the measurement geometry might be determining for the observed sign if the intrinsic mechanism is dominant. This means that the sample preparation and crystallinity are probably crucial for the final balance in the competition between different mechanisms to dominate the ISHE in IrO_2. Thus, the explanation for the differences observed between samples with [100] preferential texture and previously reported results in polycrystalline IrO_2 may be found here. The samples studied in reference [213], polycrystalline, were prepared by reactive sputtering from a pure Ir target and then patterned using e-beam lithography. Qiu and collaborators in reference [223] mentioned that they used RF sputtering. Competition between SOC mechanisms opposite in sign but similar in magnitude could be responsible for —or at least, contribute significantly to— the low ISHE signal they observed in their experiment, together with a low spin mixing conductance.

6.3 LSSE and ISHE in multilayered structures

Different strategies have been explored in literature in order to enhance the SSE/ISHE performance; for example, nanostructuration in devices such as SSE-based thermopiles [310] or multilayered structures of stacked (FM/NM) bilayer units [268], or heterostructuration with an antiferromagnetic insulating layer sandwiched between NM and FM layers [311, 312].

In this work, the multilayer approach was studied using IrO_2 as NM layer for ISHE detection of the thermal spin currents. Here, I present the results of such experiments using γ-Fe_2O_3 as FM.

First, $(\gamma\text{-}Fe_2O_3/IrO_2)_n$ multilayers with $n = 1$, $n = 2$ and $n = 3$ were prepared onto (001) MgO and (0001) Al_2O_3 substrates with dimensions $2 \times 7 \times 0.5$ mm^3. Thickness of the layers were ≈ 60 nm for γ-Fe_2O_3 and ≈ 3.5 nm for IrO_2 throughout every bilayer unit. LSSE experiments were performed using the external heater setup and setting different thermal drops across the sample.

During the simultaneous deposition of the multilayers on both substrates, it was possible to observe a striking difference between them: whereas the first maghemite layer showed this material's characteristic brown-yellowish color in both substrates, the second an third maghemite layers displayed a remarkable different reddish tone in samples grown on Al_2O_3 (see Fig. 6.8(a)). This is typically indicative of the formation of α-Fe_2O_3 phase (hematite). Aiming at elucidating this, XRD and magnetic characterizations were carried out.

The XRD patterns around the substrates Bragg peak are shown in Fig. 6.8(b) and (c) for the $n = 2$ samples. Only the (004) γ-Fe_2O_3 and (002) MgO are present in the sample deposited on MgO (Fig. 6.8(b)). However, the XRD spectra of the sample deposited on Al_2O_3 indeed features the (006) α-Fe_2O_3 reflection, in addition to (006) Al_2O_3 and (222) γ-Fe_2O_3 ones. In fact, (006) α-Fe_2O_3 peak diffracts more intensely than (222) γ-Fe_2O_3 one, suggesting that the sample contains a bigger amount of that phase. Two possible scenarios seem possible: (1) second and third layer consist of mainly of α-Fe_2O_3 whilst the first layer remains in the γ-Fe_2O_3 phase; or (2) all present layers for $n = 2$ and $n = 3$ samples contain both γ-Fe_2O_3 and

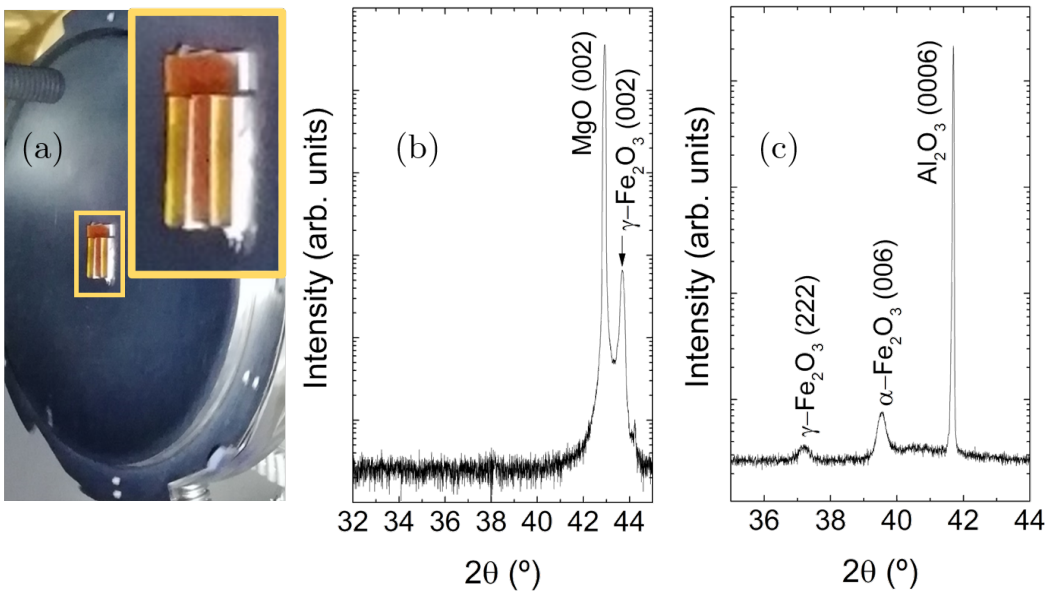

Figure 6.8 (a) Picture taken right after the deposition and annealing of the second iron oxide layer (before deposition of topmost IrO_2 layer) during the fabrication of $(\gamma\text{-}Fe_2O_3/IrO_2)_2$ multilayered structures. The reddish-colored samples correspond to Al_2O_3 substrates, whereas the brown-yellowish-colored samples correspond to MgO substrates. (b)-(c) XRD $2\theta/\omega$ scan around substrate Bragg's peak performed in (b) $MgO//(\gamma\text{-}Fe_2O_3/IrO_2)_2$ and (c) $Al_2O_3//(\gamma\text{-}Fe_2O_3/IrO_2)_2$.

α-Fe_2O_3, meaning that the initial all-maghemite first layer was partially transformed into hematite upon heating to deposition temperature (600°C) for the subsequent layers.

Magnetic characterization helps to assess which scenario is more plausible. The magnetization hysteresis loops at room temperature were measured by VSM. In the case of on-Al_2O_3 deposited samples, the magnetization is drastically reduced for $n = 2$ and $n = 3$ multilayers, as noticeable in Fig. 6.9(a). Besides, the fact that $n = 2$ and $n = 3$ display similar saturation magentization values, M_s, seems to point to the (2) scenario; if the scenario (1) were the actual situation, a $M_s(n = 3) < M_s(n = 2)$ behavior would be expected instead. Broadening of the coercivity also suggests change in the magnetic material. Concerning the magnetic $M(H)$ loops of multilayers deposited on MgO substrates, only a small decrease of the saturation not

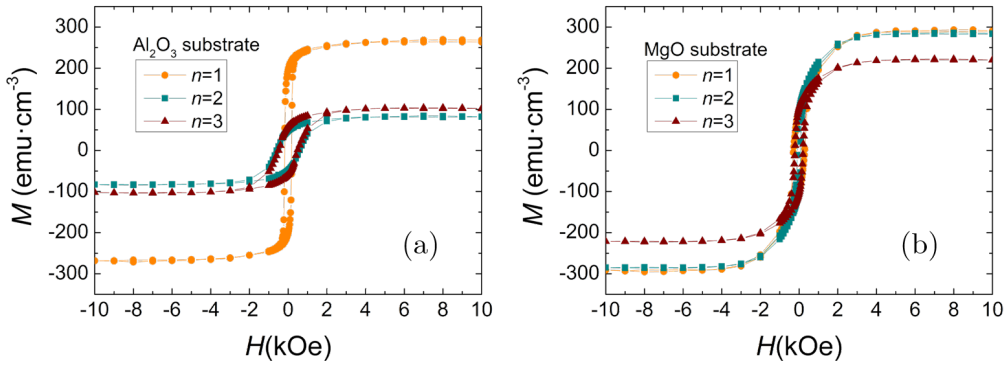

Figure 6.9 Magnetic hysteresis loops $M(H)$ measured at room temperature in (a) on-(0001) Al_2O_3 deposited $(\gamma\text{-}Fe_2O_3/IrO_2)_n$ multilayers and (b) on-(001) MgO deposited $(\gamma\text{-}Fe_2O_3/IrO_2)_n$ multilayers

accompanied by an enlargement of coercivity is observed for the $n = 3$ multilayer, whereas $n = 1$ and $n = 2$ samples share a similar behavior, as illustrated in Fig. 6.9(b). This is most likely due to a degradation of maghemite's quality in the topmost bilayer due to crystal coherence loss.

Finally, LSSE experiments were carried out in all six samples. Exemplary antysimmetric ISHE voltage dependences on sweeping magnetic field for $\Delta T = 1$ K are shown in Fig. 6.10(a) and (b). Linear fits of $\Delta V_{\mathrm{ISHE}}(\Delta T)$ are plotted in 6.10(c), and the obtained slopes are depicted as a function of the number of periods n in Fig. 6.10(d), along with the measured longitudinal charge resistivity ρ_c. The displayed behaviors are remarkably different: in the case of samples grown on Al_2O_3, the sign is inverted for $n = 2$ and $n = 3$ with respect to $n = 1$, as illustrated in Fig. 6.10(a). Additionally, the saturation voltage is substantially increased, and the loop coercivity in widened in consonance with the corresponding magnetic hysteresis loops shown in Fig. 6.9(a). ΔV_{ISHE} enhancement is especially striking considering the important presence of antiferromagnetic $\alpha\text{-}Fe_2O_3$ in $n = 2$ and $n = 3$ samples according to structural and magnetic characterization. The inversion of ISHE sign points to a change in the balance between the SOC mechanisms governing ISHE; polycrystalline IrO_2 shows $\theta_{\mathrm{SH}} > 0$ [213], which suggests that texture is lost in the

topmost IrO_2 layer in $n = 2$ and $n = 3$ samples. Such a change in the main ISHE mechanism could also lead to an increase of θ_{SH}. ρ_c data supports this interpretation, as it decreases to a common value for $n = 2$ and $n = 3$ which is reduced by approximately 50% with respect $n = 1$. This decrease in ρ_c may involve a change in the conduction regimen in IrO_2 from intermediate (where intrinsic mechanism dominates spin-dependent scattering) to clean (where skew scattering plays the main role) [47, 63]. This is also consistent with the negative θ_{SH} observed for the intrinsic mechanism in Section 6.2 and posistive values reported in literature for polycrystalline IrO_2. Note that this different regime in which the skew scattering

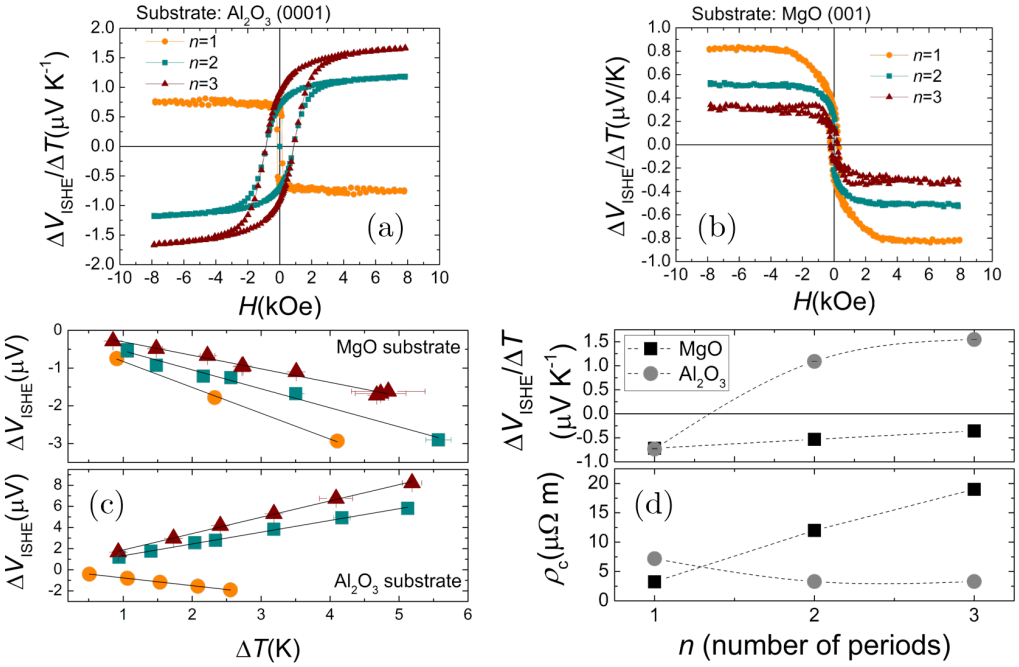

Figure 6.10 (a) Exemplary $\Delta V_{ISHE}/\Delta T$ measured dependences on magnetic field for $Al_2O_3//(\gamma\text{-}Fe_2O_3/IrO_2)_n$ multilayered structures, with $n = 1$, 2 and 3. (b) Exemplary $\Delta V_{ISHE}/\Delta T$ measured dependences on magnetic field for $MgO//(\gamma\text{-}Fe_2O_3/IrO_2)_n$ multilayered structures, with $n = 1$, 2 and 3. (c) Linear fits of $\Delta V_{ISHE}/(\Delta T)$ for $n = 1$, 2 and 3 multilayers deposited on both substrates. (d) Top panel: $\Delta V_{ISHE}(\Delta T)$ slopes obtained for both substrates as a function of the number of periods n. Bottom panel: longitudinal charge resistivity ρ_c as a function of n for both substrates.

governs ISHE implies a different scaling for θ_{SH}: it is now independent of ρ_{c}, and the $\theta_{\mathrm{SH}} \propto \rho_c$ scaling does not hold anymore [11, 47, 52]. That is why an increment of θ_{SH} is compatible with a reduction of ρ_{c}

Regarding multilayered structures grown on MgO substrates, as displayed in Fig. 6.10(b), signal decreases on increasing n. This is likely due to the degradation of the quality of IrO_2 and γ-Fe_2O_3 on the second and third bilayer units, which also explains the deterioration of its resistivity ρ_{c}.

6.4 Conclusions

In this chapter, the ISHE spin-to-charge conversion in PLD-grown thin films of IrO_2 has been investigated. To this end, spin currents were thermally excited by of LSSE and the transverse ISHE voltage was measured.

From the fundamental LSSE experiment performed in γ-Fe_2O_3(50 nm)/IrO_2(6 nm) bilayers, a spin Seebeck coefficient of $S_{zy} \approx -7.25 \times 10^{-8}$ $\mathrm{VK}^{-}1$ was obtained for samples deposited both on MgO and Al_2O_3 substrates.

Next, the IrO_2 thickness dependence of the LSSE/ISHE process was studied. Analysis of the obtained data within the theoretical models established that the spin Hall angle scales with the longitudinal electrical as $\theta_{\mathrm{SH}} \propto \rho_c$, a result that excludes a predominant role of skew scattering in ISHE. The fitting of the theoretical model in Ref. [302] to $J_{\mathrm{c}}\left(t_{\mathrm{IrO_2}}\right)$ provided a spin diffusion length of $\lambda_{\mathrm{IrO_2}} = 3.3(7)$ nm, which is in accordance with the value previously reported by Fujiwara using a lateral spin-valve methodology [213]. This spin diffusion length is comparable to that of pure metals, such as those reported for prototypical Pt, which range between 1.2 and 8.0 nm [302, 313–317].

Besides, the sign of the spin Hall angle remained negative throughout all the experiments, including temperature variation. This is in contrast to what was described in the other two works on the ISHE in polycrystalline or amorphous IrO_2 grown using other techniques. This can be attributed to the dominant role of intrinsic ISHE in the entire temperature range, with a negative intrinsic spin Hall conductivity, as proposed by [228]. This effect might be enhanced by the textured

growth of IrO_2 thin films, in view of the anisotropic nature predicted for IrO_2 [228]. These results reveal the delicate competition between SOC mechanisms in IrO_2 which brings the possibility of tuning the desired functionality of high resistance spin-Hall-based devices.

Finally, multilayered structures γ-Fe_2O_3/IrO_{2n} with $n = 1$, 2 and 3 were prepared on both MgO and Al_2O_2 substrates. The results for multilayers deposited onto MgO showed a decrease of LSSE/ISHE signal on increasing n, as well as an increase in the longitudinal resistivity. These results together with magnetic and structural characterization indicate that IrO_2 and γ-Fe_2O_3, layers are degraded upon increasing n. Concerning multilayers deposited on Al_2O_2 substrates, the observed results are radically different: structural an magnetic characterization suggest the formation of the antiferromagnetic α-Fe_2O_3 phase for $n > 1$. In spite of this, LSSE/ISHE signal significantly increases upon increasing n and, more strikingly, θ_{SH} change sign from negative for $n = 1$ to positive for $n = 2$ and $n = 3$. This sign reversal is accompanied by a drop in the charge resistivity. This result points to a change in the conduction regimen from intermediate to clean regime, which in turn entails a modification of the mechanism dominating ISHE (from intrinsic to skew scattering). This change might be triggered for the loss of IrO_2 crystal texture upon increasing n, in agreement with the positive θ_{SH} reported in literature for polycrystalline IrO_2.

These results are relevant for the achievement of a better control of spin-to-charge conversion in IrO_2, a material showing great potential to be exploited in spintronic technologies once a deeper understanding of the SOC in this system. In particular, they bring the possibility to tune the desired functionality of high resistance spin Hall-based devices, in sight of the tunable balance between the different SOC mechanisms which govern ISHE.

Conclusions and outlook

The purpose of this thesis has been the study of the thermal spin transport —specifically, of the spin Seebeck effect (SSE)— in bilayer structures composed by a thin film of a magnetically ordered material (FM) and, on top of this, a thin film of a nonmagnetic metal (NM) with strong spin-orbit coupling (SOC). In particular, the work has focused on the use of the ferrimagnetic insulating γ-Fe_2O_3 as FM material, and has also explored the performance of IrO_2 as NM in spin-to-charge conversion. In both cases, the work has been guided by a double goal: the expansion of the current understanding of the fundamental mechanisms behind the SSE and the ISHE, and the prospect of the enhancement of the efficiency of the spin transport processes in order to facilitate their implementation in technological applications.

In this chapter, the final conclusions extracted from the key results of this thesis are presented together with a brief outlook on future research that this work may stimulate.

(a) Growth of materials as thin films

Spintronics requires three fundamental operations: generation, transport and detection of spin angular momentum. In this regard, two kinds of material are essential: firstly, electrical insulators with long-range magnetic order (MOIs) are ideal for the support of magnon spin currents, avoiding Joule power dissipation. In addition, metals displaying a strong SOC can be used for spin-to-charge current conversion and *vice versa* by means of the inverse and direct spin Hall effects (ISHE

and SHE), respectively. Thus, they constitute suitable platforms for the creation or detection of spin currents.

Concerning the first group of materials (MOIs), both the fabrication of epitaxial thin films of maghemite (γ-Fe_2O_3) by means of the pulsed laser deposition technique (PLD) and the fabrication of epitaxial thin films of $Y_2Fe_5O_{12}$ (YIG) by the chemical technique of polymer assisted deposition (PAD) have been addressed in this thesis. Concerning the second group of materials, the preparation of IrO_2 thin films by PLD has been optimized.

Maghemite is a classic material with many past and current applications. Throughout this thesis, its potential to be also emplyed within the field of spintronics has been proved. The fabrication of γ-Fe_2O_3 thin films on MgO substrates has been optimized in a two-step process: first, the deposition in high-vacuum conditions of Fe_3O_4 thin films, and, next, an *in situ* annealing in which the full transformation of Fe_3O_4 to γ-Fe_2O_3 takes place. The value of the deposition parameters which ensure a total $Fe_3O_4 \rightarrow \gamma$-$Fe_2O_3$ transformation have been determined. This optimization process has been supported by a complete structural, chemical, magnetic and electrical characterization, ruling out the spurious presence of other iron oxide phases and ensuring the attainment of the desired properties in γ-Fe_2O_3.

As for YIG, it is a material of outstanding technological relevance, due to its exceptional magnetic and magneto-optic properties. However, its application in emerging fields such as spintronics requires its fabrication as thin films down to a few nanometers of thickness; such a control is not achievable by the standard fabrication procedures, forcing the use of physical deposition techniques (PVD), expensive and displaying limited scalability. In this thesis, the fabrication of YIG epitaxial thin films of few nanometers of thickness using the chemical technique of PAD has been successfully addressed. The obtained thin films exhibit properties comparable to those of some of the films grown by PVD methods. In particular, the low coercivity and small magnetic Gilbert damping obtained must be highlighted. This is a relevant result from the technological point of view as it enables the fabrication of YIG epitaxial thin films with the thickness and adequate properties

for emerging applications using a technique which is fast, cheap and highly scalable to the industry level.

In this regard, a natural step arising from this work is the exploration of the feasibility of PAD to fabricate γ-Fe_2O_3 thin films, in order to favor its technological implementation at the industrial scale, since its suitability for thermal spintronics applications has been demonstrated in this thesis.

Finally, the optimized growth parameters for PLD-fabrication of IrO_2 thin films with the desired properties for spin-to-charge conversion have been found. The use of IrO_2 responds to two potential advantages over the usually used materials (noble metals with high atomic number, e.g., Pt): its high electrical resistivity, which makes it especially suitable for spin current detection, and its oxide nature, which provides high chemical stability and optical transparency, which may be a requirement for specific applications.

(b) The spin Seebeck effect in γ-Fe_2O_3/Pt bilayers

Throughout this thesis, the SSE has been extensively studied in γ-Fe_2O_3/Pt bilayers, both in quasi-static conditions, and under ultrafast photoexcitation with the purpose of studying SSE dynamics.

Static conditions

Firstly, the SSE has been studied using the external heater method. Concerning the magnitude of the phenomenon, results are very promising, since the output voltages are larger than those reported in literature using other MOIs. Besides, the two contributions to the thermal spin current in the SSE —that of the interfacial SSE (iLSSE) and the one originated from the thermally induced bulk magnon accumulation in the FM thickness (bLSSE)— have been successfully disentangled, with the relative quantification of each one. It has been thereby proved that, in the usual range of a magnetic layer thickness of tens of nanometers, neither of both mechanisms can be neglected for a rigorous interpretation of LSSE experiments

under steady heating conditions, although *b*LSSE dominates over *i*LSSE. This reuslt brings insight into the global picture of the LSSE, improving its description, and may guide the design of SSE-based devides, assisting the optimization of the involved parameters. Finally, the temperature dependence of the SSE has been characterized, identifying three different regions. The behaviors inside these ranges have been explained in terms of the competition between different magnon transport-related mechanisms in the γ-Fe_2O_3 layer together with the evolution with temperature of the mechanism governing ISHE in Pt.

In this line, future research devoted to the γ-Fe_2O_3 thickness analysis for different temperatures could provide the individual-contribution evolution with the temperature, giving overall insight on this complex dependence. Furthermore, the identification of ways to enhance the individual contributions should be addressed in order to engineer future applications.

Secondly, an alternative method for the SSE study has been implemented: the current-induced or Joule-induce SSE (JSSE). The comparative analysis of the results obtained for identical samples using this method and the external heater method has demonstrated the equivalence between both of them. This is evidenced by the heat-flux scaling of the spin Seebeck coefficient. The current-induced method displays the advantages of higher experimental simplicity and lower experimental error.

Furthermore, it has been shown that the current-induced methods enables the simultaneous observation of the spin Hall magnetoresistance (SMR) when studying the angular dependence. The SMR characteristic parameters has been obtained for γ-Fe_2O_3/Pt, finding that they compare very well with those reported in literature for YIG/Pt. This suggests that the transfer of spin angular momentum across both interfaces is highly similar.

Time evolution

With the purpose of studying the temporal evolution of the SSE, a technique able to access the expected time scale of the phenomenon has been utilized: the

Terahertz Emission Spectroscopy (TES). Using this technique, the SSE dynamics has been investigated in FM/Pt bilayers (where FM stands for a magnetically-ordered material) through optical excitation at the femtosecond scale, employing as FM three different materials: insulating γ-Fe_2O_3, half-metallic Fe_3O_4 and metallic iron.

Concerning γ-Fe_2O_3/Pt, the measured time evolution of the spin current has been compared to that of YIG/Pt previously reported. The obtained results show that the SSE dynamics are identical for both systems, entailing that the spin current is solely determined by the relaxation dynamics of the electrons in the NM layer (here, Pt). Furthermore, the magnitude of the thermal spin current excited in γ-Fe_2O_3/Pt is two times larger than that excited in YIG/Pt, showing maghemite's potential to be used in magneto-optic devices in the spectral range of teraherzts.

In the case of Fe_3O_4/Pt, the results reveal two spin-current components, one faster than the other. The overall spin current can be well reproduced by a linear combination of the spin currents measured in γ-Fe_2O_3/Pt and Fe/Pt, implying that one contribution is the magnon spin current originated by SSE, and the faster being the conduction-electron spin current originated by spin-dependent Seebeck effect (SDSE). Therefore, the separated observation of both effects has been achieved. In addition, the SDSE component is negative with respect the SSE component and/or with respect the spin current in γ-Fe_2O_3/Pt: this constitutes an experimental evidence of half-metallic nature of Fe_3O_4, which exhibits a negative spin-polarization at the Fermi level. In this regard, a temperature-dependent experiment of the SSE down to the magnetite's Verwey transition, below which SDSE should not be operative, may bring new insight into the mechanisms behind this enigmatic transition, which, to date, have not been fully elucidated.

In general, spintronics has positioned itself as a promising candidate to provide efficient emitters and sensors in the elusive "THz gap"; in this work, the thermal spin currents potential has been proved, by showing that their temporal scale lies precisely within this spectral window.

(c) Inverse spin Hall effect in IrO_2

Lastly, the feasibility of IrO_2 thin films to be used for spin-to-charge current conversion by ISHE has been investigated in this thesis. In particular, γ-Fe_2O_3/IrO_2 bilayer structures have been fabricated on Al_2O_3 substrates. It has been shown that IrO_2 exhibits, in these samples, a strongly textured crystal structure (i.e., with a preferential crystal orientation).

Using thermal excitation of spin currents in these bilayers, it has been shown that ISHE is operative in IrO_2, allowing the spin-to-charge current conversion. Moreover, the spin Hall angle shows a negative sign in the whole range of temperatures in which measurements have been performed, in contrast to previous reports on amorphous of fully polycrystalline IrO_2 without a preferred crystal orientation.

Through the analysis of the ISHE voltage dependence on the IrO_2 layer thickness, the SOC mechanism governing ISHE in IrO_2 at room temperature has been investigated. The observed scaling of the spin Hall angle with the electrical conductivity as $\theta_{SH} \propto \sigma_c$ rules out a dominant role of the skew scattering, pointing to the intrinsic mechanism as the foremost contribution.

The negative sign of the spin Hall angle observed in these samples with a preferential texture, unlike previous reports on non-oriented samples and in context of a highly anisotropic value of the intrinsic spin Hall conductivity in this material, brings the possibility of tuning the desired functionality (via the sign and value of the spin Hall angle) of high-resistance spin-Hall-based devices through the control of crystal properties. In order to achieve this ambitious objective, a first step involves spin-to-charge conversion experiments either in IrO_2 samples displaying different crystal orientations, either injecting spin current in different directions within one sample.

Conclusiones y perspectivas

El objetivo de esta tesis ha sido el estudio del trasporte térmico de espín —en concreto, del efecto Seebeck de espín (SSE)— en estructuras tipo bicapa compuestas por una película delgada de un material con orden magnético de largo alcance (FM) y, sobre esta, una película delgada adyacente de un material metálico no magnético (NM) con un fuerte acoplamiento espín-órbita (SOC). En particular, el trabajo se ha centrado en el uso del aislante ferrimagnético γ-Fe_2O_3 como material FM, y también ha explorado el funcionamiento del IrO_2 como NM para conversión entre corrientes de espín y carga. En ambos casos, el trabajo se ha guiado por un doble objetivo: la expansión del conocimiento actual acerca de los mecanismos fundamentales tras el SSE y el ISHE, y la expectativa de ampliar la eficiencia en los procesos de transporte de espín con el objetivo de posibilitar su implementación en aplicaciones tecnológicas.

En este capítulo, se presentan las conclusiones finales extraídas de los resultados clave de esta tesis, junto con un breve apunte acerca de futuras líneas de investigación que este trabajo podría estimular.

(a) Crecimiento de materiales en forma de películas delgadas

Las operaciones fundamentales que requiere la espintrónica son la generación, el transporte y la detección de momento angular de espín. En este sentido, dos tipos de materiales resultan esenciales: por un lado, los aislantes eléctricos que presentan orden magnético de largo alcance (MOIs) resultan ideales para transportar corrientes

de espín magnónicas sin pérdidas por efecto Joule. Por otro lado, los metales con alto SOC permiten convertir corrientes de carga en corrientes de espín y viceversa, mediante los efectos Hall de espín directo e inverso (SHE e ISHE), lo que los convierte en medios apropiados para la creación o la detección de corriente de espín.

Respecto al primer grupo de materiales (MOIs), en esta tesis se ha estudiado la fabricación de láminas delgadas epitaxiales de maghemita (γ-Fe_2O_3) mediante deposición por láser pulsado (PLD) y la fabricación de láminas delgadas epitaxiales de $Y_2Fe_5O_12$ (YIG) mediante la técnica química de deposición asistida por polímeros. En cuanto al segundo grupo de materiales, se ha optimizado la preparación de láminas delgadas de IrO_2 mediante PLD.

La maghemita es un material clásico con multitud de aplicaciones recientes y pasadas. A lo largo de esta tesis, se ha demostrado su gran potencial para ser empleada también en el campo de la espintrónica. Se ha optimizado la fabricación de películas delgadas de γ-Fe_2O_3, sobre sustratos de MgO a través de un procedimiento en dos pasos: en primer lugar, el depósito en condiciones de alto vacío de películas delgadas de Fe_3O_4 y, a continuación, el recocido *in situ* para llevar a cabo la transformación total de la Fe_3O_4 en γ-Fe_2O_3. Se han encontrado los parámetros óptimos para este recocido que aseguran que la transformación de $Fe_3O_4 \rightarrow \gamma$-$Fe_2O_3$ es total, obteniendo películas epitaxiales de γ-Fe_2O_3 de gran calidad. Este proceso de optimización se ha apoyado en una completa caracterización estructural, química, magnética y eléctrica para probar la ausencia de otras fases de óxido de hierro y la consecución de las propiedades buscadas en la γ-Fe_2O_3.

Por su parte, el YIG es un material de interés tecnológico especialmente notable debido a sus excepcionales propiedades magnéticas y magneto-ópticas. Sin embargo, su aplicación en campos emergentes como el de la espintrónica requiere de la fabricación de películas delgadas de pocos nanómetros de espesor; este control no es posible mediante la técnica de fabricación estándar y hace necesario recurrir a técnicas físicas de elevado coste y reducida escalabilidad. En esta tesis, se ha conseguido fabricar películas delgadas epitaxiales de YIG de pocos nanómetros de espesor mediante la técnica química de PAD. Las películas

obtenidas muestran propiedades comparables a las fabricadas mediante métodos físicos. En especial, cabe resaltar los reducidos valores de coercitividad y atenuación magnética obtenidos. Este resultado es especialmente relevante desde el punto de vista tecnológico, puesto que posibilita la fabricación de películas expitaxiales de YIG con el espesor y las propiedades requeridas para las aplicaciones emergentes mediante una técnica rápida, barata y escalable a nivel industrial.

Es este sentido, un paso natural después de esta tesis sería la investigación de la posibilidad de fabricar películas delgadas de γ-Fe_2O_3 mediante la técnica de PAD, para favorecer su implementación tecnológica a gran escala, una vez demostrada en este trabajo su idoneidad en aplicaciones de termoespintrónica.

Por último, se han encontrado los parámetros de crecimiento que permiten fabricar mediante PLD películas delgadas de IrO_2 con las propiedades adecuadas para ser utilizados en procesos de conversión de corrientes de espín en corrientes de carga. El propósito de usar IrO_2 responde a dos ventajas frente a los materiales usados habitualmente (metales puros de elevado número atómico, como por ejemplo el Pt): su elevada resistividad, que lo hace especialmente idóneo para la detección de corrientes de espín; y, como óxido, su alta estabilidad química y su transparencia, que puede ser requerida para algunas aplicaciones.

(b) Efecto Seebeck de espín en bicapas γ-Fe_2O_3/Pt

A lo largo de esta tesis se ha estudiado de manera extensa el SSE en bicapas γ-Fe_2O_3/Pt, tanto en condiciones cuasi-estáticas como bajo fotoexcitación ultrarrápida con el objetivo de estudiar investigar su dinámica.

Condiciones estáticas

En primer lugar, se ha estudiado el SSE empleando el método de calentamiento mediante una resistencia externa. Respecto a la magnitud del fenómeno, se han observado resultados muy prometedores, ya que los voltajes de salida son superiores a los reportados en literatura para otros MOIs. Además, mediante el estudio del

SSE en función del espesor de la capa de γ-Fe_2O_3, se ha conseguido separar las dos contribuciones a la corriente térmica de espín: la del SSE interfacial (iLSSE) y la de la acumulación de magnones inducida térmicamente en el espesor de la γ-Fe_2O_3 (bLSSE), cuantificando la contribución relativa de ambas. Así, se ha demostrado que, en el rango de espesores de decenas de nanómetros, ninguno de los dos mecanismos puede despreciarse en una interpretación rigurosa del fenómeno en condiciones estáticas, si bien la contribución del bLSSE domina sobre la del iLSSE. Este resultado mejora la descripción del SSE y sirve de guía para la optimización de parámetros en el diseño de dispositivos basados en el SSE. Por último, se ha caracterizado la evolución del SSE con la variación de temperatura, identificando tres rangos de comportamiento diferentes. Estos rangos se han explicado en términos de la competición entre diferentes mecanismos relacionados con el transporte de magnones en la capa de γ-Fe_2O_3 junto con la evolución con la temperatura del principal mecanismo dominando el ISHE en la capa de Pt.

En este sentido, sería interesante repetir el análisis en función del espesor para diferentes temperaturas con el objetivo de caracterizar de manera individual la dependencia de cada mecanismo (iLSSE y bLSSE) con la temperatura. De esta manera, se podría arrojar luz sobre la compleja dependencia global. Además, debería abordarse el estudio de formas de aumentar individualmente cada contribución con el objetivo de diseñar futuras aplicaciones.

En segundo lugar, se ha implementado un método alternativo para la medida del SSE: el método de calentamiento inducido por corriente o método de calentamiento Joule (JSSE). El análisis comparativo de los resultados obtenidos en muestras idénticas mediante este método y el de calentamiento mediante resistencia externa ha probado la equivalencia entre ambos métodos de medida. Esta equivalencia se hace evidente al emplear la normalización por el flujo de calor del coeficiente Seebeck de espín. El método de calentamiento inducido por corriente tiene las ventajas de una mayor simplicidad experimental y una reducción considerable en el error experimental.

Además, se ha comprobado que el método de calentamiento inducido por

corriente permite la observación simultánea del fenómeno de magnetorresistencia Hall de espín (SMR) al estudiar la dependencia angular, habiendo obtenido que los parámetros que caracterizan este efecto en bicapas γ-Fe_2O_3/Pt comparan muy bien con los reportados en literatura para YIG/Pt. Esto indica que la transferencia de momento angular de espín entre las dos intercaras es muy similar.

Evolución temporal

Con el objeto de estudiar la evolución temporal del SSE, se ha recurrido a una técnica que permita caracterizar la escala temporal del fenómeno: la Espectroscopía de Emisión de Terahercios (TES). Mediante esta técnica, se ha estudiado la dinámica del efecto SSE en bicapas tipo FM/Pt mediante excitación óptica en la escala de femtosegundos, empleando como FM tres materiales diferentes: el aislante γ-Fe_2O_3, el mediometal Fe_3O_4 y el Fe metálico.

En lo relativo a la bicapa γ-Fe_2O_3/Pt, se ha comparado la evolución temporal obtenida para la corriente de espín con la reportada previamente en bicapas de YIG/Pt. Los resultados obtenidos muestran que la dinámica del SSE es idéntica en ambos sistemas, de manera que la corriente de espín está únicamente determinada por la dinámica de los electrones de la capa NM (Pt, en este caso). Además, la magnitud de la corriente medida en γ-Fe_2O_3/Pt es doble que la medida en YIG/Pt, demostrando el potencial de la γ-Fe_2O_3 para ser utilizada en dispositivo magneto-ópticos en el rango de frecuencias de los terahercios.

En el caso de la Fe_3O_4, los resultados revelan dos componentes de la corriente de espín: una rápida y otra más lenta. El hecho de que estas componentes puedan reproducirse mediante una combinación linear de las corrientes obtenidas en la γ-Fe_2O_3 y en el Fe indica que provienen de las contribuciones del SSE y del efecto Seebeck dependiente de espín (SDSE), respectivamente. Por lo tanto, se ha podido observar de manera separada ambos efectos que, habitualmente, aparecen superpuestos. Además, la componente del SDSE es negativa respecto de la componente del SSE o de la corriente de espín observada en el sistema Fe/Pt: este resultado es una evidencia del carácter mediometálico de la Fe_3O_4 que posee

polarización negativa de espín de los electrones en el nivel de Fermi. En este sentido, resultaría interesante realizar el experimento de la evolución del SDSE y del SSE con la temperatura, hasta observar la transición de Verwey de la Fe_3O_4, por debajo de la cual la contribución del SDSE debería desaparecer. Esta caracterización de la transición podría arrojar nueva luz sobre los mecanismos que la inducen, que a día de hoy no han sido totalmente dilucidados.

En general, la espintrónica se ha posicionado como una candidata muy prometedora para proveer de emisores y sensores eficientes en el elusivo rango espectral de los terahercios; aquí se demostrado el potencial de las corrientes de espín excitadas térmicamente, al determinar que su escala temporal cae precisamente dentro de esta ventana.

(c) Efecto Hall de espín inverso en IrO_2

Finalmente, en esta tesis se ha estudiado la posibilidad de emplear películas delgadas de IrO_2 para detección de corriente de espín mediante ISHE. En particular, se han implementado mediante la técnica de PLD bicapas γ-Fe_2O_3/IrO_2 sobre sustratos de Al_2O_3. Se ha comprobado que el IrO_2 presenta en estas muestras una estructura cristalina fuertemente texturada (es decir, con una dirección cristalina preferente).

Mediante la generación térmica de corrientes de espín en estas bicapas, se ha comprobado que el ISHE es operativo en el IrO_2, permitiendo la conversión de corrientes de espín en corrientes de carga. Asimismo, se ha observado que el signo del ángulo Hall de espín es negativo en todo el rango de temperaturas explorado, a diferencia de lo reportado en la literatura para muestras amorfas o policristalinas sin dirección preferencial.

A través del análisis de la dependencia del voltaje procedente del ISHE con el espesor de la película de IrO_2, se ha indagado sobre el mecanismo de SOC que gobierna el ISHE en las muestras texturadas de IrO_2 a temperatura ambiente. Se ha observado que la relación del ángulo Hall de espín con la conductividad eléctrica es $\theta_{SH} \propto \sigma_c$, lo que descarta un papel dominante de la dispersión asimétrica (*skew scattering*) y señalando al mecanismo intrínseco como principal contribución.

El signo negativo del ángulo Hall de espín observado en muestras con dirección cristalina preferencial en un contexto de una conductividad Hall de espín intrínseca fuertemente anisotrópica abre las puertas a la posibilidad de ajustar la funcionalidad (a través del valor y el signo de este parámetro) mediante el control de las propiedades cristalinas. Para alcanzar este ambicioso objetivo, se precisa la realización de experimentos de conversión de corrientes de carga en corrientes de espín bien en muestras de IrO_2 con diferentes direcciones cristalina, bien inyectando la corriente de espín en distintas direcciones.

List of publications

Part of the work presented in this doctoral thesis has been the source of 3 articles already published in peer-reviewed international journals that belong to the Science Citation Index. In addition, there are 2 articles under peer-review process and another one in preparation.

(1) P. Jiménez-Cavero, I. Lucas, A. Anadón, R. Ramos, T. Niizeki, M. H. Aguirre, P. A. Algarabel, K. Uchida, M. R. Ibarra, E. Saitoh, L. Morellón. "Spin Seebeck effect in epitaxial insulating γ-Fe_2O_3 thin films." *APL Mater.* 5, 026103 (2017).

(2) I. Lucas, P. Jiménez-Cavero, J. M. Vila-Fungueiriño, C. Magén, S. Sangiao, J. M. de Teresa, L. Morellón and F. Rivadulla. "Chemical solution synthesis and ferromagnetic resonance of epitaxial thin films of yttrium iron garnet." *Phys. Rev. Mat.* 1, 074407 (2017).

(3) P. Jiménez-Cavero, I. Lucas, D. Bugallo, C. López-Bueno, R. Ramos, P. A. Algarabel, M. R. Ibarra, F. Rivadulla and L. Morellón. "Quantification of the interfacial and bulk contributions to the longitudinal spin Seebeck effect". Accepted for publication in *Appl. Phys. Lett.* 118(9) (February 2021).

(4) E. Arias-Egido, M. A. Laguna-Marco, C. Piquer, P. Jiménez-Cavero, I. Lucas, L. Morellón, F. Gallego, A. Rivera-Calzada, J. Santamaria, G. Fabbris, D. Haskel, R. Boada, and S. Díaz-Moreno. "Dimensionality-Driven Metal-Insulator Transition in SpinOrbit-Coupled IrO_2". *Submitted* (December 2020).

(5) P. Jiménez-Cavero, I. Lucas, J. Ara-Arteaga, M. R. Ibarra, P. A. Algarabel and

L. Morellón. "Spin Hall mechanism in PLD-grown IrO_2 thin films". *Submitted* (February 2021).

(6) P. Jiménez-Cavero*, Oliver Gueckstock*, Irene Lucas, Lukáš Nádvorník, Martin Wolf, Piet W. Brouwer, Gerhard Jakob, Mathias Kläui, Chenyang Guo, Caihua Wan, Xiufeng Han, Zuanming Jin, Di Wu11, Luis Morellón and Tobias Kampfrath. "Ultrafast photoinduced spin currents in bilayers of Pt and magnets with different conductivity: Spin-dependent vs spin Seebeck effect". *In preparation.*

* *contributed equally*

Other publications:

(7) E. Ferreiro-Vila, L. Iglesias, I. Lucas, N. Varela-Domínguez, C. T. Bui, B. Rivas-Murias, J. M. Vila-Fungueiriño, P. Jiménez-Cavero, C. Magen, L. Morellón, V. Pardo and F. Rivadulla. "Apparent auxetic to non-auxetic crossover driven by Co^{2+} redistribution in $CoFe_2O_4$ thin films" *APL Mater.* 7, 031109 (2019).

(8) B. Rivas-Murias, I. Lucas, Pilar Jiménez-Cavero, C. Magén, L. Morellón and F. Rivadulla. "Independent Control of the Magnetization in Ferromagnetic $La_{2/3}Sr_{1/3}MnO_3/SrTiO_3/LaCoO_3$ Heterostructures Achieved by Epitaxial Lattice Mismatch." *Nano Lett.* 16, 1736-1740 (2016).

(9) I. Lucas, J. M. Vila-Fungueiriño, Pilar Jiménez-Cavero, B. Rivas-Murias, C. Magén, L. Morellón and F. Rivadulla. *ACS Appl. Mater. Interfaces* 6, 21279-21285 (2014).

Bibliography

[1] E. Pop, S. Sinha, and K. E. Goodson. Heat Generation and Transport in Nanometer-Scale Transistors. *Proceedings of the IEEE*, **94**(8): 1587–1601 (2006).

[2] G. E. Moore. Cramming more components onto integrated circuits. *Electronics*, **8**(3): 114 (1965).

[3] G. E. Moore. Progress in Digital Integrated Electronics. *Proc. Technical Digest Int'l Electron Devices Meeting*, **21**(3): 11–13 (1975).

[4] R. P. Feynman. There's Plenty of Room at the Bottom. *Engineering and Science*, **23**(5): 22–36 (1960).

[5] S. A. Wolf, D. D. Awschalom, R. A. Buhrman, J. M. Daughton, S. von Molnár, M. L. Roukes, A. Y. Chtchelkanova, and D. M. Treger. Spintronics: A Spin-Based Electronics Vision for the Future. *Science*, **294**(5546): 1488–1495 (2001).

[6] A. Hirohata and K. Takanashi. Future perspectives for spintronic devices. *Journal of Physics D: Applied Physics*, **47**(19): 193001 (2014).

[7] M. N. Baibich, J. M. Broto, A. Fert, F. N. Van Dau, F. Petroff, P. Etienne, G. Creuzet, A. Friederich, and J. Chazelas. Giant Magnetoresistance of (001)Fe/(001)Cr Magnetic Superlattices. *Phys. Rev. Lett.*, **61**: 2472–2475 (1988).

[8] G. Binasch, P. Grünberg, F. Saurenbach, and W. Zinn. Enhanced magnetoresistance in layered magnetic structures with antiferromagnetic interlayer exchange. *Phys. Rev. B*, **39**: 4828–4830 (1989).

[9] S. Bader and S. Parkin. Spintronics. *Annual Review of Condensed Matter Physics*, **1**(1): 71–88 (2010).

[10] J. Sinova and I. Žutić. New moves of the spintronics tango. *Nature Materials*, **11**(5): 368–371 (2012).

[11] A. Hoffmann. Spin Hall Effects in Metals. *IEEE Trans. Magn.*, **49**(10): 5172–5193 (2013).

[12] E. Y. Vedmedenko, R. K. Kawakami, D. D. Sheka, P. Gambardella, A. Kirilyuk, A. Hirohata, C. Binek, O. Chubykalo-Fesenko, S. Sanvito, B. J. Kirby, J. Grollier, K. Everschor-Sitte, T. Kampfrath, C. Y. You, and A. Berger. The 2020 magnetism roadmap. *Journal of Physics D: Applied Physics*, **53**(45) (2020).

[13] A. V. Chumak, V. I. Vasyuchka, A. A. Serga, and B. Hillebrands. Magnon spintronics. *Nature Physics*, **11**(6): 453–461 (2015).

[14] A. Hoffmann and S. D. Bader. Opportunities at the Frontiers of Spintronics. *Phys. Rev. Applied*, **4**: 047001 (2015).

[15] C. Cohen-Tannoudji, B. Diu, and F. Laloë. *Quantum mechanics*. Wiley, New York, NY (1977). Trans. of : Mécanique quantique. Paris : Hermann, 1973.

[16] G. Uhlenbeck and S. Goudsmit. Ersetzung der Hypothese vom unmechanischen Zwang durch eine Forderung bezüglich des inneren Verhaltens jedes einzelnen Elektrons. *Naturwissenschaften*, **13**(47): 953–954 (1925).

[17] W. Nolting and A. Ramakanth. *Quantum Theory of Magnetism*. Springer Berlin Heidelberg (2009).

[18] P. A. M. Dirac and R. H. Fowler. The quantum theory of the electron. *Proceedings of the Royal Society of London. Series A, Containing Papers of a Mathematical and Physical Character*, **117**(778): 610–624 (1928).

[19] S. Maekawa, S. Valenzuela, E. Saitoh, and T. Kimura. *Spin Current*. Oxford Science Publications, Oxford University Press (2015).

[20] J. Coey. *Magnetism and Magnetic Materials*. Cambridge University Press (2010).

[21] C. Kittel. *Introduction to Solid State Physics*. Wiley, 7 edition (2004).

[22] N. W. Ashcroft and N. D. Mermin. *Solid State Physics*. Saunders College Publishers (1976).

[23] L. J. Cornelissen, K. J. H. Peters, G. E. W. Bauer, R. A. Duine, and B. J. van Wees. Magnon spin transport driven by the magnon chemical potential in a magnetic insulator. *Phys. Rev. B*, **94**: 014412 (2016).

[24] K. Vandaele, S. J. Watzman, B. Flebus, A. Prakash, Y. Zheng, S. R. Boona, and J. P. Heremans. Thermal spin transport and energy conversion. *Materials Today Physics*, **1**: 39 – 49 (2017).

[25] S. S.-L. Zhang and S. Zhang. Magnon Mediated Electric Current Drag Across a Ferromagnetic Insulator Layer. *Phys. Rev. Lett.*, **109**: 096603 (2012).

[26] A. Hoffmann. Pure spin-currents. *physica status solidi c*, **4**(11): 4236–4241 (2007).

[27] M. Althammer. Pure spin currents in magnetically ordered insulator/normal metal heterostructures. *J. Phys. D. Appl. Phys.*, **51**: 313001 (2018).

[28] M. Julliere. Tunneling between ferromagnetic films. *Physics Letters A*, **54**(3): 225 – 226 (1975).

[29] H. Adachi, K. I. Uchida, E. Saitoh, and S. Maekawa. Theory of the spin Seebeck effect. *Reports on Progress in Physics*, **76**(3) (2013).

[30] M. Sparks. *Ferromagnetic-relaxation Theory.* McGraw-Hill advanced physics monograph series, McGraw-Hill (1964).

[31] A. Gurevich and G. Melkov. *Magnetization Oscillations and Waves.* Taylor & Francis (1996).

[32] Y. Kajiwara, K. Harii, S. Takahashi, J. Ohe, K. Uchida, M. Mizuguchi, H. Umezawa, H. Kawai, K. Ando, K. Takanashi, S. Maekawa, and E. Saitoh. Transmission of electrical signals by spin-wave interconversion in a magnetic insulator. *Nature*, **464**(7286): 262–266 (2010).

[33] L. J. Cornelissen, J. Liu, R. A. Duine, J. B. Youssef, and B. J. Van Wees. Long-distance transport of magnon spin information in a magnetic insulator at room temperature. *Nature Physics*, **11**: 1022–1026 (2015).

[34] B. L. Giles, Z. Yang, J. S. Jamison, and R. C. Myers. Long-range pure magnon spin diffusion observed in a nonlocal spin-Seebeck geometry. *Phys. Rev. B*, **92**: 224415 (2015).

[35] J. M. Gomez-Perez, S. Vélez, L. E. Hueso, and F. Casanova. Differences in the magnon diffusion length for electrically and thermally driven magnon currents in $Y_3Fe_5O_{12}$. *Phys. Rev. B*, **101**: 184420 (2020).

[36] M. Althammer, S. T. B. Goennenwein, and R. Gross. Magnetically Ordered Insulators for Advanced Spintronics (2017).

[37] Q.-f. Sun and X. C. Xie. Definition of the spin current: The angular spin current and its physical consequences. *Phys. Rev. B*, **72**: 245305 (2005).

[38] T. S. *Handbook of Spintronics*, chapter Physical Principles of Spin Pumping. Springer, Dordrecht (2016).

[39] Y. Tserkovnyak, A. Brataas, G. E. W. Bauer, and B. I. Halperin. Nonlocal magnetization dynamics in ferromagnetic heterostructures. *Rev. Mod. Phys.*, **77**: 1375–1421 (2005).

[40] A. Brataas, Y. V. Nazarov, and G. E. W. Bauer. Finite-Element Theory of Transport in Ferromagnet–Normal Metal Systems. *Phys. Rev. Lett.*, **84**: 2481–2484 (2000).

[41] H. Ohno, D. Chiba, F. Matsukura, T. Omiya, E. Abe, T. Dietl, and Y. Ohno. Electric-field control of ferromagnetism. *Nature*, **408**: 944—-946 (2000).

[42] M. Dyakonov and V. Perel. Possibility of orienting electron spins with current. *Soviet Journal of Experimental and Theoretical Physics Letters*, **13**(11): 657–660 (1971).

[43] M. Dyakonov and V. Perel. Current-induced spin orientation of electrons in semiconductors. *Physics Letters A*, **35**(6): 459 – 460 (1971).

[44] J. E. Hirsch. Spin Hall Effect. *Phys. Rev. Lett.*, **83**: 1834–1837 (1999).

[45] Y. K. Kato, R. C. Myers, A. C. Gossard, and D. D. Awschalom. Observation of the Spin Hall Effect in Semiconductors. *Science*, **306**(5703): 1910–1913 (2004).

[46] S. Zhang. Spin Hall effect in the presence of spin diffusion. *Phys. Rev. Lett.*, **85**(2): 393–396 (2000).

[47] N. Nagaosa, J. Sinova, S. Onoda, A. H. MacDonald, and N. P. Ong. Anomalous Hall effect. *Rev. Mod. Phys.*, **82**: 1539–1592 (2010).

[48] S. O. Valenzuela and M. Tinkham. Direct electronic measurement of the spin Hall effect. *Nature*, **442**(7099): 176–179 (2006).

[49] E. Saitoh, M. Ueda, H. Miyajima, and G. Tatara. Conversion of spin current into charge current at room temperature: Inverse spin-Hall effect. *Appl. Phys. Lett.*, **88**(18): 1–4 (2006).

[50] J. Wunderlich, B. Kaestner, J. Sinova, and T. Jungwirth. Experimental Observation of the Spin-Hall Effect in a Two-Dimensional Spin-Orbit Coupled Semiconductor System. *Phys. Rev. Lett.*, **94**: 047204 (2005).

[51] T. Kimura, Y. Otani, T. Sato, S. Takahashi, and S. Maekawa. Room-Temperature Reversible Spin Hall Effect. *Phys. Rev. Lett.*, **98**: 156601 (2007).

[52] J. Sinova, S. O. Valenzuela, J. Wunderlich, C. H. Back, and T. Jungwirth. Spin Hall effects. *Rev. Mod. Phys.*, **87**(4): 1213–1260 (2015).

[53] M. Gradhand, D. V. Fedorov, P. Zahn, and I. Mertig. Extrinsic spin hall effect from first principles. *Phys. Rev. Lett.*, **104**(18): 2–5 (2010).

[54] J. Smit. The spontaneous hall effect in ferromagnetics I. *Physica*, **21**(6): 877 – 887 (1955).

[55] J. Smit. The Spontaneous Hall Effect in Ferromagnets II. *Physica*, **24**: 39–51 (1958).

[56] L. Berger. Side-jump mechanism for the hall effect of ferromagnets. *Phys. Rev. B*, **2**(11): 4559–4566 (1970).

[57] J. Sinova, D. Culcer, Q. Niu, N. A. Sinitsyn, T. Jungwirth, and A. H. MacDonald. Universal intrinsic spin Hall effect. *Phys. Rev. Lett.*, **92**(12): 1–4 (2004).

[58] S. Murakami, N. Nagaosa, and S.-c. Zhang. Dissipationless Quantum Spin Current at Room Temperature. *Science*, **301**(September): 1348–1351 (2003).

[59] R. Karplus and J. M. Luttinger. Hall Effect in Ferromagnetics. *Phys. Rev.*, **95**: 1154–1160 (1954).

[60] M.-C. Chang and Q. Niu. Berry phase, hyperorbits, and the Hofstadter spectrum: Semiclassical dynamics in magnetic Bloch bands. *Phys. Rev. B*, **53**: 7010–7023 (1996).

[61] G. Sundaram and Q. Niu. Wave-packet dynamics in slowly perturbed crystals: Gradient corrections and Berry-phase effects. *Phys. Rev. B*, **59**: 14915–14925 (1999).

[62] S. Sangiao, L. Morellon, G. Simon, J. M. De Teresa, J. A. Pardo, J. Arbiol, and M. R. Ibarra. Anomalous Hall effect in Fe (001) epitaxial thin films over a wide range in conductivity. *Phys. Rev. B*, **79**: 014431 (2009).

[63] E. Sagasta, Y. Omori, M. Isasa, M. Gradhand, L. E. Hueso, Y. Niimi, Y. Otani, and F. Casanova. Tuning the spin Hall effect of Pt from the moderately dirty to the superclean regime. *Phys. Rev. B*, **94**: 060412 (2016).

[64] S. Onoda, N. Sugimoto, and N. Nagaosa. Intrinsic Versus Extrinsic Anomalous Hall Effect in Ferromagnets. *Phys. Rev. Lett.*, **97**: 126602 (2006).

[65] S. Onoda, N. Sugimoto, and N. Nagaosa. Quantum transport theory of anomalous electric, thermoelectric, and thermal Hall effects in ferromagnets. *Phys. Rev. B*, **77**: 165103 (2008).

[66] K. Uchida, S. Takahashi, K. Harii, J. Ieda, W. Koshibae, K. Ando, S. Maekawa, and E. Saitoh. Observation of the spin Seebeck effect. *Nature*, **455**: 778–781 (2008).

[67] K. Uchida, J. Xiao, H. Adachi, J. Ohe, S. Takahashi, J. Ieda, T. Ota, Y. Kajiwara, H. Umezawa, H. Kawai, G. E. Bauer, S. Maekawa, and E. Saitoh. Spin Seebeck insulator. *Nature Materials*, **9**(11): 894–897 (2010).

[68] K. I. Uchida, H. Adachi, T. Ota, H. Nakayama, S. Maekawa, and E. Saitoh. Observation of longitudinal spin-Seebeck effect in magnetic insulators. *Applied Physics Letters*, **97**(17) (2010).

[69] C. M. Jaworski, J. Yang, S. Mack, D. D. Awschalom, J. P. Heremans, and R. C. Myers. Observation of the spin-Seebeck effect in a ferromagnetic semiconductor. *Nature Materials*, **9**: 898–903 (2010).

[70] J. Xiao, G. E. W. Bauer, K.-c. Uchida, E. Saitoh, and S. Maekawa. Theory of magnon-driven spin Seebeck effect. *Phys. Rev. B*, **81**: 214418 (2010).

[71] H. Adachi, J.-i. Ohe, S. Takahashi, and S. Maekawa. Linear-response theory of spin Seebeck effect in ferromagnetic insulators. *Phys. Rev. B*, **83**: 094410 (2011).

[72] S. Hoffman, K. Sato, and Y. Tserkovnyak. Landau-Lifshitz theory of the longitudinal spin Seebeck effect. *Phys. Rev. B*, **88**: 064408 (2013).

[73] S. M. Rezende, R. L. Rodríguez-Suárez, R. O. Cunha, A. R. Rodrigues, F. L. A. Machado, G. A. Fonseca Guerra, J. C. Lopez Ortiz, and A. Azevedo. Magnon spin-current theory for the longitudinal spin-Seebeck effect. *Phys. Rev. B*, **89**: 014416 (2014).

[74] J. Flipse, F. K. Dejene, D. Wagenaar, G. E. W. Bauer, J. B. Youssef, and B. J. van Wees. Observation of the Spin Peltier Effect for Magnetic Insulators. *Phys. Rev. Lett.*, **113**: 027601 (2014).

[75] S. M. Wu, J. E. Pearson, and A. Bhattacharya. Paramagnetic Spin Seebeck Effect. *Phys. Rev. Lett.*, **114**: 186602 (2015).

[76] S. Seki, T. Ideue, M. Kubota, Y. Kozuka, R. Takagi, M. Nakamura, Y. Kaneko, M. Kawasaki, and Y. Tokura. Thermal Generation of Spin Current in an Antiferromagnet. *Phys. Rev. Lett.*, **115**: 266601 (2015).

[77] S. M. Wu, W. Zhang, A. KC, P. Borisov, J. E. Pearson, J. S. Jiang, D. Lederman, A. Hoffmann, and A. Bhattacharya. Antiferromagnetic Spin Seebeck Effect. *Phys. Rev. Lett.*, **116**: 097204 (2016).

[78] A. Slachter, F. L. Bakker, J. P. Adam, and B. J. Van Wees. Thermally driven spin injection from a ferromagnet into a non-magnetic metal. *Nature Physics*, **6**(11): 879–882 (2010).

[79] J. Flipse, F. L. Bakker, A. Slachter, F. K. Dejene, and B. J. V. Wees. Direct observation of the spin-dependent Peltier effect. *Nature Nanotechnology*, **7**(March): 166–168 (2012).

[80] G.-m. Choi, C.-h. Moon, B.-c. Min, K.-j. Lee, and D. G. Cahill. Thermal spin-transfer torque driven by the spin-dependent Seebeck effect in metallic spin-valves. *Nature Physics*, **11**(July) (2015).

[81] M. Agrawal, V. I. Vasyuchka, A. A. Serga, A. Kirihara, P. Pirro, T. Langner, M. B. Jungfleisch, A. V. Chumak, E. T. Papaioannou, and B. Hillebrands. Role of bulk-magnon transport in the temporal evolution of the longitudinal spin-Seebeck effect. *Phys. Rev. B*, **89**: 224414 (2014).

[82] J. Kimling, G.-M. Choi, J. T. Brangham, T. Matalla-Wagner, T. Huebner, T. Kuschel, F. Yang, and D. G. Cahill. Picosecond Spin Seebeck Effect. *Phys. Rev. Lett.*, **118**: 057201 (2017).

[83] T. S. Seifert, S. Jaiswal, J. Barker, S. T. Weber, I. Razdolski, J. Cramer, O. Gueckstock, S. F. Maehrlein, L. Nadvornik, S. Watanabe, C. Ciccarelli, A. Melnikov, G. Jakob, M. Münzenberg, S. T. B. Goennenwein, G. Woltersdorf, B. Rethfeld, P. W. Brouwer, M. Wolf, M. Kläui, and T. Kampfrath. Femtosecond formation dynamics of the spin Seebeck effect revealed by terahertz spectroscopy. *Nat. Commun.*, **9**: 2899 (2018).

[84] G. E. W. Bauer, E. Saitoh, B. J. V. Wees, and P. St. Spin caloritronics. *Nature Publishing Group*, **11**(5): 391–399 (2012).

[85] S. R. Boona, R. C. Myers, and J. P. Heremans. Spin caloritronics. *Energy Environ. Sci.*, **7**: 885–910 (2014).

[86] F. K. Dejene, J. Flipse, and B. J. van Wees. Spin-dependent Seebeck coefficients of $Ni_{80}Fe_{20}$ and Co in nanopillar spin valves. *Phys. Rev. B*, **86**: 024436 (2012).

[87] K. Uchida, M. Ishida, T. Kikkawa, A. Kirihara, T. Murakami, and E. Saitoh. Longitudinal spin seebeck effect: From fundamentals to applications. *Journal of Physics Condensed Matter*, **26**(343202): 1–15 (2014).

[88] T. Valet and A. Fert. Theory of the perpendicular magnetoresistance in magnetic multilayers. *Phys. Rev. B*, **48**: 7099–7113 (1993).

[89] K. Morrison, A. J. Caruana, and C. Cox. Towards a standard spin Seebeck measurement. *arXiv, 1705.02491* (2017).

[90] A. Sola, P. Bougiatioti, M. Kuepferling, D. Meier, G. Reiss, M. Pasquale, T. Kuschel, and V. Basso. Longitudinal spin Seebeck coefficient: heat flux vs. temperature difference method. *Sci. Rep.*, **7**: 46752 (2017).

[91] U. Ritzmann, D. Hinzke, and U. Nowak. Propagation of thermally induced magnonic spin currents. *Phys. Rev. B*, **89**: 024409 (2014).

[92] S. Rezende, R. Rodríguez-Suárez, R. Cunha, J. López Ortiz, and A. Azevedo. Bulk magnon spin current theory for the longitudinal spin Seebeck effect. *Journal of Magnetism and Magnetic Materials*, **400**: 171 – 177 (2016). Proceedings of the 20th International Conference on Magnetism (Barcelona) 5-10 July 2015.

[93] J. P. Heremans, M. S. Dresselhaus, L. E. Bell, and D. T. Morelli. When thermoelectrics reached the nanoscale. *Nature Nanotechnology*, **8**(July): 471–473 (2013).

[94] H. J. Goldsmid. *Introduction to Thermoelectricity*. Springer, pimera edition (2010).

[95] S. Y. Huang, W. G. Wang, S. F. Lee, J. Kwo, and C. L. Chien. Intrinsic Spin-Dependent Thermal Transport. *Phys. Rev. Lett.*, **107**: 216604 (2011).

[96] D. Meier, T. Kuschel, L. Shen, A. Gupta, T. Kikkawa, K. Uchida, E. Saitoh, J.-M. Schmalhorst, and G. Reiss. Thermally driven spin and charge currents in thin $NiFe_2O_4$/Pt films. *Phys. Rev. B*, **87**: 054421 (2013).

[97] R. Ramos, M. H. Aguirre, A. Anadón, J. Blasco, I. Lucas, K. Uchida, P. A. Algarabel, L. Morellón, E. Saitoh, and M. R. Ibarra. Anomalous Nernst effect of Fe_3O_4 single crystal. *Phys. Rev. B*, **90**: 054422 (2014).

[98] C. Fang, C. H. Wan, Z. H. Yuan, L. Huang, X. Zhang, H. Wu, Q. T. Zhang, and X. F. Han. Scaling relation between anomalous Nernst and Hall effect in $[Pt/Co]_n$ multilayers. *Phys. Rev. B*, **93**: 054420 (2016).

[99] H. Nakayama, M. Althammer, Y.-T. Chen, K. Uchida, Y. Kajiwara, D. Kikuchi, T. Ohtani, S. Geprägs, M. Opel, S. Takahashi, R. Gross, G. E. W. Bauer, S. T. B. Goennenwein, and E. Saitoh. Spin Hall Magnetoresistance Induced by a Nonequilibrium Proximity Effect. *Phys. Rev. Lett.*, **110**: 206601 (2013).

[100] Y.-T. Chen, S. Takahashi, H. Nakayama, M. Althammer, S. T. B. Goennenwein, E. Saitoh, and G. E. W. Bauer. Theory of spin Hall magnetoresistance. *Phys. Rev. B*, **87**: 144411 (2013).

[101] M. Althammer, S. Meyer, H. Nakayama, M. Schreier, S. Altmannshofer, M. Weiler, H. Huebl, S. Geprägs, M. Opel, R. Gross, D. Meier, C. Klewe, T. Kuschel, J.-M. Schmalhorst, G. Reiss, L. Shen, A. Gupta, Y.-T. Chen, G. E. W. Bauer, E. Saitoh, and S. T. B. Goennenwein. Quantitative study of the spin Hall magnetoresistance in ferromagnetic insulator/normal metal hybrids. *Phys. Rev. B*, **87**: 224401 (2013).

[102] H. M. Christen and G. Eres. Recent advances in pulsed-laser deposition of complex oxides. *J. Phys. Condens. Matter*, **20**: 264005 (2008).

[103] T. Venkatesan, X. D. Wu, A. Inam, and J. B. Wachtman. Observation of two distinct components during pulsed laser deposition of high Tc superconducting films. *Appl. Phys. Lett.*, **52**(14): 1193–1195 (1988).

[104] *Pulsed Laser Deposition of Thin Films: Applications-Led Growth of Functional Materials*. John Wiley & Sons, Inc. (2006).

[105] J. A. Greer and M. D. Tabat. Large-area pulsed laser deposition: Techniques and applications. *Journal of Vacuum Science & Technology A*, **13**(3): 1175–1181 (1995).

[106] J. Greer, M. Tabat, and C. Lu. Future trends for large-area pulsed laser deposition. *Nuclear Instruments and Methods in Physics Research Section B: Beam Interactions with Materials and Atoms*, **121**(1): 357 – 362 (1997). Materials Synthesis and Modification by Ion and/or Laser Beams.

[107] Pulsed laser vaporization and deposition. *Rev. Mod. Phys.*, **72**(1): 315–328 (2000).

[108] D. Chrisey and G. Hubler, editors. *Pulsed Laser Deposition of Thin Films*. John Wiley & Sons, Inc. (1994).

[109] H. Fujioka. *Handbook of Crystal Growth*, chapter 8: Pulsed Laser Deposition. Elsevier (2014).

[110] P. J. Kelly and R. D. Arnell. Magnetron sputtering: a review of recent developments and applications. *Vacuum*, **56**: 159–172 (2000).

[111] M. Ohring. *Materials Science of Thin Films*. Academic Press (Elsevier) (2002).

[112] K. S. Harsha. *Principles of Vapor Deposition of Thin Films*. Elsevier Science (2005).

[113] J. M. Vila-Fungueiriño, B. Rivas-Murias, J. Rubio-Zuazo, A. Carretero-Genevrier, M. Lazzari, and F. Rivadulla. Polymer assisted deposition of epitaxial oxide thin films. *J. Mater. Chem. C*, **6**: 3834–3844 (2018).

[114] Q. X. Jia, T. M. McCleskey, A. K. Burrell, Y. Lin, G. E. Collis, H. Wang, A. D. Li, and S. R. Foltyn. Polymer-assisted deposition of metal-oxide films. *Nat. Mater.*, **3**(8): 529–532 (2004).

[115] F. Rivadulla, Z. Bi, E. Bauer, B. Rivas-Murias, J. M. Vila-Fungueiriño, and Q. Jia. Strain-Induced Ferromagnetism and Magnetoresistance in Epitaxial Thin Films of $LaCoO_3$ Prepared by Polymer-Assisted Deposition. *Chem. Mat.*, **25**: 55–58 (2012).

[116] E. Ferreiro-Vila, L. Iglesias, I. Lucas Del Pozo, N. Varela-Dominguez, C. T. Bui, B. Rivas-Murias, J. M. Vila-Fungueiriño, P. Jiménez-Cavero, C. Magén, L. Morellón, V. Pardo, and F. Rivadulla. Apparent auxetic to non-auxetic crossover driven by Co^{2+} redistribution in $CoFe_2O_4$ thin films. *APL Mater.*, **7**: 031109 (2019).

[117] I. Lucas, P. Jiménez-Cavero, J. M. Vila-Fungueiriño, C. Magén, S. Sangiao, J. M. De Teresa, L. Morellón, and F. Rivadulla. Chemical solution synthesis and ferromagnetic resonance of epitaxial thin films of yttrium iron garnet. *Phys. Rev. Mater.*, **1**(7): 1–6 (2017).

[118] B. Rivas-Murias, I. Lucas, P. Jiménez-Cavero, C. Magén, L. Morellón, and F. Rivadulla. Independent Control of the Magnetization in Ferromagnetic $La_{2/3}Sr_{1/3}MnO_3/SrTiO_3/LaCoO_3$ Heterostructures Achieved by Epitaxial Lattice Mismatch. *Nano Lett.*, **16**(3): 1736–1740 (2016).

[119] M. Birkholz, P. F. Fewster, and C. Genzel. *Thin Film Analysis by X-Ray Scattering*. Wiley-VCH (2006).

[120] J. I. Langford and A. J. C. Wilson. Scherrer after sixty years: A survey and some new results in the determination of crystallite size. *J. Appl. Cryst.*, (11): 102–113 (1978).

[121] D. B. Williams and C. B. Carter. *Transmission Electron Microscopy: A Textbook for Materials Science*. Springer (2009).

[122] L. A. Bendersky and F. W. Gayle. Electron diffraction using transmission electron microscopy. *J. Res. Natl. Inst. Stand. Technol.*, **106**(6): 997–1012 (2001).

[123] D. A. Muller. Structure and bonding at the atomic scale by scanning transmission electron microscopy. *Nat. Mater.*, **8**(4): 263–270 (2009).

[124] R. L. Fagaly. Superconducting quantum interference device instruments and applications. *Rev. Sci. Instrum.*, **77**(10): 101101 (2006).

[125] L. J. Van der Pauw. A method of measuring the resistivity and Hall coefficient on lamellae of arbitrary shape. *Philips Tech. Rev.*, **20**(8): 220–224 (1958).

[126] J. Edwards, K. Kawabe, G. Stevens, and R. Tredgold. Space charge conduction and electrical behaviour of aluminium nitride single crystals. *Solid State Commun.*, **3**(5): 99–100 (1965).

[127] G. A. Slack, R. A. Tanzilli, R. O. Pohl, and J. W. Vandersande. The intrinsic thermal conductivity of AIN. *J. Phys. Chem. Solids*, **48**(7): 641–647 (1987).

[128] M. Schreier, N. Roschewsky, E. Dobler, S. Meyer, H. Huebl, R. Gross, and S. T. B. Goennenwein. Current heating induced spin Seebeck effect. *Appl. Phys. Lett.*, **103**: 242404 (2013).

[129] W. X. Wang, S. H. Wang, L. K. Zou, J. W. Cai, Z. G. Sun, and J. R. Sun. Joule heating-induced coexisted spin Seebeck effect and spin Hall magnetoresistance in the platinum/$Y_3Fe_5O_12$ structure. *Appl. Phys. Lett.*, **105**: 182403 (2014).

[130] T. Tritt. *Thermal Conductivity: Theory, Properties, and Applications*. Physics of Solids and Liquids, Springer US (2005).

[131] D. G. Cahill. Thermal conductivity measurement from 30 to 750 K: The 3ω method. *Rev. Sci. Instrum.*, **61**(2): 802–808 (1990).

[132] S. M. Lee and D. G. Cahill. Heat transport in thin dielectric films. *J. Appl. Phys.*, **81**(6): 2590–2595 (1997).

[133] J. Alvarez-Quintana and J. Rodríguez-Viejo. Extension of the 3ω method to measure the thermal conductivity of thin films without a reference sample. *Sensors Actuators, A Phys.*, **142**(1): 232–236 (2008).

[134] D. G. Cahill, M. Katiyar, and J. Abelson. Thermal conductivity of alpha-Si thin films. *Phys. Rev. B*, **50**(9): 6077–6082 (1994).

[135] C. Kübler, R. Huber, and A. Leitenstorfer. Ultrabroadband terahertz pulses: Generation and field-resolved detection. *Semicond. Sci. Technol.*, **20**(7): 128–133 (2005).

[136] E. Bründermann, H. W. Hübers, and M. F. G. Kimmitt. *Terahertz techniques*, volume 151 of *Springer Series in Optical Sciences*. Springer (2012).

[137] X. Zhang and J. Xu. *Introduction to THz Wave Photonics*. Springer (2009).

[138] H. Y. Hwang, S. Fleischer, N. C. Brandt, B. G. Perkins, M. Liu, K. Fan, A. Sternbach, X. Zhang, R. D. Averitt, and K. A. Nelson. A review of non-linear terahertz spectroscopy with ultrashort tabletop-laser pulses. *J. Mod. Opt.*, **62**(18): 1447–1479 (2015).

[139] E. Beaurepaire, J. C. Merle, A. Daunois, and J. Y. Bigot. Ultrafast spin dynamics in ferromagnetic nickel. *Phys. Rev. Lett.*, **76**(22): 4250–4253 (1996).

[140] Z. Jin, A. Tkach, F. Casper, V. Spetter, H. Grimm, A. Thomas, T. Kampfrath, M. Bonn, M. Kläui, and D. Turchinovich. Accessing the fundamentals of magnetotransport in metals with terahertz probes. *Nat. Phys.*, **11**(9): 761–766 (2015).

[141] R. Shimano, Y. Ikebe, K. S. Takahashi, M. Kawasaki, N. Nagaosa, and Y. Tokura. Terahertz Faraday rotation induced by an anomalous Hall effect in the itinerant ferromagnet SrRuO3. *Epl*, **95**(1) (2011).

[142] T. J. Huisman, R. V. Mikhaylovskiy, T. Rasing, A. V. Kimel, A. Tsukamoto, B. De Ronde, L. Ma, W. J. Fan, and S. M. Zhou. Sub-100-ps dynamics of the anomalous Hall effect at terahertz frequencies. *Phys. Rev. B*, **95**(9): 1–8 (2017).

[143] T. Kampfrath, M. Battiato, P. Maldonado, G. Eilers, J. Nötzold, S. Mährlein, V. Zbarsky, F. Freimuth, Y. Mokrousov, S. Blügel, M. Wolf, I. Radu, P. M. Oppeneer, and M. Münzenberg. Terahertz spin current pulses controlled by magnetic heterostructures. *Nat. Nanotechnol.*, **8**(4): 256–260 (2013).

[144] T. Seifert, S. Jaiswal, U. Martens, J. Hannegan, L. Braun, P. Maldonado, F. Freimuth, A. Kronenberg, J. Henrizi, I. Radu, E. Beaurepaire, Y. Mokrousov, P. M. Oppeneer, M. Jourdan, G. Jakob, D. Turchinovich, L. M. Hayden, M. Wolf, M. Münzenberg, M. Kläui, and T. Kampfrath. Efficient metallic spintronic emitters of ultrabroadband terahertz radiation. *Nat. Photonics*, **10**(7): 483–488 (2016).

[145] T. Kampfrath. *Charge-Carrier Dynamics in Solids and Gases Observed by Time-Resolved Terahertz Spectroscopy.* Ph.D. thesis, Freie Universität Berlin (2005).

[146] L. Z. Braun. *Electron and Phonon Dynamics in Topological Insulators at THz Frequencies.* Ph.D. thesis, Freie Universität Berlin (2016).

[147] T. S. Seifert. *Spintronics with Terahertz Radiation: Probing and driving spins at highest frequencies.* Ph.D. thesis, Freie Universität Berlin (2017).

[148] R. Boyd and D. Prato. *Nonlinear Optics.* Elsevier Science (2008).

[149] D. Faivre. *Iron Oxides: From Nature to Applications.* Wiley (2016).

[150] R. Cornell and U. Schwertmann. *The Iron Oxides: Structure, Properties, Reactions, Occurrences and Uses.* Wiley (2003).

[151] M. Fonin, Y. S. Dedkov, U. Rüdiger, and G. Güntherodt. Magnetite: a search for the half-metallic state. *J. Phys. Condens. Matter*, **19**: 315217 (2007).

[152] D. Ihle and B. Lorenz. Small-polaron band versus hopping conduction in Fe3O4. *J. Phys. C Solid State Phys.*, **18**(21): L647–L650 (1985).

[153] E. J. W. Verwey. Electronic Conduction of Magnetite (Fe_3O_4) and its Transition Point at Low Temperatures. *Nature*, **144**: 327–328 (1939).

[154] R. W. Millar. The heat capacities at low temperatures of the oxides of tin and lead. *J. Am. Chem. Soc.*, **51**(1): 207–214 (1929).

[155] F. Walz. The Verwey transition - a topical review. *Journal of Physics: Condensed Matter*, **14**(12): 285–340 (2002).

[156] M. S. Senn, J. P. Wright, J. Cumby, and J. P. Attfield. Charge localization in the Verwey structure of magnetite. *Phys. Rev. B - Condens. Matter Mater. Phys.*, **92**(2): 1–7 (2015).

[157] P. Piekarz, K. Parlinski, and A. M. Olé. Mechanism of the verwey transition in magnetite. *Phys. Rev. Lett.*, **97**(15): 5–8 (2006).

[158] G. Subías, J. García, J. Blasco, M. G. Proietti, H. Renevier, and M. C. Sánchez. Magnetite, a model system for mixed-valence oxides, does not show charge ordering. *Phys. Rev. Lett.*, **93**(15): 15–18 (2004).

[159] J. García and G. Subías. The Verwey transition—a new perspective. *Journal of Physics: Condensed Matter*, **16**(7): R145–R178 (2004).

[160] M. Hoesch, P. Piekarz, A. Bosak, M. Le Tacon, M. Krisch, A. Kozłowski, A. M. Oleå, and K. Parlinski. Anharmonicity due to electron-phonon coupling in magnetite. *Phys. Rev. Lett.*, **110**(20): 1–5 (2013).

[161] P. A. Wagner. Changes in the oxidation of iron in magnetite. *Econ. Geol.*, **22**: 845–846 (1927).

[162] A. H. Morrish. Morphology and Physical Properties of Gamma Iron Oxide. In H. C. Freyhardt, editor, *Growth and Properties. Crystals (Growth, Properties, and Applications)*, volume 2, pages 171–197. Springer, Berlin (1980).

[163] R. Dronskowski. The little maghemite story: A classic functional material. *Adv. Funtional Mater.*, **11**(1): 27–29 (2001).

[164] K. Momma and F. Izumi. *VESTA3* for three-dimensional visualization of crystal, volumetric and morphology data. *Journal of Applied Crystallography*, **44**(6): 1272–1276 (2011).

[165] H. Yanagihara, M. Hasegawa, E. Kita, Y. Wakabayashi, H. Sawa, and K. Siratori. Iron vacancy ordered γ-Fe2O3(001) epitaxial films: The crystal structure and electrical resistivity. *Journal of the Physical Society of Japan*, **75**(5): 4708 (2006).

[166] H. Takei and S. Chiba. Vacancy ordering in epitaxially-grown single crystals of gfe2o3. *Journal of the Physical Society of Japan*, **21**(7): 1255–1263 (1966).

[167] P. B. Braun. A superstructure in spinels. *Nature*, **170**: 1123 (1952).

[168] G. W. Van Oosterhout and C. J. Rooijmans. A new superstructure in gamma-ferric oxide. *Nature*, **181**(4601): 44 (1958).

[169] C. Greaves. A powder neutron diffraction investigation of vacancy ordering and covalence in γ-Fe_2O_3. *Journal of Solid State Chemistry*, **49**(3): 325–333 (1983).

[170] S. Kachi, K. Momiyama, and S. Shimizu. An electron diffraction study and a theory of the transformation from $\gamma-Fe_2O_3$ to $\alpha-Fe_2O_3$. *Journal of the Physical Society of Japan*, **18**(1): 106–116 (1962).

[171] H. Ho, E. Goo, and G. Thomas. Crystal structure of acicular $\gamma-Fe_2O_3$ particles used in recording media. *Journal of Applied Physics*, **59**(1606): 44 (1986).

[172] C. Pecharromán and J. E. Gonzalez-Carreno, T., Iglesias. The Infrared Dielectric Properties of Maghemite ,γ-Fe_2O_3, from Reflectance Measurement on Pressed Powders. *Physics and Chemistry of Minerals*, **22**(1): 21–29 (1995).

[173] H. Shokrollahi. A review of the magnetic properties, synthesis methods and applications of maghemite. *Journal of Magnetism and Magnetic Materials*, **426**: 74 – 81 (2017).

[174] Magnesium oxide (MgO) crystal structure, lattice parameters, thermal expansion: Datasheet from Landolt-Börnstein - Group III Condensed Matter

· Volume 41B: "II-VI and I-VII Compounds; Semimagnetic Compounds" in SpringerMaterials (https://doi.org/10.1007/10681719_206). Part of SpringerMaterials.

[175] L. W. Martin, Y. H. Chu, and R. Ramesh. Advances in the growth and characterization of magnetic, ferroelectric, and multiferroic oxide thin films. *Materials Science and Engineering R: Reports*, **68**(4-6): 89–133 (2010).

[176] J. M. Orna. *Epitaxial Growth of half-metallic magnetic oxide thin films by Pulsed Laser Deposition.* Ph.D. thesis, University of Zaragoza (2010).

[177] J. P. Shepherd, R. Aragón, J. W. Koenitzer, and J. M. Honig. Changes in the nature of the Verwey transition in nonstoichiometric magnetite (Fe_3O_4). *Phys. Rev. B*, **32**: 1818–1819 (1985).

[178] Z. Kąkol and J. M. Honig. Influence of deviations from ideal stoichiometry on the anisotropy parameters of magnetite $Fe_{3(1-\delta)}O_4$. *Phys. Rev. B*, **40**: 9090–9097 (1989).

[179] J. P. Shepherd, J. W. Koenitzer, R. Aragón, J. Spal/ek, and J. M. Honig. Heat capacity and entropy of nonstoichiometric magnetite $Fe_{3(1-\delta)}O_4$: The thermodynamic nature of the Verwey transition. *Phys. Rev. B*, **43**: 8461–8471 (1991).

[180] V. A. M. Brabers, F. Walz, and H. Kronmüller. Impurity effects upon the Verwey transition in magnetite. *Phys. Rev. B*, **58**: 14163–14166 (1998).

[181] R. Aragón, P. M. Gehring, and S. M. Shapiro. Stoichiometry, percolation, and Verwey ordering in magnetite. *Phys. Rev. Lett.*, **70**: 1635–1638 (1993).

[182] P. Li, E. Y. Jiang, and H. L. Bai. Fabrication of ultrathin epitaxial γ-Fe_2O_3 films by reactive sputtering. *Journal of Physics D: Applied Physics*, **44**(7): 075003 (2011).

[183] T. Tepper, C. A. Ross, and G. F. Dionne. Microstructure and optical properties of pulsed-laser-deposited iron oxide films. *IEEE Transactions on Magnetics*, **40**(3): 1685–1690 (2004).

[184] X. Huang, Y. Yang, and J. Ding. Epitaxial growth of $\gamma-Fe_2O_3$ thin films on MgO substrates by pulsed laser deposition and their properties. *Acta Materialia*, **61**(2): 548 – 557 (2013).

[185] C. Brundle, T. Chuang, and K. Wandelt. Core and valence level photoemission studies of iron oxide surfaces and the oxidation of iron. *Surface Science*, **68**: 459 – 468 (1977).

[186] P. Mills and J. L. Sullivan. A study of the core level electrons in iron and its three oxides by means of X-ray photoelectron spectroscopy. *Journal of Physics D: Applied Physics*, **16**(5): 723–732 (1983).

[187] A. Fujimori, M. Saeki, N. Kimizuka, M. Taniguchi, and S. Suga. Photoemission satellites and electronic structure of Fe_2O_3. *Phys. Rev. B*, **34**: 7318–7328 (1986).

[188] S. Gota, E. Guiot, M. Henriot, and M. Gautier-Soyer. Atomic-oxygen-assisted MBE growth of $\alpha-Fe_2O_3$ on $\alpha-Al_2O_3(0001)$: Metastable FeO(111)-like phase at subnanometer thicknesses. *Phys. Rev. B*, **60**: 14387–14395 (1999).

[189] C. Ruby, B. Humbert, and J. Fusy. Surface and interface properties of epitaxial iron oxide thin films deposited on MgO(001) studied by XPS and Raman spectroscopy. *Surface and Interface Analysis*, **29**(6): 377–380 (2000).

[190] R. P. Gupta and S. K. Sen. Calculation of multiplet structure of core p-vacancy levels. *Phys. Rev. B*, **10**: 71–77 (1974).

[191] M. C. Biesinger, B. P. Payne, A. P. Grosvenor, L. W. Lau, A. R. Gerson, and R. S. Smart. Resolving surface chemical states in XPS analysis of first row transition metals, oxides and hydroxides: Cr, Mn, Fe, Co and Ni. *Applied Surface Science*, **257**(7): 2717 – 2730 (2011).

[192] P. Graat and M. A. J. Somers. Quantitative analysis of overlapping XPS peaks by spectrum reconstruction: determination of the thickness and composition of thin iron oxide films. *Surface and Interface Analysis*, **26**(11): 773–782 (1998).

[193] T. Yamashita and P. Hayes. Analysis of XPS spectra of Fe^{2+} and Fe^{3+} ions in oxide materials. *Applied Surface Science*, **254**(8): 2441 – 2449 (2008).

[194] N. S. McIntyre and D. G. Zetaruk. X-ray photoelectron spectroscopic studies of iron oxides. *Analytical Chemistry*, **49**(11): 1521–1529 (1977).

[195] J. M. Zuo and J. C. Mabon. Web-Based Electron Microscopy Application Software: Web-EMAPS. *Microscopy and Microanalysis*, **10**(S02): 1000 – 1001 (2004).

[196] W. Ryden, A. Lawson, and C. Sartain. Temperature dependence of the resistivity of RuO2 and IrO2. *Physics Letters A*, **26**(5): 209 – 210 (1968).

[197] W. D. Ryden, A. W. Lawson, and C. C. Sartain. Electrical Transport Properties of IrO_2 and RuO_2. *Phys. Rev. B*, **1**: 1494–1500 (1970).

[198] T. Nakamura, Y. Nakao, A. Kamisawa, and H. Takasu. Preparation of Pb(Zr,Ti)O3 thin films on electrodes including IrO2. *Applied Physics Letters*, **65**(12): 1522–1524 (1994).

[199] C. U. Pinnow, I. Kasko, N. Nagel, T. Mikolajick, C. Dehm, F. Jahnel, M. Seibt, U. Geyer, and K. Samwer. Oxygen tracer diffusion in IrO2 barrier films. *Journal of Applied Physics*, **91**(3): 1707–1709 (2002).

[200] R. Kötz, H. Neff, and S. Stucki. Anodic Iridium Oxide Films: XPS-Studies of Oxidation State Changes and. *Journal of The Electrochemical Society*, **131**(1): 72–77 (1984).

[201] A. Osaka, T. Takatsuna, and Y. Miura. Iridium oxide films via sol-gel processing. *Journal of Non-Crystalline Solids*, **178**: 313 – 319 (1994). Proceding of the First PAC RIM Metting on Glass and Optical Materials.

[202] T. Katsube, I. Lauks, and J. Zemel. pH-sensitive sputtered iridium oxide films. *Sensors and Actuators*, **2**: 399 – 410 (1981).

[203] A. Fog and R. P. Buck. Electronic semiconducting oxides as pH sensors. *Sensors and Actuators*, **5**(2): 137 – 146 (1984).

[204] S. Cogan, T. Plante, R. McFadden, and R. Rauh. Solar modulation in a-WO3/a-IrO2 and c-KxWO3+(x/2)/a-IrO2 complementary electrochromic windows. *Solar Energy Materials*, **16**(5): 371 – 382 (1987).

[205] K. Yamanaka. Anodically Electrodeposited Iridium Oxide Films (AEIROF) from Alkaline Solutions for Electrochromic Display Devices. *Japanese Journal of Applied Physics*, **28**(Part 1, No. 4): 632–637 (1989).

[206] B. O'Brien and W. Carroll. The evolution of cardiovascular stent materials and surfaces in response to clinical drivers: A review. *Acta Biomaterialia*, **5**(4): 945 – 958 (2009).

[207] K. Pásztor, A. Sekiguchi, N. Shimo, N. Kitamura, and H. Masuhara. Iridium oxide-based microelectrochemical transistors for pH sensing. *Sensors and Actuators B: Chemical*, **12**(3): 225 – 230 (1993).

[208] B. O'Brien and C. Chandrasekaran. Development of Iridium Oxide as a Cardiovascular Stent Coating. *Advanced Materials & Processes*, **162**(11): 82–84 (2005).

[209] L. Atanasoska, P. Gupta, C. Deng, R. Warner, S. Larson, and J. Thompson. XPS, AES, and Electrochemical Study of Iridium Oxide Coating Materials for Cardiovascular Stent Application. *ECS Transactions*, **16**(38): 37–48 (2019).

[210] H.-J. Cho, C. S. Kang, C. S. Hwang, J.-W. Kim, H. Horii, B. T. Lee, S. I. Lee, and M. Y. Lee. Structural and Electrical Properties of $Ba_{0.5}Sr_{0.5}TiO_3$ Films on Ir and IrO_2 Electrodes. *Japanese Journal of Applied Physics*, **36**(Part 2, No. 7A): L874–L876 (1997).

[211] J. P. Clancy, N. Chen, C. Y. Kim, W. F. Chen, K. W. Plumb, B. C. Jeon, T. W. Noh, and Y.-J. Kim. Spin-orbit coupling in iridium-based 5*d* compounds probed by x-ray absorption spectroscopy. *Phys. Rev. B*, **86**: 195131 (2012).

[212] S. R. Butler and J. L. Gillson. Crystal growth, electrical resistivity and lattice parameters of RuO_2 and IrO_2. *Mater. Res. Bull.*, **6**(2): 81–89 (1971).

[213] K. Fujiwara, Y. Fukuma, J. Matsuno, H. Idzuchi, Y. Niimi, Y. Otani, and H. Takagi. 5d iridium Oxide As a Material for Spin-Current Detection. *Nature Communications*, **4**(2893): 1–6 (2013).

[214] Y. Tokura. Correlated-electron physics in transition-metal oxides. *Physics Today*, **56**(7): 50–55 (2003).

[215] J. G. Rau, E. K.-H. Lee, and H.-Y. Kee. Spin-Orbit Physics Giving Rise to Novel Phases in Correlated Systems: Iridates and Related Materials. *Annual Review of Condensed Matter Physics*, **7**(1): 195–221 (2016).

[216] G. Cao and P. Schlottmann. The challenge of spin–orbit-tuned ground states in iridates: a key issues review. *Reports on Progress in Physics*, **81**(4): 042502 (2018).

[217] K. Matsuhira, M. Wakeshima, R. Nakanishi, T. Yamada, A. Nakamura, W. Kawano, S. Takagi, and Y. Hinatsu. Metal-insulator transition in pyrochlore iridates $Ln_2Ir_2O_7$ (Ln = Nd, Sm, and Eu). *J. Phys. Soc. Japan*, **76**(43706): 1–5 (2007).

[218] B. J. Yang and Y. B. Kim. Topological insulators and metal-insulator transition in the pyrochlore iridates. *Phys. Rev. B - Condens. Matter Mater. Phys.*, **82**(85111): 1–11 (2010).

[219] S. Nakatsuji, Y. MacHida, Y. Maeno, T. Tayama, T. Sakakibara, J. Van Duijn, L. Balicas, J. N. Millican, R. T. MacAluso, and J. Y. Chan. Metallic spin-liquid behavior of the geometrically frustrated kondo lattice $Pr_2Ir_2O_7$. *Phys. Rev. Lett.*, **96**(87204): 1–4 (2006).

[220] S. M. Disseler, S. R. Giblin, C. Dhital, K. C. Lukas, S. D. Wilson, and M. J. Graf. Magnetization and Hall effect studies on the pyrochlore iridate Nd 2Ir2O7. *Phys. Rev. B - Condens. Matter Mater. Phys.*, **87**(60403): 1–5 (2013).

[221] B. J. Kim, H. Ohsumi, T. Komesu, S. Sakai, T. Morita, H. Takagi, and T. Arima. Phase-Sensitive Observation of a Spin-Orbital Mott State in Sr_2IrO_4. *Science*, **323**: 1329–1332 (2009).

[222] H.-S. Kim, C. H. Kim, H. Jeong, H. Jin, and J. Yu. Strain-induced topological insulator phase and effective magnetic interactions in Li_2IrO_3. *Phys. Rev. B*, **87**: 165117 (2013).

[223] Z. Qiu, D. Hou, T. Kikkawa, K. I. Uchida, and E. Saitoh. All-oxide spin Seebeck effects. *Applied Physics Express*, **8**(83001) (2015).

[224] L. F. Mattheiss. Electronic structure of RuO_2, OsO_2, and IrO_2. *Phys. Rev. B*, **13**: 2433–2450 (1976).

[225] G. K. Wertheim and H. J. Guggenheim. Conduction-electron screening in metallic oxides: IrO_2. *Phys. Rev. B*, **22**: 4680–4683 (1980).

[226] J. M. Kahk, C. G. Poll, F. E. Oropeza, J. M. Ablett, D. Céolin, J.-P. Rueff, S. Agrestini, Y. Utsumi, K. D. Tsuei, Y. F. Liao, F. Borgatti, G. Panaccione, A. Regoutz, R. G. Egdell, B. J. Morgan, D. O. Scanlon, and D. J. Payne. Understanding the Electronic Structure of IrO_2 Using Hard-X-ray Photoelectron Spectroscopy and Density-Functional Theory. *Phys. Rev. Lett.*, **112**: 117601 (2014).

[227] Y. Ping, G. Galli, and W. A. Goddard. Electronic Structure of IrO2: The Role of the Metal d Orbitals. *J. Phys. Chem. C*, **119**: 11570–11577 (2015).

[228] Y. Sun, Y. Zhang, C. X. Liu, C. Felser, and B. Yan. Dirac nodal lines and induced spin Hall effect in metallic rutile oxides. *Physical Review B*, **95**(235104): 1–7 (2017).

[229] P. K. Das, J. Sławińska, I. Vobornik, J. Fujii, A. Regoutz, J. M. Kahk, D. O. Scanlon, B. J. Morgan, C. McGuinness, E. Plekhanov, D. Di Sante, Y. S. Huang, R. S. Chen, G. Rossi, S. Picozzi, W. R. Branford, G. Panaccione, and D. J. Payne. Role of spin-orbit coupling in the electronic structure of Ir O2. *Physical Review Materials*, **2**(65001): 1–7 (2018).

[230] R. R. Daniels, G. Margaritondo, C.-A. Georg, and F. Lévy. Electronic states of rutile dioxides: RuO_2, IrO_2, and $Ru_xIr_{1-x}O_2$. *Phys. Rev. B*, **29**: 1813–1818 (1984).

[231] J. S. de Almeida and R. Ahuja. Electronic and optical properties of RuO_2 and IrO_2. *Phys. Rev. B*, **73**: 165102 (2006).

[232] Y. Hirata, K. Ohgushi, J.-i. Yamaura, H. Ohsumi, S. Takeshita, M. Takata, and T.-h. Arima. Complex orbital state stabilized by strong spin-orbit coupling in a metallic iridium oxide IrO_2. *Phys. Rev. B*, **87**: 161111 (2013).

[233] J. K. Kawasaki, M. Uchida, H. Paik, D. G. Schlom, and K. M. Shen. Evolution of electronic correlations across the rutile, perovskite, and Ruddelsden-Popper iridates with octahedral connectivity. *Physical Review B*, **94**(121104): 1–6 (2016).

[234] W. J. Kim, S. Y. Kim, C. H. Kim, C. H. Sohn, O. B. Korneta, S. C. Chae, and T. W. Noh. Spin-orbit coupling induced band structure change and orbital character of epitaxial IrO_2 films. *Physical Review B*, **93**(45104): 1–5 (2016).

[235] J. Riga, C. Tenret-Noël, J. J. Pireaux, R. Caudano, J. J. Verbist, and Y. Gobillon. Electronic structure of rutile oxides TiO_2, RuO_2 and IrO_2 studied by X-ray Photoelectron Spectroscopy. *Phys. Scr.*, **16**(5-6): 351–354 (1977).

[236] M. A. El Khakani, M. Chaker, and E. Gat. Pulsed laser deposition of highly conductive iridium oxide thin films. *Applied Physics Letters*, **69**(14): 2027–2029 (1996).

[237] M. El Khakani and M. Chaker. Reactive pulsed laser deposition of iridium oxide thin films. *Thin Solid Films*, **335**(1): 6 – 12 (1998).

[238] Y. Liu, H. Masumoto, and T. Goto. Preparation of IrO₂ Thin Films by Oxidating Laser-ablated Ir. *MATERIALS TRANSACTIONS*, **45**(3): 900–903 (2004).

[239] L. Zhang, Y. Gong, C. Wang, Q. Shen, and M. Xia. Substrate temperature dependent morphology and resistivity of pulsed laser deposited iridium oxide thin films. *Thin Solid Films*, **496**(2): 371 – 375 (2006).

[240] M. Uchida, W. Sano, K. S. Takahashi, T. Koretsune, Y. Kozuka, R. Arita, Y. Tokura, and M. Kawasaki. Field-direction control of the type of charge carriers in nonsymmorphic IrO_2. *Phys. Rev. B*, **91**: 241119 (2015).

[241] J. Hämäläinen, M. Kemell, F. Munnik, U. Kreissig, M. Ritala, and M. Leskelä. Atomic Layer Deposition of Iridium Oxide Thin Films from Ir(acac)3 and Ozone. *Chemistry of Materials*, **20**(9): 2903–2907 (2008).

[242] S.-W. Kim, S.-H. Kwon, D.-K. Kwak, and S.-W. Kang. Phase control of iridium and iridium oxide thin films in atomic layer deposition. *Journal of Applied Physics*, **103**(2): 023517 (2008).

[243] S. K. Panda, S. Bhowal, A. Delin, O. Eriksson, and I. Dasgupta. Effect of spin orbit coupling and Hubbard U on the electronic structure of IrO_2. *Phys. Rev. B*, **89**: 155102 (2014).

[244] X. Ming, K. Yamauchi, T. Oguchi, and S. Picozzi. Metal-Insulator Transition and Jeff = 1/2 Spin-Orbit Insulating State in Rutile-based IrO2/TiO2 Superlattices (2017).

[245] J. D. Adam, L. E. Davis, G. F. Dionne, E. F. Schloemann, and S. N. Stitzer. Ferrite devices and materials. *IEEE Transactions on Microwave Theory and Techniques*, **50**(3): 721–737 (2002).

[246] B. J. H. Stadler and T. Mizumoto. Integrated Magneto-Optical Materials and Isolators: A Review. *IEEE Photonics Journal*, **6**(1): 1–15 (2014).

[247] E. Mallmann, A. Sombra, J. Goes, and P. Fechine. Yttrium Iron Garnet: Properties and Applications Review. *Solid State Phenomena*, **202**: 65–96 (2013).

[248] S. Geller and M. Gilleo. The crystal structure and ferrimagnetism of yttrium-iron garnet, Y3Fe2(FeO4)3. *Journal of Physics and Chemistry of Solids*, **3**(1): 30 – 36 (1957).

[249] E. E. Anderson. Molecular Field Model and the Magnetization of YIG. *Phys. Rev.*, **134**: A1581–A1585 (1964).

[250] A. A. Serga, A. V. Chumak, and B. Hillebrands. YIG magnonics. *Journal of Physics D: Applied Physics*, **43**(26): 264002 (2010).

[251] M. C. Onbasli, A. Kehlberger, D. H. Kim, G. Jakob, M. Kläui, A. V. Chumak, B. Hillebrands, and C. A. Ross. Pulsed laser deposition of epitaxial yttrium iron garnet films with low Gilbert damping and bulk-like magnetization. *APL Materials*, **2**(10): 106102 (2014).

[252] H. Yu, O. D'Allivy Kelly, V. Cros, R. Bernard, P. Bortolotti, A. Anane, F. Brandl, R. Huber, I. Stasinopoulos, and D. Grundler. Magnetic thin-film insulator with ultra-low spin wave damping for coherent nanomagnonics. *Scientific Reports*, **4**: 2–6 (2014).

[253] C. Hauser, T. Richter, N. Homonnay, C. Eisenschmidt, M. Qaid, H. Deniz, D. Hesse, M. Sawicki, S. G. Ebbinghaus, and G. Schmidt. Yttrium Iron Garnet Thin Films with Very Low Damping Obtained by Recrystallization of Amorphous Material. *Scientific Reports*, **6**(February): 1–8 (2016).

[254] N. S. Sokolov, V. V. Fedorov, A. M. Korovin, S. M. Suturin, D. A. Baranov, S. V. Gastev, B. B. Krichevtsov, K. Y. Maksimova, A. I. Grunin, V. E. Bursian, L. V. Lutsev, and M. Tabuchi. Thin yttrium iron garnet films grown by pulsed

laser deposition: Crystal structure, static, and dynamic magnetic properties. *Journal of Applied Physics*, **119**(2): 023903 (2016).

[255] J. Barker and G. E. W. Bauer. Thermal Spin Dynamics of Yttrium Iron Garnet. *Phys. Rev. Lett.*, **117**: 217201 (2016).

[256] H. Wang, C. Du, P. Chris Hammel, and F. Yang. Spin current and inverse spin Hall effect in ferromagnetic metals probed by Y3Fe5O12-based spin pumping. *Applied Physics Letters*, **104**(20): 202405 (2014).

[257] C. Dubs, O. Surzhenko, R. Linke, A. Danilewsky, U. Brückner, and J. Dellith. Sub-micrometer yttrium iron garnet LPE films with low ferromagnetic resonance losses. *Journal of Physics D: Applied Physics*, **50**(20): 204005 (2017).

[258] S. Li, W. Zhang, J. Ding, J. E. Pearson, V. Novosad, and A. Hoffmann. Epitaxial patterning of nanometer-thick Y3Fe5O12 films with low magnetic damping. *Nanoscale*, **8**: 388–394 (2016).

[259] H. Chang, P. Li, W. Zhang, T. Liu, A. Hoffmann, L. Deng, and M. Wu. Nanometer-Thick Yttrium Iron Garnet Films With Extremely Low Damping. *IEEE Magnetics Letters*, **5**: 1–4 (2014).

[260] Y. Sun, Y.-Y. Song, H. Chang, M. Kabatek, M. Jantz, W. Schneider, M. Wu, H. Schultheiss, and A. Hoffmann. Growth and ferromagnetic resonance properties of nanometer-thick yttrium iron garnet films. *Applied Physics Letters*, **101**(15): 152405 (2012).

[261] T. Liu, H. Chang, V. Vlaminck, Y. Sun, M. Kabatek, A. Hoffmann, L. Deng, and M. Wu. Ferromagnetic resonance of sputtered yttrium iron garnet nanometer films. *Journal of Applied Physics*, **115**(17): 17A501 (2014).

[262] S. S. Kalarickal, P. Krivosik, J. Das, K. S. Kim, and C. E. Patton. Microwave damping in polycrystalline Fe-Ti-N films: Physical mechanisms

and correlations with composition and structure. *Phys. Rev. B*, **77**: 054427 (2008).

[263] P. Pirro, T. Brächer, A. V. Chumak, B. Lägel, C. Dubs, O. Surzhenko, P. Görnert, B. Leven, and B. Hillebrands. Spin-wave excitation and propagation in microstructured waveguides of yttrium iron garnet/Pt bilayers. *Applied Physics Letters*, **104**(1): 012402 (2014).

[264] R. Ramos, T. Kikkawa, A. Anadón, I. Lucas, T. Niizeki, K. Uchida, P. A. Algarabel, L. Morellón, M. H. Aguirre, M. R. Ibarra, and E. Saitoh. Interface-induced anomalous Nernst effect in Fe_3O_4/Pt-based heterostructures. *Applied Physics Letters*, **114**(11): 113902 (2019).

[265] H. B. Vasili, M. Gamino, J. Gàzquez, F. Sánchez, M. Valvidares, P. Gargiani, E. Pellegrin, and J. Fontcuberta. Magnetoresistance in Hybrid Pt/CoFe2O4 Bilayers Controlled by Competing Spin Accumulation and Interfacial Chemical Reconstruction. *ACS Applied Materials & Interfaces*, **10**(14): 12031–12041 (2018). PMID: 29546753.

[266] P. Jiménez-Cavero, I. Lucas, A. Anadón, R. Ramos, T. Niizeki, M. H. Aguirre, P. A. Algarabel, K. Uchida, M. R. Ibarra, E. Saitoh, and L. Morellón. Spin Seebeck effect in insulating epitaxial $\gamma-Fe_2O_3$ thin films. *APL Materials*, **5**(2): 026103 (2017).

[267] R. Ramos, T. Kikkawa, K. Uchida, H. Adachi, I. Lucas, M. H. Aguirre, P. Algarabel, L. Morellón, S. Maekawa, E. Saitoh, and M. R. Ibarra. Observation of the spin Seebeck effect in epitaxial Fe3O4 thin films. *Applied Physics Letters*, **102**(7): 072413 (2013).

[268] R. Ramos, T. Kikkawa, M. H. Aguirre, I. Lucas, A. Anadón, T. Oyake, K. Uchida, H. Adachi, J. Shiomi, P. A. Algarabel, L. Morellón, S. Maekawa, E. Saitoh, and M. R. Ibarra. Unconventional scaling and significant enhancement of the spin Seebeck effect in multilayers. *Phys. Rev. B*, **92**: 220407 (2015).

[269] T. Kikkawa, K. Uchida, Y. Shiomi, Z. Qiu, D. Hou, D. Tian, H. Nakayama, X.-F. Jin, and E. Saitoh. Longitudinal Spin Seebeck Effect Free from the Proximity Nernst Effect. *Phys. Rev. Lett.*, **110**: 067207 (2013).

[270] A. Kehlberger, U. Ritzmann, D. Hinzke, E.-J. Guo, J. Cramer, G. Jakob, M. C. Onbasli, D. H. Kim, C. A. Ross, M. B. Jungfleisch, B. Hillebrands, U. Nowak, and M. Kläui. Length Scale of the Spin Seebeck Effect. *Phys. Rev. Lett.*, **115**: 096602 (2015).

[271] K.-i. Uchida, T. Nonaka, T. Ota, and E. Saitoh. Longitudinal spin-Seebeck effect in sintered polycrystalline (Mn,Zn)Fe2O4. *Applied Physics Letters*, **97**(26): 262504 (2010).

[272] J. D. Arboleda, O. Arnache Olmos, M. H. Aguirre, R. Ramos, A. Anadón, and M. R. Ibarra. Spin Seebeck effect in a weak ferromagnet. *Applied Physics Letters*, **108**(23): 232401 (2016).

[273] E.-J. Guo, A. Herklotz, A. Kehlberger, J. Cramer, G. Jakob, and M. Kläui. Thermal generation of spin current in epitaxial CoFe2O4 thin films. *Applied Physics Letters*, **108**(2): 022403 (2016).

[274] B. W. Wu, G. Y. Luo, J. G. Lin, and S. Y. Huang. Longitudinal spin Seebeck effect in a half-metallic $La_{0.7}Sr_{0.3}MnO_3$ film. *Phys. Rev. B*, **96**: 060402 (2017).

[275] Y.-J. Chen and S.-Y. Huang. Light-induced thermal spin current. *Phys. Rev. B*, **99**: 094426 (2019).

[276] W. Eerenstein, T. T. M. Palstra, T. Hibma, and S. Celotto. Origin of the increased resistivity in epitaxial Fe_3O_4 films. *Phys. Rev. B*, **66**: 201101 (2002).

[277] E. Langenberg, E. Ferreiro-Vila, V. Leborán, A. O. Fumega, V. Pardo, and F. Rivadulla. Analysis of the temperature dependence of the thermal conductivity of insulating single crystal oxides. *APL Materials*, **4**(10): 104815 (2016).

[278] G. A. Slack. Thermal Conductivity of MgO, Al_2O_3, $MgAl_2O_4$, and Fe_3O_4 Crystals from 3° to 300°K. *Phys. Rev.*, **126**: 427–441 (1962).

[279] M. Schreier, A. Kamra, M. Weiler, J. Xiao, G. E. W. Bauer, R. Gross, and S. T. B. Goennenwein. Magnon, phonon, and electron temperature profiles and the spin Seebeck effect in magnetic insulator/normal metal hybrid structures. *Phzs. Rev. B*, **88**: 094410 (2013).

[280] R. M. Costescu, M. A. Wall, and D. G. Cahill. Thermal conductance of epitaxial interfaces. *Phys. Rev. B*, **67**: 054302 (2003).

[281] K. Uchida, M. Ishida, T. Kikkawa, A. Kirihara, T. Murakami, and E. Saitoh. Longitudinal spin Seebeck effect: from fundamentals to applications. *J. Phys. Condens. Matter*, **26**(34): 343202 (2014).

[282] K. Uchida, H. Adachi, T. Kikkawa, A. Kirihara, M. Ishida, S. Yorozu, S. Maekawa, and E. Saitoh. Thermoelectric Generation Based on Spin Seebeck Effects. *Proceedings of the IEEE*, **104**(10): 1946–1973 (2016).

[283] A. Hoffmann. Spin Hall Effects in Metals. *IEEE Trans. Magn.*, **49**(10): 5172–5193 (2013).

[284] A. Anadón, R. Ramos, I. Lucas, P. A. Algarabel, L. Morellón, M. R. Ibarra, and M. H. Aguirre. Characteristic length scale of the magnon accumulation in Fe_3O_4/Pt bilayer structures by incoherent thermal excitation. *Appl. Phys. Lett.*, **109**(012404) (2016).

[285] F. D. Czeschka, L. Dreher, M. S. Brandt, M. Weiler, M. Althammer, I.-M. Imort, G. Reiss, A. Thomas, W. Schoch, W. Limmer, H. Huebl, R. Gross, and S. T. B. Goennenwein. Scaling Behavior of the Spin Pumping Effect in Ferromagnet-Platinum Bilayers. *Phys. Rev. Lett.*, **107**: 046601 (2011).

[286] E.-J. Guo, J. Cramer, A. Kehlberger, C. A. Ferguson, D. A. MacLaren, G. Jakob, and M. Kläui. Influence of Thickness and Interface on the

Low-Temperature Enhancement of the Spin Seebeck Effect in YIG Films. *Phys. Rev. X*, **6**: 031012 (2016).

[287] A. Sola, M. Kuepferling, V. Basso, M. Pasquale, T. Kikkawa, K. Uchida, and E. Saitoh. Evaluation of thermal gradients in longitudinal spin Seebeck effect measurements. *Journal of Applied Physics*, **117**(17): 17C510 (2015).

[288] A. J. Caruana, M. D. Cropper, J. Zipfel, Z. Zhou, G. D. West, and K. Morrison. Demonstration of polycrystalline thin film coatings on glass for spin Seebeck energy harvesting. *physica status solidi (RRL) – Rapid Research Letters*, **10**(8): 613–617 (2016).

[289] S. R. Marmion, M. Ali, M. McLaren, D. A. Williams, and B. J. Hickey. Temperature dependence of spin Hall magnetoresistance in thin YIG/Pt films. *Phys. Rev. B*, **89**: 220404 (2014).

[290] B.-W. Dong, L. Baldrati, C. Schneider, T. Niizeki, R. Ramos, A. Ross, J. Cramer, E. Saitoh, and M. Kläui. Antiferromagnetic NiO thickness dependent sign of the spin Hall magnetoresistance in $\gamma-Fe_2O_3$/NiO/Pt epitaxial stacks. *Applied Physics Letters*, **114**(10): 102405 (2019).

[291] A. Prakash, B. Flebus, J. Brangham, F. Yang, Y. Tserkovnyak, and J. P. Heremans. Evidence for the role of the magnon energy relaxation length in the spin Seebeck effect. *Phys. Rev. B*, **97**: 020408 (2018).

[292] M. Schreier, F. Kramer, H. Huebl, S. Geprägs, R. Gross, S. T. B. Goennenwein, T. Noack, T. Langner, A. A. Serga, B. Hillebrands, and V. I. Vasyuchka. Spin Seebeck effect at microwave frequencies. *Phys. Rev. B*, **93**: 224430 (2016).

[293] D. W. Lynch and W. Hunter. - Comments on the Optical Constants of Metals and an Introduction to the Data for Several Metals. In E. D. Palik, editor, *Handbook of Optical Constants of Solids*, pages 275 – 367. Academic Press, Burlington (1997).

[294] D. W. Lynch and W. Hunter. - An Introduction to the Data for Several Metals. In E. D. Palik, editor, *Handbook of Optical Constants of Solids*, pages 341 – 419. Academic Press, Burlington (1997).

[295] A. Schlegel, S. F. Alvarado, and P. Wachter. Optical properties of magnetite (Fe_3O_4). *Journal of Physics C: Solid State Physics*, **12**(6): 1157–1164 (1979).

[296] M. Battiato, K. Carva, and P. M. Oppeneer. Theory of laser-induced ultrafast superdiffusive spin transport in layered heterostructures. *Phys. Rev. B*, **86**: 024404 (2012).

[297] L. Braun, G. Mussler, A. Hruban, M. Konczykowski, T. Schumann, M. Wolf, M. Münzenberg, L. Perfetti, and T. Kampfrath. Ultrafast photocurrents at the surface of the three-dimensional topological insulator Bi2Se3. *Nature Communications*, **7**: 1–9 (2016).

[298] T. Seifert, U. Martens, S. G′unther, M. A. W. Schoen, F. Radu, X. Z. Chen, I. Lucas, R. Ramos, M. H. Aguirre, P. A. Algarabel, A. Anadón, H. S. K′orner, J. Walowski, C. Back, M. R. Ibarra, L. Morellón, E. Saitoh, M. Wolf, C. Song, K. Uchida, M. Münzenberg, I. Radu, and T. Kampfrath. Terahertz Spin Currents and Inverse Spin Hall Effect in Thin-Film Heterostructures Containing Complex Magnetic Compounds. *SPIN*, **07**(03): 1740010 (2017).

[299] W. Wang, J.-M. Mariot, M. C. Richter, O. Heckmann, W. Ndiaye, P. De Padova, A. Taleb-Ibrahimi, P. Le Fèvre, F. Bertran, F. Bondino, E. Magnano, J. Krempaský, P. Blaha, C. Cacho, F. Parmigiani, and K. Hricovini. Fe t_{2g} band dispersion and spin polarization in thin films of Fe_3O_4(0 0 1)/MgO(0 0 1): Half-metallicity of magnetite revisited. *Phys. Rev. B*, **87**: 085118 (2013).

[300] H.-T. Jeng, G. Y. Guo, and D. J. Huang. Charge-Orbital Ordering and Verwey Transition in Magnetite. *Phys. Rev. Lett.*, **93**: 156403 (2004).

[301] M. Weiler, M. Althammer, M. Schreier, J. Lotze, M. Pernpeintner, S. Meyer, H. Huebl, R. Gross, A. Kamra, J. Xiao, Y.-T. Chen, H. Jiao, G. E. W. Bauer,

and S. T. B. Goennenwein. Experimental Test of the Spin Mixing Interface Conductivity Concept. *Phys. Rev. Lett.*, **111**: 176601 (2013).

[302] V. Castel, N. Vlietstra, J. Ben Youssef, and B. J. Van Wees. Platinum thickness dependence of the inverse spin-Hall voltage from spin pumping in a hybrid yttrium iron garnet/platinum system. *Applied Physics Letters*, **101**(132414) (2012).

[303] Y. Saiga, K. Mizunuma, Y. Kono, J. C. Ryu, H. Ono, M. Kohda, and E. Okuno. Platinum thickness dependence and annealing effect of the spin-Seebeck voltage in platinum/yttrium iron garnet structures. *Applied Physics Express*, **7**(9): 093001 (2014).

[304] O. P. Sushkov, A. I. Milstein, M. Mori, and S. Maekawa. Relativistic effects in scattering of polarized electrons. *EPL (Europhysics Letters)*, **103**(4): 47003 (2013).

[305] A. Fert and P. M. Levy. Spin Hall Effect Induced by Resonant Scattering on Impurities in Metals. *Phys. Rev. Lett.*, **106**: 157208 (2011).

[306] K. Chadova, D. V. Fedorov, C. Herschbach, M. Gradhand, I. Mertig, D. Ködderitzsch, and H. Ebert. Separation of the individual contributions to the spin Hall effect in dilute alloys within the first-principles Kubo-Středa approach. *Phys. Rev. B*, **92**: 045120 (2015).

[307] Y. Li, D. Hou, L. Ye, Y. Tian, J. Xu, G. Su, and X. Jin. Evidence of the side jump mechanism in the anomalous Hall effect in paramagnets. *EPL (Europhysics Letters)*, **110**(2): 27002 (2015).

[308] Y. Tian, L. Ye, and X. Jin. Proper Scaling of the Anomalous Hall Effect. *Phys. Rev. Lett.*, **103**: 087206 (2009).

[309] D. Yue and X. Jin. Towards a Better Understanding of the Anomalous Hall Effect. *Journal of the Physical Society of Japan*, **86**(1): 011006 (2017).

[310] R. Ramos, A. Anadón, I. Lucas, K. Uchida, P. A. Algarabel, L. Morellón, M. H. Aguirre, E. Saitoh, and M. R. Ibarra. Thermoelectric performance of spin Seebeck effect in Fe3O4/Pt-based thin film heterostructures. *APL Materials*, **4**(10): 104802 (2016).

[311] W. Lin, K. Chen, S. Zhang, and C. L. Chien. Enhancement of Thermally Injected Spin Current through an Antiferromagnetic Insulator. *Phys. Rev. Lett.*, **116**: 186601 (2016).

[312] S. M. Rezende, R. L. Rodríguez-Suárez, and A. Azevedo. Diffusive magnonic spin transport in antiferromagnetic insulators. *Phys. Rev. B*, **93**: 054412 (2016).

[313] A. Azevedo, L. H. Vilela-Leão, R. L. Rodríguez-Suárez, A. F. Lacerda Santos, and S. M. Rezende. Spin pumping and anisotropic magnetoresistance voltages in magnetic bilayers: Theory and experiment. *Phys. Rev. B*, **83**: 144402 (2011).

[314] W. Zhang, V. Vlaminck, J. E. Pearson, R. Divan, S. D. Bader, and A. Hoffmann. Determination of the Pt spin diffusion length by spin-pumping and spin Hall effect. *Applied Physics Letters*, **103**(24): 242414 (2013).

[315] J.-C. Rojas-Sánchez, N. Reyren, P. Laczkowski, W. Savero, J.-P. Attané, C. Deranlot, M. Jamet, J.-M. George, L. Vila, and H. Jaffrès. Spin Pumping and Inverse Spin Hall Effect in Platinum: The Essential Role of Spin-Memory Loss at Metallic Interfaces. *Phys. Rev. Lett.*, **112**: 106602 (2014).

[316] M. Isasa, E. Villamor, L. E. Hueso, M. Gradhand, and F. Casanova. Temperature dependence of spin diffusion length and spin Hall angle in Au and Pt. *Phys. Rev. B*, **91**: 024402 (2015).

[317] X. Tao, Q. Liu, B. Miao, R. Yu, Z. Feng, L. Sun, B. You, J. Du, K. Chen, S. Zhang, L. Zhang, Z. Yuan, D. Wu, and H. Ding. Self-consistent determination of spin Hall angle and spin diffusion length in Pt and Pd: The role of the interface spin loss. *Science Advances*, **4**(6) (2018).